MIT Libraries
Document Services

Room 14-0551
77 Massachusetts Avenue
Cambridge, MA 02139
Ph: 617.253.5668 Fax: 617.253.1690
Email: docs@mit.edu
http://libraries.mit.edu/docs

DISCLAIMER OF QUALITY

Due to the condition of the original material, there are unavoidable flaws in this reproduction. We have made every effort possible to provide you with the best copy available. If you are dissatisfied with this product and find it unusable, please contact Document Services as soon as possible.

Thank you.

This report contains poorly cropped right side margin. Text deletion is a result.

METHODS FOR STEADY STATE THERMAL/HYDRAULIC ANALYSIS OF PRESSURIZED WATER REACTOR CORES

by

P. Moreno, C. Chiu, R. Bowring
E. Khan, J. Liu, N. Todreas

Energy Laboratory Report No. MIT-EL 76-006

Original: March, 1977
Revision 1: July, 1977

This work is presented in Three Volumes

VOLUME I: CONCLUSION AND RECOMMENDED METHODS

VOLUME II: TRANSPORT COEFFICIENTS FOR TWO DIMENSIONAL CHANNEL REPRESENTATIONS

VOLUME III: TRANSPORT COEFFICIENTS FOR THREE DIMENSIONAL CHANNEL REPRESENTATIONS

REVISION RECORD

Revision 1: This revision incorporates the following changes (June, 1977):

		Pages changed or added
A.	Clearer identification of base case check of insensitivity of DNBR of base case to parameters β, K and inlet flow maldistribution	15,15a,46a 46b (Vol. I)
B.	Examples of the simplified method layout	10a,10b,27a, 27b (Vol. I)
C.	Comparison of simplified method and THINC-IV	21a,86,86a, 86b,86c, (Vol. I)
D.	Clarification of figures describing hot channel identification procedure	28,29.(Vol. I)
E.	Correction of figures presenting transport coefficient results	46,65,66,70, 77, (Vol. II)
F.	Correction to equations presenting transport coefficient results	34, 35 (Vol. II)
G.	Limits of applicability of the simplified method	26a, (Vol. I)
H.	Delete designation of Fig. 2 of N ≡ total number of subchannels in strip and clarify nomenclature to have N ≡ number of rows of rods in a bundle and N' ≡ total number of subchannels (in a strip) equal to N/2 for N even N/2 + 1/2 for N odd Note that since the number of full rows of subchannels in a square array is equal to the number of rows of rods, N numerically represents each.	xii (Vol. I) xi (Vol. II)

VOLUME I

RECOMMENDED METHODS FOR STEADY STATE PWR CORE ANALYSIS

AUTHORS: PABLO MORENO
EHSAN KHAN
CHONG CHIU
JUSTIN LIU
NEIL E. TODREAS

ACKNOWLEDGEMENTS

This work was initiated about November, 1974 in two separate facets. As an outgrowth of ongoing work on the MEKIN project, Bob Bowring stimulated discussions and examination of the errors inherent in homogenization processes commonly being employed for thermal analysis of PWR cores. His development of the COBRA IIIC code gave us a tool for ready, economical analysis of this question. Work on this question was taken over by Chong Chiu and pursued by him under our direction ultimately producing transport coefficients for two dimensional problems as thoroughly discussed in Volume II. The second facet was the initiation of work by Ehsan Khan in February 1975 with the goal of establishing a simplified, publically available method for steady state and ultimately transient PWR analysis. In May 1975 Pablo Moreno initiated work, first on an analytic method for transport coefficients and then with Ehsan on the basic procedure. By the time of Ehsan's depart in August, 1975, the main lines of our procedure had been identi These included 1) use of COBRA IIIC/MIT in a one pass manner a 2) identification of significant uncertainties in the boundary ditions of the cascade method. This permitted us to conclude th was unnecessary to fully complete our work on making a cascade m utilizing COBRA IIIC/MIT for use in calibrating our simplified m

It remained for Pablo to exploit these conclusions and reco mend specific procedures for the simplified method. These inclu the selection of the number and distribution of radial nodes and

the number and values of transport coefficients. As part of his task Pablo undertook and accomplished the significant tasks of

1) finalizing COBRA IIIC/MIT in a form with all capabilities necessary for one pass analysis
2) identifying and justifying the minimum radial node layout for satisfactory results, and
3) extending the concepts for determination of transport coefficients from the ideal 2D to the real 3D core arrangement.

In the last stage of his work, Pablo was joined by Justin Liu whom he trained in the use of COBRA IIIC/MIT in this area. Justin completed studies on the size of interior and exterior meshes and on N_H prediction by numerical and analytic methods. In the future Justin will attempt to extend and modify as necessary the results of this effort to the analysis of PWR transients.

To all these gentlemen I owe a large debt of gratitude for their tireless efforts in expeditiously accomplishing all the analysis required in this study and for their intellect and good nature so evidently displayed in our many hours of discussions. The contributions of Pablo Moreno and Chong Chiu represent the backbone of this effort and it is to them whom I especially extend my thanks. My reference to intellect and good nature would not be complete without acknowledgement of the efforts of Ms. Irene Battalen and Mrs. Lynda DuVall who typed the many drafts and equations which comprise this report.

Finally I would like to acknowledge the financial support provided until August 1975 for the efforts of Bob Bowring and Chong Chiu by the Electric Power Research Institute and since

February 1975 for the balance of the program by the New England Electric System and Northeast Utilities Service Company as part of the Nuclear Reactor Safety Research Program under the MIT Energy Laboratory's Electric Power Program.

Neil E. Todreas
Principal Investigator
Professor of Nuclear Engineering

ABSTRACT

A one-pass simplified analysis method for steady state PWR core has been developed. The advantages over the other multistage approaches have been discussed and compared. Recommended nodal patterns for modelling the reactor core have been proposed. Also the effect due to the lumped channel technique utilized in both the simplified method and existing multistage methods has been investigated for both 2D and 3D problems. For the nodal pattern recommended with the proposed one-pass analysis method, use of the lumped channel technique introduces negligible errors.

VOLUME I

TABLE OF CONTENTS

VOLUME I

LIST OF FIGURES

VOLUME I

LIST OF TABLES

VOLUME I

LIST OF APPENDICES

NOMENCLATURE

A_i	cross-section area for subchannels i, (L^2)
A_s	cross-section area for any subchannel (L^2)
A_k	cross-section area for homogenized subchannels k (L^2)
$c_{i,j}$	thermal conduction coefficient for subchannels i and j (H/TθL)
$C_{L,R}$	thermal conduction coefficient for homogenized subchannels L and R (H/TθL)
c_i	crossflow friction force for subchannel i (F)
C	crossflow friction force for homogenized subchannels (F)
Δx	axial elevation increment, (L)
$\Delta \bar{h}$	axial change of radially averaged enthalpy in the multi-subchannel representation, (H)
ΔH	axial change of radially averaged enthalpy in the homogenized representation, (H)
F	axial friction force per unit length (F/L)
F_R	Flow ratio
$\bar{F}$	average flow rate
g	gravitational constant, (L/T^2)
g_i	mass flux of channel i
$\bar{G}$	averaged mass flux
h_i	enthalpy for subchannel i, (H)

h^*	effective enthalpy carried by diversion crossflow (H)
$\bar{h}_k$	radially averaged multi-subchannel enthalpy, (H)
H_k	homogenized enthalpy for region k, (H)
H_R	inlet enthalpy ratio
K	crossflow resistance coefficient
L	channel length, (L)
m_i	flow rate for subchannel i (M/T)
M_k	flow rate for homogenized region k, (M/T)
N	Total number of rods
$N_H, N_U, N_{TP}, N_{TF}, N_{TU}$	coupling coefficients
$\bar{N}_H$	averaged coupling coefficient
N'	total number of subchannels equal to N/2 for N even N/2 + 1/2 for N odd
p_i	pressure for subchannel i (F/L^2)
P_k	pressure for homogenized region k (F/L^2)
P_R	power ratio
q'_i	heat addition per unit length, for subchannel i (H/L)
$\bar{q}$	averaged heat addition per unit length (H/L)
Q_k	heat addition per unit length for homogenized region k (H/L)
R_H, R_p	ratio of $\bar{N}_H$ in the FLOW UPSET CASE
S	rod spacing (L)
u^*	effective velocity carried by diversion
$\bar{u}$	effective averaged velocity for adjacent channels

u_i	effective momentum velocity for subchannel i, (L/T)
U_k	effective momentum velocity for homogenized region k, (L/T)
$\bar{U}$	effective averaged velocity for homogenized region L and R
$w_{i,j}$	diversion crossflow between adjacent subchannels (M/TL)
$W_{L,R}$	diversion crossflow between homogenized region L and R (M/TL)
$w'_{i,j}$	turbulent interchange between adjacent subchannels i and j (M/TL)
$W'_{L,R}$	turbulent interchange between adjacent homogenized region L and R (M/TL)
ρ^*	density carried by the diversion crossflow (M/L3)
β	turbulent mixing parameter

Subscripts

i	subchannel identification number
k	homogenized region identification number

Variables

J	axial elevation node along the subchannels

CHAPTER 1

DESCRIPTION OF THE PROBLEM

1.0 Introduction.

The goal of this study was to develop a method for steady stat analysis of the core of a Pressurized Water Reactor using publicall available computer codes. The Connecticut Yankee PWR core with abnormally high average heat flux was selected and its physical characteristics are presented in Appendix C. The computer code cho was COBRA IIIC[1] in its MIT version, COBRA IIIC/MIT[2]. A complete tab lation of the core cases analyzed in this study is presented in Appendix

It is clear that the ideal way to analyze a reactor core utiliz the lumped subchannel approach is by taking each radial node in the analysis at least as an actual subchannel. This implies that for the Connecticut Yankee PWR core 35,325 radial nodes should be considered (because of symmetry reasons this number may be reduced to 4,416). These numbers are so large that there is no available computer which could handle this problem, and even if such a computer were available the cost would be prohibitive. Therefore this possibility has historically been ruled out and two other general approaches have been developed.

One is the chain or cascade (multi-stage) method and the other is a one-stage method. The development of both schemes has reflected the li imposed on the number of radial nodes in any single pass calculati by previously existing subchannel code formulations.

The chain method has maximized the radial mesh representation by performing a multistage analysis of the core[3,4]. In the first stage the whole core is analyzed on an assembly to assembly basis (each radial node represents an actual assembly). From this analysis the hot assembly, i.e. the one with the largest enthalpy, and its boundary conditions can be identified. In the second stage of the two stage method the hot assembly is analyzed on a subchannel basis, (each radial node is an actual subchannel or is created by lumping of a few subchannels) taking advantage of the boundary conditions found in the previous stage. The three stage method sequentially analyzes the hot assembly as four regions and then the hottest of the four by subchannels. In our subsequent discussion of the chain method we will focus on the two stage approach as an example although the uncertainties to be discussed are applicable in principle independent of the number of stages.

In the simplified one-stage method the core has been analyzed in only one stage using a fine mesh in a zone consisting of those subchannels with the larger radial peaking factors and a coarse mesh outside this zone. However because available codes require that the boundaries of any mesh node must be connected to another point or be impervious to mass, momentum and energy exchange, the coarse mesh zone has traditionally been extended to the core boundary. The severe limits on the number of radial nodes in available codes as COBRA has tended to maximize the core volume represented by each node in the coarse mesh zone.

In this study we have

(1) adopted the code COBRA IIIC/MIT for one-stage analysis thereby lifting the previous severe bound on the allowable number of radial nodes,

(2) recommended the optimum arrangement and size of fine and coarse mesh zones, and

(3) assessed the relative merits of the chain versus the simplified one-stage analysis for various cases of interest under steady state PWR operating conditions.

1.1 Uncertainties Associated with the Cascade Method

1.1.1 Boundary Conditions for the Hot Assembly Analysis

In deciding on what method of analysis to develop and recommend for PWR analysis, the option did exist for us to develop a chain method utilizing the COBRA code. This development would have required adaptation of COBRA to accept radial mass, momentum and energy transport into the hot assembly from the first stage analysis. While this could have been accomplished from a coding viewpoint, we perceived, based on our development of an approximate 2 stage method[5] that any chain approach would still have significant physical uncertainties. Specifically we refer to the following uncertainties associated with the boundary conditions applied to the hot assembly, (second stage) analysis.

a) Flow distribution inside the hot assembly.

The only information that is obtained from the first stage of the chain method is the total crossflow that is

leaving or entering each boundary of the assembly. No information is obtained regarding the distribution of axial and transverse flow between subchannels of the hot assembly. Some assumption must be made for the flow distribution but the present lack of a means to verify the assumption leads to questionable results. These problems will be more noticeable at the outer rows of subchannels where the boundary conditions established for the whole assembly will have a larger effect while in the interior of the assembly this effect will be smaller.

Additionally this treatment of diversion crossflow wil introduce a further approximation due to averaging in the estimation of lateral energy and momentum transport. Specifically, for example, the energy transport will need to be based on the average assembly enthalpy and this average crossflow whereas in fact the actual number of subchannels on a face through which crossflow and energy exchange is occuring may be localized. Further the enthalpy of the coolant undergoing crossflow may be significantly different than the bundle average. In those steps where diversion crossflow is entering or leaving the hot assembly the problem becomes important.

One final uncertainty relates to the adequacy of the crossflow boundary condition applied to the hot assembly analysis. It is clear that local conditions inside th ıo

assembly effect the crossflow distribution. These local conditions are not taken into account in the assembly to assembly analysis where the boundary conditions for the hot assembly analysis are established.

b) Mixing between the hot assembly and its adjacent channels in the hot assembly analysis.

In the hot assembly analysis no turbulent interchange is taken into account ($\beta = 0.0$) because no interconnection exists with the actual adjacent assemblies. This can lea to significant overestimation of the enthalpy in the oute row of the hot assembly subchannels. We can visualize so method to take into account this effect but the fact is that a new set of assumptions would have to be made and there is not a data base to support those assumptions.

1.1.2 Transport Coefficients for Momentum and Energy Exchange Between Homogenized Regions

In each stage of the chain analysis various size regions of the core are homogenized and represented by single nodes. The lumped analysis methods applied to these regions formulate momentum and energy exchange between these regions as proportional to differ ences in nodal properties. In reality, however, such exchanges between regions are proportional to the gradients of such propertie across the boundary between regions. This deviation between homogenized nodal differences and gradients is developed in detail in Appendices A and B. To reflect the state of the art for PWR analy

in these appendices the most detailed representation is assumed to be that of single subchannels. Therefore gradients cannot be obtained as differentials across boundaries but rather as differences between subchannel values on either side of a boundary between the homogenized regions.

Based on a two dimensional analysis carried out in Appendix E, the deviation between homogenized nodal enthalpy differences and enthalpy gradients based on boundary subchannel values is shown to be proportional to the number of subchannels in each homogenized region, N; the intensity of the turbulent interchange, β; and the axial length along the heated channel z. This result is consistent with the recognition of this problem for negligible crossflows as a thermally developing flow field which is analogous (as shown in Volumes II and III) to a transient thermal conduction problem. Section 3.1 discusses the difficulty in estimating deviations in 3D situation from those in 2D situations Table I presents deviations for the typic power upset case (different power between homogenized regions) in 2D.

This analysis shows a maximum error of 14.4 percent for conditions of maximum β, maximum axial position and intermediate N. All lumped region analyses should apply coefficients (transport coefficient N_H) to the homogenized region nodal enthalpy differences to correct these deviations Generally none are employed. In application of the THINC method, a transport coefficient of N is applied to the turbulent interchange ter in the energy equation[3]. This coefficient is exact for the two dimensional case of linear transverse enthalpy profile through th

assemblies on either side of the boundary in the absence of cross as demonstrated in Appendix F. The error involved in this assump for other various cases of interest needs further assessment. Ad tionally as Appendix A illustrates, coefficients need also to be applied to other homogenized region nodal property differences fo a complete theoretical solution. Practical bounds on application these additional coefficients need to be recommended.

1.2 PWR Analysis Needs

Two types of PWR analyses are now being performed within the nuclear industry. The first is a thermal analysis using a prescr spatial energy generation rate to find the Minimum Departure fro Nucleate Boiling Ratio. A second potential limit is void fracti However in almost all practical cases the MDNBR is the governing limit not channel void fraction. The second type of analysis be performed is coupled thermal hydraulic-neutronic analysis. Whil prime focus of this coupled analysis method is for transient ana and we have presently limited our efforts to steady state analys we consider it since our future efforts will include transient applications.

The nature of these two types of analyses lead to two diffe approaches for thermal analysis.

1.2.1 MDNBR Analysis

For a typical PWR the MDNBR is dependent on channel heat ge tion rate and enthalpy. The enthalpy of the channel is dependen upon the heat generation rate and the characteristics of its ne

channels which effect interchannel energy exchange. The dominant parameter is the heat generation rate, which implies that the most restrictive conditions will take place in the subchannel where the heat generation rate is large and not necessarily in the subchannel with largest enthalpy. This will allow identification, by inspection of the core radial power distribution, of that area of the core where the most restrictive conditions are going to occur. Then a fine mesh of subchannels will be required in this zone while outside of this zone a coarse mesh will suffice.

1.2.2 Coupled Thermal Hydraulic-Neutronic Analysis

In the coupled analysis the neutronic analysis requires the number density of all isotopes and the fuel temperature in each region. The number densities are dependent on the nodal enthalpy and void fraction. Optimum nodal sizes have not yet been established in general and in particular in MIT's MEKIN development since feedback calculations have not been performed[6]. However, such sizes will be on the order of some fraction of a PWR assembly. In any event the nodal division of the core will be more uniform than for MDNBR analysis, will comprise the whole core, and will require accurate calculation of homogenized region enthalpies and void fractions.

1.3 Recommended Analysis Methods

For each type of analysis in the previous section the simplified one pass approach using COBRA IIIC/MIT is recommended. Specific

application of this approach further requires user specification of the following factors.

1) The size and number of regions into which the core shoul be subdivided.

2) The detail in which transport coefficients for mass, momentum and energy exchange should be expressed.

The remaining chapters of this volume address and resolve these questions for the two types of analysis considered.

CHAPTER 2

ANALYSIS METHOD FOR DNBR DETERMINATION

The recommended analysis method is a one stage approach using COBRA IIIC/MIT applied in the following manner.

a) identify the hot subchannel by virtue of its radial power peaking factor and its placement in the assembly with the highest assembly peaking factor. If rod power peaking factors are available, the hot subchannel will be identified by the rod power peaking factors.

b) provide a fine mesh or internal mesh (each node represents a subchannel) of sufficient nodes, to surround the hot subchannel with at least one ring of subchannels. For our Connecticut Yankee core example where two diagonally adjacent subchannels are equally hot, this recommendation leads to sixteen required nodes. For the case of one hot subchannel, nine nodes are required.

c) provide a coarse mesh or external mesh (each node represents a homogenized region) to represent the entire core region outside the fine mesh. The number of coarse mesh nodes can be determined by the following criteria:

- Whole core analysis is necessary.*
- Layout of at least two coarse mesh nodes representing concentric regions about the fine mesh is required.

*For symmetric core, whole core representation can be replaced by some of its fractions representation.

- The size of the region represented by the most interior coarse mesh node should be larger than the area of layer of subchannels which is sufficient to surround the fine mesh. Usually, this most interior coarse mesh node represents the rest of the hot assembly.
- Computer restrictions on the minimum number of coarse mesh nodes exist due to the limited number of mesh nodes adjacent to a common node. Thus these minimum number can be considered as the lower bound of the coarse mesh nodes.

d) by virtue of b) it is not necessary to utilize any transport coefficients, as mentioned in section 1.1.2. In the COBRA IIIC/MIT input only an enthalpy factor, N_H, is built in which should be set equal to one. ($N_H = 1$ means that no enthalpy transport coefficeint will be used.)

Channel layouts conforming to the above recommendation are illustrated in Figure's 1a and 2a. Figure 1a is an example of the simplified method channel layout for one eight core (because of symmetry reasons) with only one hot subcha (numbered 1). Eight (numbered 2 thru 9) of the nine fine me

nodes form a layer of subchannels surrounding the hot subchannel (numbered 1). Concentric regions outside the fine mesh have been represented by two coarse mesh nodes: one (numbered 10) represents the rest of the half hot assembly, while the other one (numbered 11) represents the rest of the one eighth core. Similarly, Figure 2a is the simplified method channel layout for one eighth core with two equally hot subchannels. Fourteen (numbered 3 thru 16) of the sixteen fine mesh nodes form a layer of subchannels which is sufficient to surround the two hot subchannels (numbered 1 and 2). In order to satisfy the COBRA IIIC/MIT code restriction, five instead of two coarse mesh nodes must be used to represent the two concentric regions (numbered 17 thru 20 can be considered as one region, numbered 21 as the other one) outside the fine mesh.

For those cases where the hot subchannel is three or more rows from the assembly boundary, this method should give results at least as accurate as chain approaches. For those remaining cases where the hot subchannel is closer to the assembly boundary, the

boundary factors discussed in Section 1.1.1 should adversely effect the chain method compared to this recommended approach if the chain method is applied in the traditional way with the second stage restricted to the hot assembly. If instead the second stage represents subchannels around the hot subchannel independent of their parent assembly, the methods should yield comparable results although the simplified method applied as recommended in a) through d) above will require less computer time and storage space.

Before presenting the detailed basis for the above recommendations and claims it is useful to briefly examine the procedure for the key parameter effecting DNBR. These are linear power, hot channel enthalpy and hot channel flowrate. The linear power is an input parameter while the other two are calculated by a subchannel analysis procedure.

Examination of the relevant energy equation illustrates that the phenomenon labeled turbulent interchange and crossflow across the hot subchannel boundaries as well as the axial mass flow rate itself directly effect the hot channel enthalpy. We demonstrate this by writing the COBRA IIIC/MIT formulation for the hot channel enthalpy at axial position J, $h_{HC}(J)$, in terms of the properties of its neighboring subchannels i = 1, 2, 3, 4 and the turbulent interchange flows w' and crossflows w.

$$h_{HC}(J) = h_{HC}(J-1) + \frac{q'_{HC}(J-\frac{1}{2})}{m_{HC}(J-1)} \cdot \Delta x - \sum_{i=1}^{4} \frac{(t_{HC}(J-1)-t_i(J-1))C_{HC,i}\cdot\Delta x}{m_{HC}(J-1)}$$

$$- \sum_{i=1}^{4} \frac{(h_{HC}(J-1)-h_i(J-1))w'_{HC,i}(J-1}{m_{HC}(J-1)}$$

$$- \sum_{i=1}^{4} \frac{(h_{HC}(J-1)-h^*(J-1))w_{HC,i}(J-1}{m_{HC}(J-1)} \qquad (1)$$

Homogenization of the subchannels adjacent to the hot channel with its outer neighbors will introduce errors in energy exchange in turbulent interchange and crossflows across the hot subchannel's boundaries. Theoretically these errors can be eliminated by appli cation of proper transport coefficients but for cases of moderate crossflows the effects are non linear and as Appendix B demonstrat it is not fruitful to attempt to develop transport coefficients.

Therefore the most direct course is to represent all real sul channel boundaries in the region of the hot channel as single sub- channel boundaries in the analysis approach. This means represent each subchannel by a radial node yielding a so-called fine (one n per subchannel), or internal (region of the core in which the hot channel is located) mesh. For the hot channel from our analy s a 16 node interior region we estimate that the turbulent intercha and crossflow terms are 16.2% and 2.8% of the linear power term in th energy equation when each of these terms are summed from the inle to the location of MDNBR. The conduction term for these water cooled cores of small axial coolant temperature rise operating wi at least subcooled boiling is negligible and was neglected in the calculations. These estimates are based on case No. 1, but they are more or less constant for the hot channel of any other case. Notice that while the energy carried by the crossflow may be larg i.e., $h^*(J-1)w_{HC,i}(J-1)\Delta x$, the contribution to the hot channel enthalpy rise is much smaller, i.e.

$$(h_{HC}(J-1) - h^*(J-1))w_{HC,i}(J-1)\Delta x \ .$$

Also the mass flow rate has a strong direct effect on the hot channel enthalpy since it enters each term as a divisor. Consequent any error in this term will effect the enthalpy rise in the same proportion.

We can conclude then, that in order to match the results of our simplified method with the results that an actual subchannel analysis would yield, we have to obtain very close correspondence for the turbulent interchange terms and mass flow rates. Note that we can always match the linear power terms identically since these terms are input variables. For the crossflow terms, since their effect upon the enthalpy rise is very small, it is not necessary to achieve very close correspondence. However the crossflow alone d enter the continuity equation thereby affecting the mass flow rate and hence the energy equation. This effect is important and will b treated subsequently. As will be indicated below, all the above considerations, when taken together, make it possible to obtain ve good results for the MDNBR by use of the recommended simplified an sis procedure.

The following sections present the basis for the above recommendations for MDNBR calculation.

2.1 Identification of the Hot Subchannel

Examination of the W-3 correlation for a typical set of PWR core conditions has demonstrated that the onset of MDNBR is most sensitive to linear power generation rate. The other variables of channel enthalpy and flowrate are less important. This sensitivit

is demonstrated by Figures 1 and 2 based on results of a study described in Appendix G. These figures independently examine the effect of hot channel enthalpy and axial mass flowrate respectively on identification of the channel in which MDNBR occurs.

In both figures the MDNBR is calculated for a hot subchannel with an abnormally high power peaking factor of 2.266 and an adjacent subchannel with the next highest power peaking factor in the hot assembly of 2.060. Since these calculations were performed for the subchannels with adiabatic boundaries the input variations in inlet enthalpy can be interpreted and plotted in Figure 1 as enthalpy variations at the location of MDNBR. We next demonstrate on Figures 1 and 2 that for the real case of interacting channels, the MDNBR will still occur in the subchannel initially identified as the hot channel by virtue of its high power peaking factor. We do this by the following conservative procedure.

Consider first the reduction in hot subchannel enthalpy due to turbulent interchange and crossflow. This reduction is estimated to be about 16.2% + 2.8% of the adiabatic subchannel axial enthalpy rise to the location of MDNBR of 174 BTU/lbm or -33.0 BTU/lbm. On the other hand the adjacent channel enthalpy is increased by turbulent interchange and crossflow with the hot channel but decreased by turbulent interchange and crossflow with the three other adjacent channels which have smaller peaking factors. Again the net enthalpy change in the channel adjacent to the hot channel due to turbulent interchange and crossflow are calculated in Appendix G to be -21.22 BTU/lbm.

These values are plotted on Figure 1 to illustrate the margin for MDNBR shift from the high radial power factor subchannel. The margin is considerable.

Consider next the increase in hot subchannel enthalpy due t reduction in axial mass flowrate. This reduction for the hot channel and the adjacent subchannel are calculated in Appendix G to be 18.0% and 17.2%. The adjacent channel flowrate decreases less than the hot channel flowrate. Therefore the effect of mass flowrate reduction as illustrated on Figure 2 is to further increase the margin for MDNBR shift.

Based on the results of Figures 1 and 2 it can therefore be concluded that the hot subchannel can be identified by examinat of a core map of channel radial power peaking factors when axia rates have been normalized. Should the channel power factors fo case of specific interest be significantly closer than in our ex the margin would be reduced and it might be prudent to perform extra one pass calculation to confirm the validity of the ident cation made of the hot subchannel. If rod power peaking factors than channel peaking factors are available, exceptions to the a process are possible in subchannels composed of a zero power ro to a high power rod because of the cold wall effect. This case discussed in Appendix G which recommends the procedure which sh used for hot subchannel identification in this case.

2.1a Base Case

In later sections we will determine the minimum number of and coarse mesh nodes necessary. With the hot channel identifi next establish a base case using an excess number of nodes to w we can later compare our lesser node results. Cases with 54 no (Case 9) and 101 nodes (Case 5) were selected as the base case

Values of the mixing parameter β should be dependent upon

areas of the region represented by the radial nodes.[3] Different values of β should be utilized between nodes representing different sized regions. This was accomplished by introducing the transport coefficient, $N_H = N$, between channel boundaries to compare to the result obtained by using constant β. As shown in Table V, the improvement of MDNBR by the modification for the base case is negligible. Therefore, constant β can be assumed for mixing between channels with different flow areas.

Based on a sensitivity study of the cross flow resistance coefficient K to the MDNBRs of the base case (Case 5), it was demonstrated that the effect of the parameter K on MDNBR is not significant. The results of the sensitivity are shown in Table VI. Note that unrealistic values of K have been used to demonstrate the insensitivity of MDNBR to K.

The different results of MDNBR between a small nonuniform inlet flow case (Outer and Inner assemblies have 1.001 and .95 core average values respectively.) and the base case with its uniform inlet flow are shown in Table VII. Based on the small difference of MDNBR (1.1%), uniform inlet flow distribution has been assumed in the study.

2.2 Fine Mesh Size in the Region of the Hot Channel

In order to match the turbulent interchange term of the hot channel a fine mesh of actual subchannels has to be used around the hot one.

The necessary number of subchannels that have to be used in this fine mesh was established by a parameter study whose results are illustrated in Figure 3. This figure shows that 16 interior

mesh nodes are sufficient since results do not change compared to a 36 interior mesh array (Case No. 7 vs. Case No. 9, and Case No. vs. Case No. 15). However if we further reduce the mesh, for exa to 4 nodes (Case No. 16 vs. Case No. 11) the results change significantly. This result indicates that while turbulent interchange effects on the hot channel boundaries and boundaries immediately adjacent to the hot channel (16 versus 4 nodes) are important, interchange across boundaries of the other channels in the regio of the hot channel do not have a dramatic effect (36 versus 16 no The conclusion of 16 internal nodes is based on placing one layer subchannels around the hot channel. Sixteen are required in the Connecticut Yankee case examined because of the existance of two h subchannels. According to the same argument, 9 internal nodes are required if only one hot subchannel is presented.

Since there is no direct interchange between the hot subchan and the corener subchannels of the one layer channel which surro the hot ones, the fine mesh nodes can be decreased by eliminating those corner subchannels. By doing this, the requirements of sixteen and nine nodes can be decreased to twelve and four nodes respectively.

2.3 Coarse Mesh Size in Core Region Outside Fine Mesh

In order to match the mass flow rate of the hot channel, a coarse mesh or external mesh is needed outside of the fine mesh. The influence of this coarse mesh upon the MDNBR was studied from two different viewpoints. First the importance of the representation of the whole core versus the representation of only a part of the core was analyzed. The results are presented in Fig. 4, (Case No. 6 vs. Case No

and Case No. 8 vs. Case No. 12). From these results it can be concluded that it is necessary to represent the whole core in or r to have good results. The physical effect demonstrated by these pairs of cases is that radially directed crossflow is generated by the hot channel and its neighbors which normally is redistributed outward in the coarse region. The magnitude of the crossflow leaving the hot region is proportional to the pressure difference between this hot region and the rest of the core. When the whole core is not represented, the outer regions which are the coldest and the ones with lower pressure are eliminated. This implies that the pressure difference, which determines the amount of crossflows, is reduced and then less flow leaves the hot region radially. This leads to larger mass flow rate inside the hot chann which leads to smaller enthalpy rises and therefore to larger MDNBR's as indicated in Figure 4.

Once it is clear that the whole core needs to be represented, the next question is how this mesh outside of the hot region has to be established.

The question is answered in Figure 5 where Cases No. 5, 6, and 7 are represented. It can be observed that no change takes place in the MDNBR even when we go to very coarse external meshes (15 external nodes). This result was confirmed for the cases with $N_H = N$ (Cases No. 1, 2 and 3) and for the situation where the hot channel is close to the boundary (Cases No. 19 and 20). The insensitivity of MDNBR to the coarse mesh size was investigated for Case 2 and 3. It is due, as shown in Fig. 6, to the fact that very simi total radial flow leaves the hot channel in the three cases and hence the axial mass flow in the hot channel is well determined

independent of the layout of the coarse mesh. These results wer confirmed for other cases.

Also the individual crossflows leaving each boundary of the hot channel were investigated. The values obtained for Cases No. 1, 2 and 3 are given in Figures 6, 7, 8, 9 and 10. In all those cases, since the large number of external nodes, there are no lar differences of channel area. It can be observed that the influen of the external mesh on these values is quite important but becau the importance of the crossflow term upon the enthalpy rise is very small these changes do not effect the MDNBR results. The physical reason for having large differences in the individual crossflows while their sum is a constant value for the above cas is the following. When we change the external mesh, the resista to crossflow along specific directions is changed too, but the t resistance of the core to the crossflow leaving the hot channel kept unchanged. Therefore we do not influence the total flow radially leaving the hot channel but we force it to leave in different directions. Fortunately the importance of the indivic corssflow terms in the energy equation is very small and as long the total crossflow is similar we can use coarse external meshes radial nodes) to predict MDNBR with a degree of exactness as goc as with finer external meshes since the MDNBR quickly reaches ar asymptotic value (Figures 3 and 5).

The reason why the lower bound of the number of external r nodes is 5 is because of a computer limitation on permissable t pattern of whole core channel map for the 16 internal nodes cas the number of external nodes is less than 5, too many nodes wil be adjacent to a common node. Under such conditions satisfacto

results can not be obtained from the COBRA IIIC/MIT. So the question comes to this: What is the physical result if the number of external nodes is less than 5, a situation which is possible if 9 internal nodes are utilized for a single hot channel case. To explore the effect of a decrease in the number of external nodes, a series of cases were run assuming an internal mesh of 4 nodes instea 16. Four nodes were selected for economy in place of 9 in this stud In those 4 internal nodes cases, two external mesh nodes will be enc to give satisfactory results. If there is only one external node e\ if it represents the balance of the core, it will never give a good result. Also one should be very careful in laying out the external channel map as discussed later if only two external nodes are involv These conclusions were derived from analysis of the following four whole core cases.

The same internal channel map and radial power factors fo. ch four cases, and the different external maps and radial power factor: for the four cases are shown in figure 11. The pattern of channel maps in figure 11 are taken from Appendix D, but with different channel numbers. However the assigned number of each case is consi tent with the case number in Appendix D. The different results for the four cases can be seen in Table III. Comparing the MDNBR value from Table III with the values in Figure 3, it is clear that only ca 34 gives a MDNBR value which is close to the asymtotic value in fig 3. The MDNBR changes as the total cross flow out of the hot channe changes. As shown before, (figure 6, 7, 8, 9, 10), for cases with large number of exterior channels the different number of external nodes can only change the individual cross flow out of the hot ~ar but not the total cross flow out of the hot channel. Now, the tot:

cross flow out of the hot channel in the single external node c (even if it is for the whole core) is different from those tota flows out of the hot channel in two of the two external nodes c Moreover, the total cross flow out of the hot channel is differ even though the number of external nodes is the same but with d pattern of channel maps.

Referring to figure 11 the reason of the unsatisfactory r which come from the three cases (cases 35, 37, 38) can be seen: case 35, since only one external node exists, there is no cross from channel 5 to channel 6. Therefore, the total cross flow o the hot channel is small. In case 38, the two external channel not concentric. The channel pattern has the same effect on the cross flow out of the hot channel as the single external node c case 37, the area of the first layer of the external channels s to the area of one single subchannel layer which surrounds the internal meshes. Since the difference of the channel area betw two external nodes is huge, the result is questionable. Note layout of case 37 is like case 31 (Refers to Appendix D) excep case 31 the first layer of external nodes (2, 13, 12, 17) comp an area closer to case 34 than 37. Because of the first layer area differences, case 34 gives a result which is close to the totic values in figure 3.

The criteria for the layout of coarse mesh were based on facts presented in this section.

2.4 Use of Transport Coefficients

Because the interior region is represented on a subchanne basis, all transport coefficients are unity by definition. F

our selection of the size of this region was made to insure that uncertainties in calculated enthalpies of exterior region nodes did not effect hot channel enthalpies. The results of Table II in which extremes of N_H were employed (Cases 1, 2, 3, 5, 6, and 7) demonstrate that our selection accomplishes this goal and hence use of transport coefficients is not required for MDNBR prediction.

2.5 Accuracy of Results - This Method Compared to the Cascade Metho

The uncertainties associated with the hot assembly boundaries in the cascade method were identified in Section 1.1. Since the simplified method inherently provides an improved method of dealing with these uncertainties, it should give at least as accurate results as the cascade method. Additionally in principle the cascade method should be increasingly poorer as the hot channel location moves to the assembly boundary and these uncertainties effect hot subchannel conditions. This presumption was investigate by a series of cases 21, 23 and 24 in which the hot subchannel was in the first row and the simplified analysis method was used but in a manner to progressively represent the cascade method. The base case, 21, provided an internal mesh about the hot channel whi overlapped assembly boundaries as necessary. In Case 23, the cascade restriction on the subchannel or interior mesh that it lie within the hot assembly only was applied. Finally in Case 24 the additional restriction of no turbulent interchange along the hot assembly boundaries was added. The predicted MDNBR's for these cases are presented in Table IV. Overall the effect of the bound conditions (Case 21 vs. 24) is only 2%. In part this result occur because the successive changes introduced in Cases 23 and 24 effect the MDNBR in opposite directions. In another general case

it is possible that these effects would not oppose each other. I would be interesting to examine the conditions of Case 21 with th cascade method as suggested by the last entry in Table IV. Howev from the results available it appears that in practice the hot assembly boundary conditions do not cause significant uncertainti on the prediction of MDNBR. Conversely we can conclude that the simplified method and the cascade method will yield very comparat results for the typical PWR core cases analyzed here.

3. Comparison with THINC-IV Results

To check the accuracy of the MDNBR results by the simplified method, a Westinghouse PWR core has been analyzed by the one-stage method. Since different numerical schemes and correlations are used in the computer codes COBRA IIIC and THINC-IV, different results may be expected. Perhaps coincidently, the differences between results from the two different methods (chain method using THINC-IV and one-stage method using COBRA IIIC) were not significant as shown in Table VIII (Case 39, Case 40 see Appendix WE can conclude that the simplified method and the chain method will yield very comparable results for the typical PWR cases analyzed here.

CHAPTER 3

ANALYSIS METHOD FOR COUPLED THERMAL HYDRAULIC-NEUTRONIC ANALYSIS

The goal of this calculation is presumed to be the determination of the gross radial power distribution in the core. The thermal portion of this calculation is therefore aimed at yielding channel enthalpy and fuel temperature of homogenized regions. MDNBR's are not calculated in this first phase of the calculation but could be obtained using this gross distribution to yield a fine radial power distribution in an analysis of the type recommended in Chapter 3. Consequently for this first stage coupled analysis it is presumed that neutronics considerations will establish the desired mesh size, i.e. number of subchannels represented by each radial node.

The recommended analysis method is a one pass approach using COBRA IIIC/MIT applied in the following manner.

a) Identify the number of subchannels represented by each radial node. From Table I or Appendix E determine the percent error in homogenized region enthalpy for the assumed turbulent interchange coefficient β based on two dimensional analysis under the applicable case conditions, typically a power upset case. Errors in three dimensional analysis should differ only slightly from the two dimensional values. These errors can be reduced in varying degrees by the steps outlined below if their influence on the neutronics portion of the calculation warrents.

b) It is generally sufficient to apply only N_H transport coefficients on the correction to the turbulent interchange and crossflow terms in the energy equation.

c) Determine the numerical values of $N_H(z)$ for a boundary between homogenized regions of the size identified in a) for a range of radial power distributions typical of core to be analyzed. The method of determining $N_H(z)$ is a multiregion COBRA IIIC/MIT analysis as detailed in Volume II. Since these multiregion analyses are time consuming it would be desirable to characterize the dependence of $N_H(z)$ on radial power distribution in a way to minimize the number of multiregion analyses required.

It should be emphasized that steps b) and c) should only be utilized if the increased accuracy in channel enthalpy determination is justified. Based on work to date in this area[6], known by the authors, no assessment of the range of error which warrents reduction is available.

3.1 Enthalpy Errors in 3D vs. 2D Analysis

In order to predict the relative importance of $N_H(z)$ in a 3D problem versus a 2D problem, the value of $N_H(z)$ for boundary A of Cases No. 25, 26, 27 and 28 in Volume III, was calculated. These cases represent a variety of 3D channel layouts of the channels around boundary A. These cases represent a sequence in which the 3D problem of interest (Case 28) is approached using 3D representations in progressive steps from the characteristic 2D problem (Case 25) which was extensively studied as described

in Chapter 2. The results of this sequence show that the proximity of the additional upper and lower strip of channels about the center 2D strip exerts an important effect (Case 28 vs. 27) and care should be exercised to make the dimensions of boundary A and the upper and lower channels comparable. The results are presented in Figure 12. From these results it can be concluded that for the particular cases analyzed the error found in a 3D problem will be larger than for the corresponding 2D problem. However it is not possible to say "a priori" whether or not this is the general trend, and it is expected that for some other power distributions the trend could change and the 2D errors may become the upper bound of the corresponding 3D problems instead of the lower one.

3.2 Application of Only the N_H Transport Coefficient

This conclusion is drawn from a two dimensional study of the improvements in enthalpy prediction which result from progressive application of additional transport coefficients to the energy and momentum equations. Section 4.1.4, Volume II presents the results of this study for the typical power upset case and demonstrates the small gain achieved by applying more coefficients than solely N_H.

3.3 Numerical Value of $N_H(z)$ from 3D Multiregion Analysis

The 3D multiregion analysis presented in detail in Volume III utilizes the channel layout of Figure 13 with nodes representing an array of 3 x 3 subchannels. The $N_H(z)$ result is plotted in Figure 14 for illustration. Further this calculation yields the error in homogenized channel enthalpy which would be obtained without application of $N_H(z)$ as indicated in Figure 15.

CHAPTER 4

CONCLUSIONS

This study has investigated only steady state conditions. Two types of PWR analysis are needed. One is a thermal analysis using a prescribed spatial energy generation rate to find the Minimum Departure from Nucleate Boiling Ratio (MDNBR). Another is a coupled thermal hydraulic-neutronic analysis. Since feedback calculations have not been performed, only analysis methods for MDNBR have been extensively investigated in this study. Based on MDNBR criteria, a so-called one-stage simplified method was developed. The optimum modeling technique for this one-stage method for PWR cores under steady state conditions can be categorized as follows:

a) Methods For Identifying Hot Subchannel:

The hot subchannel can be identified by examination of a core map of subchannel radial power peaking factor when axial power rates have been normalized. If the normalized rod radial power peaking factors are available, the procedure to identify the worst location will be: first, to identify the highest rod radial power peaking factor as the hottest rod; second, to check the existence of any cold rod (zero power rod) in the neighborhood of the hottest rod. If there is indeed a cold rod which exists in the neighborhood of the hottest rod, a two-channel COBRA IIIC/MIT analysis has to be performed in order to find the lower MDNBR of the hottest rod in the hot channel and the hottest rod in the cold channel considering the cold wall effect.

b) Fine Mesh Around Hot Subchannel

A fine mesh (each node represents a subchannel) of sufficient node to surround the hot subchannel with at least one ring of subchannels ha

to be provided. For the Connecticut Yankee core example where two diagonally adjacent subchannels are equally hot, 16 nodes are required. For the case of one hot subchannel, 9 subchannels nodes are required to surround the hot subchannel.

c) Coarse Mesh Outside the Fine Mesh:

It is necessary to represent the radial extent of the whole core not a partial core by the coarse mesh. Specifically a partial, say 1/8. core segment can still be used as long as the full core radius is utilized.

Layout of at least two concentric layers of external channel about the internal nodes is required. Also the area of the first layer of the external channels should be at least larger than the area of the one subchannel layer which surrounds the internal meshes For economic reasons, the minimum number of coarse mesh limited by COBRA IIIC/MIT can be considered as the number of coarse mesh nodes. For example, for 16 internal mesh nodes, 5 coarse mesh nodes are needed for 4 internal mesh nodes, even 1 coarse mesh node satisfies requirements of COBRA MIT/IIIC but from the above argument, 2 coarse mesh nodes are required.

d) Application of Transport Coefficients

If no coupling coefficients are applied, an error will result in the predicted exit enthalpy of the homogenized representation. For DNBR analyses by the chain method this error is probably tolerable since the absolute value of the errors is modest and the effect of hot channel compared to linear power on the DNBR is minimal Also analysis by the simplified one-stage method eliminates the error by virtue of the proposed nodal layout. Therefore the utilizati

of transport coefficients is not necessary. However increasing interest is developing on methods for coupled neutronic-thermal hydraulic analysis. Here more accurate prediction of channel enthalpy is desired although coupled calculations have not been performed to date to assess either the degree of accuracy required or whether it can be achieved solely by proper sizing of the homogenized regions. Consequently derivation and prediction of transport coefficients is of potential application in the future development of these coupled analysis methods.

e) Limits of Applicability of the Simplified Method

The key core parameters which relate to the applicability of the method are the radial power peaking distribution and the inlet flow distribution. Significant changes in the power distribution from that assumed here may make the identification of the hot subchannel difficult. However, uncertainties in this area can be handled by performing an extra single pass calculation centered on the alternate suspected hot channel location.

Significant changes in the inlet flow distribution from that assumed (outer and inner assemblies have 1.001 and 0.95 core average values respectively) may lead to changes in the predicted MDNBR from the base case. While it is possible that the simplified method may correctly follow the change in MDNBR, a study of the limits of usefulness of the simplified method regarding inlet flow distribution has not been accomplished. Therefore the care should be taken in applying the simplified method for analysis of more severe flow upset situations than that considered here.

REFERENCES

1. Donald Rowe, COBRA IIIC, BNWL-1695, Pacific Northwest Laboratories (1973).

2. Robert Bowring and Pablo Moreno, COBRA IIIC/MIT Computer Code Manual, to be issued as an EPRI Report.

3. Joel Weisman and Robert Bowring, Methods for Detailed Thermal and Hydraulic Analysis of Water-Cooled Reactors, Nuclear Science and Engineering 57, 255-276 (1975).

4. Westinghouse Reference Safety Analysis Report (WRESAR), Revision 3, Volume III, pg. 4.4-40-pg. 4.4-46, Westinghouse Energy Systems, June 1972.

5. Pablo Moreno, Thermal/Hydraulic Analysis Methods for PWR's, M.S. Thesis, M.I.T. Dept. of Nuclear Engineering, May 1976.

6. Robert Bowring, John Stewart, Robert Shober, and Randal Sims, MEKIN: MIT-EPRI Nuclear Reactor Core Kinetics Code, September 1975.

7. Rowe, D.S., "COBRA III: A Digital Computer Program for Steady State and Transient Thermal Hydraulic Analysis of Rod Bundle Nuclear Fuel Elements" BNWL-B-82, Pacific Northwest Laboratory (1972).

Hot Subchannel: numbered 1*
Fine Mesh: numbered 2 through 9
Coarse Mesh: numbered 10 through 11

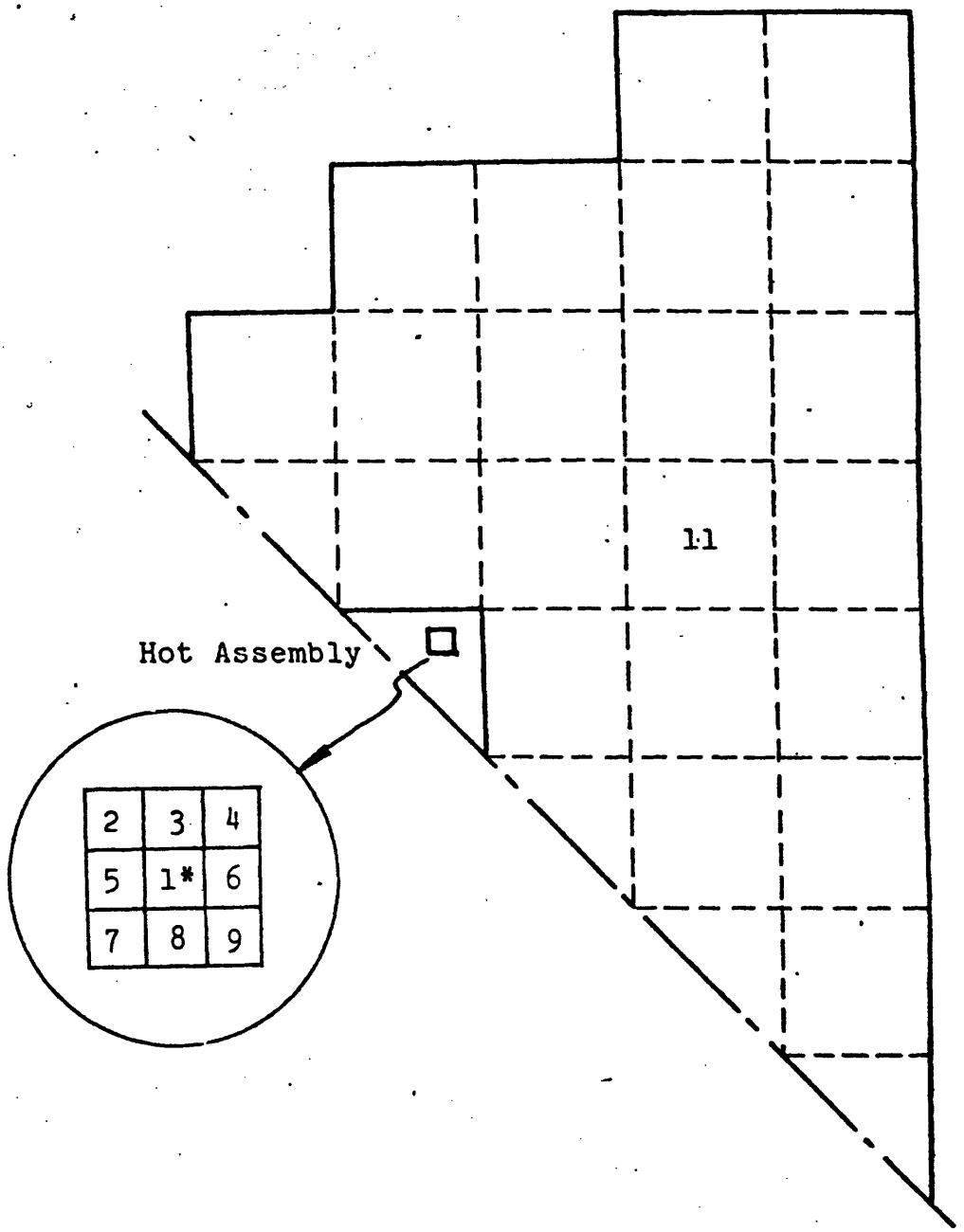

Figure 1.a EXAMPLE OF LAYOUT OF CHANNELS USED IN SIMPLIFIED METHOD FOR ONE HOT SUBCHANNEL IN 1/8 PWR CORE

Hot Subchannel: numbered 1* and 2*
Fine Mesh: numbered 3 through 16
Coarse Mesh: numbered 17 through 21

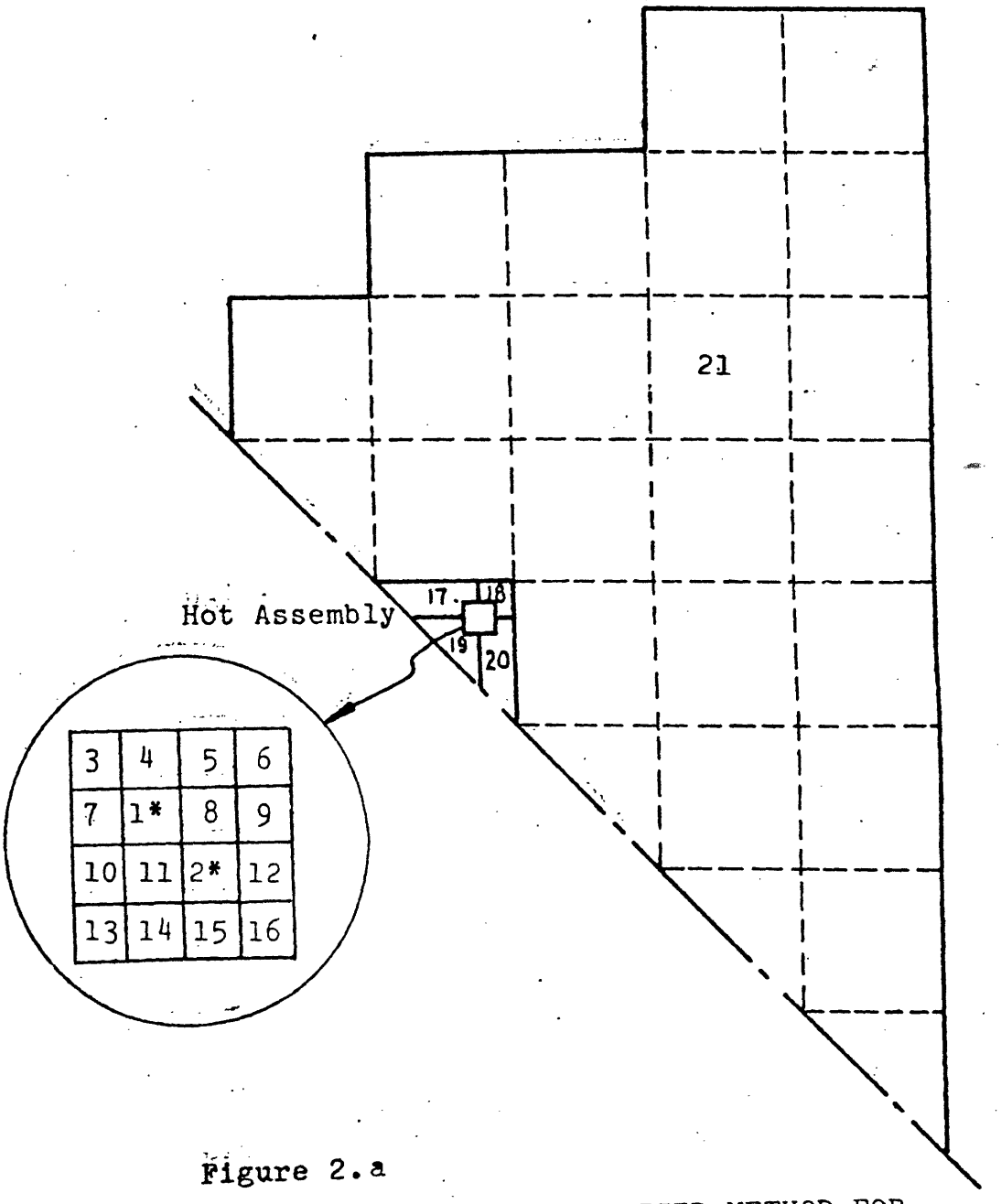

Figure 2.a

EXAMPLE OF LAYOUT OF CHANNELS USED IN SIMPLIFIED METHOD FOR TWO EQUALLY HOT SUBCHANNELS IN 1/8 PWR CORE

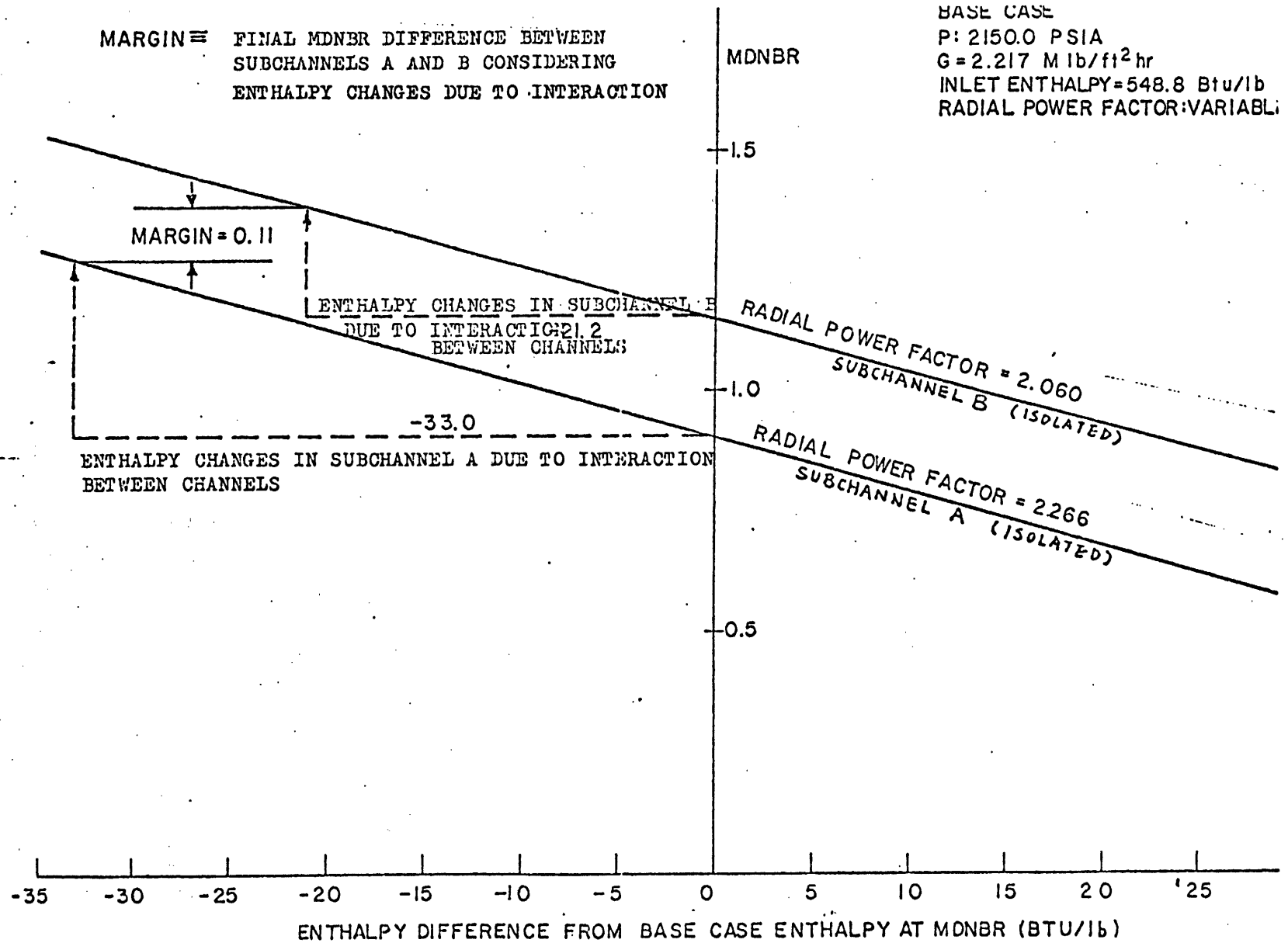

Figure 1 The Variation of MDNBR as a Function of Enthalpy Difference from Base Case for Different Radial Power Factors

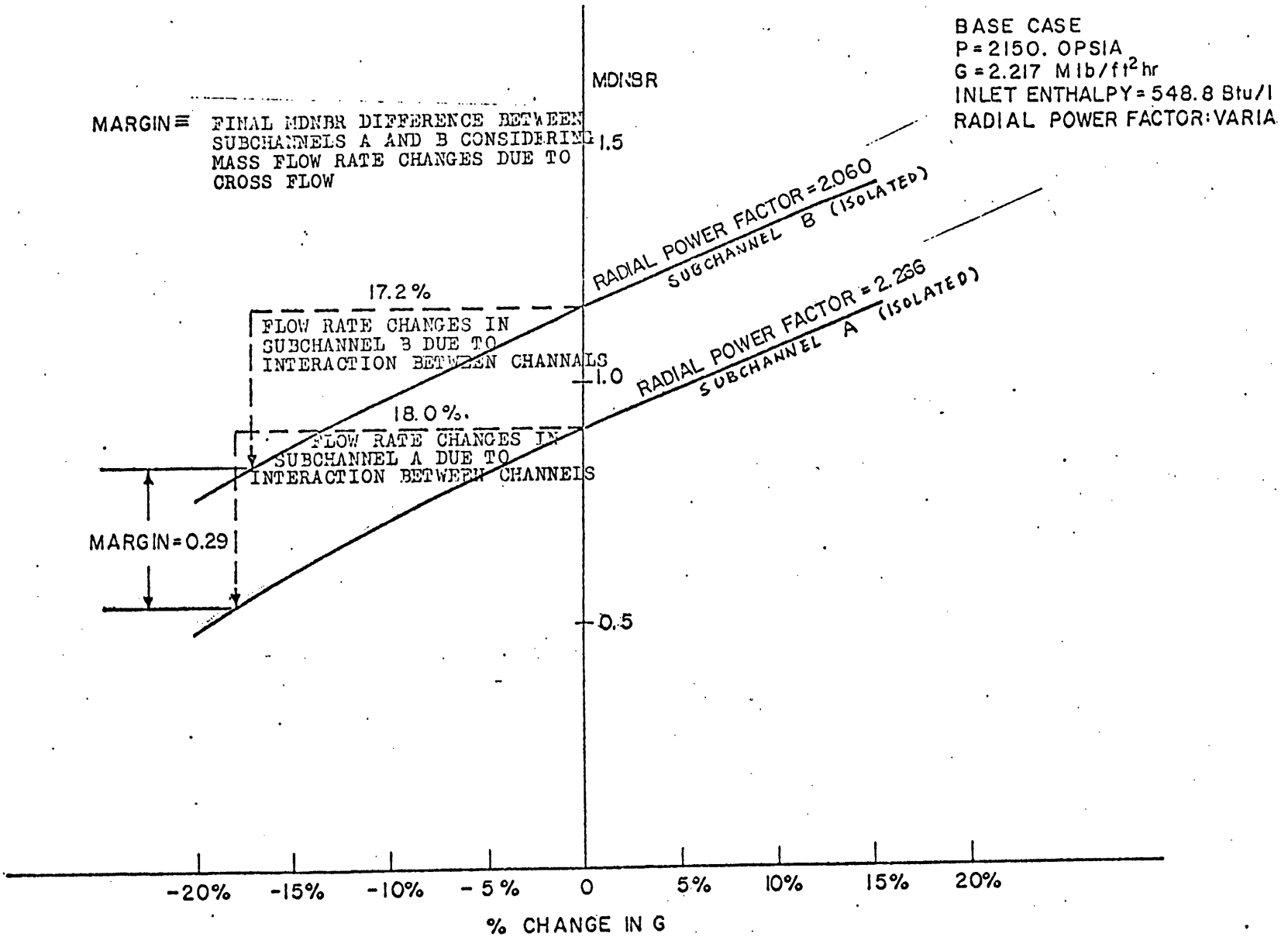

Figure 2 The Variation of MDNBR as a Function of % Change in Mass Flow Rate for Different Radial Power Factors

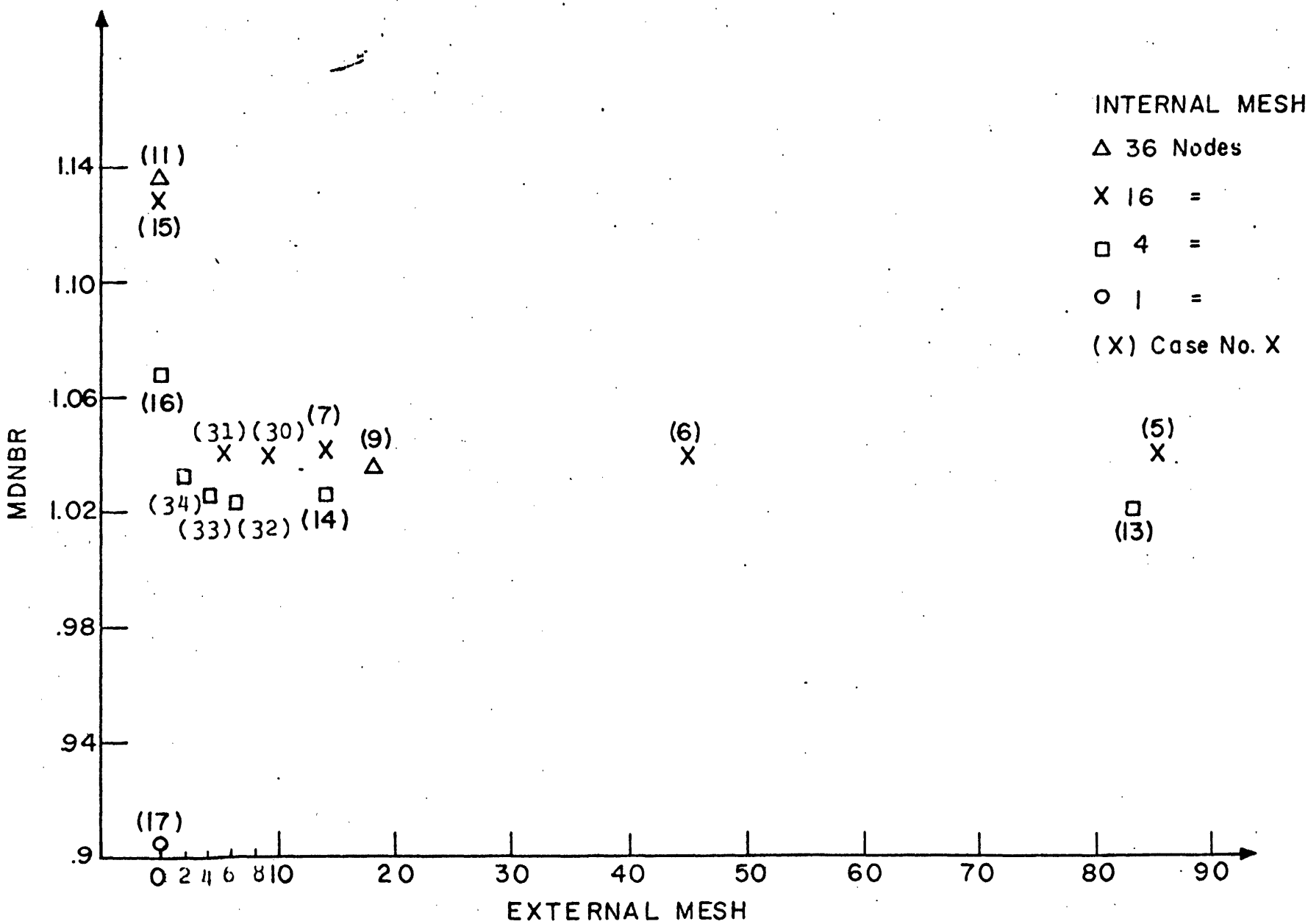

Figure 3 Effect of the Internal and External Size on MDNBR

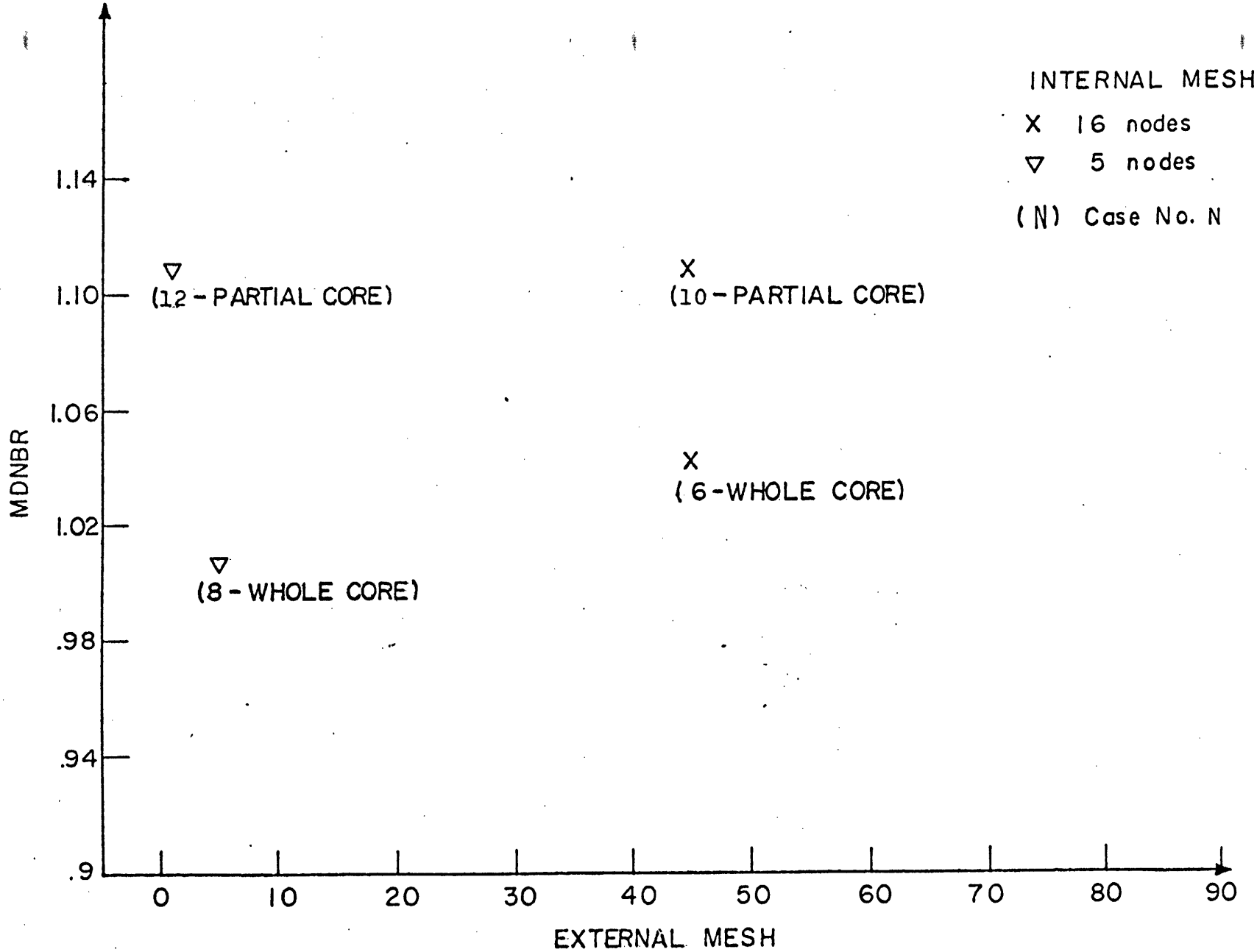

Figure 4 Effect of the representation of the whole core versus partial core on MDNBR

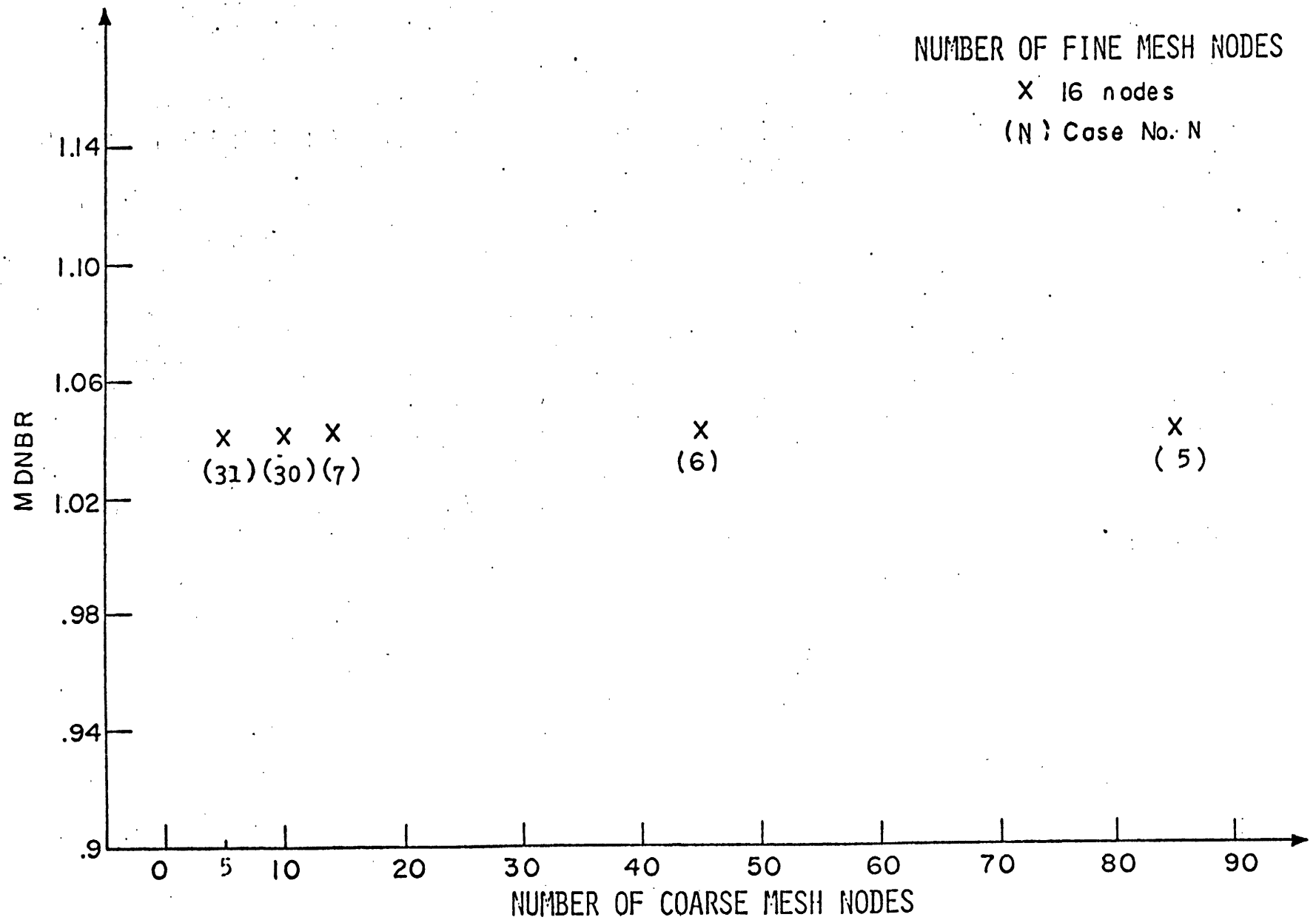

FIGURE 5: EFFECT OF THE NUMBER OF COARSE MESH NODES ON MDNBR

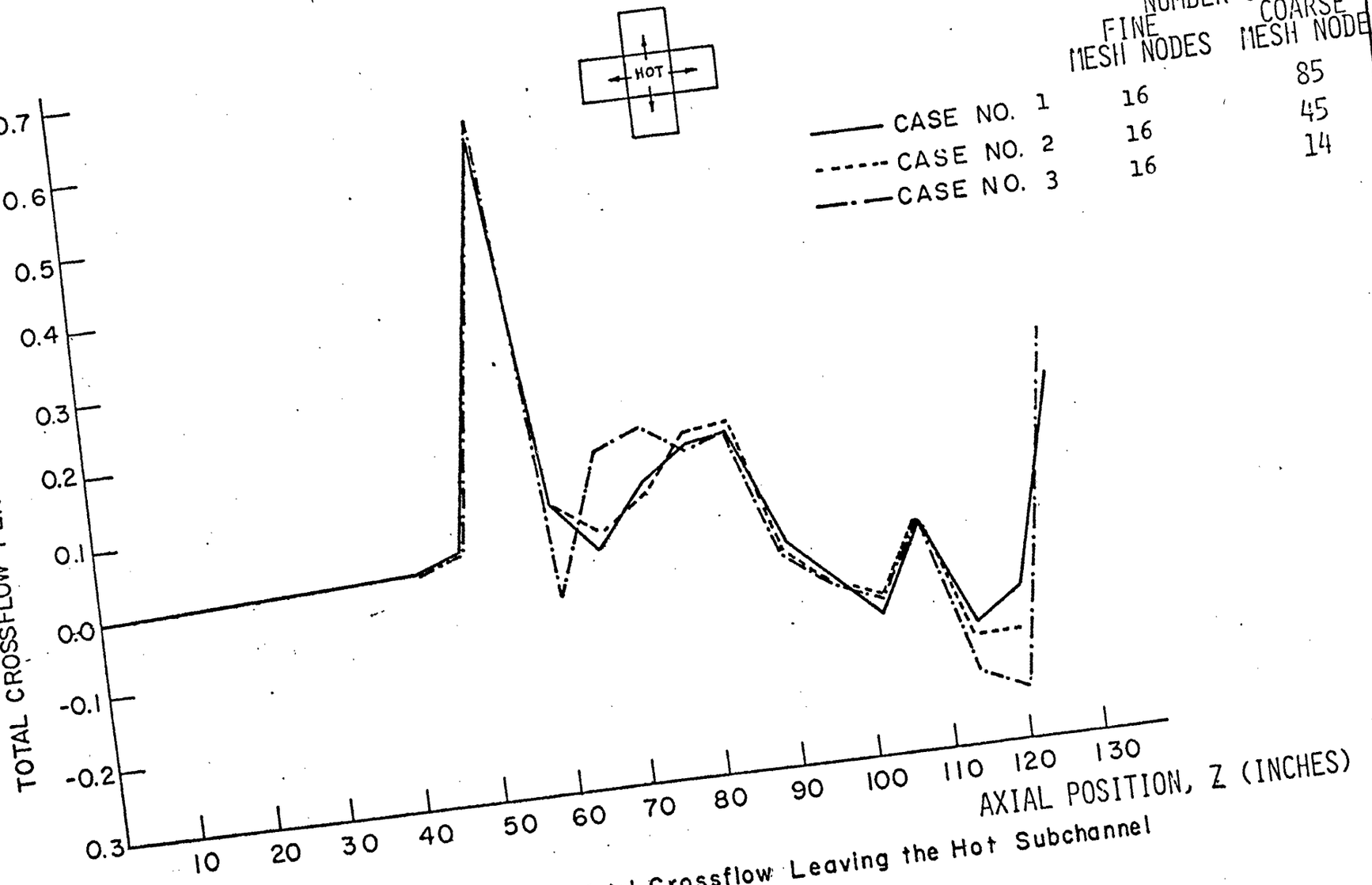

Figure 6: Comparison Between the Total Crossflow Leaving the Hot Subchannel in the Three Cases

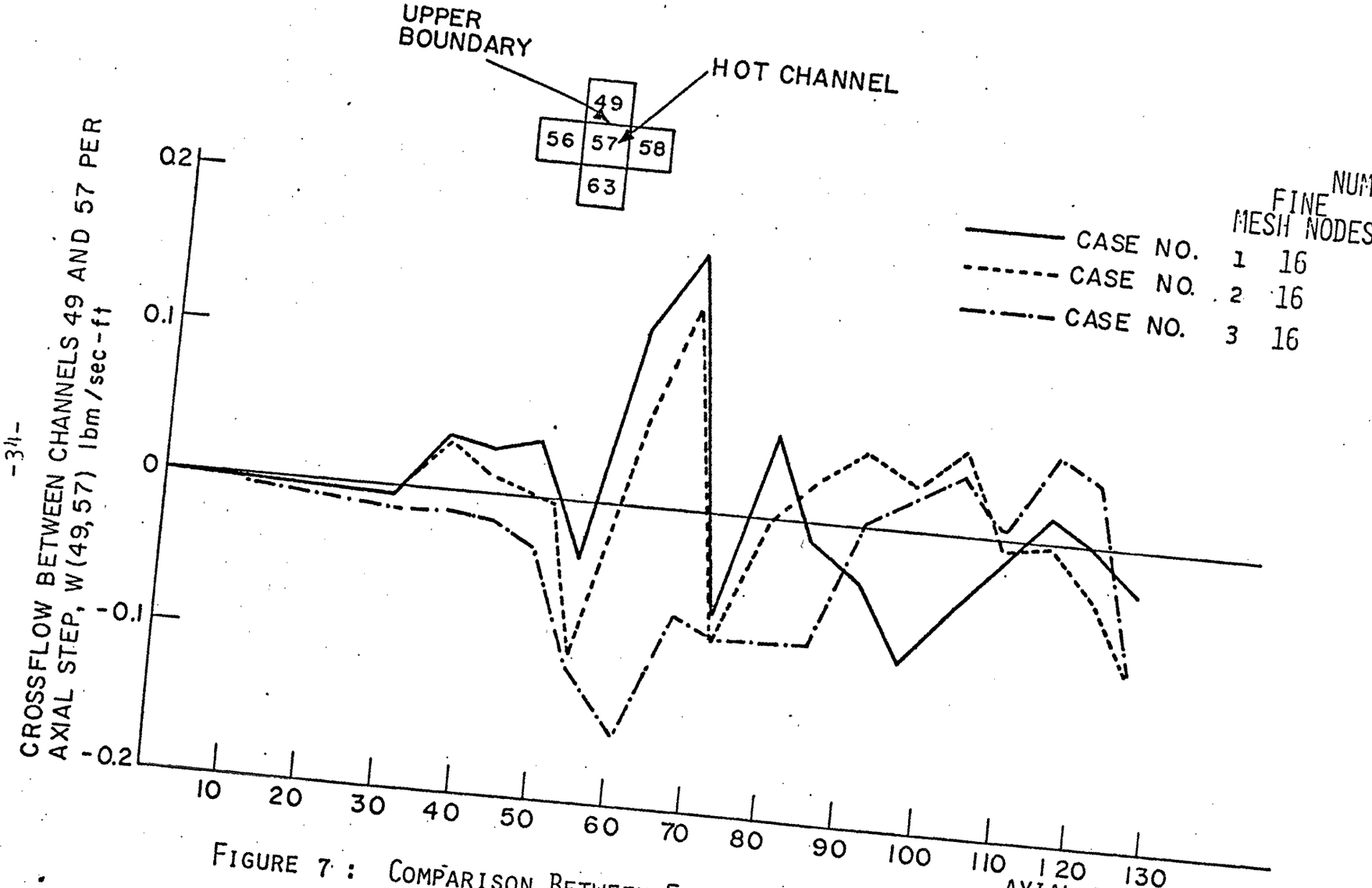

FIGURE 7 : COMPARISON BETWEEN FLOWS CROSSING THE UPPER BOUNDARY OF THE HOT SUBCHANNEL IN THE THREE CASES.

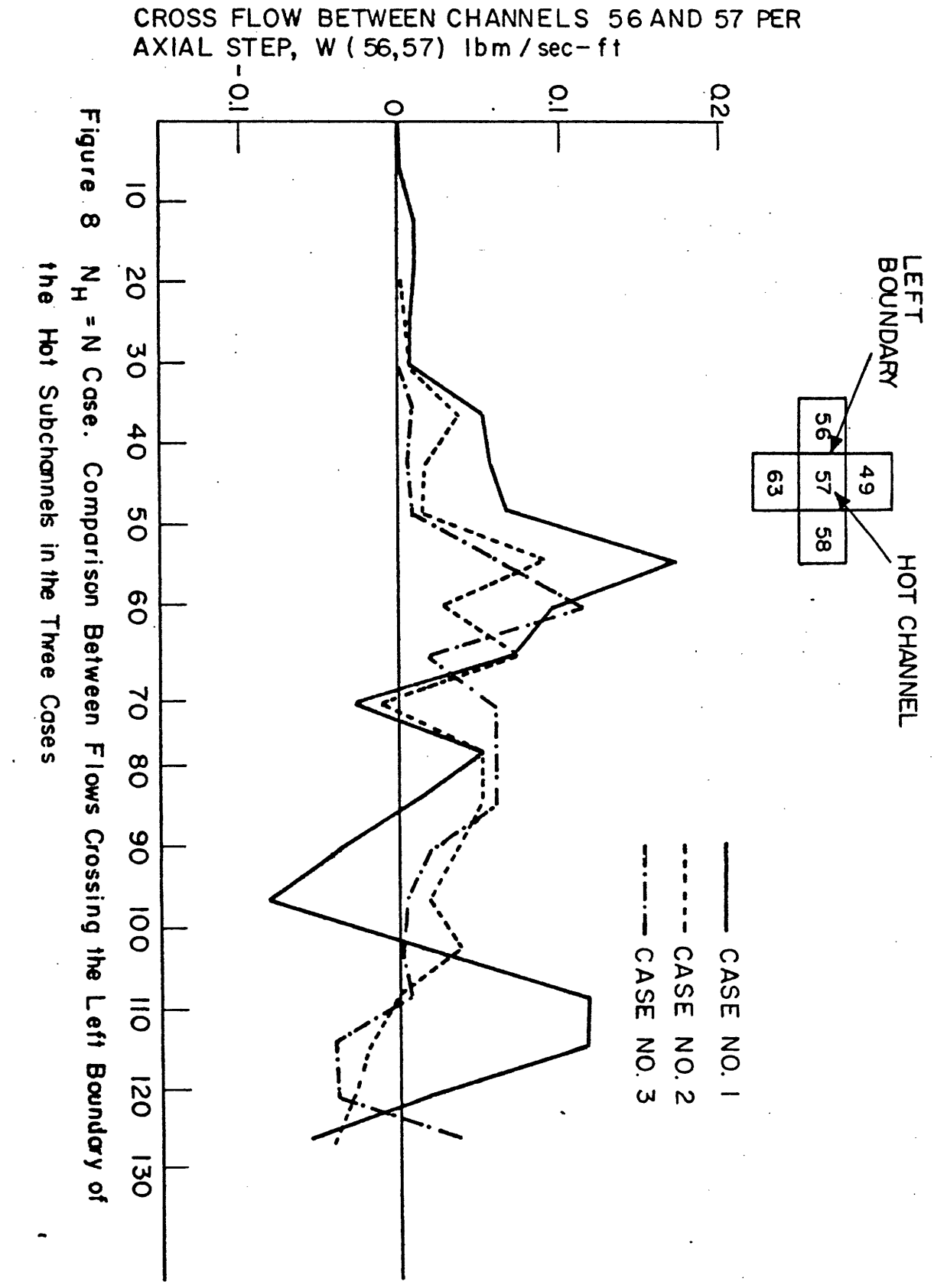

Figure 8 $N_H = N$ Case. Comparison Between Flows Crossing the Left Boundary of the Hot Subchannels in the Three Cases

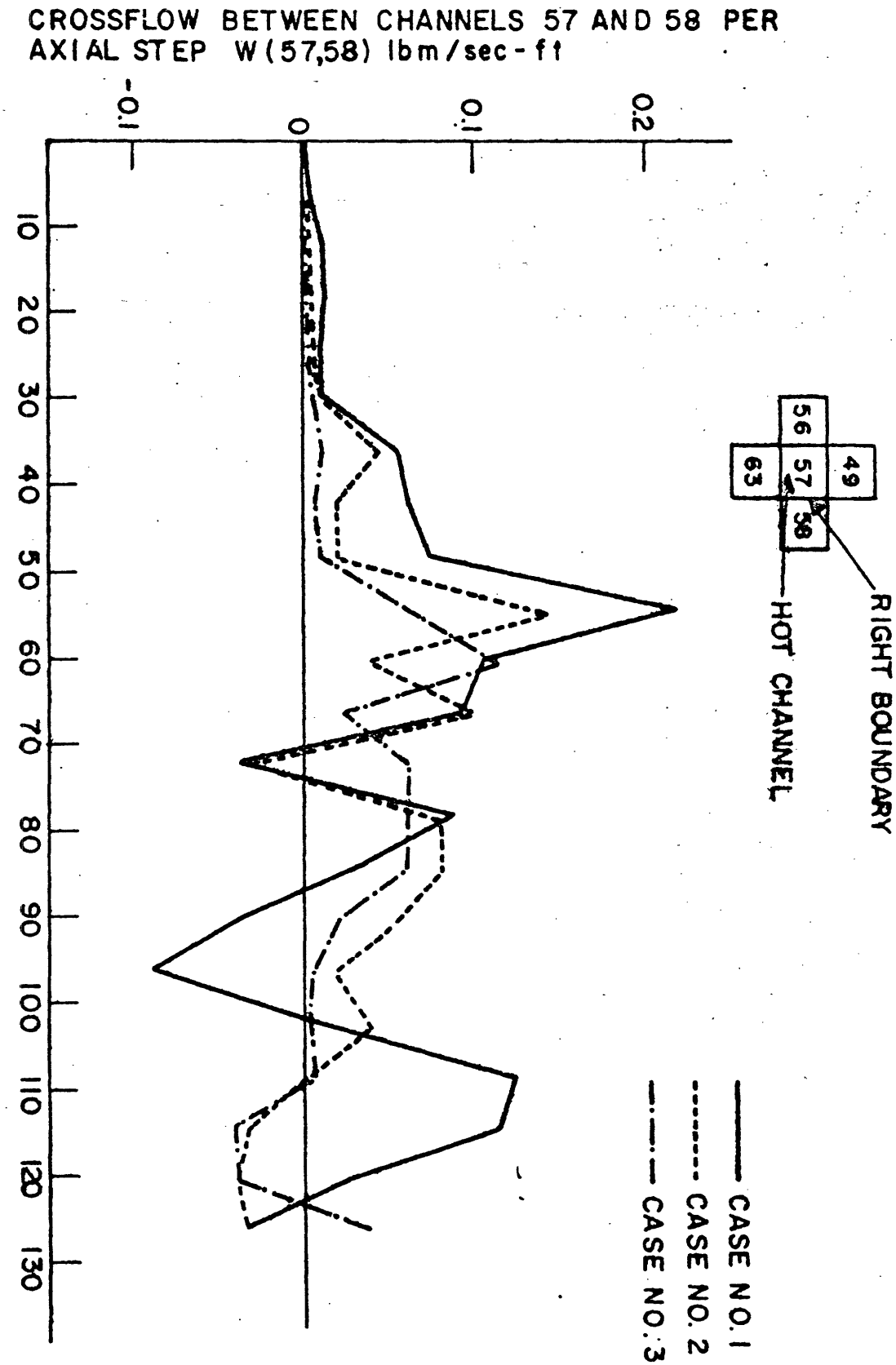

Figure 9 $N_H = N$ Case. Comparison Between Flows Crossing the Right Boundary of the Hot Subchannel in the Three Cases

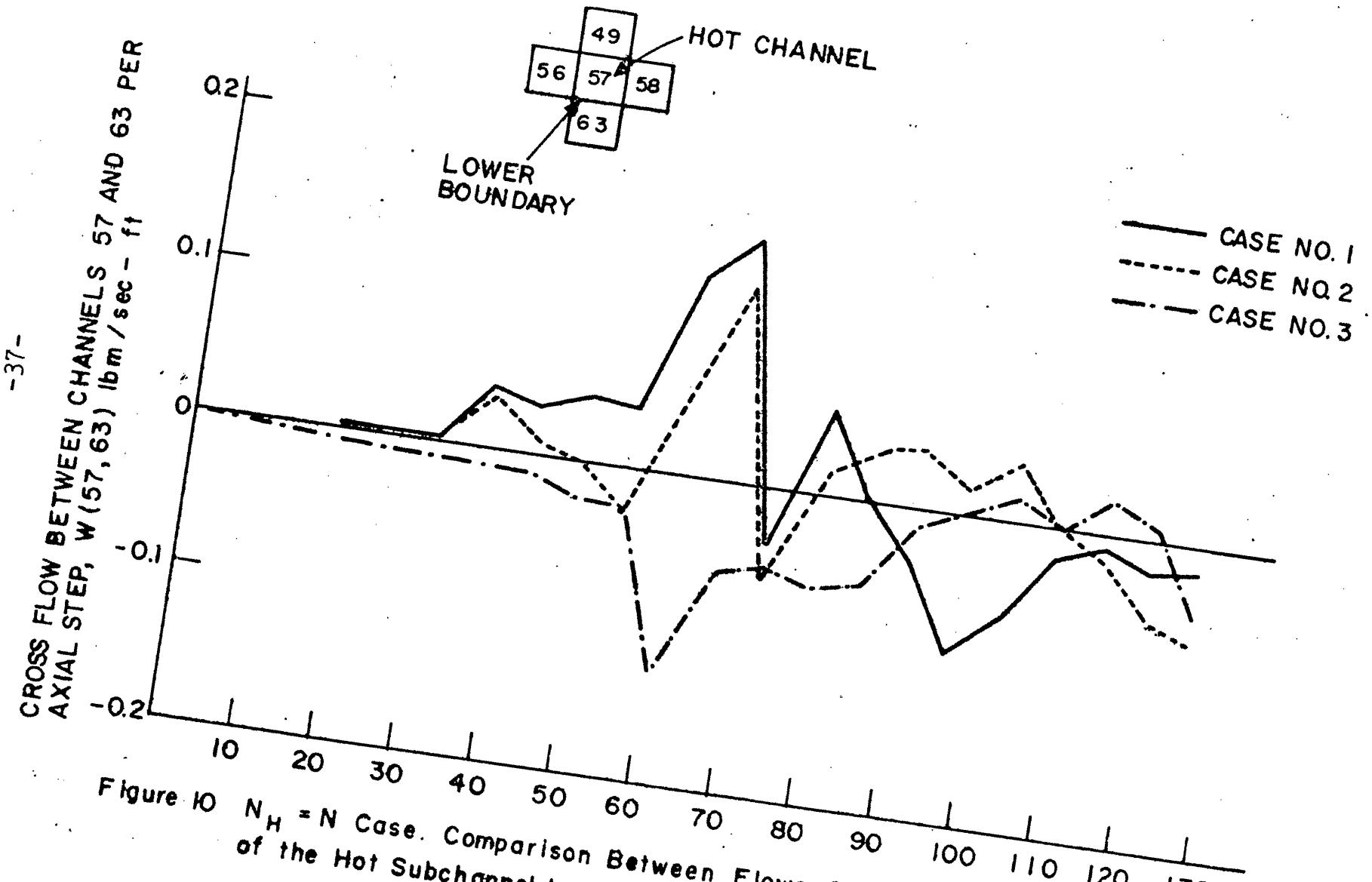

Figure 10 $N_H = N$ Case. Comparison Between Flows Crossing the Lower Boundary of the Hot Subchannel In the Three Cases.

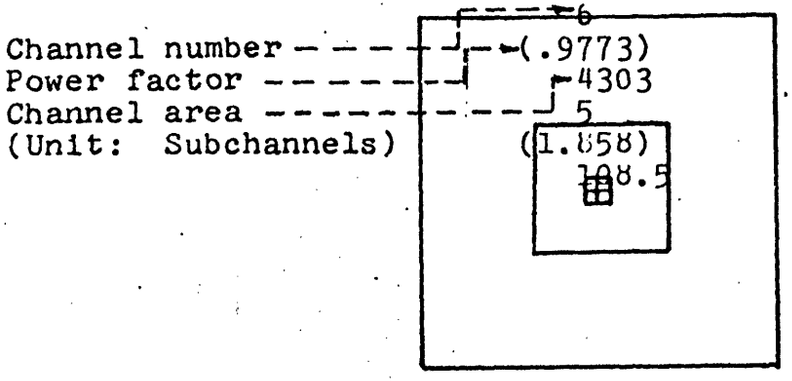

Case 34

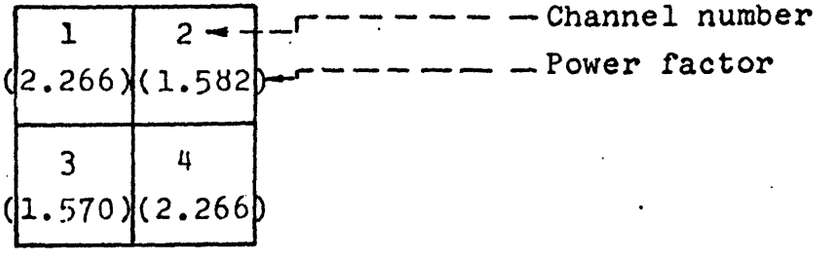

Internal Mesh

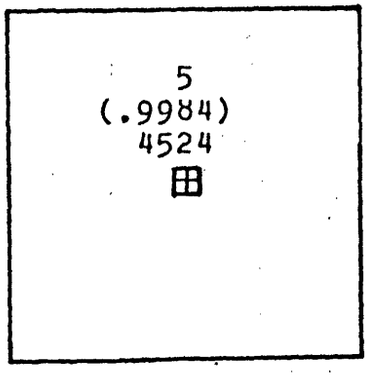

Case 35

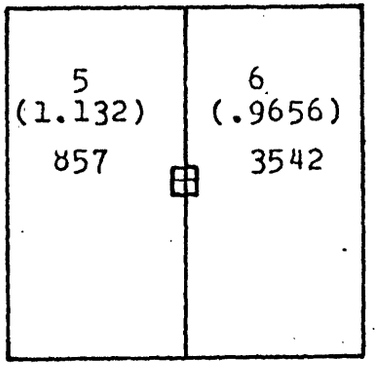

Case 38

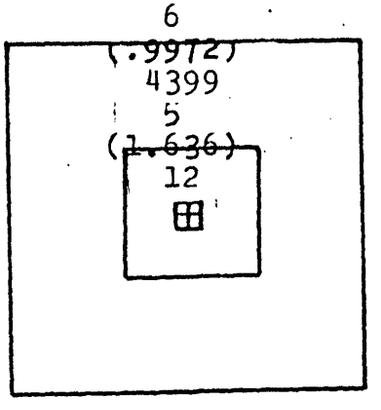

Case 37

Figure 11. Different Patterns of Channels with Small Numbers of External Node in Whole Core Analysis

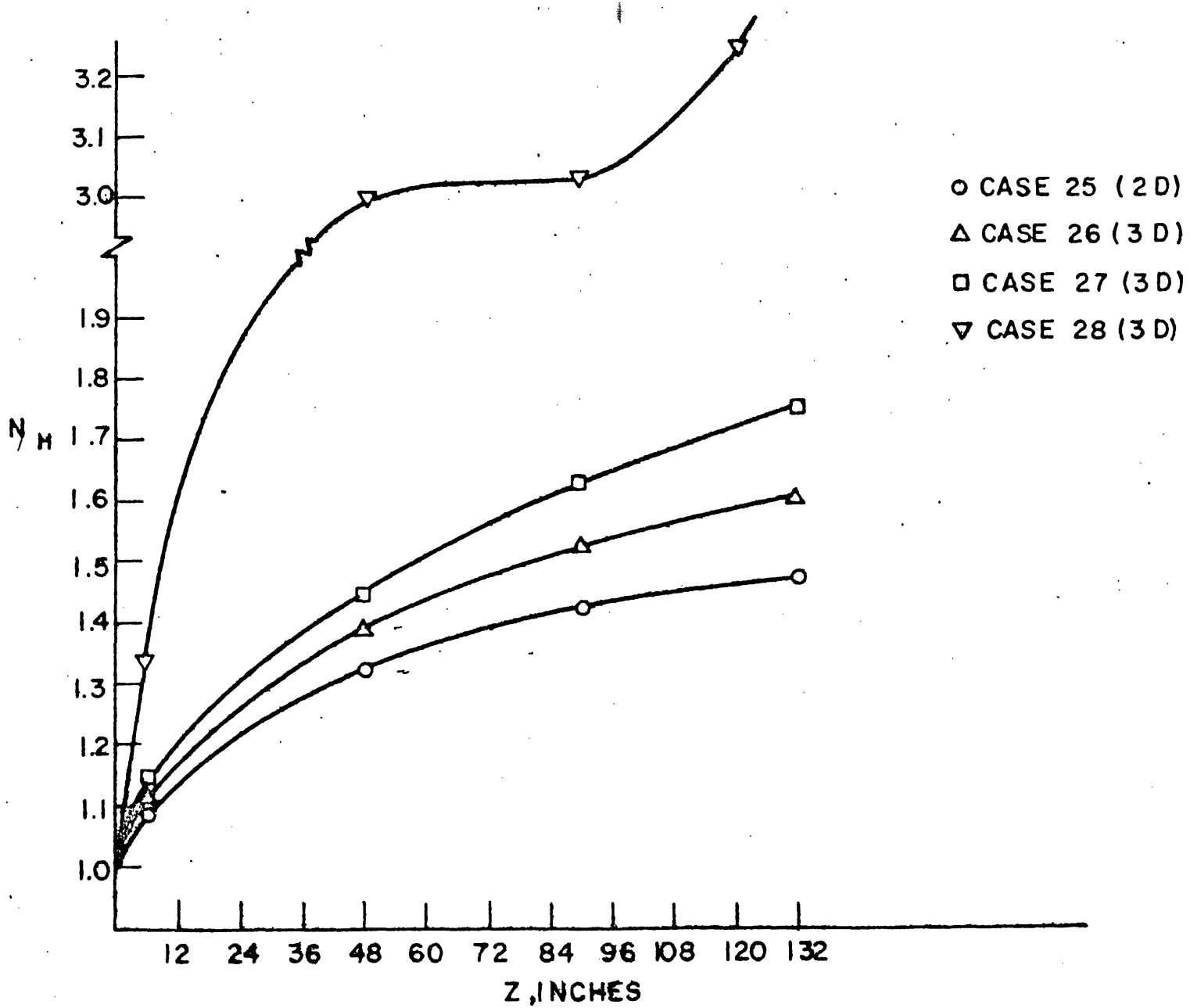

Figure 12. Comparison of $N_H(Z)$ Determined by 2D and Various 3D Representations

MULTICHANNEL REPRESENTATION

Properties and dimensions of the channels are those of Appendix C.

1	2	3	4	5	6	7	8	9	10	11	12
13	14	15	16	17	18	19	20	21	22	23	24
25	26	27	28	29	30	31	32	33	34	35	36
37	38	39	40	41	42	43	44	45	46	47	48
49	50	51	52	53	54	55	56	57	58	59	60
61	62	63	64	65	66	67	68	69	70	71	72
73	74	75	76	77	78	79	80	81	82	83	84
85	86	87	88	89	90	91	92	93	94	95	96
97	98	99	100	101	102	103	104	105	106	107	108

Boundary A

HOMOGENIZED REGIONS REPRESENTATION

(x) = Radial Power Factor in the Region = X

1 (.8)	2 (1.5)	3 (1.7)	4 (2.0)
5 (.9)	6 (1.3)	7 (1.5)	8 (1.7)
9 (.6)	10 (1.0)	11 (1.2)	12 (1.4)

Boundary A

Channel Layout for the 3D Multiregion Analysis

Figure 13

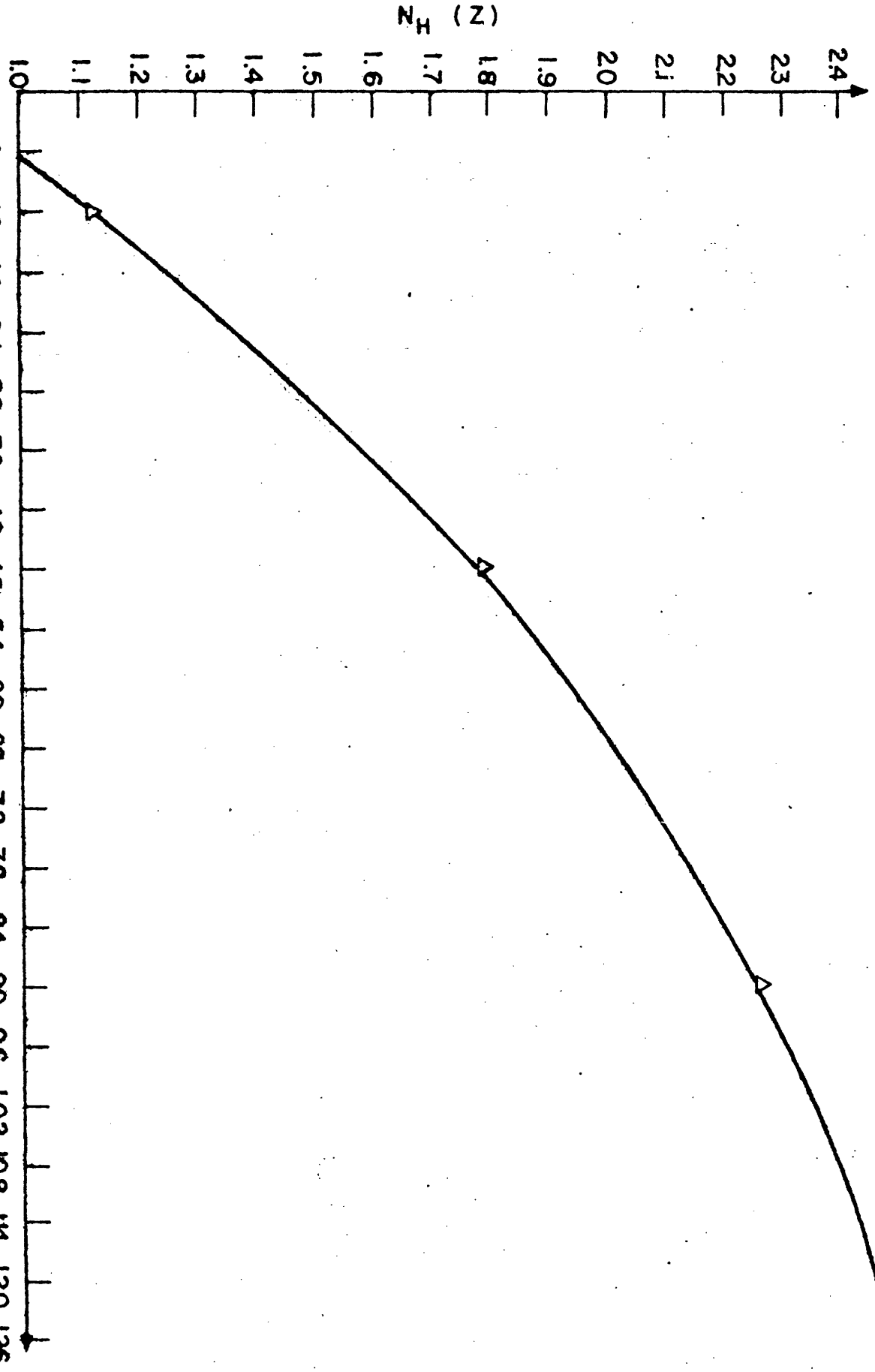

Figure 14 / N_H (Z) for the 3D problem of Figure 13

$$(x) \equiv \frac{y-z}{z-h_{inlet}}$$

y ≡ Exit enthalpy of the region found with the homogeneous region analysis

(z) ≡ Average exit enthalpy of the region found the the multichannel analysis

(4.5%) 635.40 (636.66)	(-1.73%) 673.18 (675.38)	(-2.36%) 696.76 (700.35)	(-2.91%) 716.08 (721.09)
(2.96%) 633.59 (631.15)	(-.53%) 660.91 (661.51)	(-2.56%) 681.59 (685.08)	(-1.44%) 697.09 (699.27)
(7.50%) 617.86 (613.04)	(2.36%) 643.00 (640.83)	(1.14%) 662.74 (661.45)	(.48%) 677.40 (676.79)

ERRORS FOUND WITHOUT USING TRANSPORT COEFFICIENTS

Figure 15.

TABLE I

EXPECTED ERRORS IN 2D HOMOGENIZED REGION ENTHALPY FOR POWER UPSET CASE

β \ N	2	3	4	5	7	9	11	15	23
0.0	0	0	0	0	0	0	0	0	0
0.005	0	-0.66	-0.61	-0.53	-0.40	-0.33	-0.27	-0.206	-0.135
0.02	0	-3.4	-3.6	-3.2	-2.3	-2.0	-1.72	-1.3	-0.86
0.04	0	-7.83	-8.5	-7.56	-5.31	-4.63	-3.9	-2.83	-1.83
0.06	0	-13.3	-14.4	-12.3	-9.34	-7.4	-6.12	-4.53	-2.36

NOTE: This table is built by using

$$\text{ERROR\%} = \frac{1 - \frac{1}{\overline{N_H}}}{\frac{P_R N A_s}{(P_r - 1) L \beta S} - \frac{1}{\overline{N_H}}}$$

Equation E.20 Negative value of ERROR % means that the exit enthalpy of two-channel case is less than multi-channel case.

where $L = 12'$
$A_s = 0.00519\ ft^2$
$P_r = 1.5$
$S = 0.22"$

$$\overline{N_H} = 1 + \ln\{1 + [353(\frac{N-2}{N})^{\frac{3.5\beta}{0.015+\beta}} \beta^1]\} \pm 5\%$$ Equation 5.1.1

Case No.	Total Channels	Internal Mesh	External Mesh	$N_H = 1$	$N_H = N$
1,5	101	16	85	1.040	1.047
2,6	61	16	45	1.040	1.042
3,7	30	16	14	1.041	1.043

MDNBR FOR THE DIFFERENT CASES ANALYZED

TABLE II

Case No.	Enthalpy in Channel 1 Btu/lb	Flow rate in Channel 1 lb/sec	Total cross flow out of Channel 1 lb/sec	Mass density decrease rate of Channel 5 by cross flow to Channel 6 lb/in^3-sec	MDNBR
34	686.45	0.5889	0.1403	11.95	1.034
35	649.71	0.6622	0.067	inapplicable	1.349
37	670.86	0.6174	0.1118	9.172	1.159
38	649.03	0.6632	0.066	0.329	1.356

Table III Effect of Different Patterns of Channels

Case No.	Internal Mesh	External Mesh	Features of Case	Turbulent Interchange Along Hot Assembly Boundary	MDNBR for $N_H = 1$
21	16	17	Hot Rod Centered Overlap Boundaries	Included	1.008
23	16	13	Hot Rod Non Centered Non Overlap Boundary	Included	1.019
24	16	13	Hot Rod Non Centered Non Overlap Boundary	Not Included	0.990
Cascade	Equivalent to 16 *	Equivalent to 16 **	Per Standard Cascade Approach	Not Included	?

* Nodes in 2nd Stage

** Nodes in 1st Stage

EFFECT OF HOT CHANNEL BOUNDARY CONDITIONS ON MDNBR

TABLE IV

CASE	MIXING	MDNBR
Base Case 85 coarse mesh	Constant β	1.040
16 fine mesh (case 5)	Variable β	1.047

TABLE V Sensitivity of MDNBR to β

CASE	K	MDNBR
Base Case 85 coarse mesh	0.0001	1.042
16 fine mesh (case 5)	0.5	1.040
	5.0	1.041

TABLE VI Demonstration of the Insensitivity of MDNBR to K

CASE	INLET FLOW	MDNBR
Base Case 85 coarse mesh	Uniform	1.040
16 fine mesh (case 5)	Outer Assemblies - 1.001 Inner Assemblies - .95 core avg.	1.028

TABLE VII Effect of Inlet Flow Distribution on MDNBR

COMPARISON WITH THINC-IV RESULTS

METHODS	NO. OF FINE MESH NODES	NO. OF COARSE MESH NODES	COMPUTER CODE	MDNBR
ONE-STAGE SIMPLIFIED METHOD	9	5	COBRA IIIC/MIT	2.042
ONE-STAGE INTERMEDIATE METHOD	45	32	COBRA IIIC/MIT	2.049
THREE-STAGE METHOD			THINC-IV	1.959

TABLE VIII

APPENDIX A

DERIVATIONS OF THE COUPLING COEFFICIENTS

In this appendix, the coupling coefficients, N_H, N_U, N_{TP}, N_{TF} and N_{TU} are derived in (A.1), (A.2) and (A.3). The multi-subchannel layout and homogenized representation layout can be seen in Figures A.2 and A.3 respectively. For N odd, subchannels C and D can be regarded as half channels. For N even, subchannels C and D can be regarded as full channels. The derivations presented here for these coupling coefficients are valid for N either even or odd.

A.1 Derivation of N_H

The steady state energy equation for adjacent subchannels i and j following (7, equation A-6) can be written as:

$$\frac{\partial m_i h_i}{\partial x} = q_i - \sum_{j=1}^{N} (t_i - t_j) c_{i,j} - \sum_{j=1}^{N} (h_i - h_j) w'_{i,j} - \sum_{j=1}^{N} w_{i,j} h^* \qquad \text{(A.1.1)}$$

where

$$\begin{cases} w_{i,j} h^* = w_{i,j} h_i & \text{if } w_{i,j} > 0 \qquad \text{(A.1.2a)} \\ w_{i,j} h^* = w_{i,j} h_j & \text{if } w_{i,j} < 0 \qquad \text{(A.1.2b)} \end{cases}$$

Note that $w_{i,j} > 0$ means the direction of diversion cross-flow is from channel i to channel j, and $w_{i,j} < 0$ means

the direction of diversion crossflow is from channel j to channel i.

We consider a multi-subchannel layout shown in Figure A.2 and write the energy equation for each subchannel.

$$\frac{\partial m_A h_A}{\partial x} = q'_A - (t_A - t_B)c_{A,B} - (h_A - h_B)w'_{A,B} - w_{A,B}h^* \qquad \text{(A.1.3a)}$$

$$\frac{\partial m_B h_B}{\partial x} = q'_B - (t_B - t_C)c_{B,A} - (t_B - t_A)c_{B,A} - (h_B - h_C)w'_{B,C} - (h_B - h_A)w'_{B,A} - w_{B,C}h^* - w_{B,A}h^* \qquad \text{(A.1.3b)}$$

$$\frac{\partial m_C h_C}{\partial x} = q'_C - (t_C - t_D)c_{C,D} - (t_C - t_B)c_{C,B} - (h_C - h_D)w'_{C,D} - (h_C - h_B)w'_{C,B} - w_{C,D}h^* - w_{C,B}h^* \qquad \text{(A.1.3c)}$$

$$\frac{\partial m_D h_D}{\partial x} = q'_D - (t_D - t_E)c_{D,E} - (t_D - t_C)c_{D,C} - (h_D - h_E)w'_{D,E} - (h_D - h_C)w'_{D,C} - w_{D,E}h^* - w_{D,C}h^* \qquad \text{(A.1.3d)}$$

$$\frac{\partial m_E h_E}{\partial x} = q'_E - (t_E - t_F)c_{E,F} - (t_E - t_D)c_{E,D} - (h_E - h_F)w'_{E,F} - (h_E - h_D)w'_{E,D} - w_{E,F}h^* - w_{E,D}h^* \qquad \text{(A.1.3e)}$$

$$\frac{\partial m_F h_F}{\partial x} = q'_F - (t_F - t_F)c_{F,E} - (h_F - h_E)w'_{F,E} - w_{F,E}h^* \qquad \text{(A.1.3f)}$$

Some relationships exist for each pair of channels between the energy carried by diversion flows, conductivity factors $c_{i,j}$ and energy carried by turbulent interchanges. For example for the channel pair A,B, the following relationships hold:

$$c_{A,B} = c_{B,A} \tag{A.1.4a}$$

$$w'_{A,B} = w'_{B,A} \tag{A.1.4b}$$

$$w_{A,B} = -w_{B,A} \tag{A.1.4c}$$

$$\begin{cases} w_{A,B}h^* = w_{A,B}h_A \\ \\ w_{B,A}h^* = w_{B,A}h_A \end{cases} \quad \text{if } w_{A,B} > 0 \text{ (i.e. } w_{B,A} < 0) \tag{A.1.4d}$$

$$\begin{cases} w_{A,B}h^* = w_{A,B}h_B \\ \\ w_{B,A}h^* = w_{B,A}h_B \end{cases} \quad \text{if } w_{A,B} < 0 \text{ (i.e. } w_{B,A} > 0) \tag{A.1.4e}$$

Therefore, a simple relationship between $w_{A,B}h^*$ and $w_{B,A}h^*$ can be derived from equations (A.1.4c), (A.1.4d) and (A.1.4e).

$$w_{A,B}h^* = -w_{B,A}h^* \quad \text{for} \quad w_{A,B} \gtrless 0 \tag{A.1.5}$$

We define the region composed of subchannels A, B, and C as region L, and similarly, D, E, and F as region R. Now adding the energy equations for region L and region R and utilizing the relations of equations (A.1.4a, A.1.4b) and (A.1.5) we obtain the following two energy equations:

$$\sum_{i=A}^{C} \frac{\partial h_i m_i}{\partial x} = \sum_{i=A}^{C} q_i' - (t_C - t_D)c_{C,D} - (h_C - h_D)w'_{C,D} - h^* w_{C,D} \qquad \text{(A.1.6a)}$$

$$\sum_{i=D}^{F} \frac{\partial h_i m_i}{\partial x} = \sum_{i=D}^{E} q_i' - (t_D - t_C)c_{D,C} - (h_D - h_C)w'_{D,C} - h^* w_{D,C} \qquad \text{(A.1.6b)}$$

On the other hand, we can express the energy equation for the homogenized regions of Figure A.3 in (Volume II) directly as

$$\frac{\partial H_L M_L}{\partial x} = Q'_L - \left(\frac{T_L - T_R}{N''_H}\right) C_{L,R} - \left(\frac{H_L - H_R}{N_H}\right) W'_{L,R} - \frac{H^*}{N_H'} W_{L,R} \qquad \text{(A.1.7a)}$$

$$\frac{\partial H_R M_R}{\partial x} = Q'_R - \left(\frac{T_R - T_L}{N''_H}\right) C_{R,L} - \left(\frac{H_R - H_L}{N_H}\right) W'_{R,L} - \frac{H^*}{N_H'} W_{R,L} \qquad \text{(A.1.7b)}$$

If we assume

$$\sum_{i=A}^{C} \frac{\partial h_i m_i}{\partial x} = \frac{\partial H_L M_L}{\partial x} \qquad \text{(A.1.8a)}$$

$$\sum_{i=D}^{F} \frac{\partial h_i m_i}{\partial x} = \frac{\partial H_R M_R}{\partial x} \qquad \text{(A.1.8b)}$$

$$Q'_L \equiv \sum_{i=A}^{C} q_i' \qquad \text{(A.1.8c)}$$

$$Q'_R \equiv \sum_{i=D}^{F} q'_i \qquad \text{(A.1.8d)}$$

and

$$W'_{L,R} = w'_{C,D} \qquad \text{(A.1.8e)}$$

$$W_{L,R} = w_{C,D} \qquad \text{(A.1.8f)}$$

then N_H, N'_H, and N''_H can be defined as follows:

$$N''_H \equiv \frac{T_L - T_R}{t_C - t_D} \qquad \text{(A.1.9a)}$$

$$N_H \equiv \frac{H_L - H_R}{h_C - h_D} \qquad \text{(A.1.9b)}$$

$$N'_H \equiv \frac{H^*}{h^*} \quad \text{where} \quad \frac{H^*}{h^*} = \frac{H_L}{h_C} \text{ if } W_{L,R} > 0 \qquad \text{(A.1.9c)}$$

$$\frac{H^*}{h^*} = \frac{H_R}{h_D} \text{ if } W_{R,L} < 0$$

If we assume the specific heat at each elevation is constant, then

$$N''_H = N_H \ . \qquad \text{(A.1.10)}$$

Also the subchannel enthalpy h^* can be expressed as a function of N_H in the following manner by virtue of the definitions of H_L, H_R and N_H (eqn. A.1.9b) and the assumption of a symmetric enthalpy profile with respect to the central boundary (see Appendix B Volume II for derivation of following relations).

$$\frac{h_C + h_D}{2} = \frac{H_L + H_R}{2} \qquad \text{(A.1.11)}$$

$$h^* = \frac{H_L+H_R}{2} + \frac{H_L - \frac{H_L+H_R}{2}}{N_H} \quad \text{if } w_{C,D} > 0 \qquad \text{(2.3.1)(Vol}$$

$$\text{and} \quad h^* = \frac{H_L+H_R}{2} - \frac{H_R - \frac{H_L+H_R}{2}}{N_H} \quad \text{if } w_{C,D} < 0 \qquad \text{(2.3.1a)(Vo}$$

Therefore, we can obtain N_H' in terms of N_H and other known quantities.

$$N_H' = \frac{H^*}{h^*} = \frac{H_L}{\frac{H_L+H_R}{2} + \frac{H_L - \frac{H_L+H_R}{2}}{N_H}} \quad \text{if } w_{C,D} > 0 \qquad \text{(A.1.12a)}$$

$$\text{and} \quad N_H' = \frac{H^*}{h^*} = \frac{H_R}{\frac{H_L+H_R}{2} - \frac{H_R - \frac{H_L+H_R}{2}}{N_H}} \quad \text{if } w_{C,D} < 0 \qquad \text{(A.1.12b)}$$

From the above derivation we have determined the coupling coefficients required in the energy equations (A.1.7a) and (A.1.7b). By virtue of equations (A.1.10) and (A.1.12a and b) these coefficients are all expressable in terms of the single coefficient N_H.

A.2 Derivation of N_U

The steady state axial momentum equation for channel i and adjacent channels j following (7, equation A-11) can be written as:

$$-F_i - gA_i\rho_i\cos\theta - A_i \frac{\partial p_i}{\partial x} = \frac{\partial}{\partial x} m_i u_i + (u_i - u_j)w'_{i,j} + u^* w_{i,j} \qquad (A.2.1)$$

where

$$F = \text{friction factor} = \left[\frac{A\nu f\phi}{2D} + \frac{ak\nu'}{2\Delta x} \right] \left[\frac{m}{A} \right]^2$$

where the parameters in the definition are per Cobra, BNWL-

$$u^* w_{i,j} = u_i w_{i,j} \quad \text{if } w_{i,j} > 0$$

$$u^* w_{i,j} = u_j w_{i,j} \quad \text{if } w_{i,j} < 0$$

Consider a multi-subchannel layout shown in Figure A2 and write the axial momentum equation for each channel. In the steady state condition, obtain:

$$A_A \frac{\partial p_A}{\partial x} = \frac{\partial}{\partial x}(m_A u_A) - (F+\rho g A \cos\theta)_A - w'_{A,B}(u_A - u_B) + u^* w_{A,B} \quad \text{(A.1.2a)}$$

$$A_B \frac{\partial p_B}{\partial x} = \frac{\partial}{\partial x}(m_B u_B) - (F+\rho g A \cos\theta)_B - w'_{B,C}(u_B - u_C) - w'_{B,A}(u_B - u_A) + u^* w_{B,C} + u^* w_{B,A} \quad \text{(A.2.2b)}$$

$$A_C \frac{\partial p_C}{\partial x} = \frac{\partial}{\partial x}(m_C u_C) - (F+\rho g A \cos\theta)_C - w'_{C,D}(u_C - u_D) - w'_{C,B}(u_C - u_B) + u^* w_{C,D} + u^* w_{C,B} \quad \text{(A.2.2c)}$$

$$A_D \frac{\partial p_D}{\partial x} = \frac{\partial}{\partial x}(m_D u_D) - (F+\rho g A \cos\theta)_D - w'_{D,E}(u_D - u_E) - w'_{D,C}(u_D - u_C) + u^* w_{D,E} + u^* w_{D,C} \quad \text{(A.2.2d)}$$

$$A_E \frac{\partial p_E}{\partial x} = \frac{\partial}{\partial x}(m_E u_E) - (F+\rho g A \cos\theta)_E - w'_{E,F}(u_E - u_F) - w'_{E,D}(u_E - u_D) + u^* w_{E,F} + u^* w_{E,D} \quad \text{(A.2.2e)}$$

$$A_F \frac{\partial p_F}{\partial x} = \frac{\partial}{\partial x}(m_F u_F) - (F+\rho g A \cos\theta)_F - w'_{F,E}(u_F - u_E) + u^* w_{F,E} \quad \text{(A.2.2f)}$$

where $$w'_{i,j} = w'_{j,i} \quad \text{(A.2.3a)}$$

$$w_{i,j} = -w_{j,i} \quad \text{(A.2.3b)}$$

$$u^* w_{i,j} = u_i w_{i,j} \quad \text{if} \quad w_{i,j} > 0 \quad \text{(A.2.3c)}$$

$$= u_j w_{i,j} \quad \text{if} \quad w_{i,j} < 0 \quad \text{(A.2.3d)}$$

We define the region composed of three channels A, B, and C are region L, and similarly channels D, E, and F as region R. Now, adding all the axial momentum equations for region L and R, we obtain:

$$\sum_{i=A}^{C} \frac{\partial A_i p_i}{\partial x} = \sum_{i=A}^{C} (m_i u_i) - \sum_{i=A}^{C} [(F+g\text{Acos}\theta)_i] - w'_{C,D} (u_C - u_D) - u^* w_{C,D} \qquad \text{(A.2.4a)}$$

$$\sum_{i=D}^{F} \frac{\partial A_i p_i}{\partial x} = \sum_{i=D}^{F} (m_i u_i) - \sum_{i=D}^{F} [(F+g\text{Acos}\theta)_i] - w'_{D,C} (u_D - u_C) - u^* w_{D,C} \qquad \text{(A.2.4b)}$$

We now write the two axial momentum equations for regions L and R in the two channel representation obtained:

$$\frac{\partial A_L P_L}{\partial x} = M_L U_L - [(F+g\text{Acos}\theta)_L] - W'_{L,R} \left(\frac{U_L - U_R}{N_U}\right) - \frac{U^* W_{L,R}}{N_U'} \qquad \text{(A.2.5a)}$$

$$\frac{\partial A_R P_R}{\partial x} = M_R U_R - [(F+g\text{Acos}\theta)_R] - W'_{R,L} \left(\frac{U_R - U_L}{N_U}\right) - \frac{U^* W_{R,L}}{N_U'} \qquad \text{(A.2.5b)}$$

The N_U and N_U' can be defined as follows:

$$N_U \equiv \frac{U_L - U_R}{u_C - u_D} \qquad \text{(A.2.7a)}$$

$$N_U' \equiv \frac{U^*}{u^*} \qquad \text{(A.2.7b)}$$

where $$N_U' = \frac{U_L}{u_C} \quad \text{if} \quad w_{C,D} > 0 \qquad \text{(A.2.8a)}$$

$$N_U' = \frac{U_R}{u_D} \quad \text{if} \quad w_{C,D} < 0 \qquad \text{(A.2.8b)}$$

The subchannel velocity u^* can be expressed as a function of N_U in the following manner by virtue of the previous specified definition of N_U (equation A.2.7a) and the assumption of a symmetric axial velocity profile with respect to the central boundary

$$\frac{u_C + u_D}{2} = \frac{U_L + U_R}{2} \qquad \text{(A.2.9)}$$

$$u^* = \frac{U_L + U_R}{2} + \frac{U_L - \frac{U_L + U_R}{2}}{N_U} \quad \text{if } w_{L,R} > 0 \qquad \text{(2.3.2) (Vol. I}$$

$$u^* = \frac{U_L + U_R}{2} + \frac{U_R - \frac{U_L + U_R}{2}}{N_U} \quad \text{if } w_{L,R} < 0 \qquad \text{(2.3.2a)(Vol. I}$$

Therefore we get:

$$N_U' = \frac{U_L}{\frac{U_L+U_R}{2} + \frac{U_L - \frac{U_L+U_R}{2}}{N_U}} \quad \text{if } w_{L,R} > 0 \qquad \text{(A.2.10a)}$$

$$N_U' = \frac{U_R}{\frac{U_L+U_R}{2} + \frac{U_R - \frac{U_L+U_R}{2}}{N_U}} \quad \text{if } w_{L,R} < 0 \qquad \text{(A.2.10b)}$$

From the above derivation we have determined the coupling coefficients required in the axial momentum equations (A.1.7a) and (A.1.7b). By virtue of equations (A.2.7b) and (A.2.10a and b), these coupling coefficients are all expressible in terms of the single coefficient N_U.

A.3 Derivation of N_{TP}, N_{TU} and N_{TF}

The steady state transverse momentum equation for adjacent channels i and j following (7, equation A-17) can be written as:

$$\frac{\partial(\overline{uw}_{i,j})}{\partial x} = \frac{s}{\ell}(p_i - p_j) - c_i \qquad \text{(A.3.1)}$$

where

$$\overline{uw}_{i,j} = \frac{1}{2} (u_i + u_j) w_{i,j} \qquad \text{(A.3.2a)}$$

$$c_i = \frac{s}{\ell} \left(\frac{k|w_{i,j}|}{2s^2 \rho^*_{i,j}} \right) w_{i,j} \qquad \text{(A.3.2b)}$$

$$\rho^*_{i,j} = \rho_i \quad \text{if} \quad w_{i,j} > 0 \qquad \text{(A.3.2c)}$$

$$\rho_j \quad \text{if} \quad w_{i,j} < 0 \qquad \text{(A.3.2d)}$$

where subscripts i and j denote adjacent channels.

Consider the multichannel layout shown in Figure A.2 and write the transverse momentum equations associated with each boundary we obtain:

$$\frac{\partial(\overline{uw}_{A,B})}{\partial x} = \frac{s}{\ell} (p_A - p_B) - c_A \qquad \text{(A.3.3a)}$$

$$\frac{\partial(\overline{uw}_{B,C})}{\partial x} = \frac{s}{\ell} (p_B - p_C) - c_B \qquad \text{(A.3.3b)}$$

$$\frac{\partial(\overline{uw}_{C,D})}{\partial x} = \frac{s}{\ell} (p_C - p_D) - c_C \qquad \text{(A.3.3c)}$$

$$\frac{\partial(\bar{u}w_{D,E})}{\partial x} = \frac{s}{\ell}(p_D - p_E) - c \qquad \text{(A.3.3d)}$$

$$\frac{\partial(\bar{u}w_{E,F})}{\partial x} = \frac{s}{\ell}(p_E - p_F) - c_E \qquad \text{(A.3.3e)}$$

We can derive a combined transverse momentum for all these channels.

$$\sum_{i=A}^{E} \frac{\partial(\bar{u}w_{i,i+1})}{\partial x} = \frac{s}{\ell}(p_A - p_E) - \sum_{i=A}^{E} c_i \qquad \text{(A.3.4)}$$

If we consider these N channels as two channels, i.e., we combine channel A, B, and C as channel L and channel D, E and F as channel R, we can write the two channel transverse momentum equations as follows:

$$\frac{\partial(\bar{U}W_{L,R})}{N_{TU}\partial x} = \frac{s}{\ell}\left(\frac{P_L - P_R}{N_{TP}}\right) - \frac{C}{N_{TF}} \qquad \text{(A.3.5)}$$

where $$\bar{U} = \frac{U_L + U_R}{2} \qquad \text{(A.3.6)}$$

and N_{TU}, N_{TP}, N_{TF} are coupling coefficients introduced to match equation (A.3.4) with equation (A.3.5).

Therefore N_{TU}, N_{TP} and N_{TF} can be defined as follows:

$$N_{TU} \equiv \frac{\frac{\partial(\bar{U}W_{L,R})}{\partial x}}{\sum_{i=A}^{E} \frac{\left(\partial\ \bar{u}\ \ w_{i,i+1}\right)}{\partial x}} \qquad \text{(A.3.7a)}$$

$$N_{TP} \equiv \frac{P_L - P_R}{p_A - p_F} \qquad \text{(A.3.7b)}$$

$$N_{TF} = \frac{C}{\sum_{i=A}^{E} c_i} = \frac{\frac{W_{L,R}}{\rho^*_{L,R}}\ W_{L,R}}{\sum_{i=A}^{E} \frac{|w_{i,i+1}|\, w_{i,i+1}}{\rho^*_{i,i+1}}} \qquad \text{(A.3.7c)}$$

From the above derivation we have determined the coupling coefficients required in the transverse momentum equation (A.3.5).

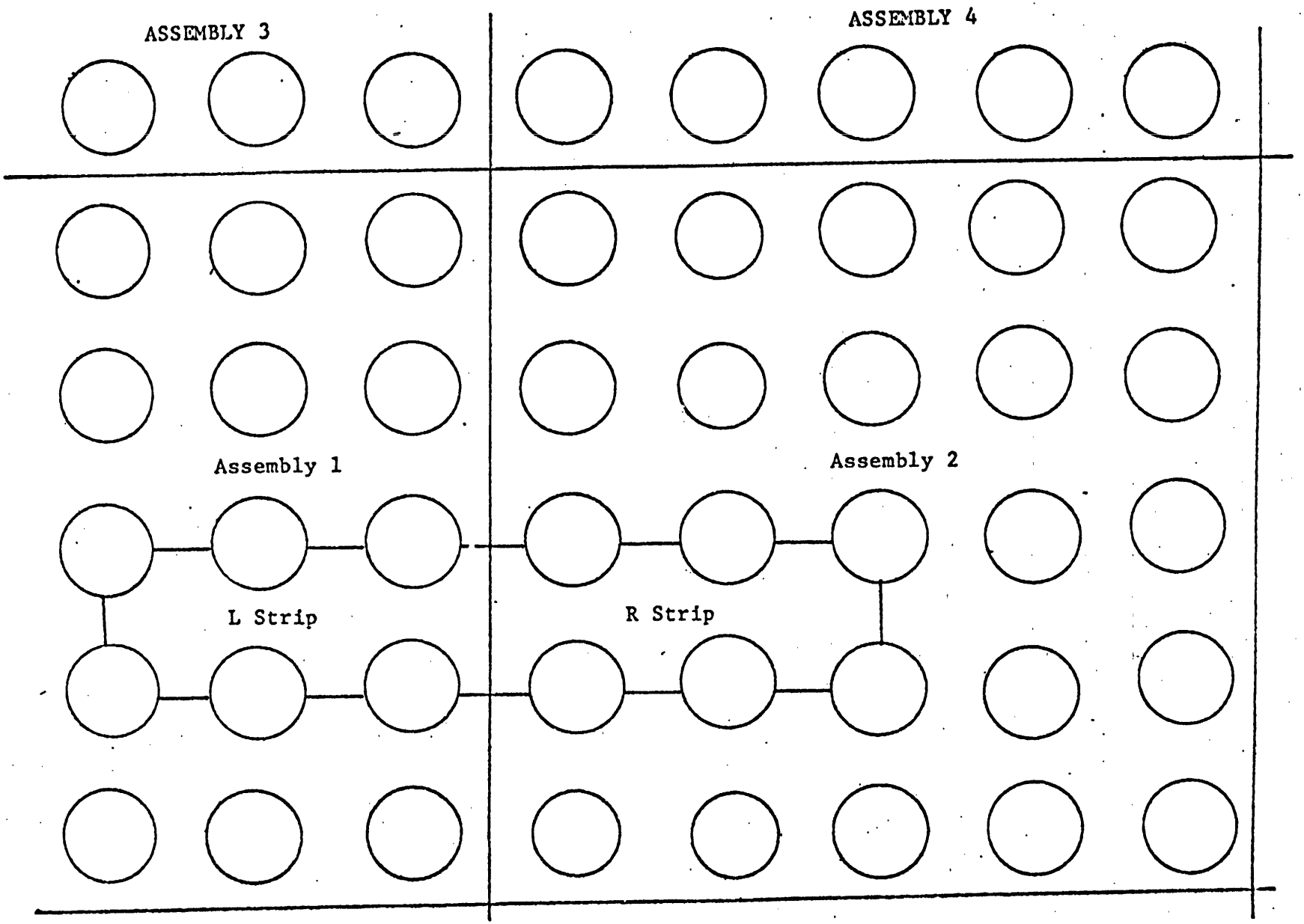

Figure A.1 NxN Rod Assemblies in Square Array, N=5

Letters - Channel Subscripts

 = Adiabatic Boundary

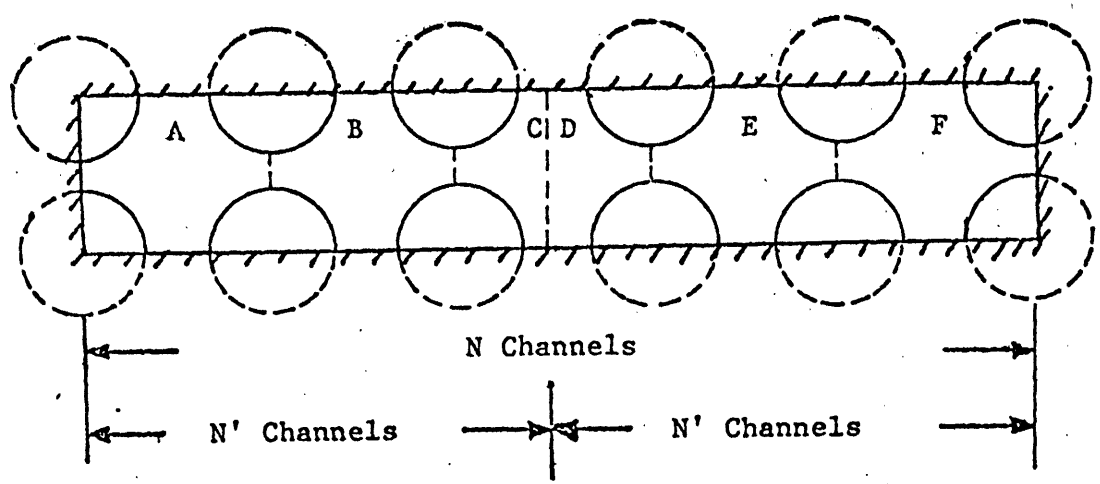

Figure A.2 Strips of Adjacent N' Channels

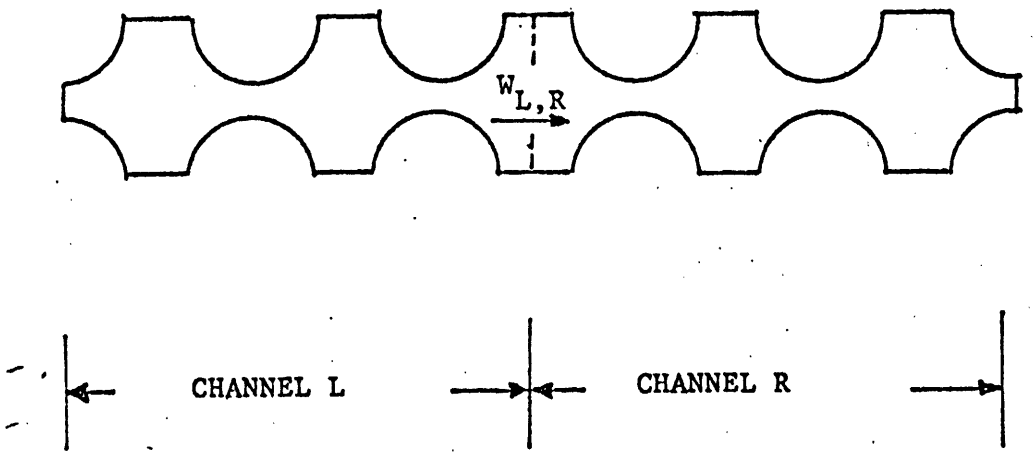

Figure A.3 Homogenized Representation of Strips of N' Subchannels

APPENDIX B

ANALYSIS OF COUPLING COEFFICIENTS IN COBRA IIIC

Introduction

The general coupling coefficients N_H, N_H', N_H'', N_U, N_U', N_{TF}, N_{TP} and N_{TU} are derived from the differential conservation equations in Appendix A. However, it is questionable whether these derivations are applicable to the difference conservation equations which are always employed in the code computation.

The purpose of this appendix is first to show the difference between H_L and $\bar{h}_L$ resulting from introduction of the coefficients N_H, N_H' and N_H'' from Appendix A into the COBRA IIIC computation, and second, to investigate a general way to derive the coupling coefficients from the difference conservation equations.

B.1 Error Between H_L and $\bar{h}_L$ Employing N_H, N_H' and N_H'' in the Homogenized Computation

If the equations used in COBRA IIIC were those described in Appendix A, both values ($\bar{h}_L$ and H_L) should be identical in cases where either the diversion crossflow is negligible or is the same for the boundary that separates the left and right hand sides. But from the results presented in the study (Section 3.1.2 Volume II) we can observe the existence of slight differences between these values.

These differences, as will be shown below, are due to the fact that the difference equations used in COBRA IIIC are not exactly those of Appendix A.

Let us take the following example:

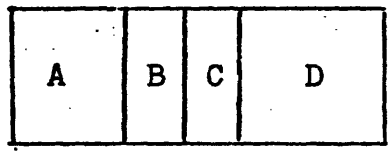

multi-subchannel layout

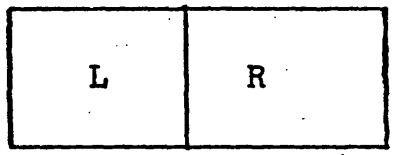

homogenized channel layout

In the COBRA IIIC formulation, the energy equations for each channel are written as:

$$h_A(J) = h_A(J-1) + \frac{q'_A(J-\frac{1}{2})}{m_A(J-1)} \cdot \Delta x - \frac{(t_A(J-1)-t_B(J-1)C_{A,B}\cdot\Delta x}{m_A(J-1)}$$

$$- \frac{(h_A(J-1)-h_B(J-1))w'_{A,B}(J-1)\cdot\Delta x}{m_A(J-1)}$$

$$- \frac{(h_A(J-1)-h^*(J-1))w_{A,B}(J-1)\cdot\Delta x}{m_A(J-1)} \qquad \text{(B.1.1)}$$

$$h_B(J) = h_B(J-1) + \frac{q'_B(J-\frac{1}{2})}{m_B(J-1)} \cdot \Delta x - \frac{(t_B(J-1)-t_C(J-1))C_{B,C}\cdot\Delta x}{m_B(J-1)}$$

$$- \frac{(t_B(J-1)-t_A(J-1))C_{A,B}\Delta x}{m_B(J-1)}$$

$$- \frac{(h_B(J-1)-h_C(J-1))}{m_B(J-1)} w'_{B,C}(J-1)\Delta x$$

$$- \frac{(h_B(J-1)-h_A(J-1))}{m_B(J-1)} w'_{B,A}(J-1)\Delta x$$

$$- \frac{(h_B(J-1)-h^*(J-1)w_{B,C}(J-1)\Delta x}{m_B(J-1)}$$

$$- \frac{(h_B(J-1)-h^*(J-1))w_{B,A}(J-1)\Delta x}{m_B(J-1)} \qquad \text{(B.1}$$

The multi-subchannel averaged enthalpy for the left hand side strip can be calculated from the following equation:

$$\bar{h}_L(J) = \frac{h_A(J)m_A(J) + h_B(J)m_B(J)}{m_A(J) + m_B(J)} \qquad \text{(B.1}$$

Inserting equations (B.1.1) and (B.1.2) into equation (B.1.3) with the assumption $C_{i,j} = 0$, we obtain

$$\bar{h}_L(J) = \frac{h_A(J-1)m_A(J) + h_B(J-1)m_B(J)}{m_A(J) + m_B(J)}$$

$$+ \frac{\left(q'_A(J-\tfrac{1}{2}) \frac{m_A(J)}{m_A(J-1)} + q'_B(J-\tfrac{1}{2}) \frac{m_B(J)}{m_B(J-1)}\right)\Delta x}{m_A(J) + m_B(J)}$$

$$- \frac{\Delta x \left[\frac{h_A(J-1)-h_B(J-1))w'_{A,B}(J-1)m_A(J)}{m_A(J-1)} + \frac{(h_B(J-1)-h_A(J-1)w'_{B,A}m_B(J)}{m_B(J-1)} \right]}{m_A(J) + m_B(J)}$$

$$+ \frac{\left[\frac{(h_B(J-1)-h_C(J-1)w'_{B,C}(J-1)\cdot m_B(J)}{m_B(J-1)} \right] \Delta x}{m_A(J) + m_B(J)}$$

$$- \left[\frac{(h_A(J-1)-h^*(J-1))w_{A,B}(J-1)m_A(J)}{m_A(J-1)} + \frac{(h_B(J-1)-h^*(J-1)w_{B,A}(J-1)m_B(J)}{m_B(J-1)} \right.$$

$$\left. + \frac{(h_B(J-1)-h^*(J-1))w_{B,C}(J-1)m_B(J)}{m_B(J-1)} \right] \frac{\Delta x}{m_A(J) + m_B(J)} \qquad \text{(B.1.4)}$$

In the COBRA IIIC formulation, the energy equation for the homogenized strip L incorporating the coupling coefficients can be written as follows:

$$H_L(J) = H_L(J-1) + \frac{Q'_L(J-\frac{1}{2})}{M_L(J-1)} \Delta x - \frac{(H_L(J-1)-H_R(J-1))W'_{L,R}(J-1)\Delta x}{M_L(J-1)N_H(J-1)}$$

$$- \frac{(H_L(J-1)-\frac{H^*(J)}{N'_H(J-1)}) W_{L,R}(J-1)\Delta x}{M_L(J-1)} \qquad \text{(B.1.5)}$$

where $N_H(J-1)$ and $N'_H(J-1)$ are the coupling coefficients for the turbulent and crossflow interchange, and are defined following equations (A.1.9a), (A.1.9b) and (A.1.9c) as:

$$N_H(J-1) \equiv \frac{H_L(J-1) - H_R(J-1)}{h_B(J-1) - h_C(J-1)} \qquad \text{(B.1.6}$$

$$N_H' \equiv \frac{H^*(J-1)}{h^*(J-1)} \quad \text{where} \quad \frac{H^*}{h^*} = \frac{H_L(J-1)}{h_B(J-1)} \quad \text{if } W_{L,R} > 0$$

$$\frac{H^*}{h^*} = \frac{H_R(J-1)}{h_D(J-1)} \quad \text{if } W_{R,L} < 0 \qquad \text{(B.1.6}$$

and $H_L(J-1)$ is defined as

$$H_L(J-1) = \frac{h_A(J-1)m_A(J-1) - h_B(J-1)m_B(J-1)}{m_A(J-1) + m_B(J-1)} \qquad \text{(B.1.6}$$

Inserting equations (B.1.6a), (B.1.6b) and (B.1.6c) int(
(B.1.5) we obtain

$$H_L(J) = H_L(J-1) + \frac{Q_L'(J-\frac{1}{2})}{[m_A(J-1)-m_B(J-1)]}\Delta x - \frac{(h_B(J-1)-h_C(J-1))W_{L,R}(J-1)\Delta x}{[m_A(J-1)+m_B(J-1)]}$$

$$- \frac{(H_L(J-1)-h^*(J-1))W_{L,R}(J-1)\Delta x}{[m_A(J-1)+m_B(J-1)]} \qquad \text{(B.1.7)}$$

Therefore, forming the desired difference from equations (B.1.4) and (B.1.7), we obtain

$$\bar{h}_L(J) - H_L(J) = \left\{ \frac{h_A(J-1)m_A(J) + h_B(J-1)m_B(J)}{m_A(J) + m_B(J)} - H_L(J-1) \right\}$$

$$+ \Delta x \left\{ \frac{q'_A(J-\tfrac{1}{2}) \dfrac{m_A(J)}{m_A(J-1)} + q'_B(J-\tfrac{1}{2}) \dfrac{m_B(J)}{m_B(J-1)}}{m_A(J) + m_B(J)} - \frac{Q_L(J-\tfrac{1}{2})}{m_A(J-1) + m_B(J-1)} \right\}$$

$$+ \left\{ \frac{(h_A(J-1)-h_B(J-1))w'_{A,B}(J-1)m_A(J)}{[m_A(J) + m_B(J)]m_A(J-1)} + \frac{(h_B(J-1)-h_A(J-1)w'_{B,A}(J-1)m_B(J)}{[m_A(J) + m_B(J)]m_B(J-1)} \right.$$

$$\left. + \frac{(h_B(J-1)-h_C(J-1))w'_{B,C}(J-1)m_B(J)}{[m_A(J) + m_B(J)]m_B(J-1)} - \frac{(h_B(J-1)-h_C(J-1))W'_{L,R}(J-1)}{[m_A(J-1) + m_B(J-1)]} \right\} \Delta x$$

$$+ \left\{ \frac{(h_A(J-1)-h^*(J-1))w_{A,B}(J-1)m_A(J)}{m_A(J-1)} + \frac{(h_B(J-1)-h^*(J-1))w_{B,A}(J-1)m_B(J)}{m_B(J-1)} \right.$$

$$+ \left[\frac{h_B(J-1)-h^*(J-1)w_{B,C}(J-1)m_B(J)}{m_B(J-1)} \right] \frac{1}{m_B(J) + m_A(J)}$$

$$\left. - \frac{(H_L(J-1)-h^{**}J-1))W_{L,R}(J-1)}{m_A(J-1) + m_B(J-1)} \right\} \Delta x$$

$$= \text{ERROR 1} + \text{ERROR 2} + \text{ERROR 3} + \text{ERROR 4} \qquad \text{(B.1.8)}$$

From the above formulation, we find that the error between $\bar{h}_L(J)$ and $H_L(J)$ is composed of four terms, i.e., the four terms in parentheses ({}) in equation (B.1.8). Now, we examine equation (B.1.8) term by term to highlight the

factors causing the error between $\bar{h}_L$ and $H_L(J)$.

B.1.1 Error on the Averaged Enthalpy at (J-1)

From the first term of equation (B.1.8), the error due to the averaged enthalpy at (J-1) can be rewritten as:

$$\text{ERROR1}(J) = \frac{h_A(J-1)m_A(J)+h_B(J-1)m_B(J)}{m_A(J) + m_B(J)} - \frac{h_A(J-1)m_A(J-1)+h_B(J-1)m_B(J-1)}{m_A(J-1) + m_B(J-1)} \qquad \text{(B.1.1.1)}$$

From equation (B.1.1.1) we observe that ERROR1(J) increases as the diversion crossflow and subchannel enthalpy increase

B.1.2 Error on the Heat Added from Rods

The second term of equation (B.1.8) is

$$\text{ERROR2}(J) = \left\{ \frac{\left[q_A'(J-\tfrac{1}{2}) \frac{m_A(J)}{m_A(J-1)} + q_B'(J-\tfrac{1}{2}) \frac{m_B(J)}{m_B(J-1)} \right]}{m_A(J) + m_B(J)} - \frac{Q_L'(J-\tfrac{1}{2})}{m_A(J-1)+m_B(J-1)} \right\} \Delta$$

(B.1.2.1)

Now

$$Q_L'(J-\tfrac{1}{2}) = q_A'(J-\tfrac{1}{2}) + q_B'(J-\tfrac{1}{2}) \qquad \text{(B.1.2.2}$$

Inserting equation (B.1.2.2) into (B.1.2.1) we obtain

$$\text{ERROR2}(J) = \left\{ \frac{\left[q'_A(J-\tfrac{1}{2}) \frac{m_A(J)}{m_A(J-1)} + q'_B(J-\tfrac{1}{2}) \frac{m_B(J)}{m_B(J-1)} \right]}{m_A(J) + m_B(J)} - \frac{q'_A(J-\tfrac{1}{2}) + q'_B(J-\tfrac{1}{2})}{m_A(J-1) + m_B(J-1)} \right\} \Delta x \qquad \text{(B.1.2.3)}$$

From the above equation, we observe ERROR2 increases as diversion crossflow increases and the rod linear power generation rate increases. For low power generation, this term is much smaller than the other terms.

B.1.3 Error on the Energy Carried by the Turbulent Interchange

From equation (B.1.8), the error on the energy transported by the turbulent interchange between $\bar{h}_L(J)$ and $H_L(J)$ can be written as:

$$\text{ERROR3}(J) = \frac{(h_A(J-1)-h_B(J-1))w'_{A,B}(J-1)m_A(J)\ \Delta x}{[m_A(J) + m_B(J)]m_A(J-1)}$$

$$+ \frac{(h_B(J-1)-h_A(J-1))w'_{B,A}(J-1)m_B(J)\ \Delta x}{[m_A(J) + m_B(J)]m_B(J-1)}$$

$$+ \frac{(h_B(J-1)-h_C(J-1))w'_{B,C}(J-1)m_B(J)\ \Delta x}{[m_A(J) + m_B(J)]m_B(J-1)}$$

$$- \frac{(h_B(J-1)-h_C(J-1)W'_{L,R}(J-1)\ \Delta x}{m_A(J-1) + m_B(J-1)} \qquad \text{(B.1.3.1)}$$

From the above equation, we observe ERROR3 increases as the diversion crossflow and the difference between $W'_{L,R}(J-1)$ and $w'_{B,C}(J-1)$ increases. Usually, the difference between $W'_{L,R}$ and $w'_{B,C}$ is small and does not contribute too much to the ERROR3.

B.1.4 Error on the Energy Carried by the Diversion Crossflow

From equation (B.1.8), the error on the energy transported by the diversion crossflow between $\bar{h}_L(J)$ and $H_L(J)$ can be written as

$$\begin{aligned} \text{ERROR4}(J) = \Bigg\{ & \frac{[h_A(J-1)-h^*(J-1)]w_{A,B}(J-1)m_A(J)\ \Delta x}{m_A(J-1)[m_B(J) + m_A(J)]} \\ & + \frac{[h_B(J-1)-h^*(J-1)w_{B,A}(J-1)m_B(J)\ \Delta x}{m_B(J-1)[m_B(J) + m_A(J)]} \\ & + \frac{[h_B(J-1)-h^*(J-1)]w_{B,C}(J-1)m_B(J)\ \Delta x}{m_B(J-1)[m_B(J) + m_A(J)]} \\ & - \frac{[H_L(J-1)-h^*(J-1)]W_{L,R}(J-1)\ \Delta x}{m_A(J-1) + m_B(J-1)} \Bigg\} \end{aligned} \qquad \text{(B.1.4.1)}$$

$$\text{where } H_L(J-1) = \frac{h_A(J-1)m_A(J-1)+h_B(J-1)m_B(J-1)}{m_A(J-1) + m_B(J-1)} \qquad \text{(B.1.4.2)}$$

For simplicity, we assume $w_{A,B}$, $w_{B,C}$, $W_{L,R}$ are less than zero. Then

$$h^*(J-1)w_{A,B}(J-1) = h_B(J-1)w_{A,B}(J-1) \qquad \text{(B.1.4.3a)}$$

$$h^*(J-1)w_{A,B}(J-1) = h_B(J-1)w_{B,A}(J-1) \qquad \text{(B.1.4.3b)}$$

$$h^*(J-1)w_{B,C}(J-1) = h_C(J-1)w_{B,C}(J-1) \qquad \text{(B.1.4.3c)}$$

Inserting equations (B.1.4.2), (B.1.4.3a), (B.1.4.3b), (B.1.4.3c) and (B.1.4.3d) into equation (B.1.4.1) we obtain,

$$\text{ERROR4}(J) = \left\{ \frac{[h_A(J-1)-h_B(J-1)]w_{A,B}(J-1)m_A(J)\,\Delta x}{m_A(J-1)[m_B(J)+m_A(J)]} + \frac{[h_B(J-1)-h_C(J-1)]w_{B,C}(J-1)m_B(J)\,\Delta x}{m_B(J-1)[m_B(J)+m_A(J)]} - \frac{\left[\dfrac{h_A(J-1)m_A(J-1)+h_B(J-1)m_B(J-1)}{m_A(J-1)+m_B(J-1)} - h_C(J-1)\right]}{m_A(J-1)+m_B(J-1)} \right\} W_{L,R}(J-1)\,\Delta x$$

(B.1.4.4)

ERROR4(J) can be rearranged as follows:

$$\text{ERROR4}(J) = \left[\frac{W_{L,R}(J-1)\,\Delta x}{m_A(J-1)+m_B(J-1)} - \frac{w_{B,C}(J-1)m_B(J)\,\Delta x}{[m_B(J)+m_A(J)]m_B(J-1)} \right] h_C(J-1)$$

$$+ \left| \frac{w_{A,B}(J-1)m_A(J)\ \Delta x}{m_A(J-1)[m_B(J)+m_A(J)]} - \frac{m_A(J-1)W_{L,R}(J-1)\ \Delta x}{[m_A(J-1)+m_B(J-1)]^2} \right| h_A(J-1)$$

$$+ \left| \frac{w_{B,C}(J-1)m_B(J)\ \Delta x}{m_B(J-1)[m_B(J)+m_A(J)]} - \frac{w_{A,B}(J-1)m_A(J)\ \Delta x}{m_A(J-1)[m_B(J)+m_A(J)]} \right.$$

$$\left. - \frac{m_B(J-1)W_{L,R}(J-1)\ \Delta x}{[m_A(J-1)+m_B(J-1)]^2} \right| h_B(J-1) \qquad \text{(B.1.4.5)}$$

Equation (B.1.4.5) is a general expression for the error on the diversion crossflow. This error increases as diversion crossflow and subchannel enthalpies increase.

B.1.5 Numerical Values of Errors Between $\overline{h_L}$ and H_L

From the above derivation, we conclude that all these four errors vanish as the diversion crossflow goes to zero. This gives us strong confidence to neglect the error introduced by using the coefficients N_H, N_H' and N_H'' from Appendix A into the COBRA computation scheme which employs a forward differenced form for the conservation equations. However, this error may not be negligible when the diversion crossflow between subchannels is large.

Let us now evaluate the ERROR1, ERROR2, ERROR3 and ERROR4 in order to see their relative importance under two extreme conditions, i.e., low diversion corssflow condition (ENTHALPY UPSET CONDITION) and high diversion crossflow condition (POWER AND FLOW UPSET

CONDITION).

The input energy and flow conditions together with input coefficients for the cases considered in this section are listed in Table B.1.

TABLE B.1

ENTHALPY UPSET		FLOW AND POWER UPSET	
Bundle Geometry	N = 5	Bundle Geometry	N = 5
	L = 144"		L = 144"
Flow Conditions	$\bar{G}$ = 2.66 $\frac{\text{Mlbm}}{\text{hr-ft}^2}$	Flow Conditions	$\bar{G}$ = 2.66 $\frac{\text{Mlbm}}{\text{hr-ft}^2}$
	F_R = 1.0		F_R = 1.22
Energy Conditions	$\bar{H}$ = 600 Btu/lbm	Energy Conditions	$\bar{H}$ = 600 Btu/lbm
	$\bar{q}''$ = 0 $\frac{\text{MBtu}}{\text{hr-ft}^2}$		$\bar{q}''$ = 0.04 $\frac{\text{MBtu}}{\text{hr-ft}^2}$
	H_R = 1.22		H_R = 1.0
	P_R = 1.0		P_R = 1.5
Input Coefficients	β = 0.02	Input Coefficients	β = 0.02
	K = 0.5		K = 0.5
	S/L = 0.5		S/L = 0.5

The total errors between $\bar{h}_{EXIT}$ and $H_{L_{EXIT}}$ can be evaluate by using equations similar to (B.1.1.1), (B.1.2.1), (B.1.3.1) and (B.1.4.1) but reformulated to deal with five subchannels. The results are tabulated in the following table (Table B.2).

TABLE B.2

	ENTHALPY UPSET	POWER AND FLOW UPSET
ΔH	-34.4 BTU/lbm	21.5 BTU/lbm
$\sum_{J=1}^{EXIT}$ ERROR1(J)	0.097 $\frac{Btu}{lbm}$	0.058 $\frac{Btu}{lbm}$
$\sum_{J=1}^{EXIT}$ ERROR2(J)	0.0004 $\frac{Btu}{lbm}$	0.0004 $\frac{Btu}{lbm}$
$\sum_{J=1}^{EXIT}$ ERROR3(J)	0.147 $\frac{Btu}{lbm}$	0.127 $\frac{Btu}{lbm}$
$\sum_{J=1}^{EXIT}$ ERROR4(J)	-0.233 $\frac{Btu}{lbm}$	-0.130 $\frac{Btu}{lbm}$
TOTAL	0.011 $\frac{Btu}{lbm}$	0.055 $\frac{Btu}{lbm}$

B.1.6 Conclusions

The coupling coefficient derived in the differential form conservation euqations can be used in the difference form conservation equations with some practical tolerable

error. However, if the subchannel enthalpies become abnormally high (under channel blockage condition) or the diversion crossflows between subchannels becomes very large (under severe boiling condition or channel blockage), the errors between $H_{L_{EXIT}}$ and $\bar{h}_{L_{EXIT}}$ will become substantial from the practical point of view.

B.2 General Approach to Derive Coupling Coefficients From the Different Conservation Equations

Coupling coefficients derived from the differential conservation equations are applicable to the code application only if the subchannel enthalpies and diversion crossflows are within the range of normal operation, as we discussed in Section B.1.6. One way to eliminate this constraint to handle abnormal operational conditions is to derive the coupling coefficients directly from the difference conservation equations. For instance, we derive coupling coefficients in the difference conservation equations by first letting

$$\bar{h}_L(J) \equiv \bar{H}_L(J) \qquad \text{(B.2.}$$

and then define the coupling coefficients in each term of H_I to make $H_L(J)$ equal $\bar{h}_L(J)$ term by term. Using the same

procedures, we can derive the coupling coefficients for the axial velocity and axial pressure drop. However, it is worthwhile noting that the complexity of the coupling coefficients resulting from this kind of derivation generally will make them undesirable for practical application. Also results for Volume II show that the error due to no application of coupling coefficients is modest. For DNBR thermal analysis, utilization of coupling coefficients is not necessary. However more accurate predictions of channel enthalpy is desired for coupled neutronic-thermal hydraulic analysis. Consequently derivations and prediction of transport coefficients is of potential application in the future development of these coupled analysis meth

APPENDIX C

DESCRIPTION OF THE DATA USED IN THE ANALYSIS

In this appendix the data used in the present study will be given. The reactor analyzed is similar to CONNECTICUT YANKEE.

C.1.1 Operating Conditions

System Pressure 2150

Uniform Inlet Enthalpy 548.8 BTU/lb

Uniform Inlet Mass Velocity 2.217×10^6 lb/hr ft^2

Average Heat Flux 0.2034×10^6 BTU/hr ft^2

C.1.2 Dimensions of the Assemblies

The geometrical characteristics of the assemblies are:

Area 38.37 in^2

Wetted Perimeter 322.8 in

Heated Perimeter 270.5 in

Boundary Gap 2.0 in

Hydraulic Diameter 0.4755 in

Channel Length 126.7 in

Channel Orientation 0.0 degrees

C.1.3 Dimension of the Subchannels.

The geometrical characteristics of the subchannels are:

Area 0.1705 in^2

Wetted Perimeter 1.435 in

Boundary gap 0.133 in

Hydraulic diameter 0.4755 in

C.1.4 Discussions of the Rods

All the rods are taken as having the same diameter of 0.422 inches.

C.1.5 Axial Heat Flux Distribution

The following heat flux distribution was used:

Position (X/L)	Relative Flux
0.0	0.039
0.05	0.289
0.1	0.531
0.15	0.759
0.2	0.968
0.25	1.151
0.3	1.303
0.35	1.421
0.4	1.502

Position	Relative Flux
0.45	1.544
0.465	1.548
0.475	1.55
0.5	1.545
0.55	1.505
0.6	1.426
0.65	1.391
0.7	1.58
0.75	0.977
0.8	0.770
0.85	0.542
0.9	0.30
0.95	0.051
1.0	0.0

C.1.6 Radial Power Factors

There are three different distributions of radial power factors which have been used in Appendix D (Case A, Case B, and Case C). Case A represented the base case. Cases B and C were developed to permit testing of the one pass method versus a simulation of the cascade method. Therefore case B was generated to provide subchannel peaking factors in the boundary region of neighboring assembly and movement of the hot subchannels closer the assembly boundary. Case C is a varient of Case A with the hot subchannels moved closer to the assembly boundary using the same peaking factors as Case B.

The radial power factors of each assembly for Case A are given in Figure C.1. These values were taken from Figures 4.2-16 of the report GTS-75-A-136 sent to Dr. E. Khan by J. Chunis of Northeast Utilities. Also the radial power factors of each assembly for cases B and C are given in Figures C.2 and C.3 respectively which were assumed by Pablo Moreno.

The radial power factors for the subchannels of the hot assembly for Case A which were assumed by Pablo Moreno are given in figure C.4. In figure C.5, the radial power factor for the subchannels both the hot assembly and a portion of one neighboring assembly for case B are given. The radial power factor of the subchannels in hot assembly for case were assumed by Dr. E, Khan except that two hot subchannels have been moved closer to the assembly boundary. The radial power factor of the neighboring subchannels to the hot assem were obtained by multiplying the radial power factor of the subchannels in the hot assembly by a factor which is the ratio of the neighboring assembly power factor to the hot assembly power factor.

Figure C.6 gives the radial power factors for the subchannels of the hot assembly for Case C are the same as Case

C. 1.7 Spacer Data

In the following table the relative location and the type of spacer situated at that location are given.

Location (X/L)	0.005	0.159	0.324	0.492	0.658	0.824	0.995
Spacer Type No.	1	2	3	3	3	3	3

The drag coefficients assumed for each spacer type are:

Spacer Type No.	1	2	3
Drag Coefficient	4.011	0.978	1.565

C.1.8 Thermal-Hydraulic Model.

C.1.8.1 Mixing

Two values of the mixing coefficient β (0. and 0.02) have been used in the analysis.

The two-phase mixing coefficient is taken as equal to that of single phase.

Thermal conduction is neglected.

C .1.8.2 Single-Phase Friction

It is calculated by:

$$f = \frac{0.184}{R_e^{0.2}}$$

where R_e = n Reynolds Number

C .1.8.3 Two-Phase Friction

The homogeneous model friction multiplies was selected to describe the two-phase pressure drop due to friction.

C .1.8.4 Void Fraction

It was calculated using the Levy model and a slip ratio equal to one.

C .1.8.5 Flow Division at Inlet

The inlet mass velocity was taken as uniform, equal to 2.217×10^6 lb/hr ft^2 for all channels.

C. 1.8.6 Constants

The constants used are:

Cross-flow resistance (KIJ) = 0.5

Momentum Turbulent Factor (FTM) = 0.0

Transverse Momentum Factor (S/L) = 0.5

The CHF correlation used in all the calculations was W-3.

C. 1.8.7 Iteration

The flow convergence factor used was 0.01.

The number of axial steps in which the core was divided was 21. Then the length of each axial step was 6.003 inches.

All the calculations were done for steady state.

C. 1.8.8 Coupling Parameter

The following coupling parameter was used:

$$N_H = N$$

where

N = number of rods between the center lines of the channels making up the boundary conditions.

If no coupling parameter was used,

$$N_H = 1.$$

C.2 Data Used in the Westinghouse Core Case

C.2.1 Operating Conditions

System Pressure 2200 psia
Uniform Inlet Temperature 542.3 °F
Average Inlet Mass Velocity 2.51×10^6 lb/hr ft^2
Average Heat Flux 0.2021×10^6 BTU/hr ft^2

C.2.2 Dimensions of the Assemblies

Flow Area 38.11 in^2
Wetted Perimeter 348.0 in
Heated Perimeter 310.2 in
Boundary Gap 2.108 in

C.2.3 Dimensions of the Channels

Rod Diameter: 0.374 in

Rod Pitch: 0.496 in

Diameter of Guide Tubes: 0.482 in

C.2.4 Axial Heat Flux Distribution

Position (X/L)	Relative Flux
0.0	0.0
0.033	0.003
0.067	0.211
0.100	0.385
0.133	0.555
0.167	0.717
0.200	0.869
0.233	1.010
0.267	1.138
0.300	1.251
0.333	1.347
0.367	1.426
0.400	1.486
0.433	1.526
0.467	1.547
0.500	1.547

Position	Relative Flux
0.533	1.526
0.567	1.486
0.600	1.426
0.633	1.347
0.667	1.251
0.700	1.138
0.733	1.010
0.767	0.869
0.800	0.717
0.833	0.555
0.867	0.385
0.900	0.211
0.933	0.003
1.000	0.0

C.2.5 Radial Power Peaking Factors

Hot assembly rod peaking factors and Assembly average power peaking factors are shown in Figure's C.7 and C.8 respectively.

C.2.6 Spacer Data

Number of Types: 9

Single Phase Grid Coefficient for each Grid Type

Type	K_C
1	4.1
2	2.51
3	1.48
4	1.40
5	1.25
6	1.19
7	1.09
8	1.08
9	0.93

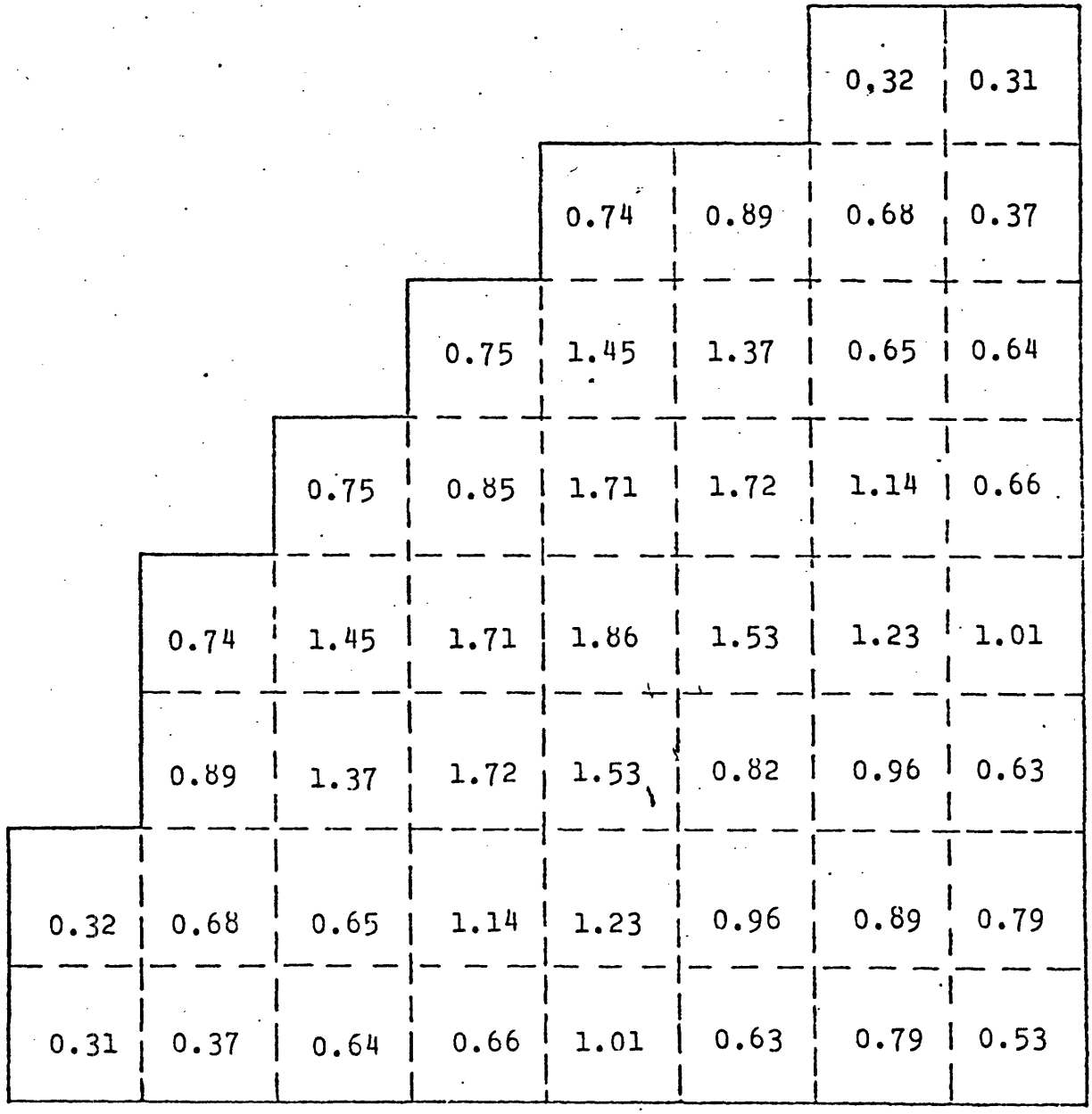

Figure C.1 Radial power factors (Case A)

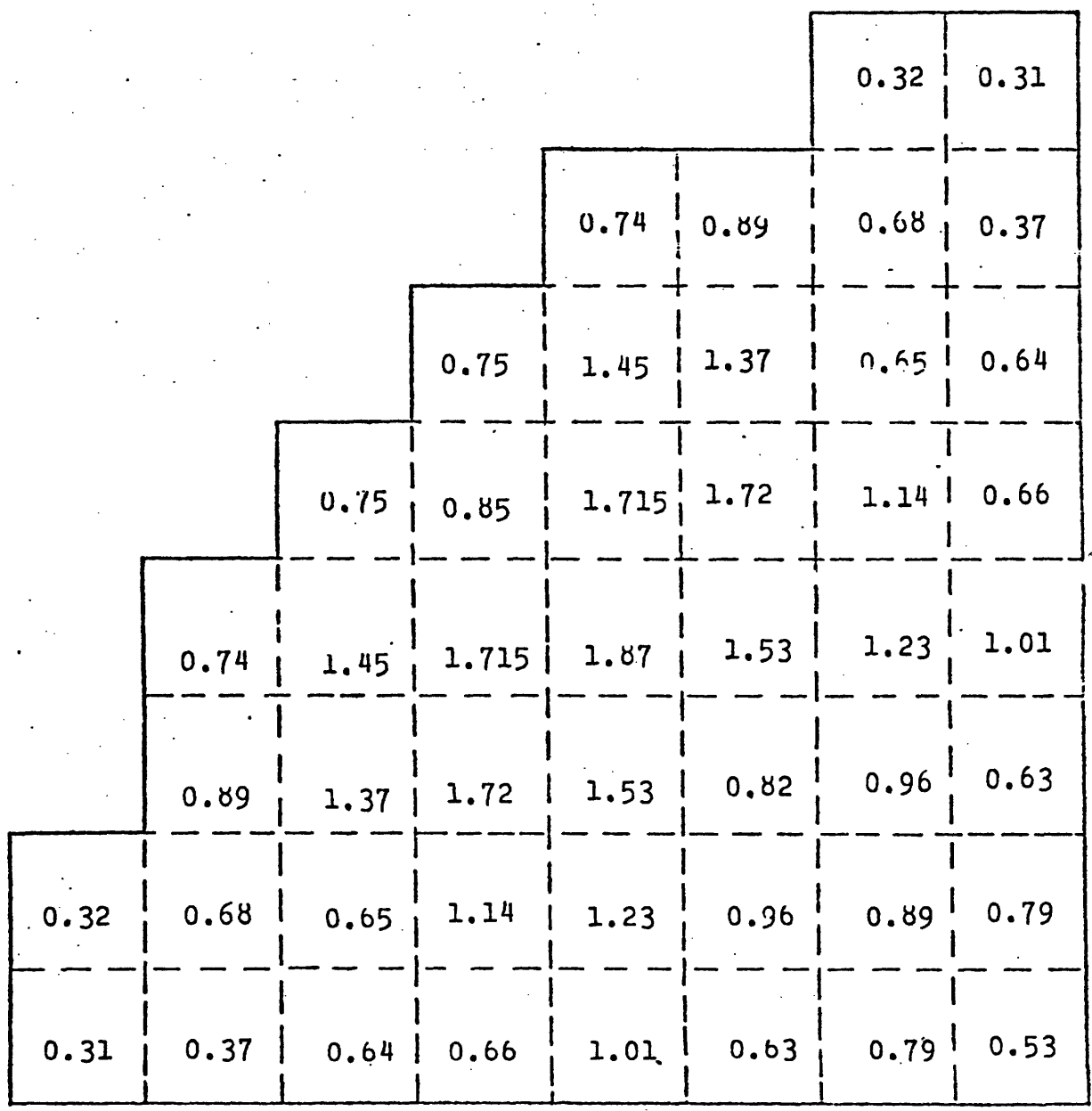

Figure C.2 Radial Power Factors (Case B)

						0.32	0.31
				0.74	0.89	0.68	0.37
			0.75	1.45	1.37	0.65	0.64
		0.75	0.85	1.71	1.72	1.14	0.66
	0.74	1.45	1.71	1.87	1.53	1.23	1.01
	0.89	1.37	1.72	1.53	0.82	0.96	0.63
0.32	0.68	0.65	1.14	1.23	0.96	0.89	0.79
0.31	0.37	0.64	0.66	1.01	0.63	0.79	0.53

Figure C.3 Radial Power Factor (Case C)

1.909	1.909	1.918	1.940	1.967	1.988	1.984	1.964	1.964	1.984	1.988	1.967	1.940	1.918	1.909	1.909
	1.909	1.918	1.940	1.967	1.988	1.934	1.964	1.964	1.984	1.988	1.967	1.940	1.918	1.909	1.909
		1.942	1.985	2.026	1.528	1.511	1.993	1.993	1.511	1.528	2.026	1.985	1.942	1.918	1.918
			1.519	1.561	1.573	1.541	2.011	2.011	1.541	1.573	1.561	1.519	1.985	1.940	1.940
				1.582	2.266	2.030	2.016	2.016	2.060	2.266	*1.582	1.561	2.026	1.967	1.967
					1.570	1.547	2.030	2.030	1.547	1.570	2.266	*1.573	1.528	1.988	1.988
						1.547	2.051	2.051	1.547	1.547	2.060	1.541	1.511	1.984	1.984
							1.545	1.545	2.051	2.030	2.016	2.011	1.993	1.964	1.964
								1.545	2.051	2.030	2.016	2.011	1.993	1.964	1.964
									1,547	1.547	2.060	1.541	1.511	1.984	1.984
										1.570	2.266	1.573	1.528	1.988	1.988
											1.582	1.561	2.026	1.967	1.967
												1.519	1.985	1.940	1.940
													1.942	1.918	1.918
														1.909	1.909
															1.909

*Hot Subchannel

Figure C.4: Radial Peaking Factors for the Subchannels Inside the Hot Assembly (Case A)

Boundaries	1.773	1.773	1.795	1.816	1.873	1.412	1.397	1.841	1.841	1.397	1.412	1.873	1.816	1.795	1.773	1.773
	1.764	1.764	1.773	1.794	1.818	1.838	1.834	1.816	1.816	1.834	1.838	1.818	1.794	1.773	1.764	1.764
	1.764	1.764	1.773	1.794	1.818	1.838	1.834	1.816	1.816	1.834	1.834	1.818	1.794	1.773	1.764	1.764
	1.919	1.919	1.923	1.951	1.978	1.999	1.995	1.975	1.775	1.995	1.979	1.973	1.951	1.928	1.919	1.919
		1.919	1.928	1.951	1.978	1.999	1.995	1.975	1.975	1.995	2.277*	1.978	1.951	1.928	1.919	1.919
			1.952	1.975	2.037	1.536	1.519	2.006	2.003	1.519	1.536	2.277*	1.995	1.952	1.928	1.928
				1.528	1.570	1.579	1.547	2.021	2.021	1.547	1.579	1.570	1.528	1.995	1.951	1.951
					1.591	2.277	2.071	2.026	2.026	2.071	1.999	1.591	1.570	2.037	1.973	1.973
						1.577	1.555	2.041	2.091	1.555	1.577	2.037	1.579	1.536	1.999	1.999
							1.555	2.062	2.062	1.555	1.535	2.071	1.567	1.516	1.995	1.995
								1.553	1.553	2.062	2.041	2.026	2.021	2.003	1.975	1.975
									1.553	2.062	2.041	2.026	2.021	2.003	1.975	1.975
										1.555	1.555	2.071	1.547	1.519	1.995	1.995
											1.578	2.277	1.579	1.536	1.999	1.999
												1.591	1.570	2.037	1.973	1.973
													1.528	1.995	1.951	1.951
														1.952	1.928	1.928
															1.919	1.919
																1.919

Assembly Boundaries

*Hot Subchannel

Figure C.5 = Radial Peaking Factors for the Subchannels inside the

1.919	1.919	1.923	1.951	1.978	1.999	1.995	1.975	1.975	1.995	1.999	1.978	1.951	1.928	1.919	1.919
	1.919	1.928	1.951	1.978	1.999	1.975	1.975	1.975	1.995	2.277*	1.978	1.951	1.928	1.919	1.919
		1.952	1.975	2.037	1.536	1.519	2.006	2.003	1.519	1.536	2.277*	1.995	1.952	1.928	1.928
			1.528	1.570	1.579	1.547	2.021	2.021	1.547	1.579	1.570	1.528	1.995	1.951	1.951
				1.591	2.277	2.071	2.026	2.026	2.071	1.999	1.591	1.570	2.037	1.973	1.973
					1.578	1.555	2.041	2.091	1.556	1.578	2.037	1.579	1.536	1.999	1.999
						1.555	2.062	2.062	1.555	1.555	2.071	1.547	1.516	1.995	1.995
							1.553	1.553	2.062	2.041	2.026	2.021	2.003	1.975	1.975
								1.553	2.062	2.041	2.026	2.021	2.003	1.975	1.975
									1.555	1.555	2.071	1.547	1.519	1.995	1.995
										1.578	2.277	1.579	1.536	1.999	1.999
											1.591	1.570	2.037	1.973	1.973
												1.528	1.995	1.951	1.951
													1.952	1.928	1.928
														1.919	1.919
															1.919
															1.919

*Hot Subchannel

Figure C.6: Radial Peaking Factors Inside the Hot Assembly (Case C)

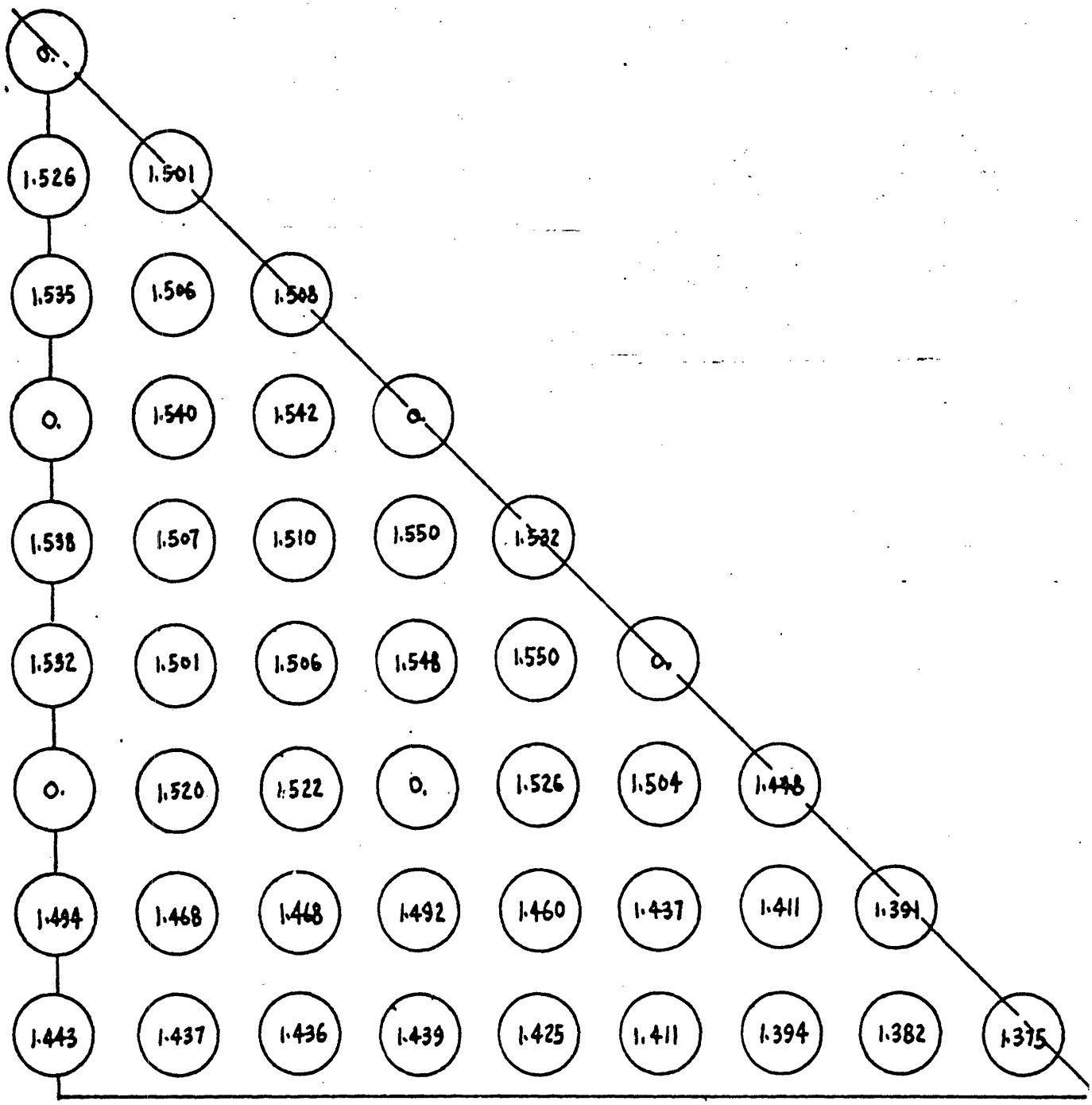

Figure C.7 1/8 Hot Assembly Rod Radial Power Peaking Factors

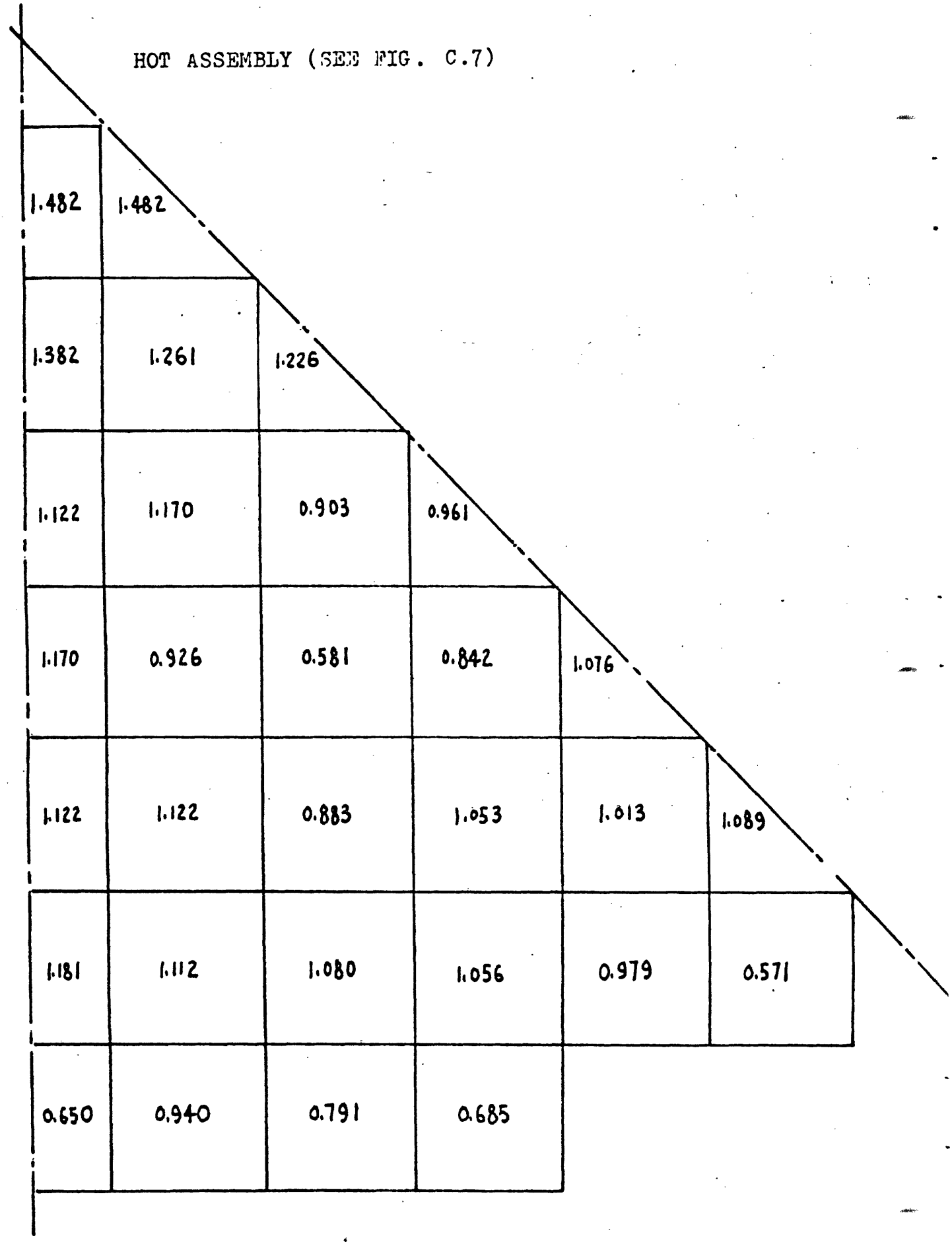

Figure C.8 Assembly Radial Power Peaking Factors

APPENDIX D

TABULATION OF CORE CASES ANALYZED IN THIS STUDY

In this appendix a summary of cases analyzed is presented in tabulated form. The pattern of channels used to represent the core and hot assembly for each case is shown in the figures. Also a discussion of some discrepancies between different cases is presented.

D.1 Summary of Cases Analyzed

There are three different power distributions (Case A, Case B, Case C in Appendix C) which have been used in the analysis. Only one β value have been applied for all of the different cases. The internal nodes and external nodes have been defined in the text. The evaluation of the predicted MDNBR is based on the W-3 empirical correlation. A case number has been assigned to each case. These numbers are the same as in the text. The channel number is indicated in the figure.

D.2 Discussions:

The MDNBR value is neither a strong function of the N_H value nor a strong function of the different number of internal and external mesh But the MDNBR does change considerably according to whether it is a whole core or a partial core analysis. All these have been discussed in the text. But still some discrepancies between different cases need to be discussed here.

Case 8 is a whole core analysis with 5 internal and 5 external meshes. Case 36 is also a whole core analysis but with 4 internal and 5 external meshes. Even these two cases have very similar number of channels, still there is 0.7% difference of the MDNBR value between them. The reason is that the pattern of channels for the internal meshes is quite different (Referring to Fig. D.8, Fig. D.51), the cross flow of the hot channel for the two cases is different. Due to the different cross flow, the predicted MDNBR based on small cross flo is larger than based on large cross flow. Case 35 is a whole core analysis with 4 internal meshes and only one external mesh. Even though it is a whole core analysis, it still can not give a good resul Since there is no cross flow from the only one external channel to other external channels, the cross flow from the hot internal channel to the external channel is small. Therefore the predicted MDNB ratio is much higher than the real value.

It also should point out that since the abnormally high average heat flux has been used, the MDNBR is estremely small.

SUMMARY OF CASES ANALYZED

Case No.	Power Distribution *	Transport Coef. N_H	β	GEOMETRY			MDNBR
				Internal Nodes	External Nodes	Figure	
1	A	N	.02	16	85	D.1,D.2	1.047
2	A	N	.02	16	45	D.3,D.4	1.042
3	A	N	.02	16	14	D.5,D.6	1.043
4	A	N	.02	5	5	D.7,D.8	1.013
5	A	1.	.02	16	85	D.1,D.2	1.040
6	A	1.	.02	16	45	D.3,D.4	1.040
7	A	1.	.02	16	14	D.5,D.6	1.041
8	A	1.	.02	5	5	D.7,D.8	1.016
9	A	1.	.02	36	18	D.9,D.10	1.036
10	A	1.	.02	16	45	D.11,D.12	1.107
11	A	1.	.02	36	0	D.13	1.137
12	A	1.	.02	5	1	D.14	1.109
13	A	1.	.02	4	83	D.15,D.16	1.021
14	A	1.	.02	4	14	D.17,D.18	1.027
15	A	1.	.02	16	0	D.19	1.129
16	A	1.	.02	4	0	D.20	1.069
17	A	1.	.02	1	0	D.21	0.901
18	B	1.	.02	5	5	D.22,D.23	0.982

CONTINUED

Case No.	Power Distribution	Transport Coef. N_H	β	GEOMETRY			MDNBR
				Internal Nodes	External Nodes	Figure	
19	B	1.	.02	16	14	D.24,D.25	1.008
20	B	1.	.02	16	95	D.26,D.27	1.019
21	B	1.	.02	16	17	D.28,D.29	1.008
22	C	1.	.02	16	85	D.30,D.31	1.015
23	C	1.	.02	16	13	D.32,D.33	1.019
24	C	1.	.02**	16	13	D.32,D.33	0.990
25	See Fig.D.34	1.	.02	Refer to Fig. D.34			-
26	See Fig. D.35	1.	.02	Refer to Fig. D.35			---
27	See Fig.D.36	1.	.02	Refer to Fig. D.36			---
28	See Fig.D.37	1.	.02	Refer to Fig. D.37			---
29	See Fig. 13(Sect. 3.3)	1.	.02	Refer to Fig. 13 (Sect. 3.3)			---
30	A	1.	.02	16	9	D.38,D.39	1.039
31	A	1.	.02	16	5	D.40,D.41	1.042
32	A	1.	.02	4	6	D.42,D.43	1.023
33	A	1.	.02	4	4	D.44,D.45	1.029
34	A	1.	.02	4	2	D.46,D.47	1.034
35	A	1.	.02	4	1	D.48,D.49	1.349
36	A	1.	.02	4	5	D.50,D.51	- 23

CONTINUED

37	A	1.	.02	4	2	D.52,D.53	1.159
38	A	1.	.02	4	2	D.54,D.55	1.356

*Power Distribution See Appendix C

**Turbulent Interchange along Hot Assembly Boundaries Not Included

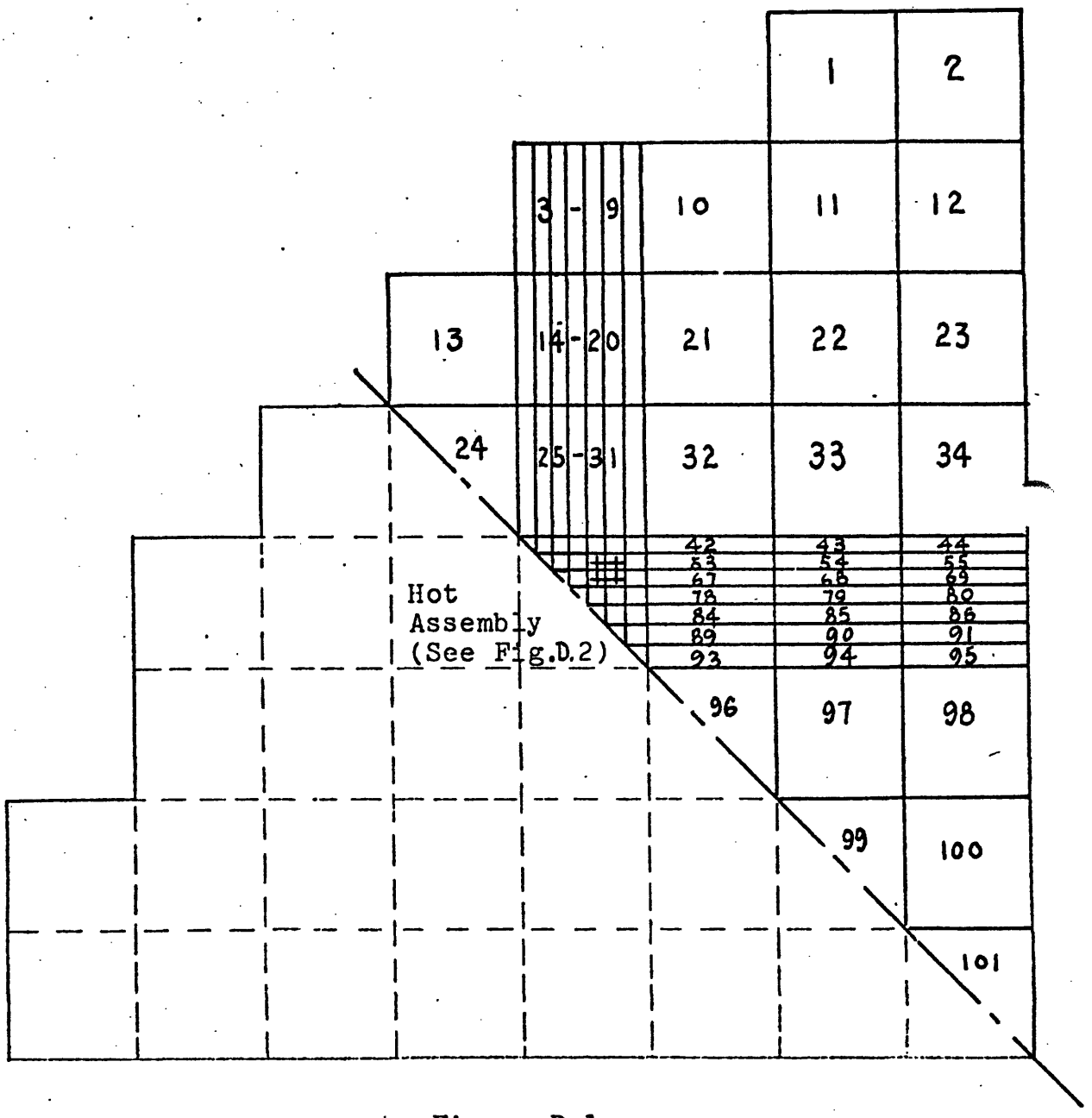

Figure D.1

Pattern of Channels Used to Represent the Core. (Case No. 1 and)

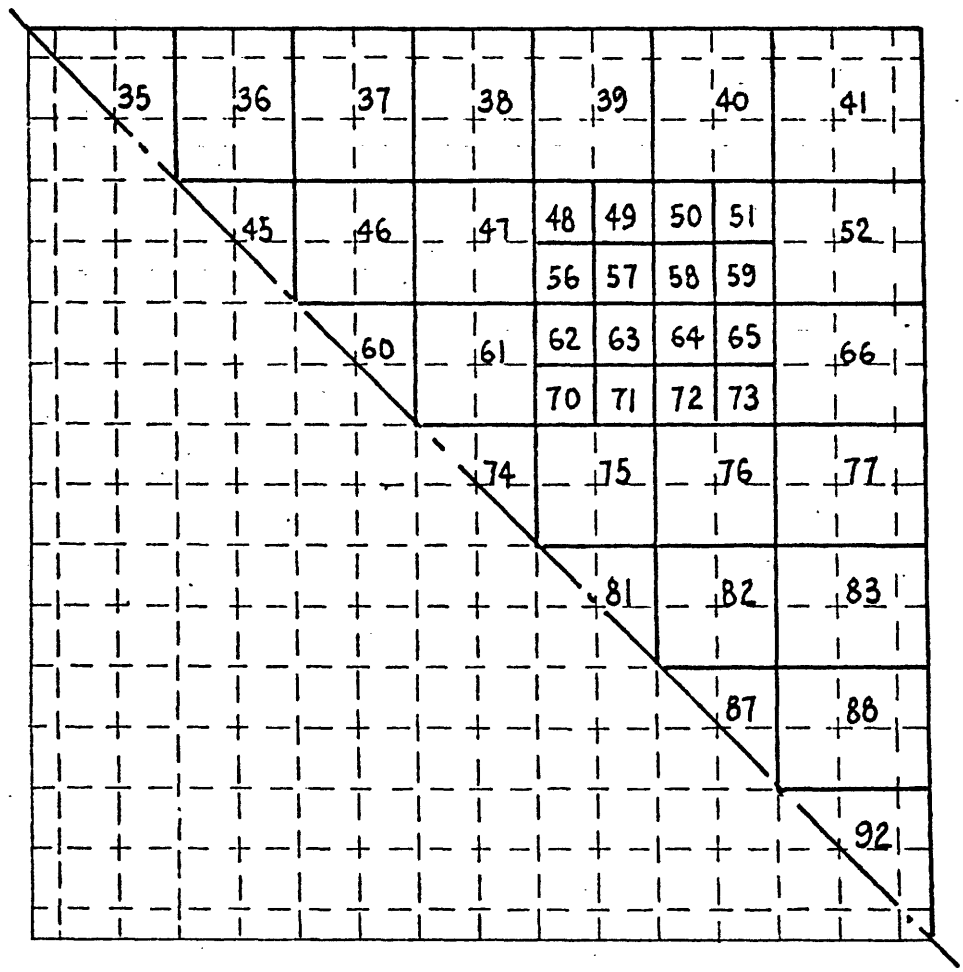

Figure D.2

Detail of the Hot Assembly (Case No. 1 and 5)

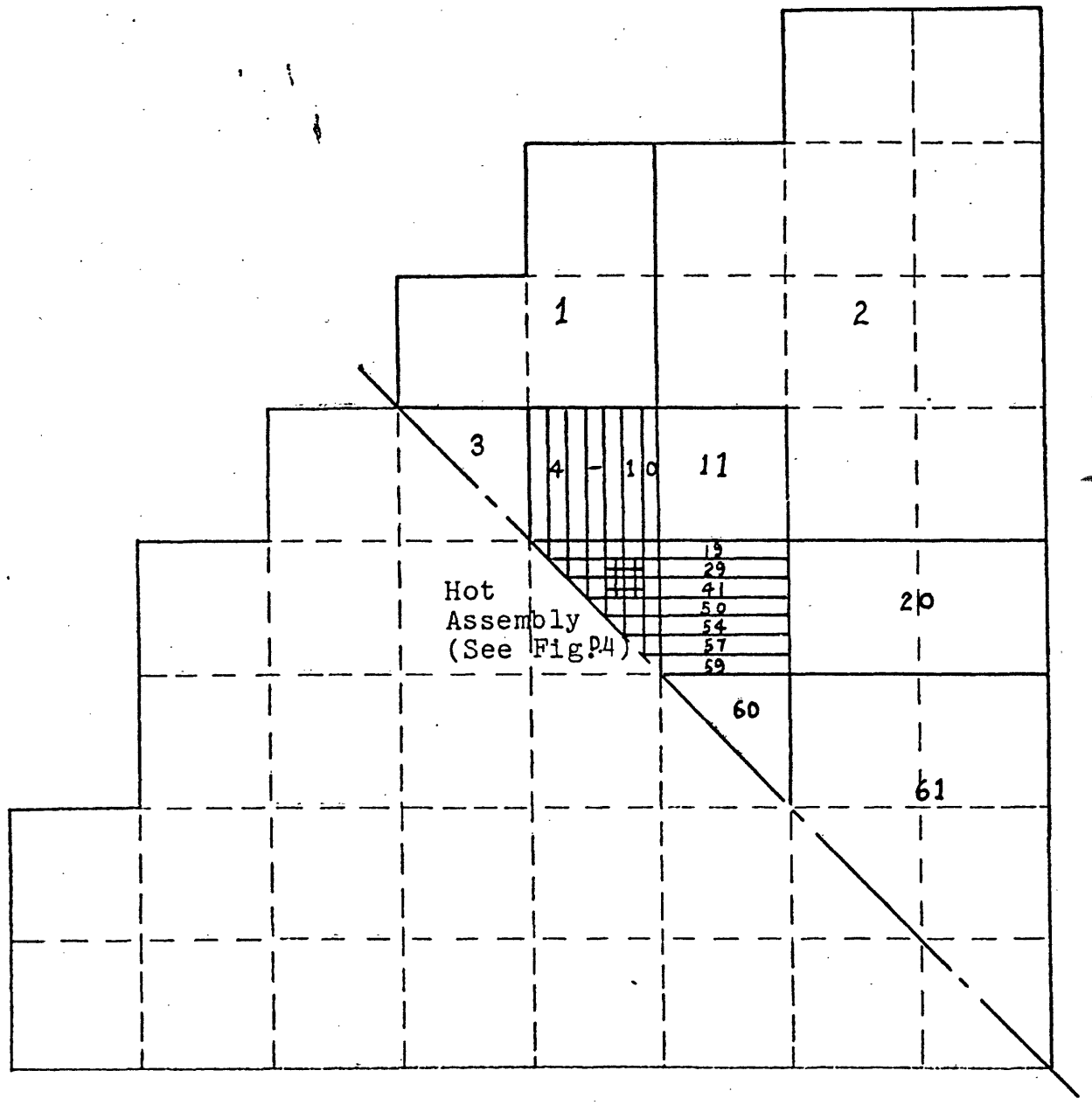

Figure D.3

Pattern of the Channels Used to Represent the Core. (Case No. 2 and 6)

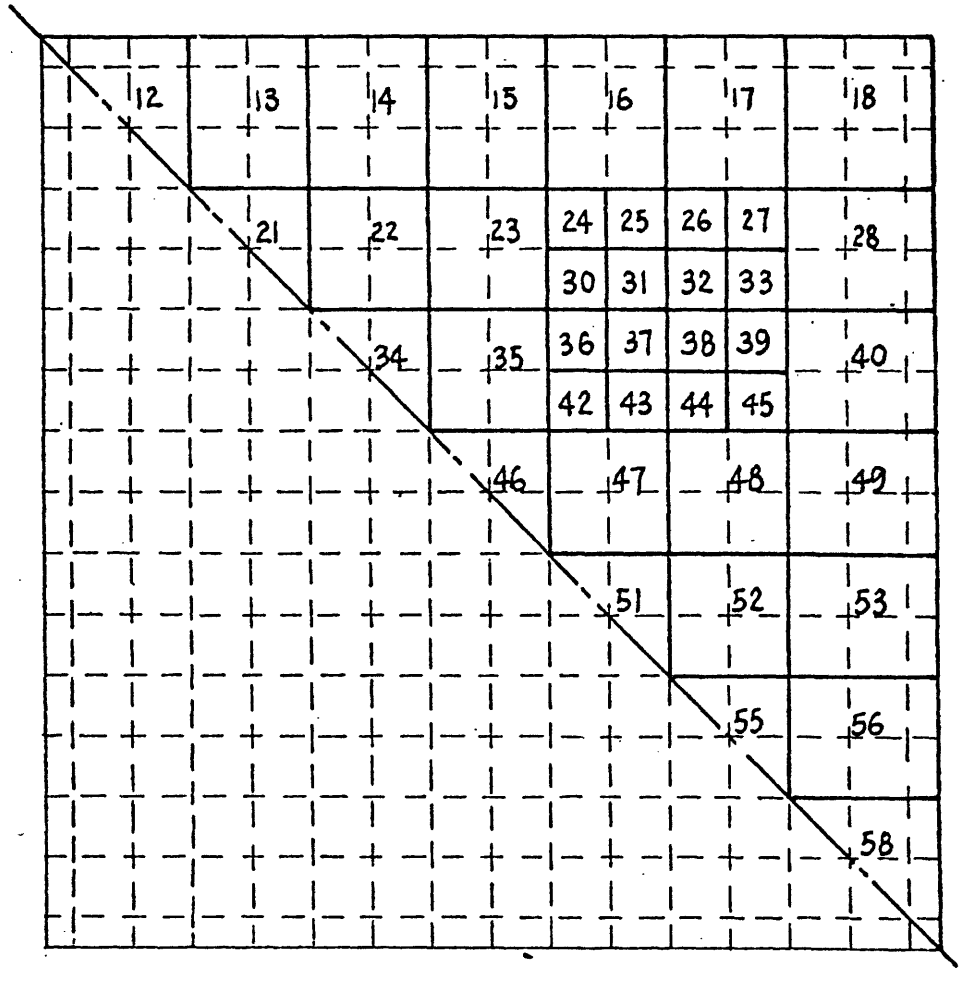

Figure D.4
Detail of the Hot Assembly (Case No. 2 and 6)

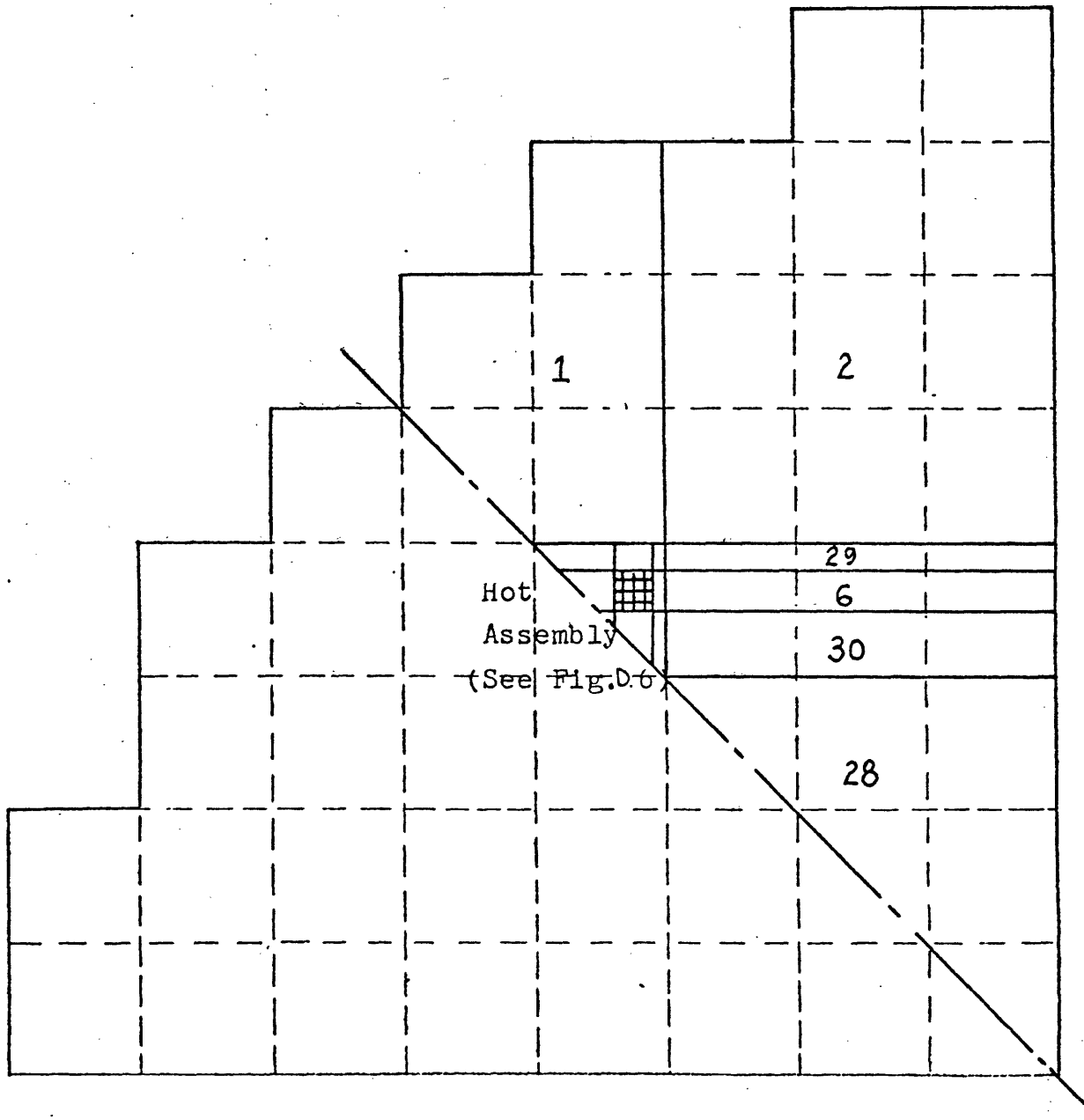

Figure D.5

Pattern of Channels Used to Represent the Core. (Case No. 3 and 7

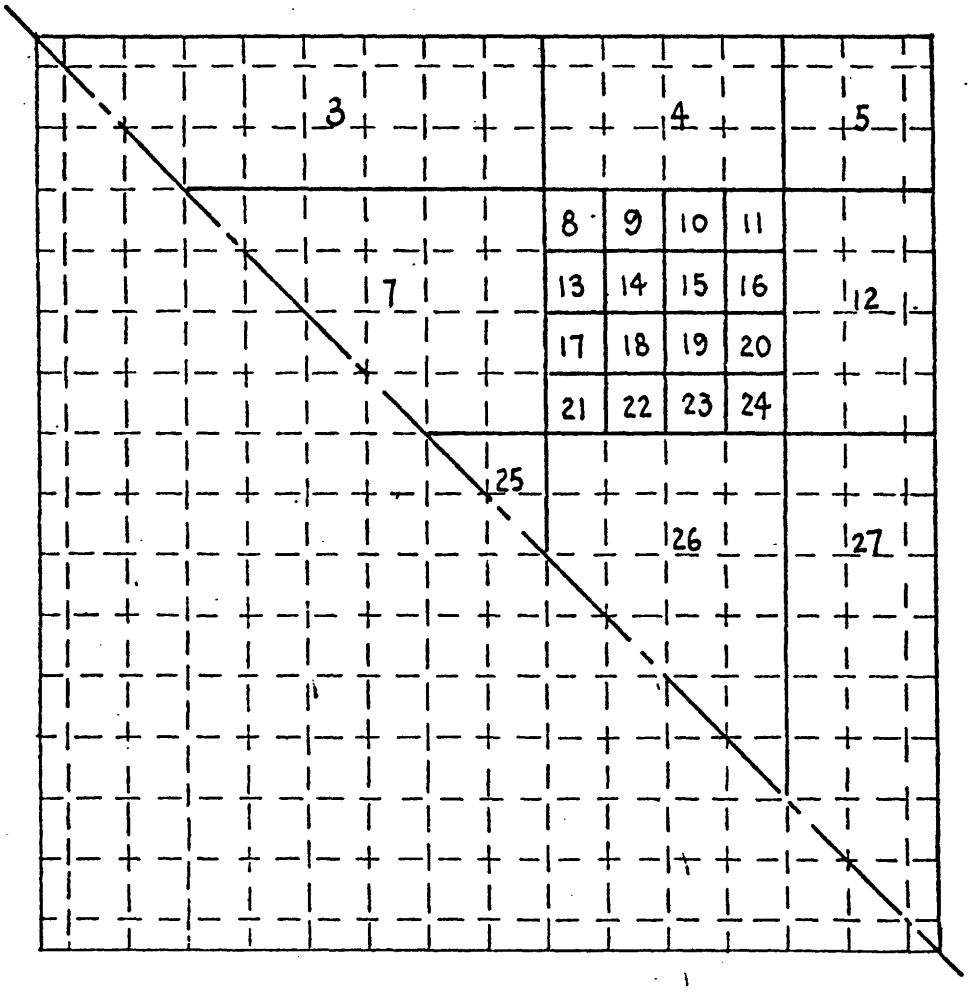

Figure D.6
Detail of the Hot Assembly (Case No. 3 and 7)

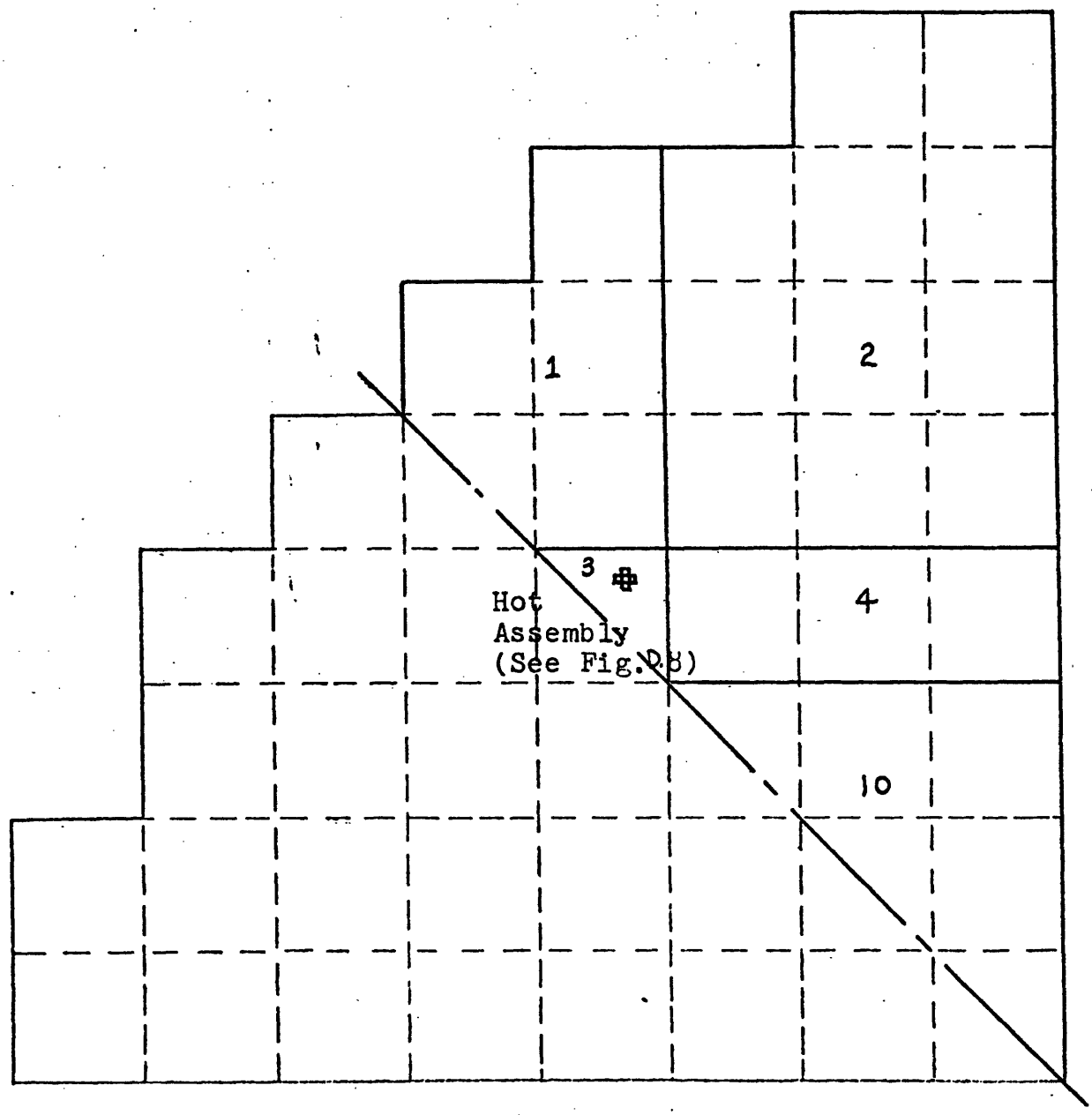

Figure D.7

Pattern of Channels Used to Represent the Core (Case No. 4 and 8)

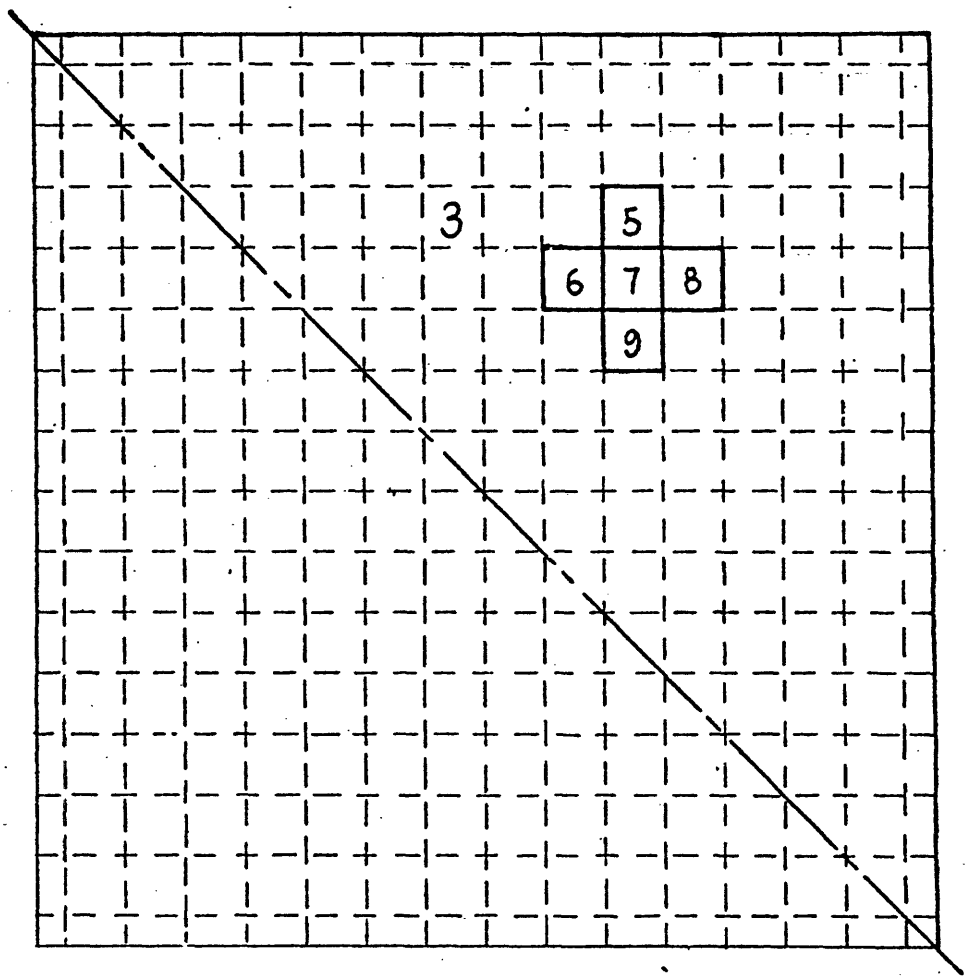

Figure D.8

Detail of the Hot Assembly (Case No. 4 and 8)

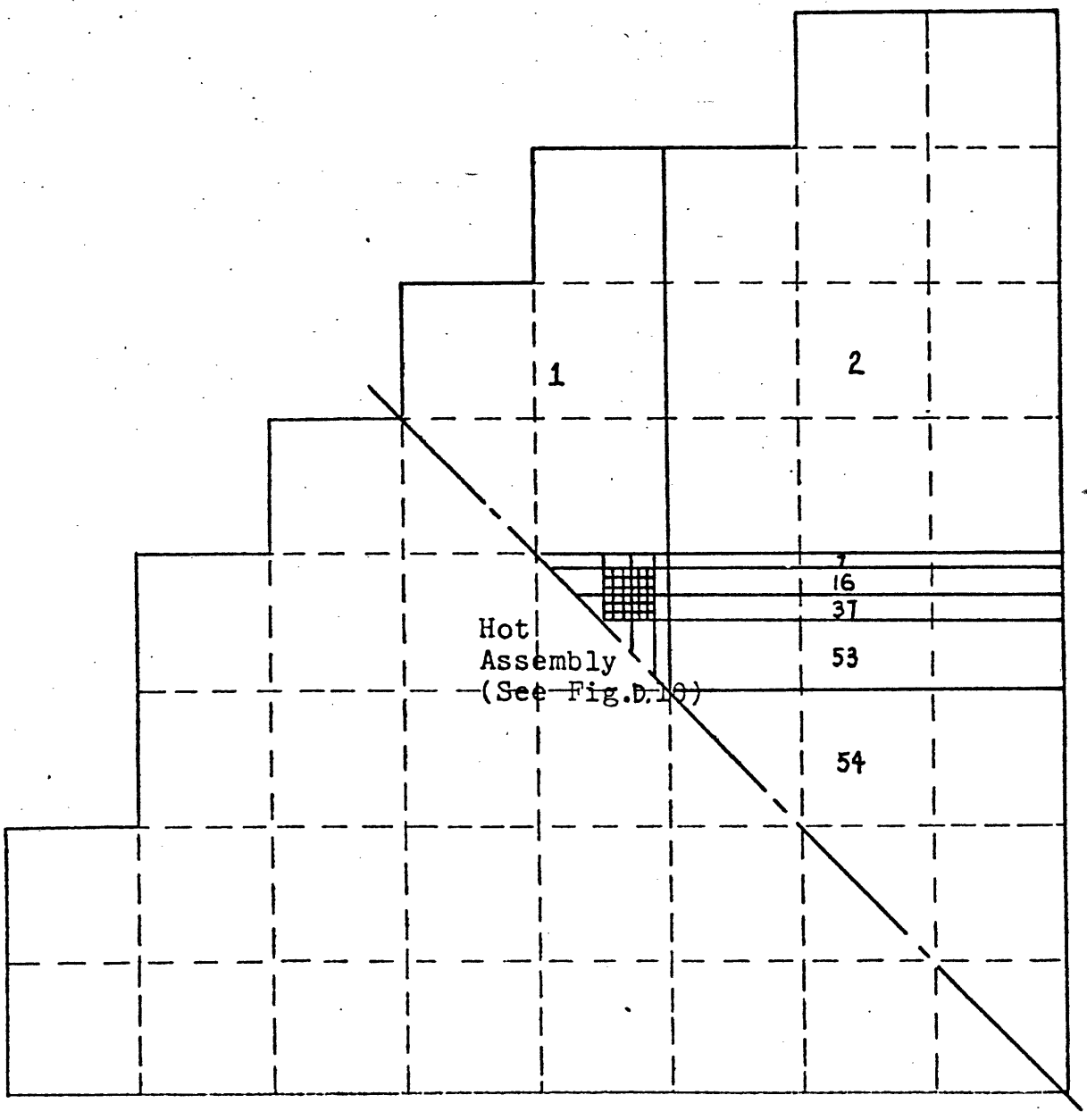

Figure D.9

Pattern of Channels Used to Represent the Core (Case No. 9)

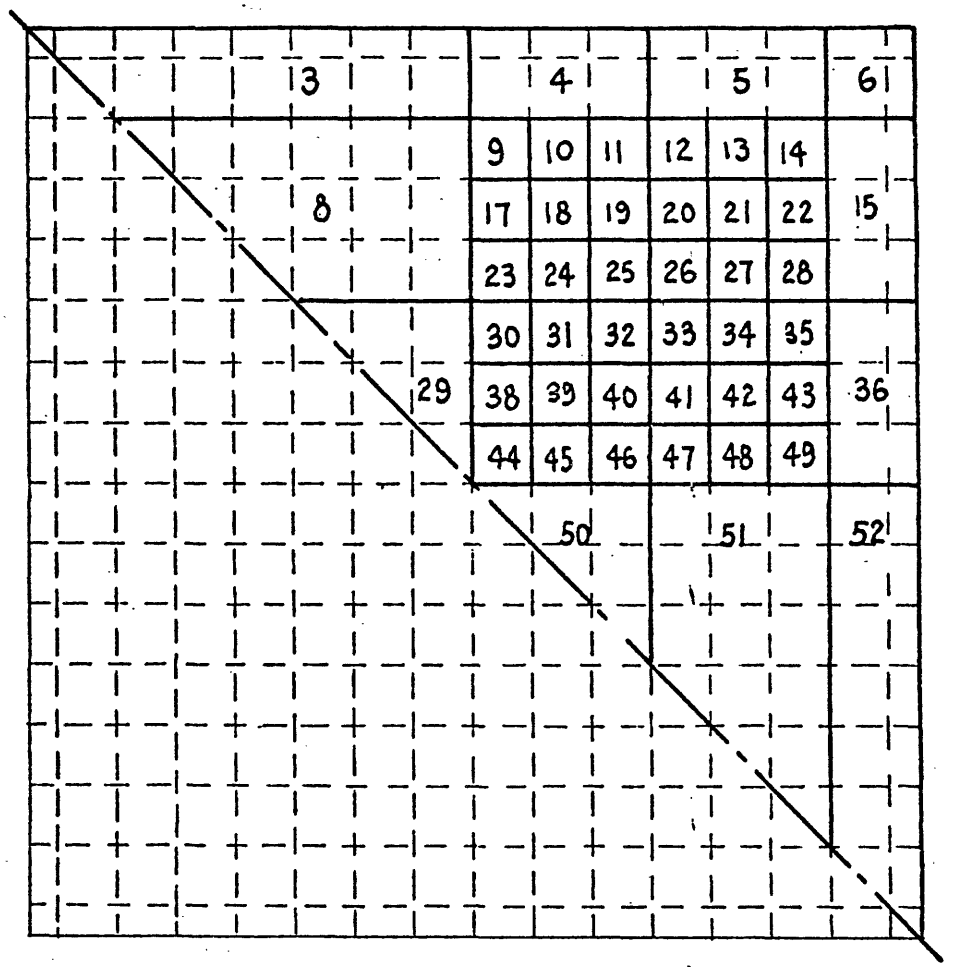

Figure D.10
Detail of the Hot Assembly (Case No. 9)

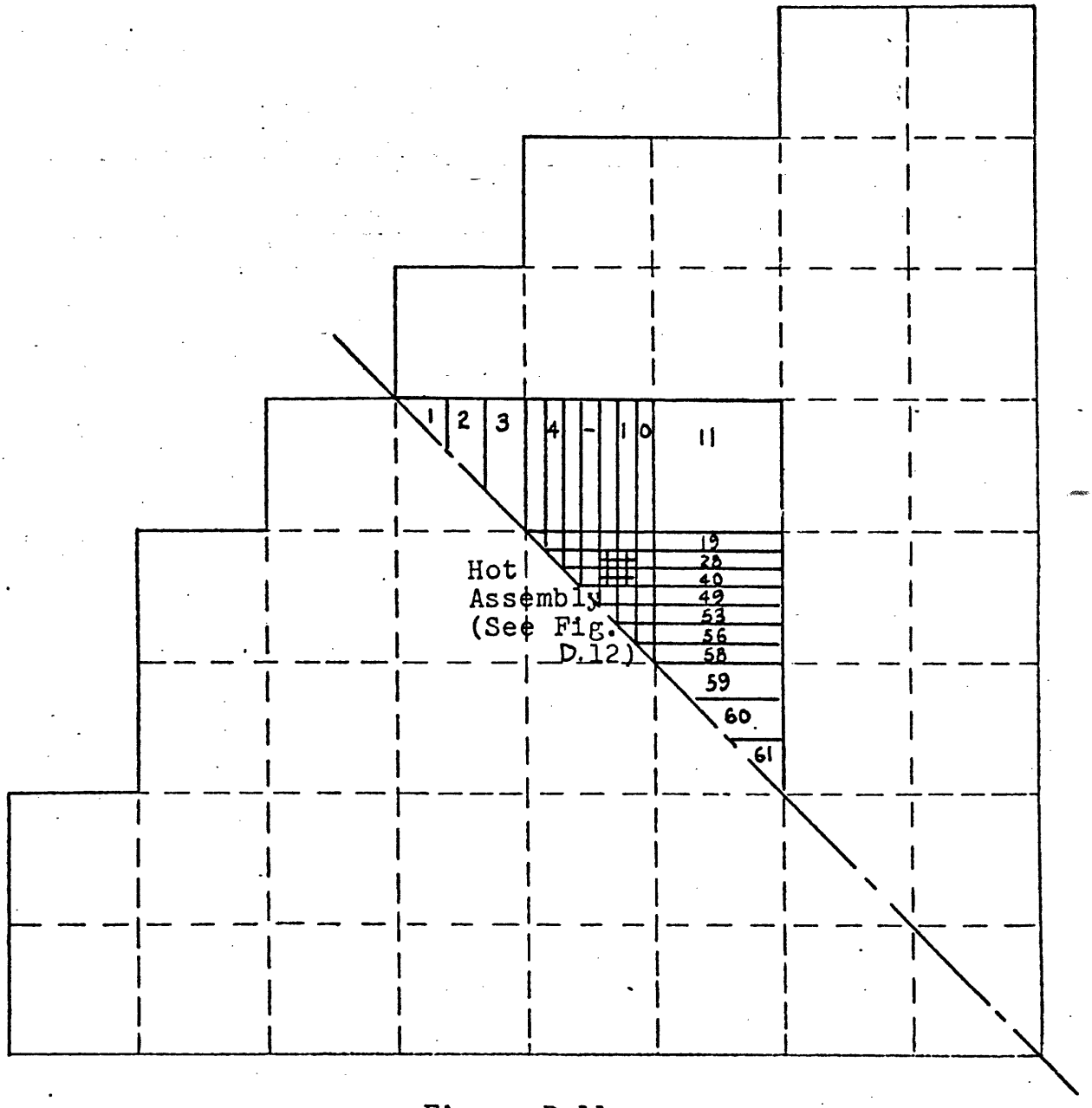

Figure D.11

Pattern of Channels Used to Represent the Core (Case No. 10)

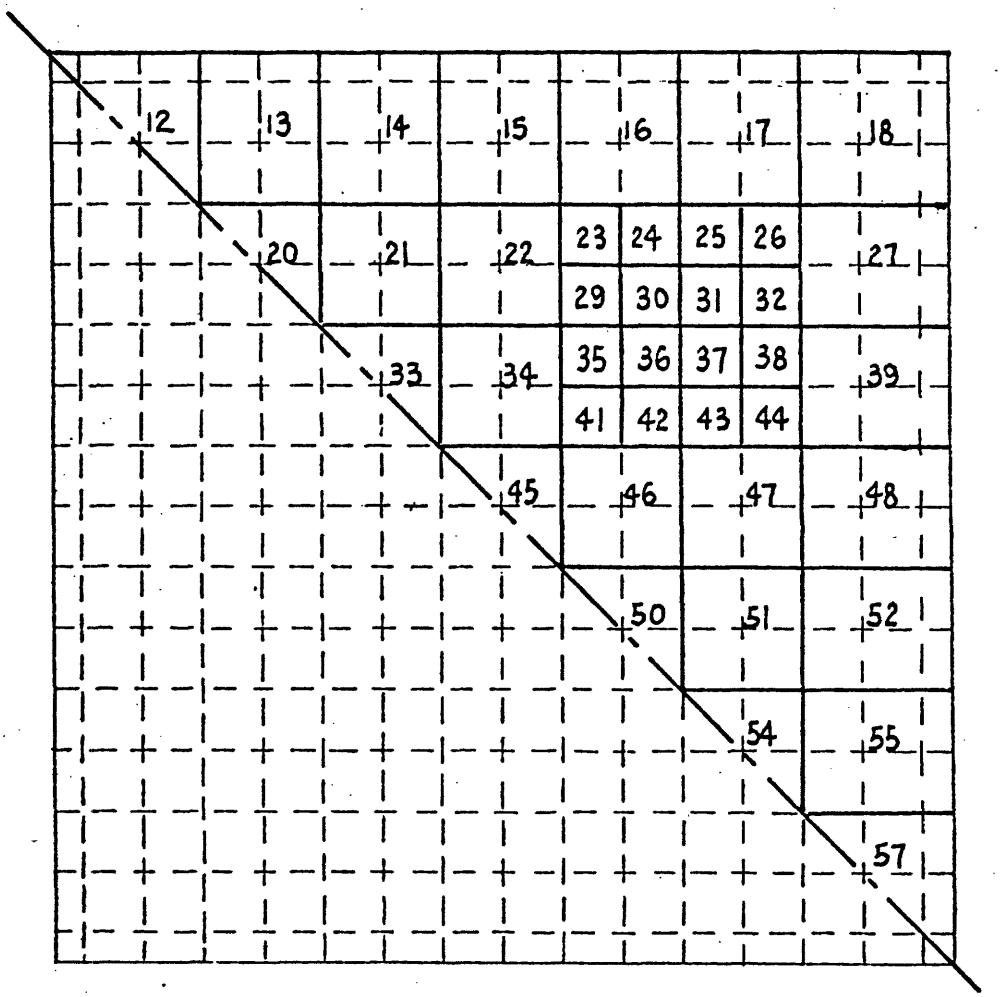

Figure D.12
Detail of the Hot Assembly (Case No. 10)

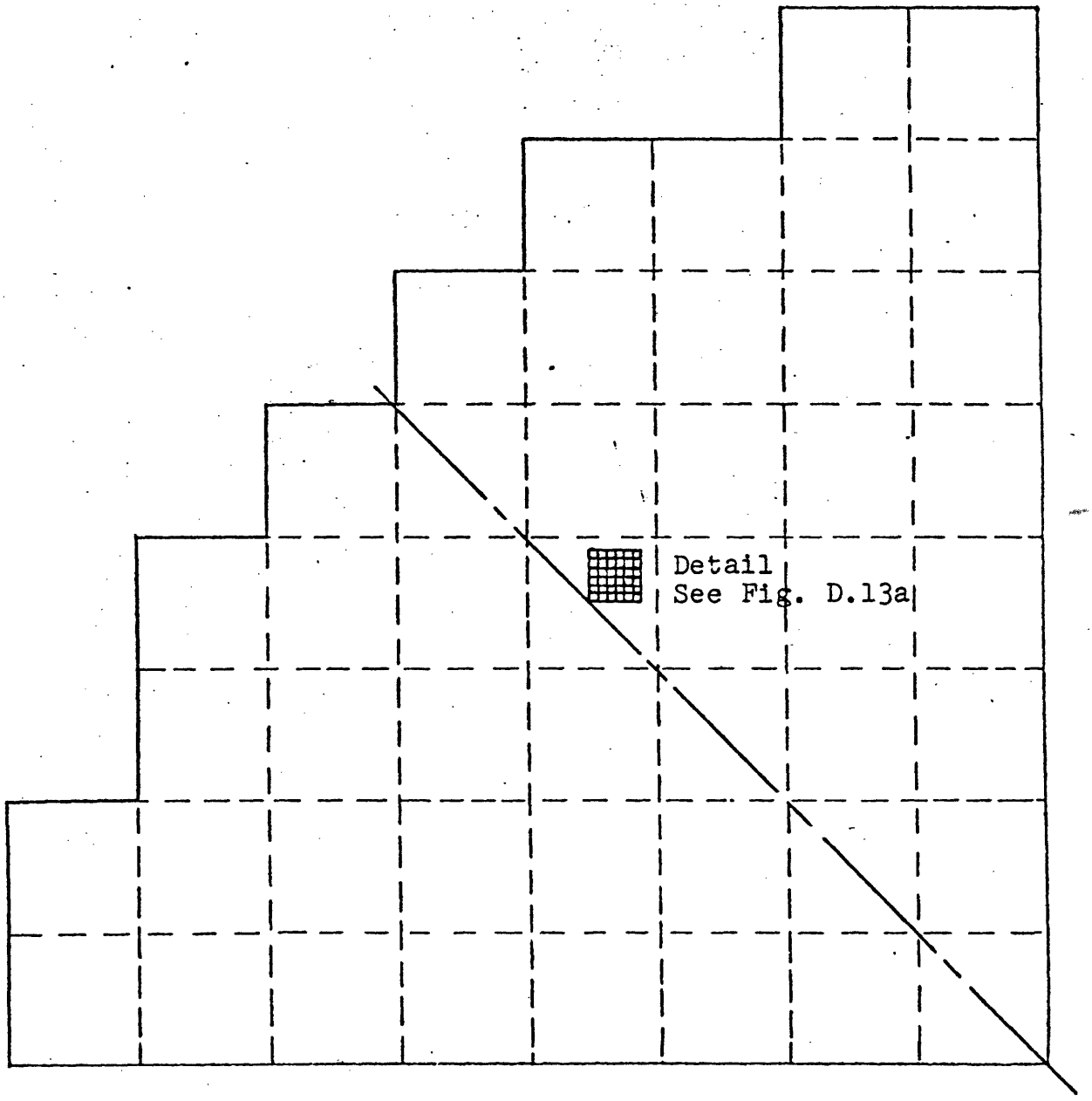

Figure D.13
Pattern of Channels Used in the Analysis (Case No. 11)

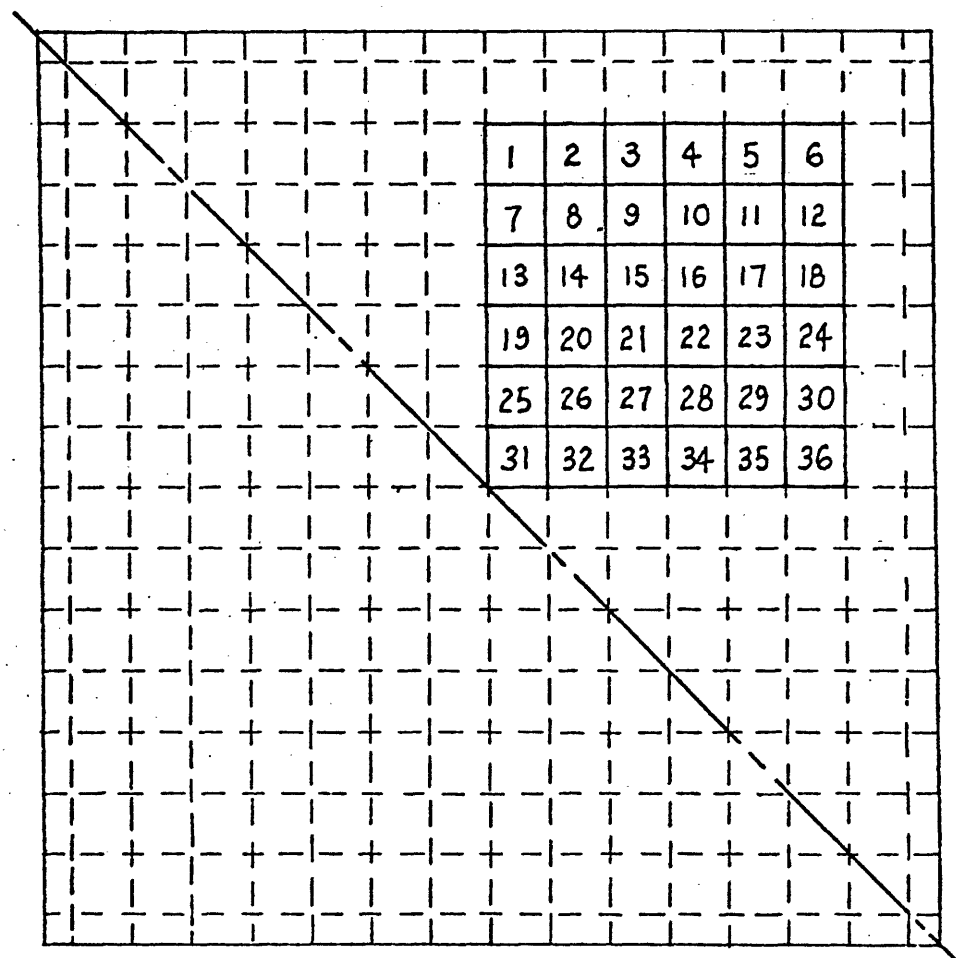

Fig. D.13a Detail of the Hot Assembly (Case No. 11)

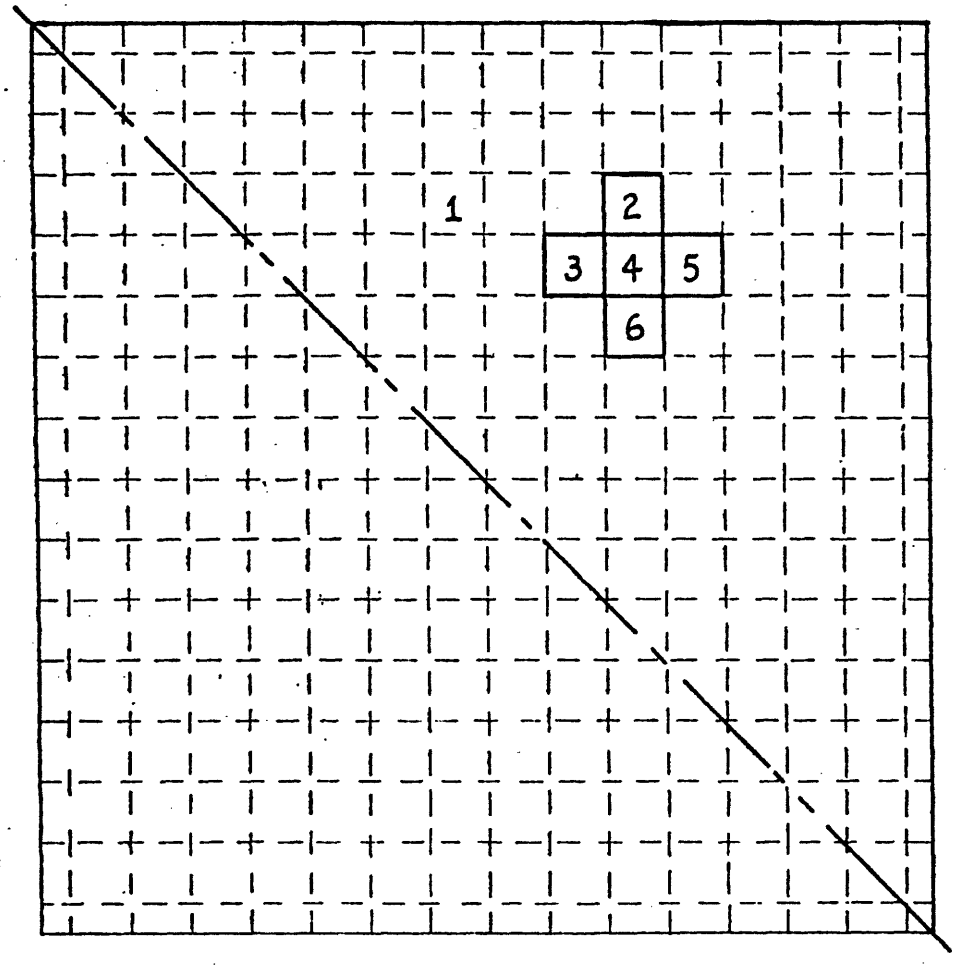

Figure D.14

Channels Used in the Analysis (Case No. 12)

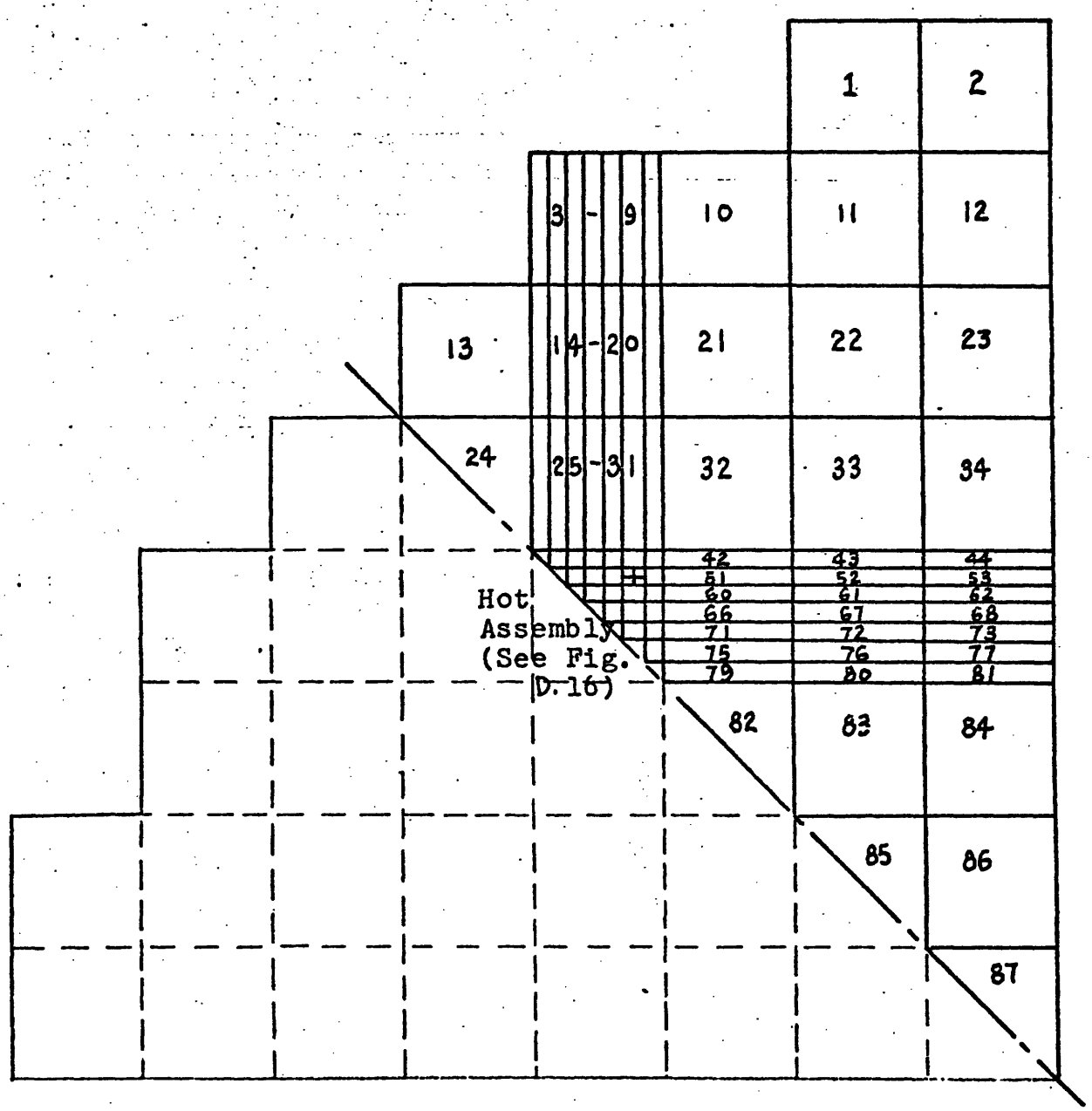

Figure D.15

Pattern of Channels Used to Represent the Core (Case No. 13)

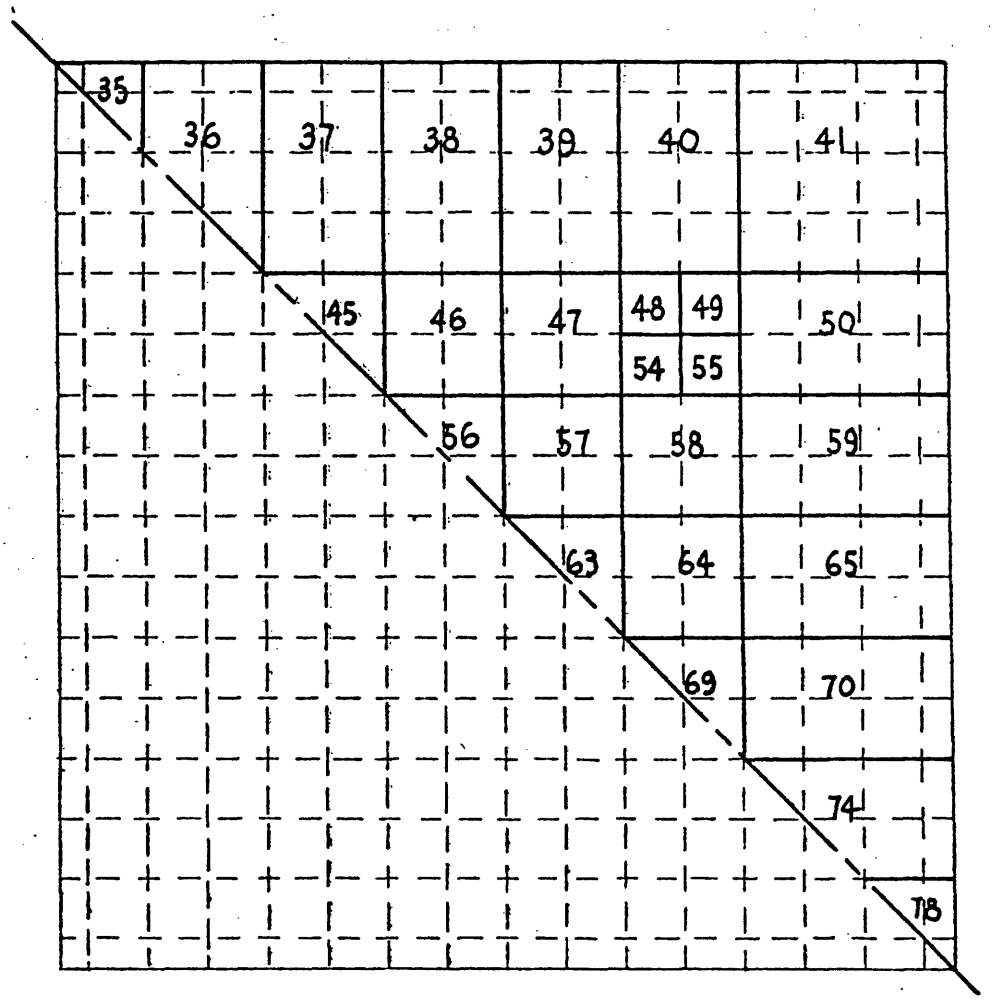

Figure D.16
Detail of the Hot Assembly (Case No. 13)

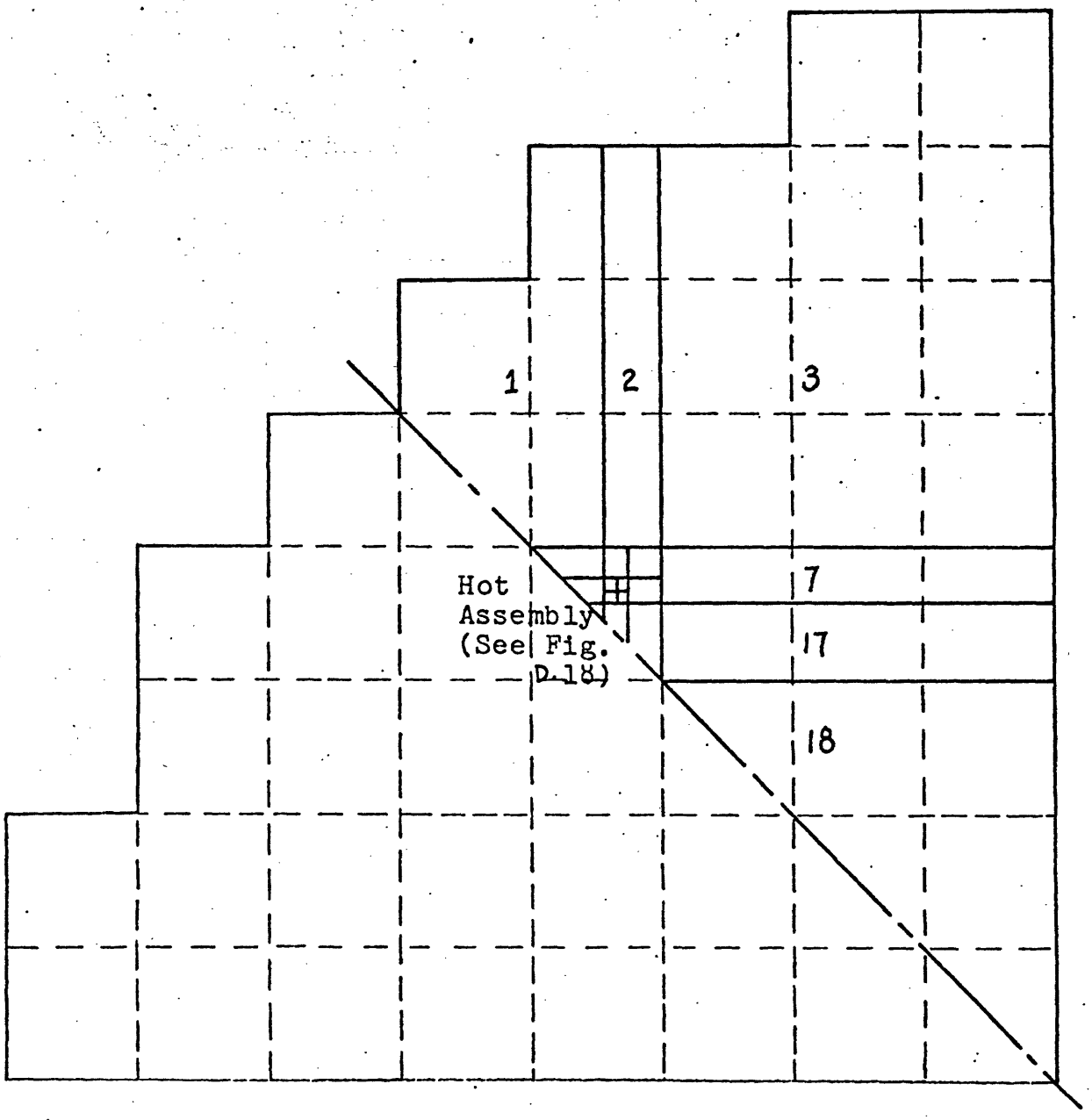

Figure D.17
Pattern of Channels Used to Represent the Core
(Case No. 14)

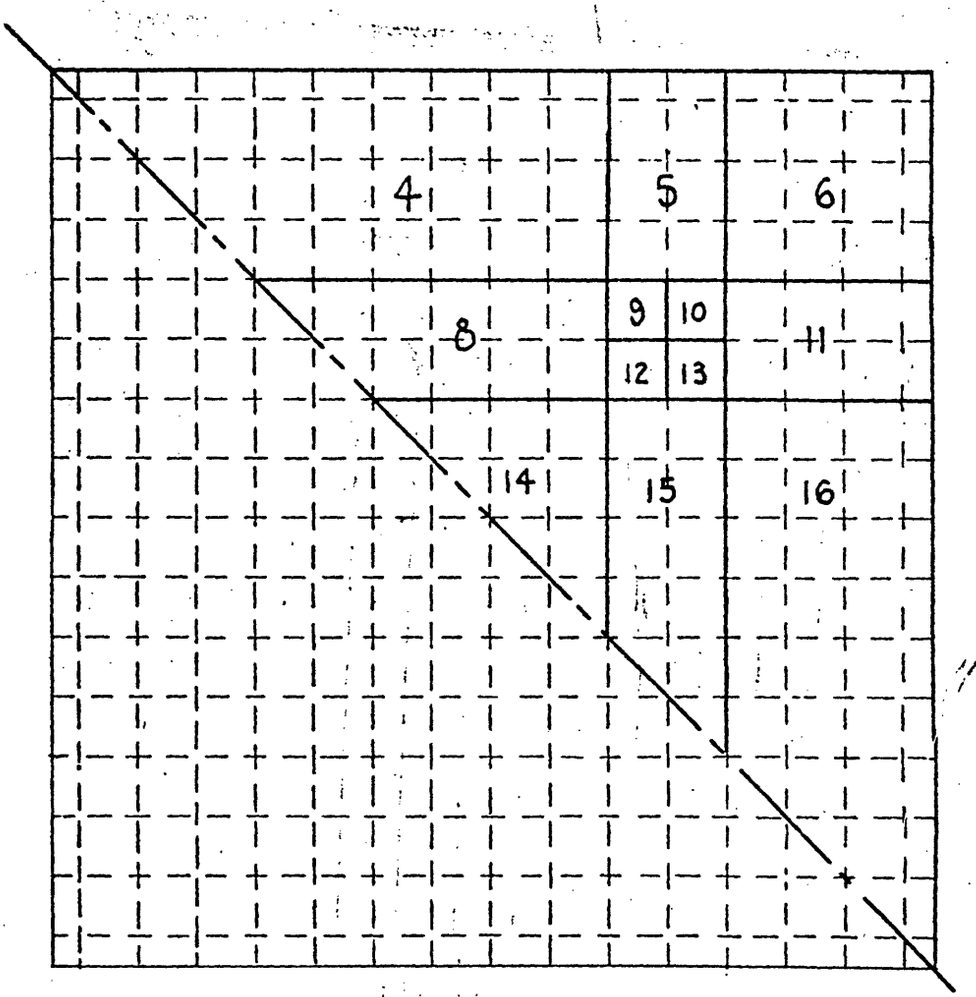

Figure D.18
Detail of the Hot Assembly (Case No. 14)

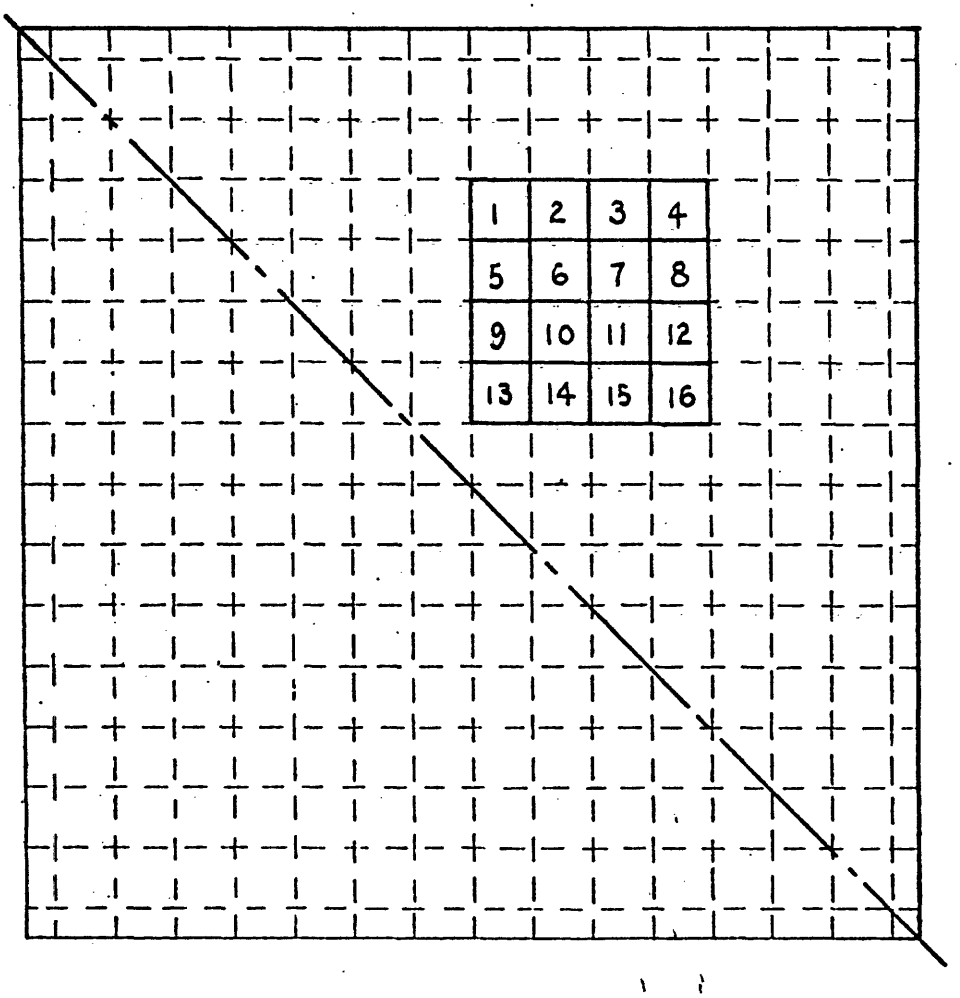

Figure D.19

Channels Used in the Analysis (Case No. 15)

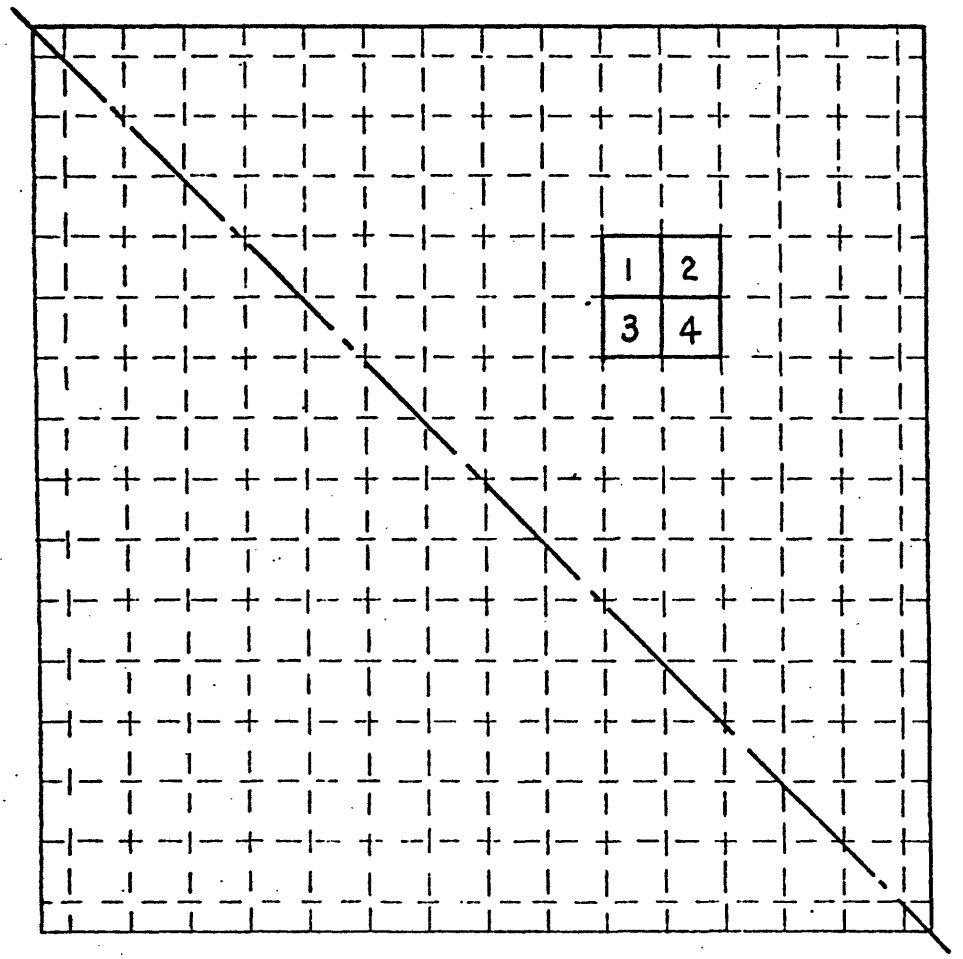

Figure D.20

Channels Used in the Analysis (Case No. 16)

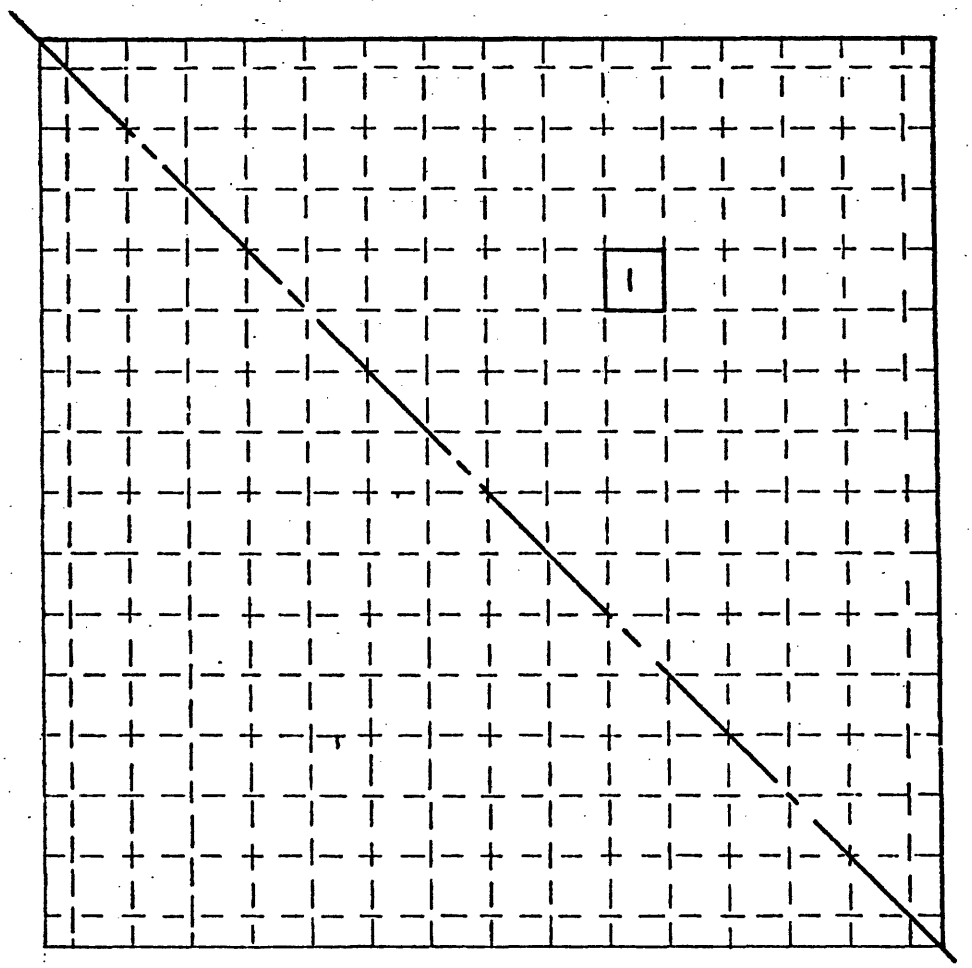

Figure D.21
Channel Used in the Analysis (Case No. 17)

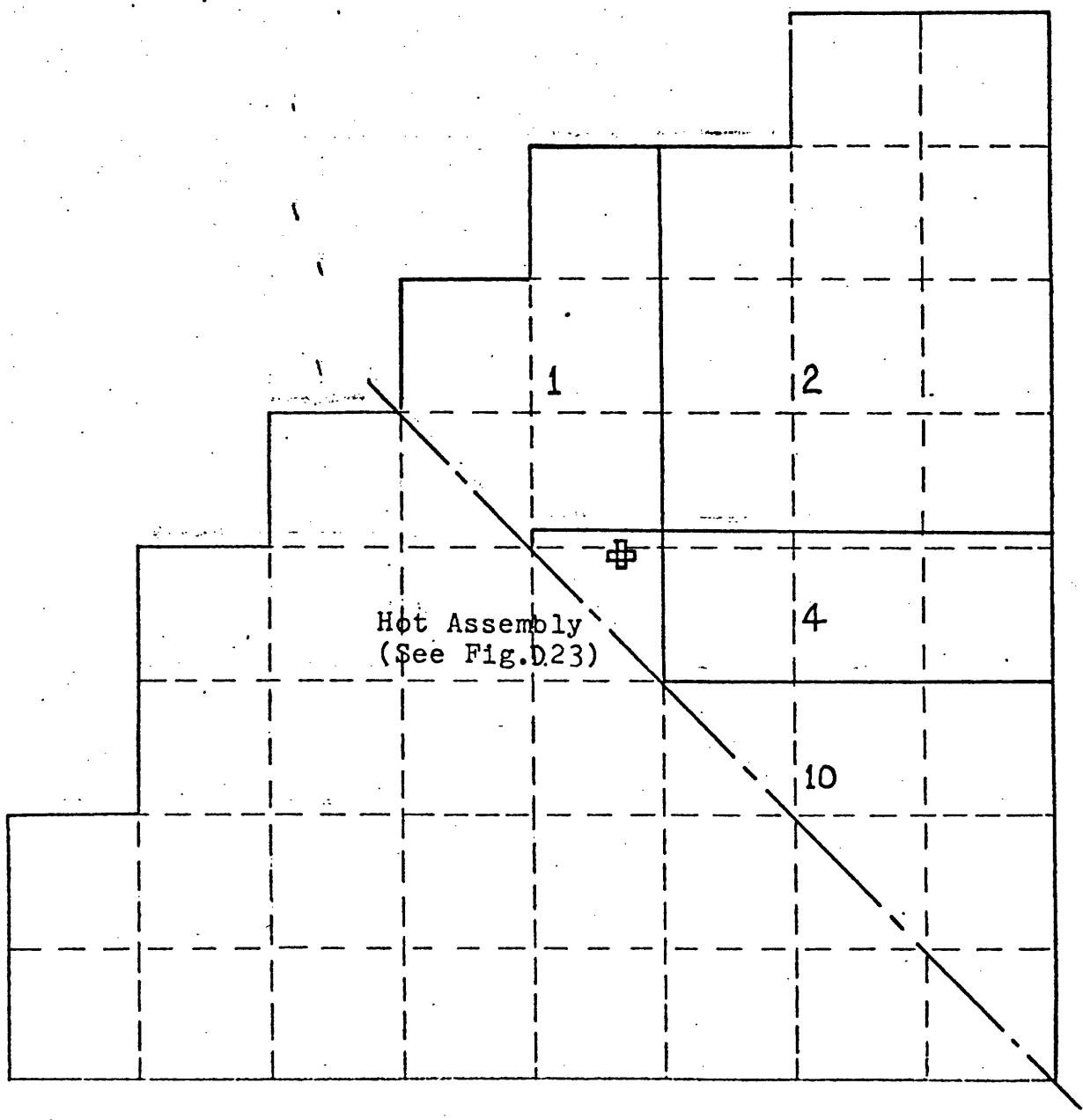

Figure D.22

Pattern of Channels Used to Represent the Core (Case 18)

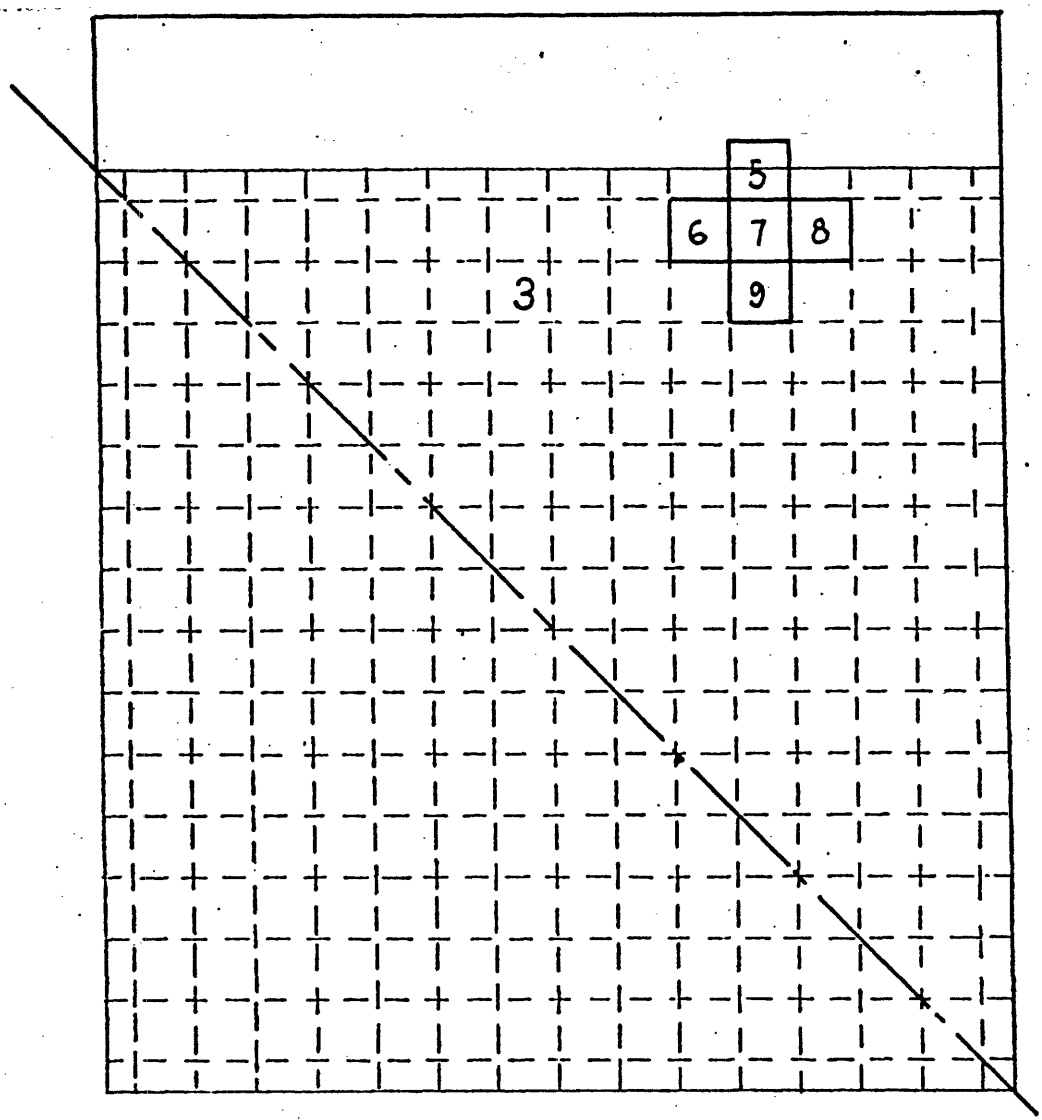

Figure D.23

Detail of the Hot Assembly (Case No. 18)

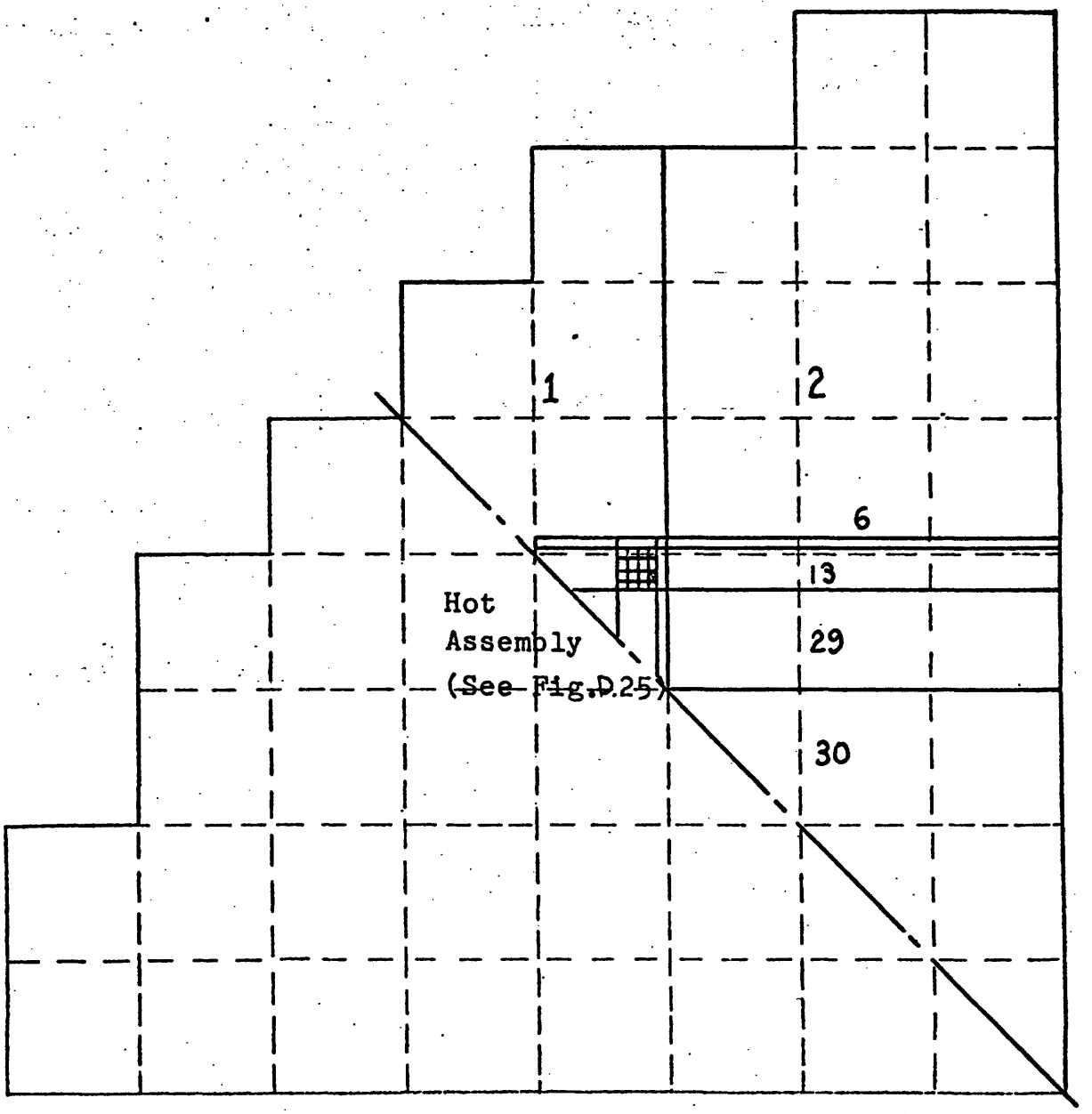

Figure D.24

Pattern of Channels Used to Represent the Core (Case No. 19)

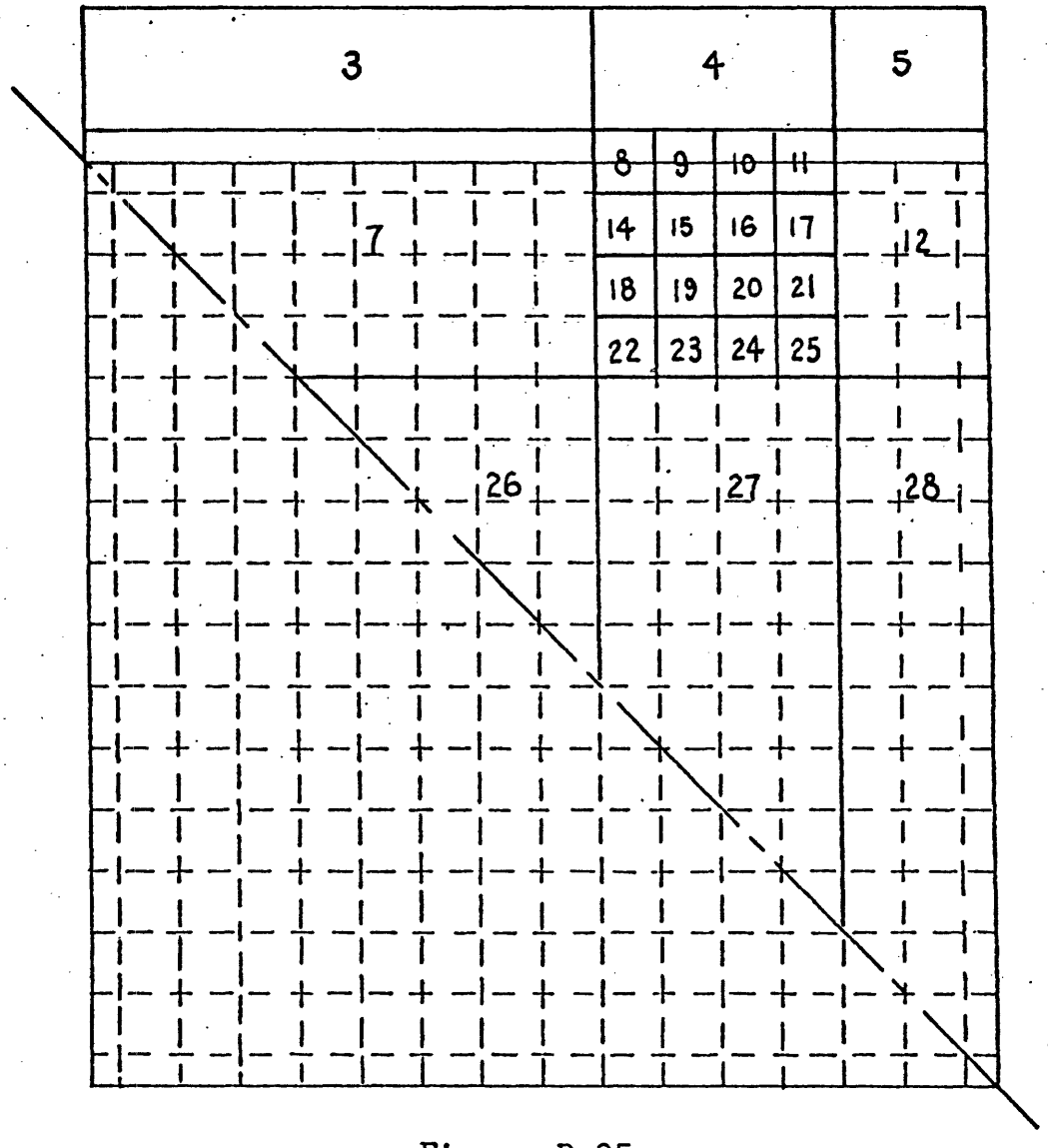

Figure D.25
Detail of the Hot Assembly (Case No. 19)

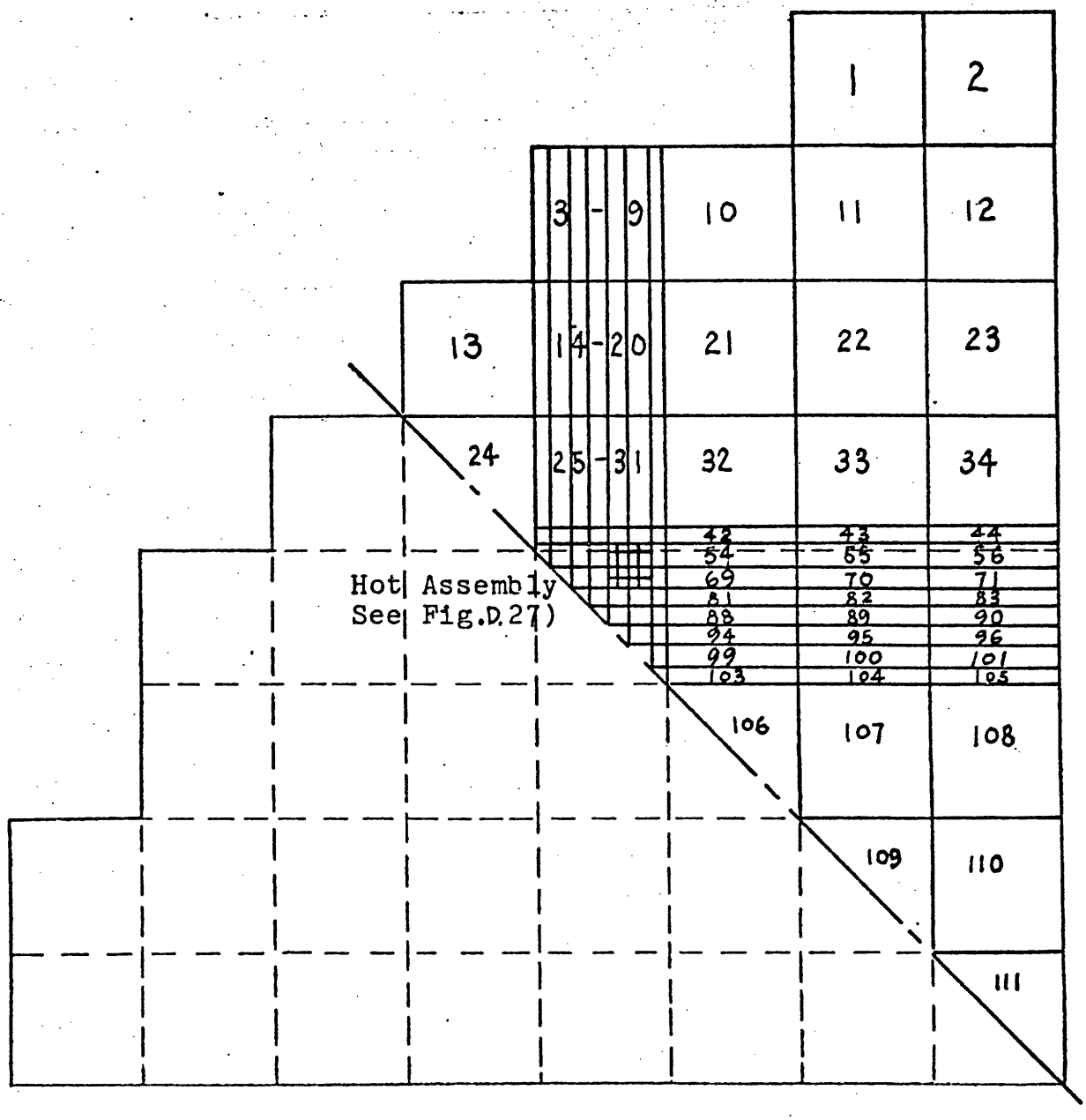

Figure D.26

Pattern of Channels Used to Represent the Core (Case No. 20)

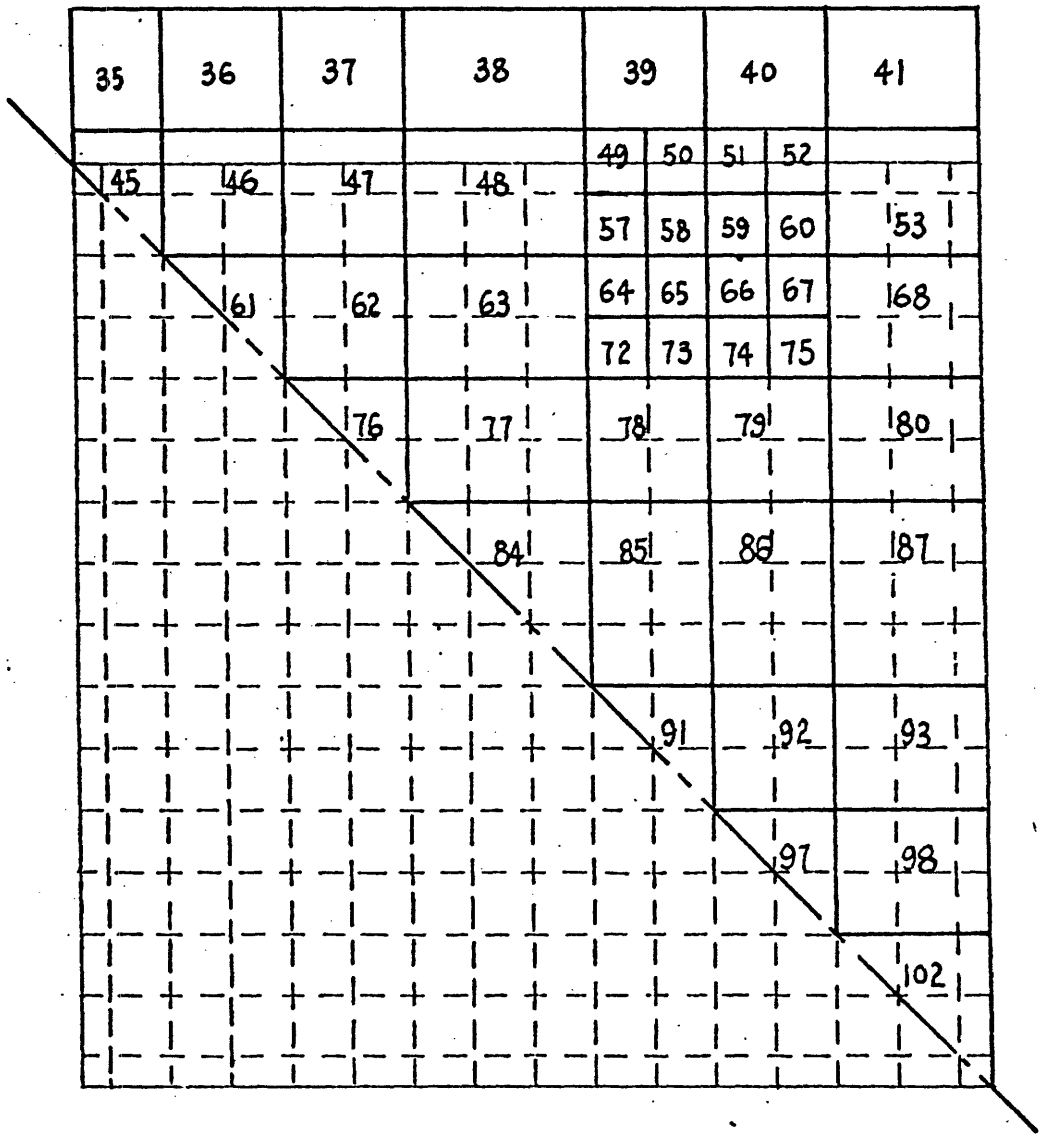

Figure D.27

Detail of the Hot Assembly (Case No. 20)

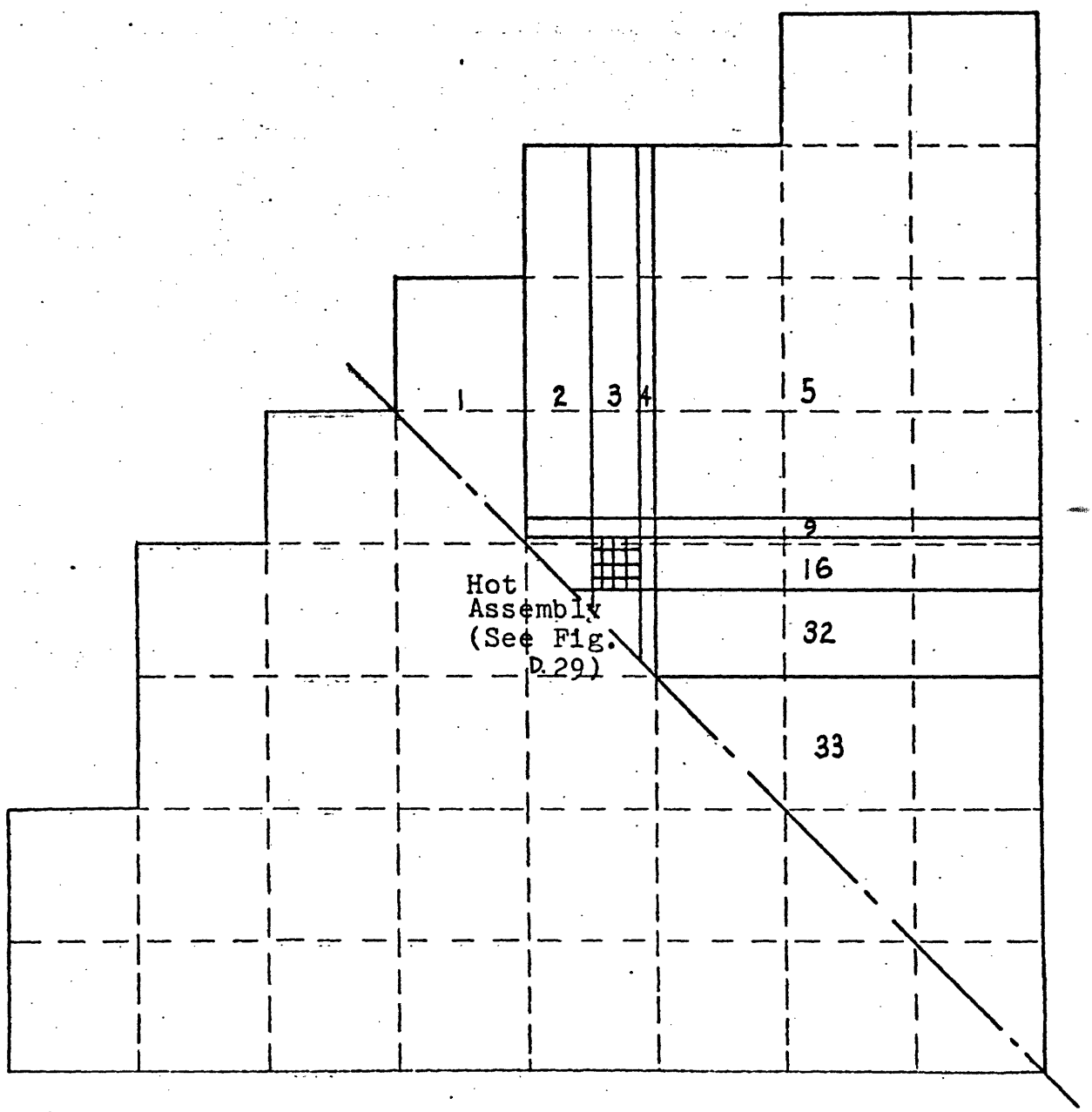

Figure D.28

Pattern of Channels Used to Represent the Core (Case No. 21)

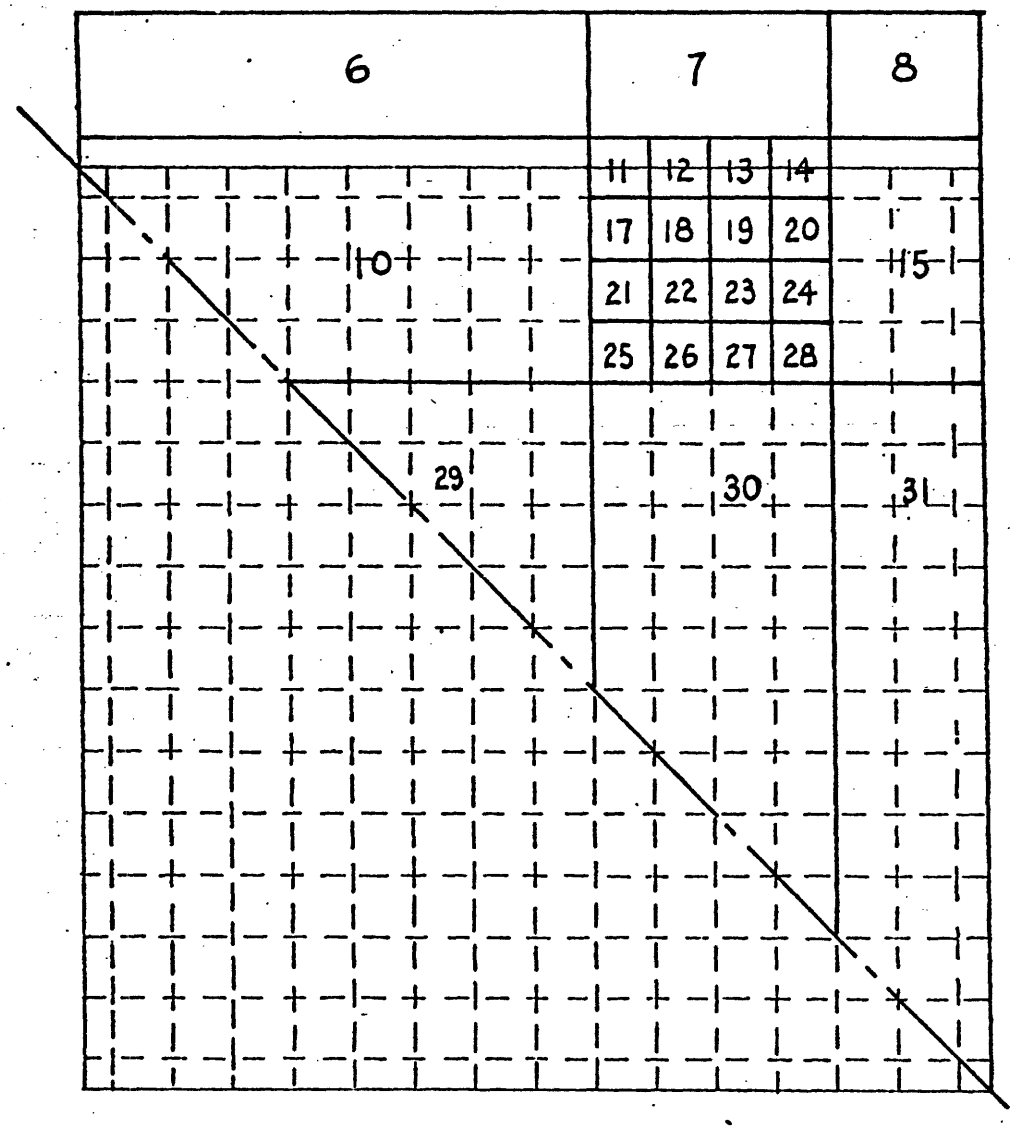

Figure D.29
Detail of the Hot Assembly (Case No. 21)

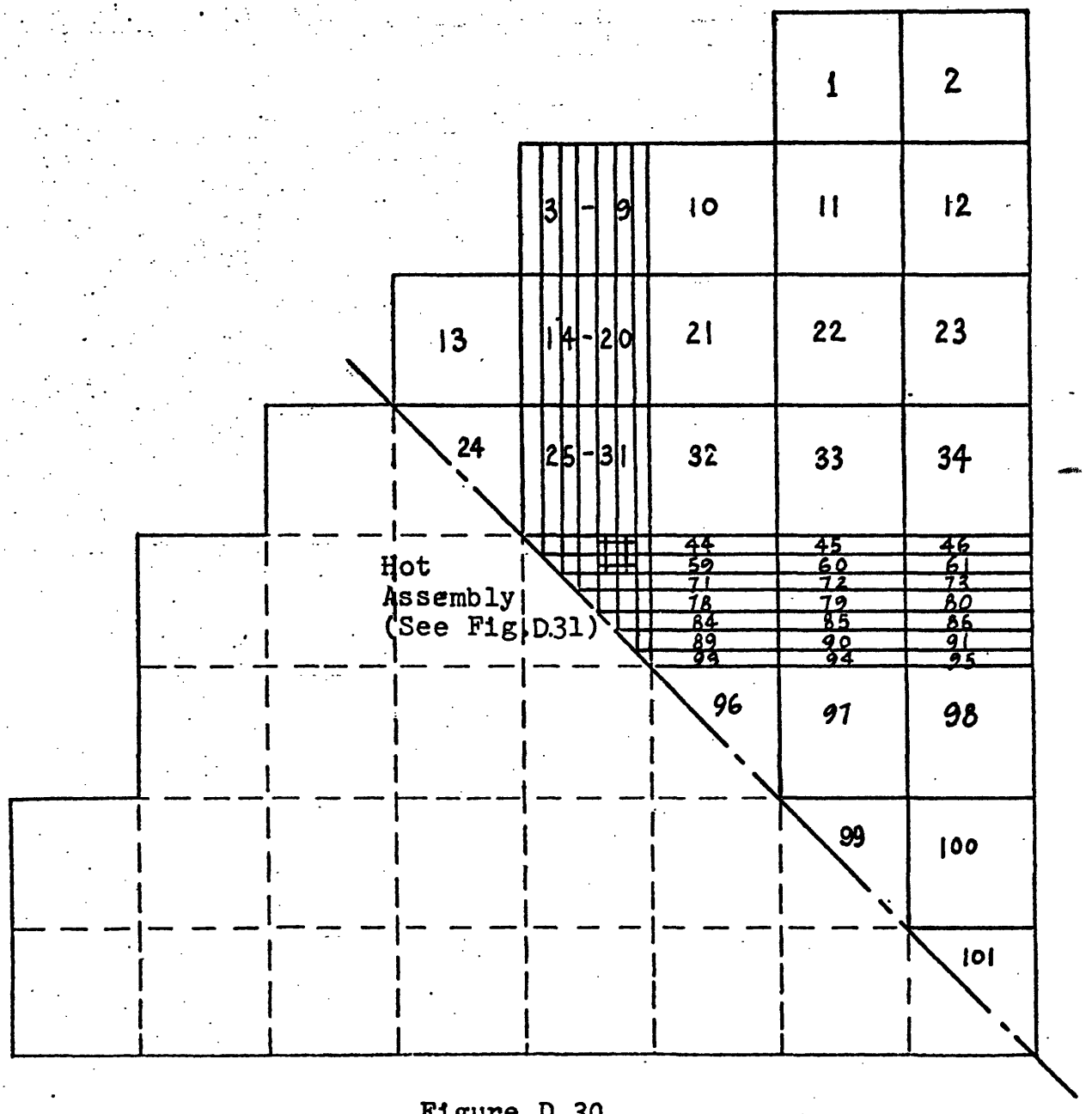

Figure D.30
Pattern of Channels Used to Represent the Core (Case No. 22)

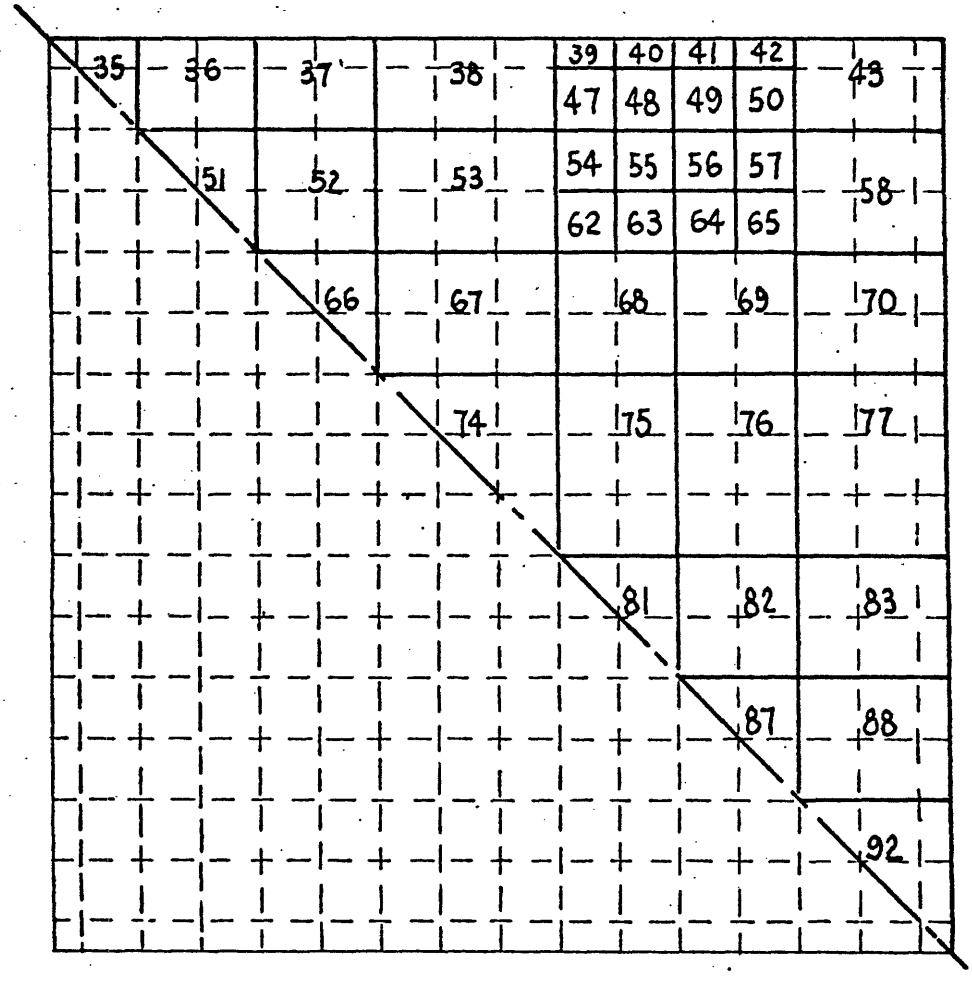

Figure D.31

Detail of the Hot Assembly (Case No. 22)

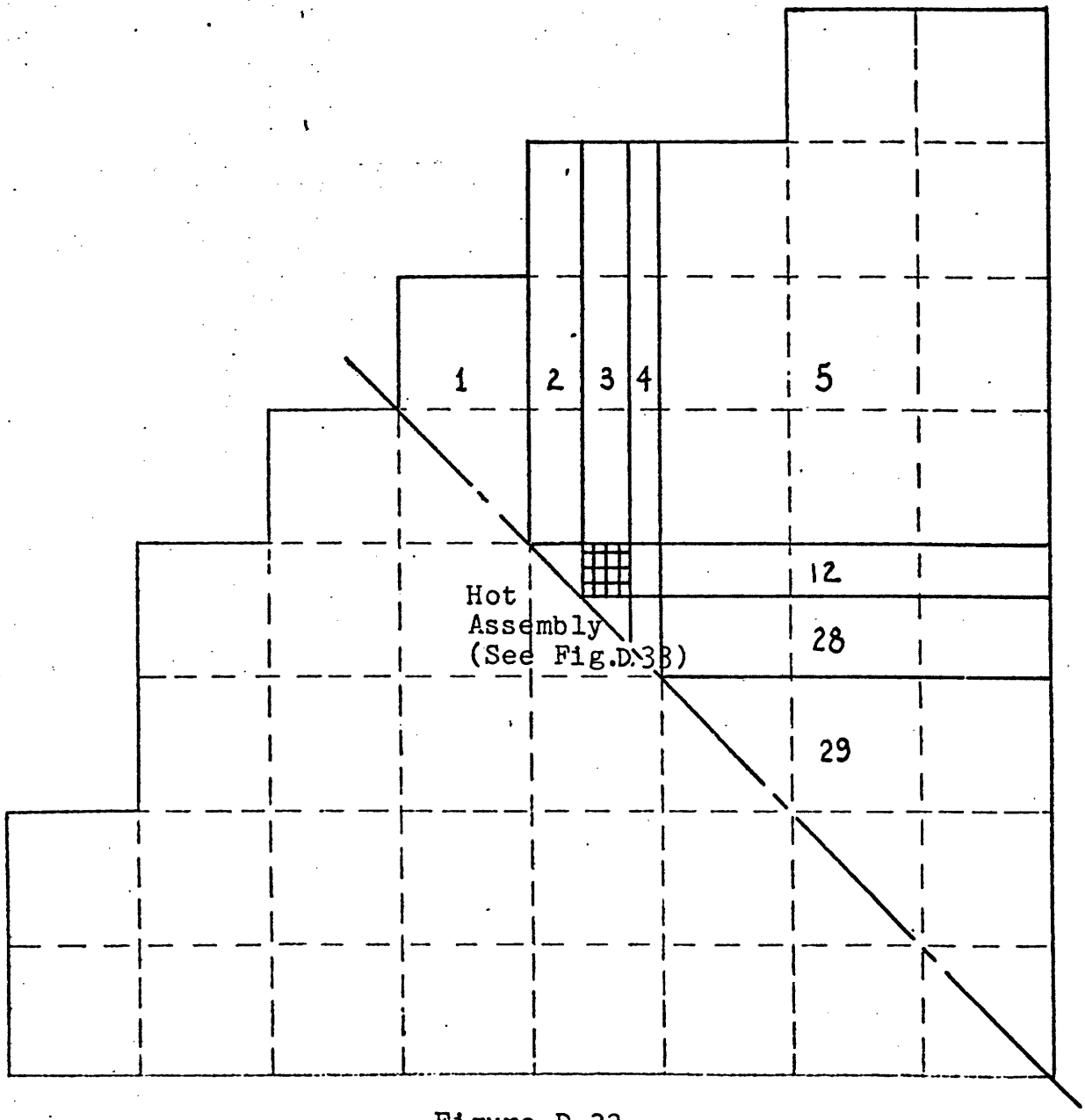

Figure D.32
Pattern of Channels Used to Represent the Core (Case No. 23 Case No. 24)

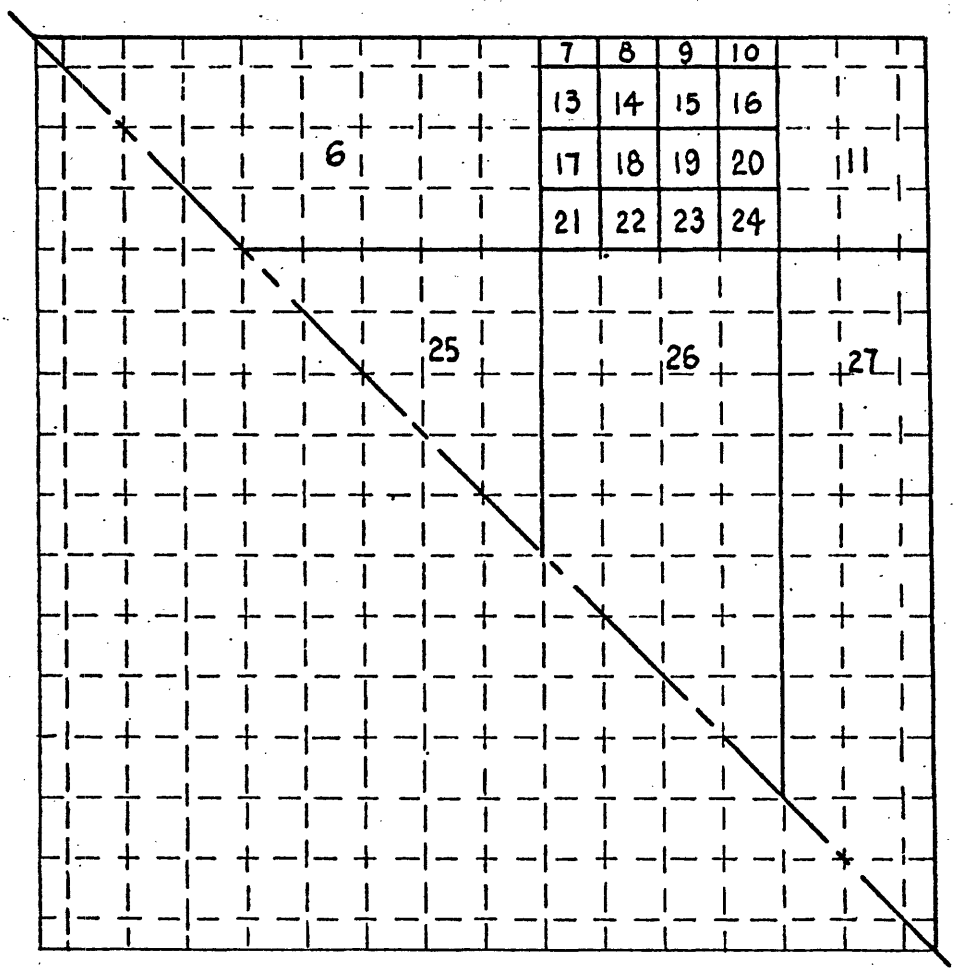

Figure D.33

Detail of the Hot Assembly (Case No. 23, Case No. 24)

(x) ≡Radial peaking power ≡x
Properties and dimensions of the channels are those of Appendix C.

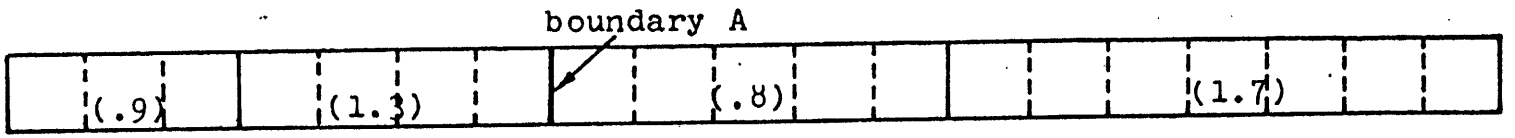

Figure D.34
Case 25, 2D problem

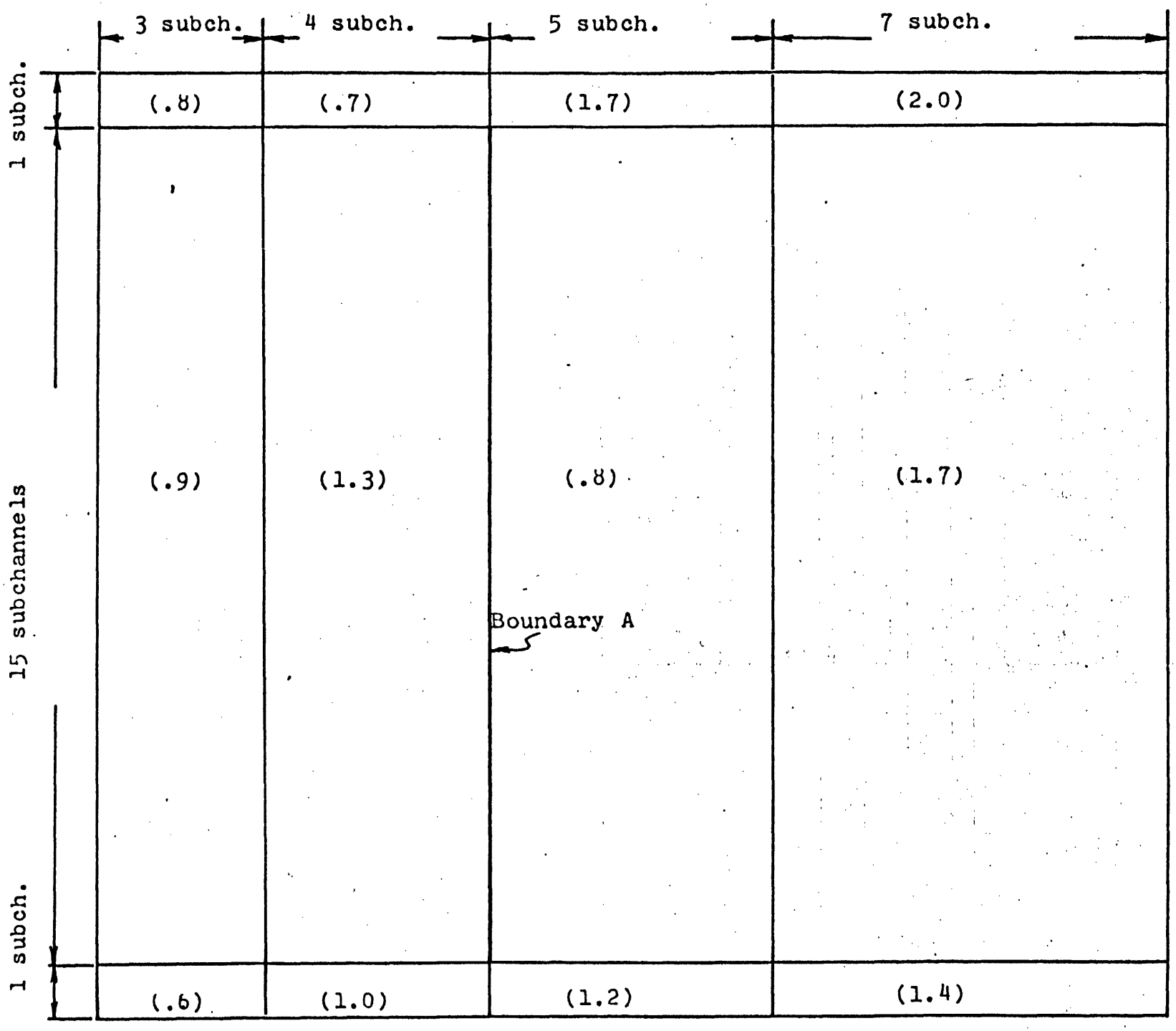

(x)≡Radial peaking power≡x

Properties and Dimensions of the Channels are those of Appendix C

Figure D.35

Case 26

(x)≡ Radial peaking factor≡x
Properties and dimensions of the channels are those of appendix C

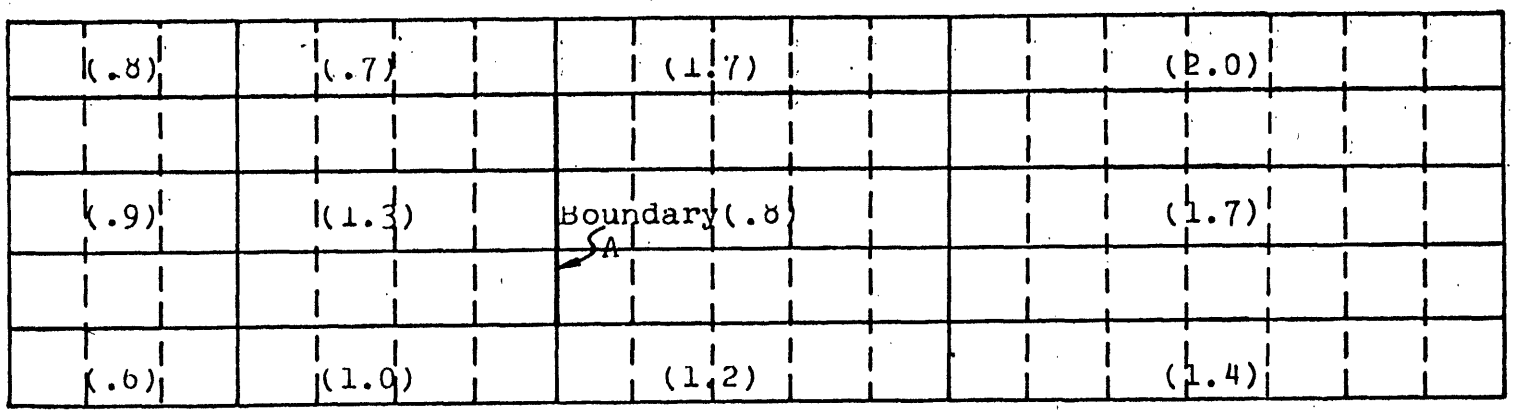

Figure D.36
Case 27

(x)≡Radial power factor≡x
Properties and dimensions of the channels are those of Appendix C

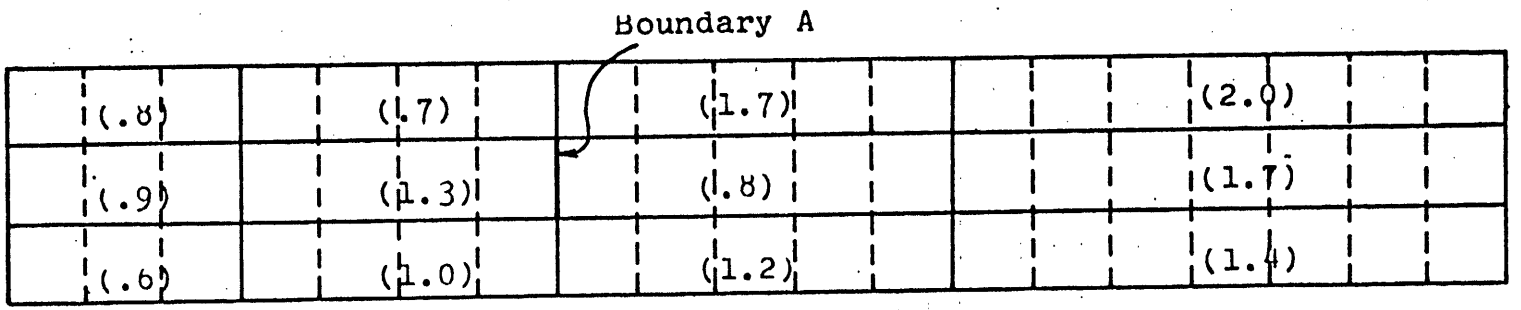

Figure D.37

Case 28

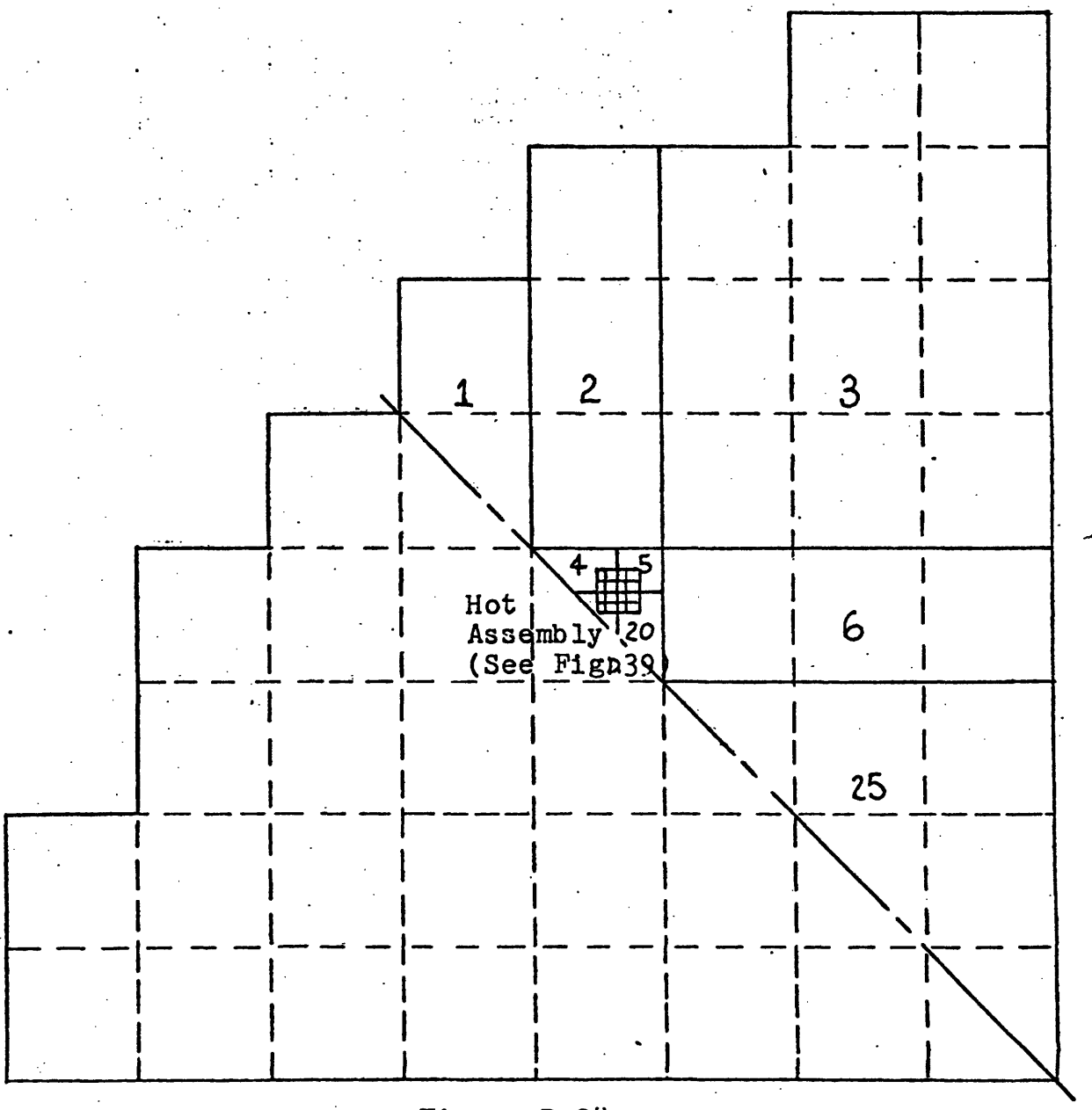

Figure D.38

Pattern of Channels Used to Represent the Core (Case No. 30)

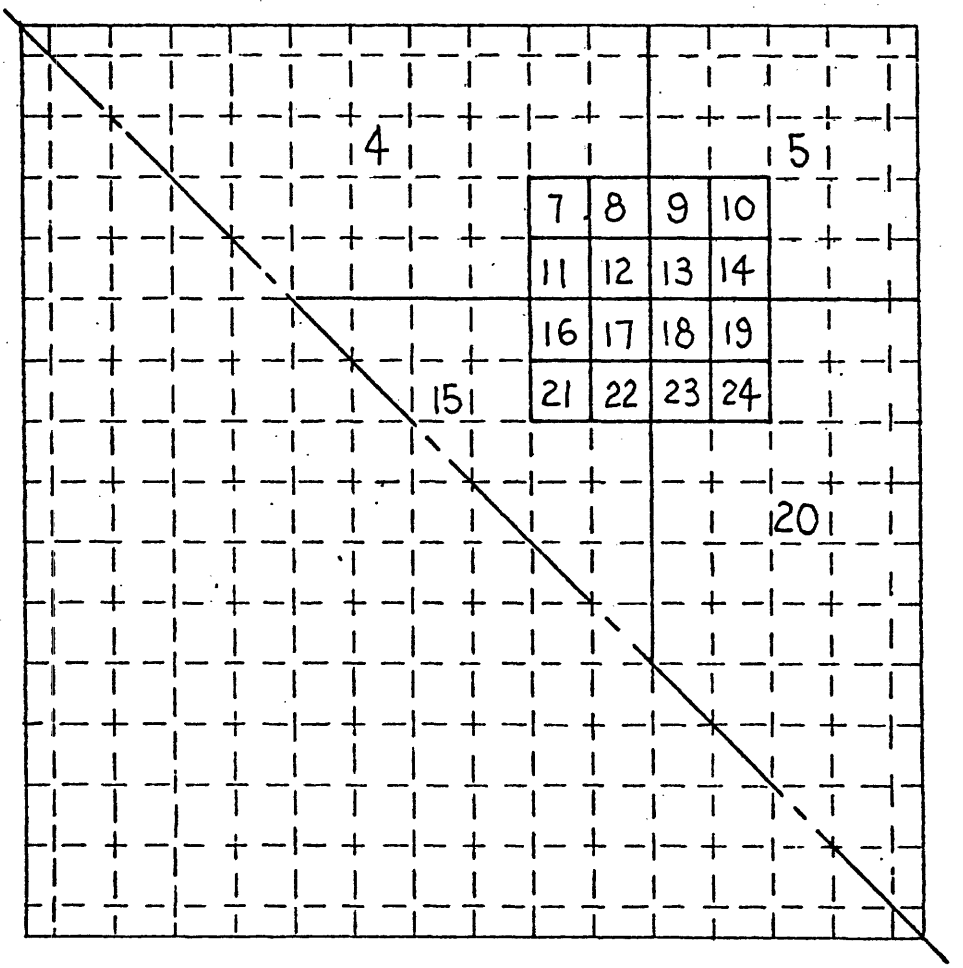

Figure D.39
Detail of the Hot Assembly (Case No. 30)

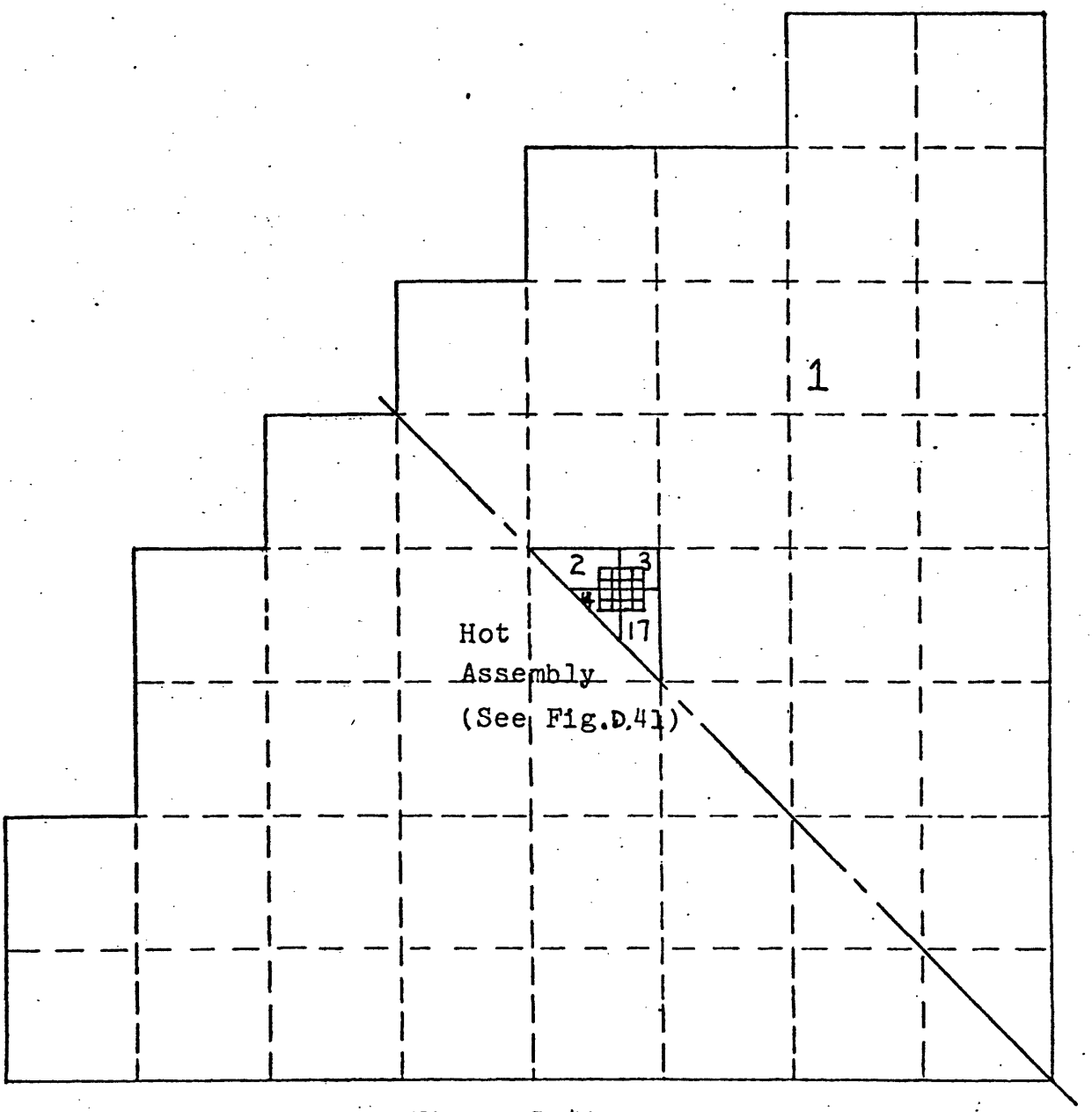

Figure D.40

Pattern of Channels Used to Represent the Core (Case No. 31)

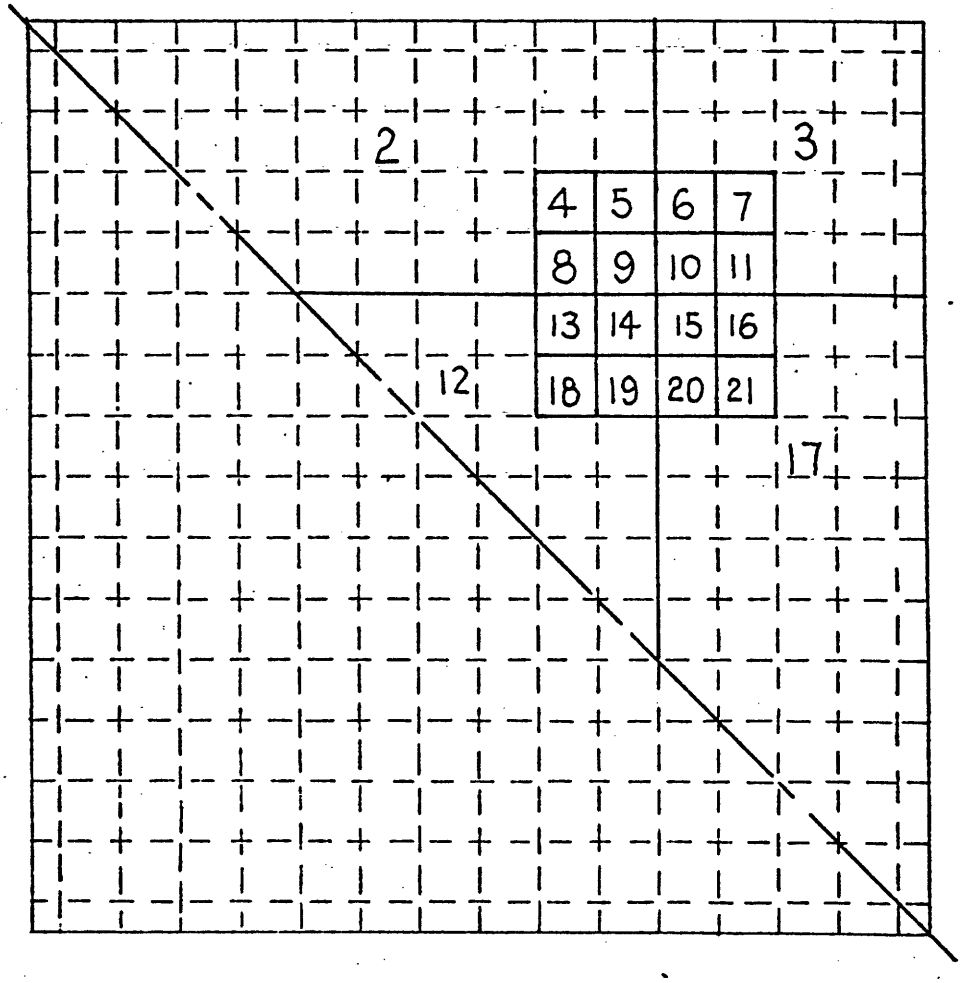

Figure D.41

Detail of the hot Assembly (Case No. 31)

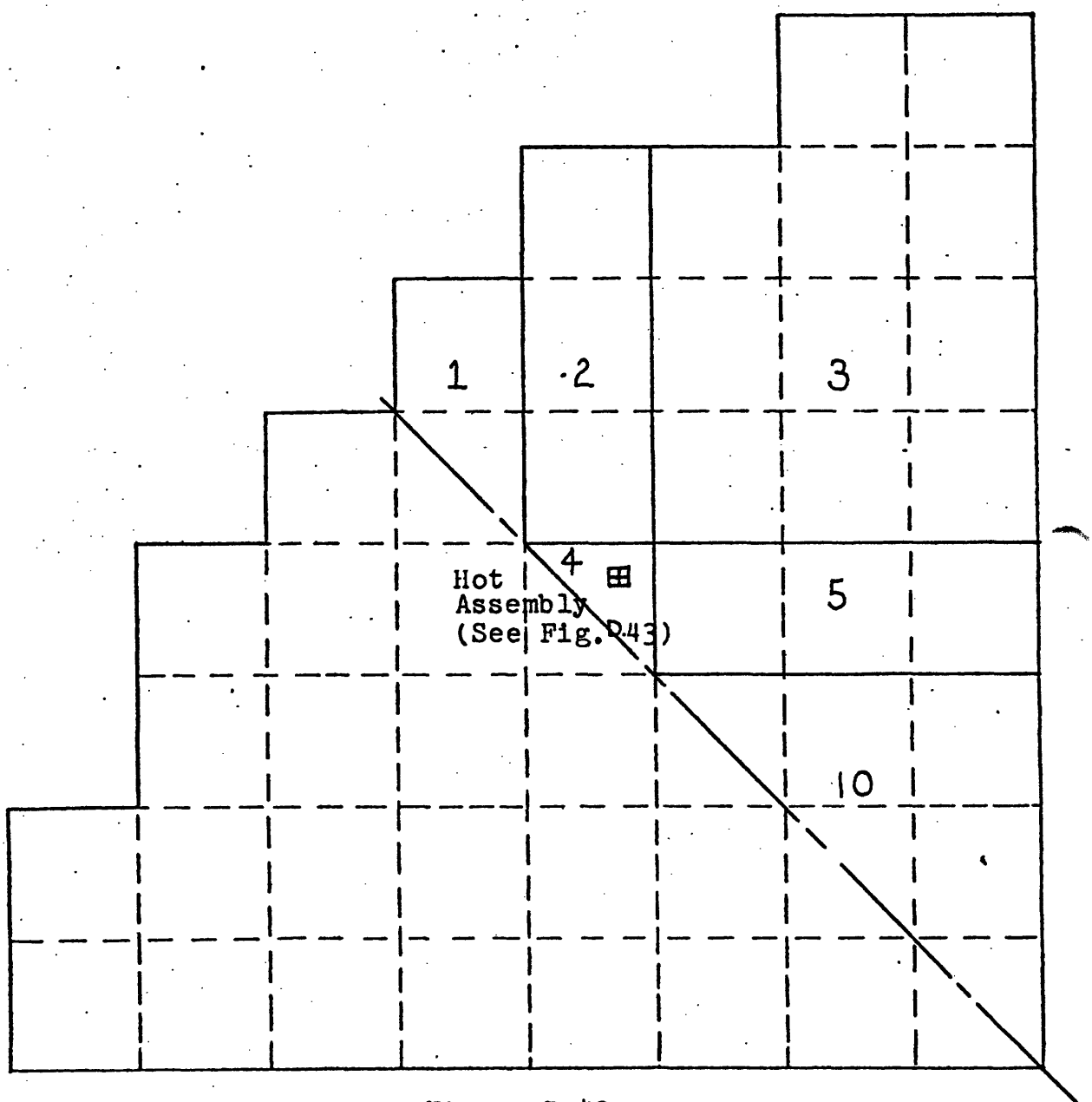

Figure D.42

Pattern of Channels Used to Represent the Core (Case No. 32)

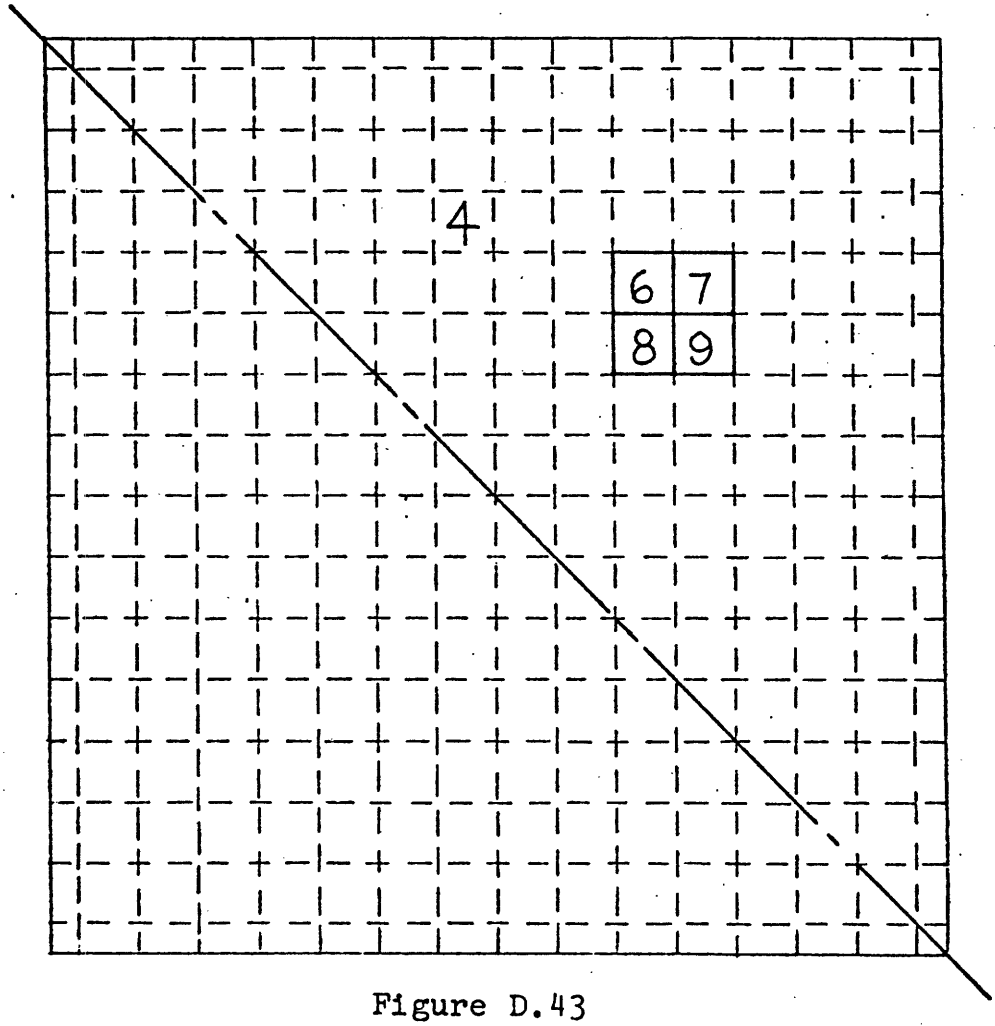

Figure D.43
Detail of the Hot Assembly (Case No. 32)

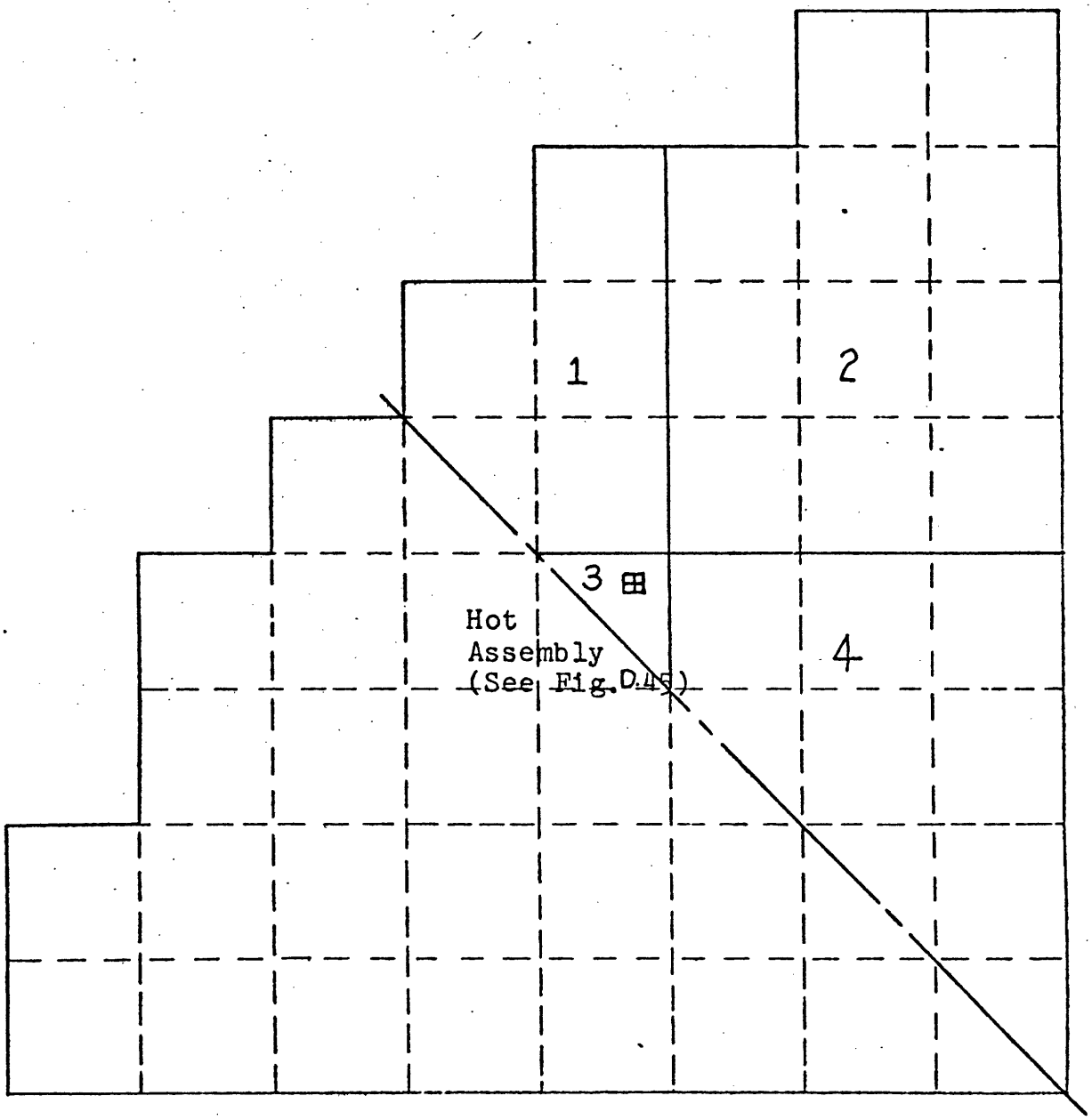

Figure D.44

Pattern of Channels Used to Represent the Core (Case No. 33)

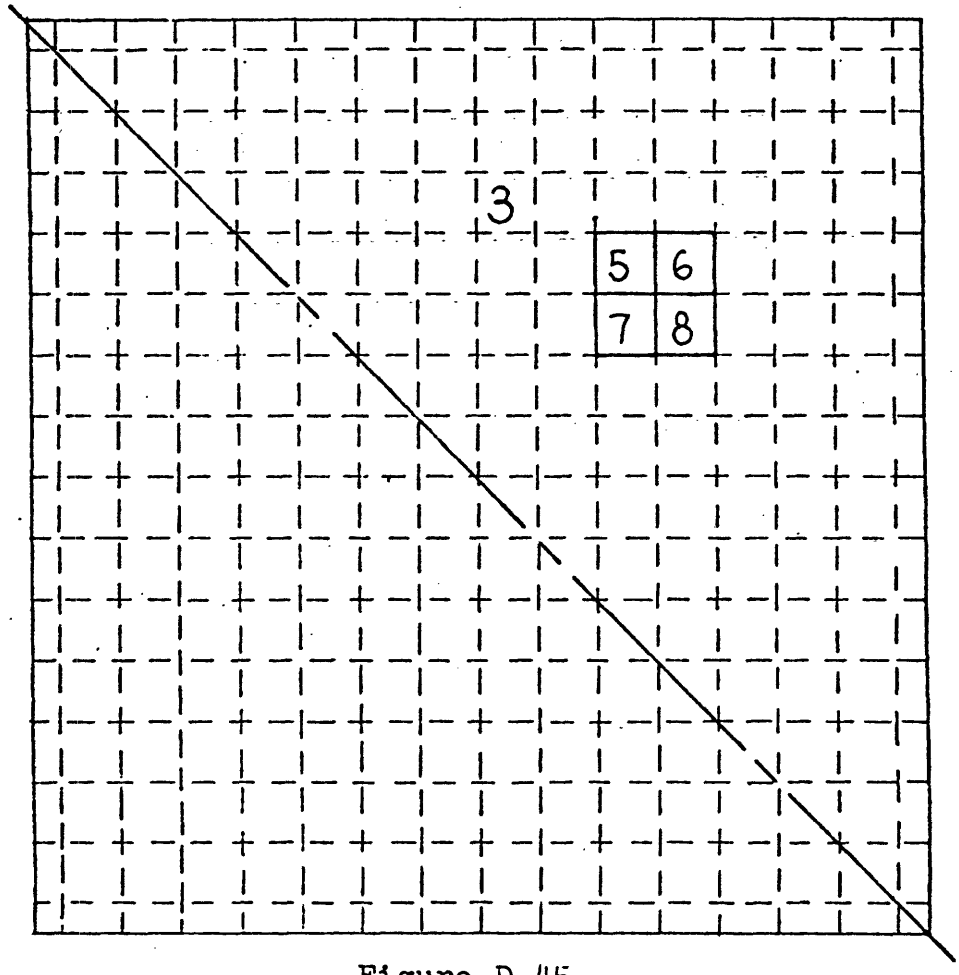

Figure D.45

Detail of the Hot Assembly (Case No. 33)

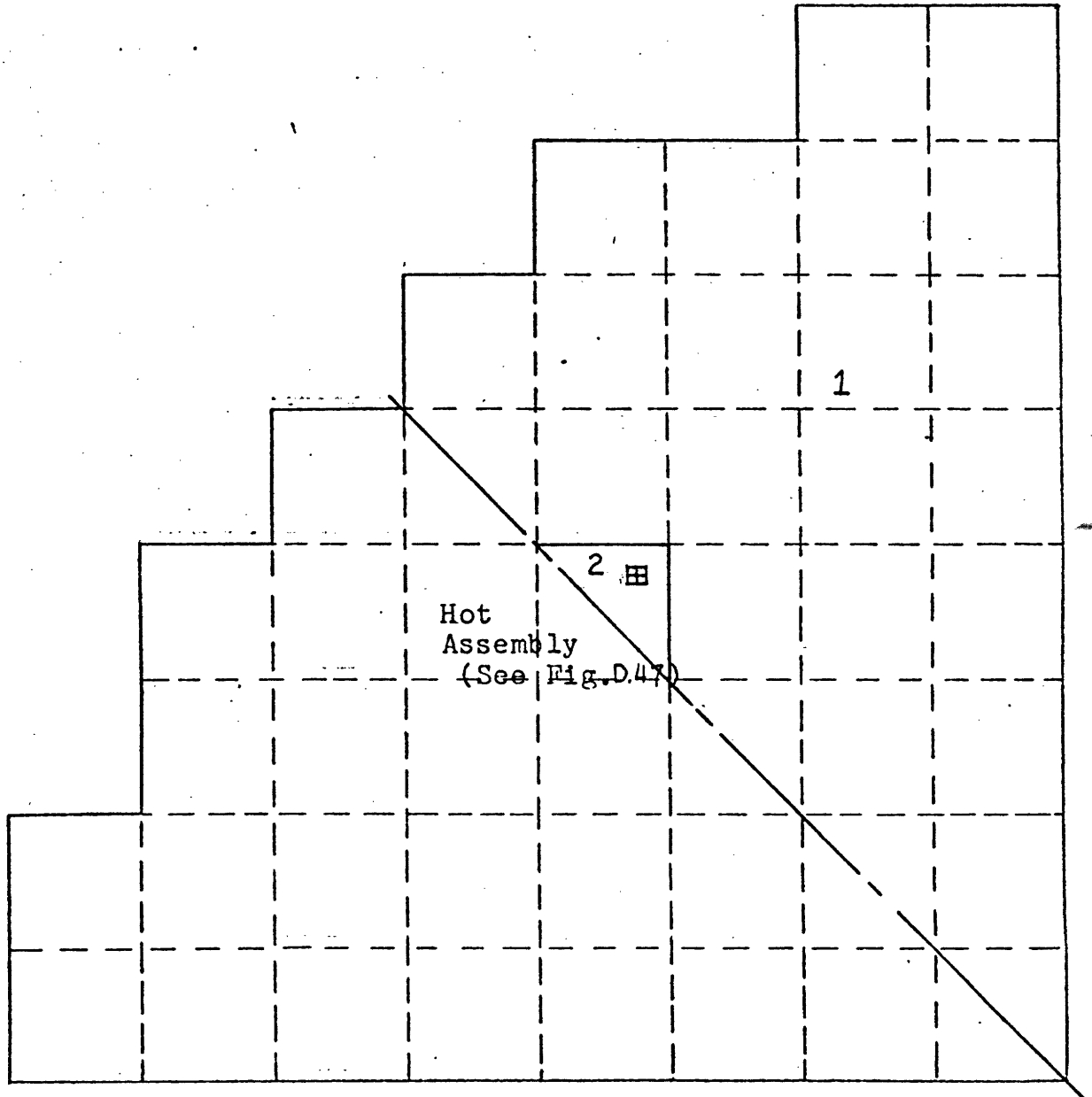

Figure D.46

Pattern of Channels Used to Represent the Core (Case No. 34)

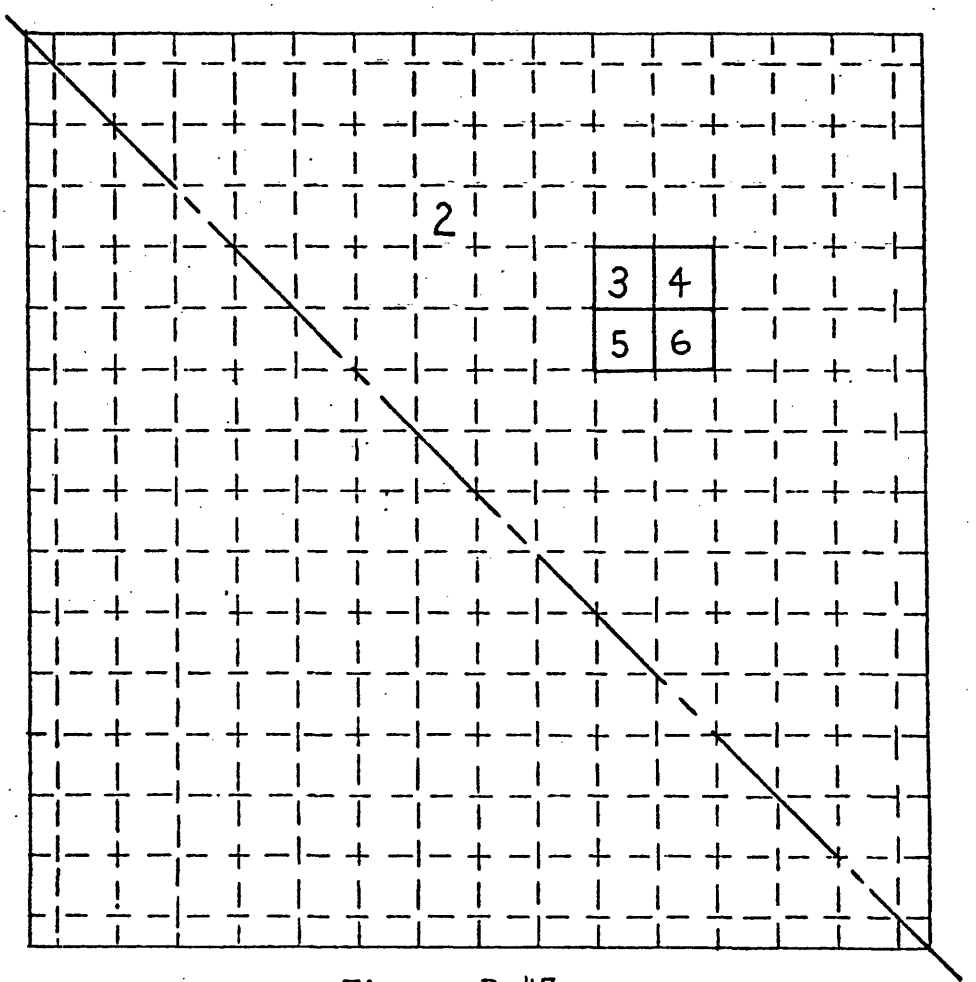

Figure D.47

Detail of the Hot Assembly (Case No. 34)

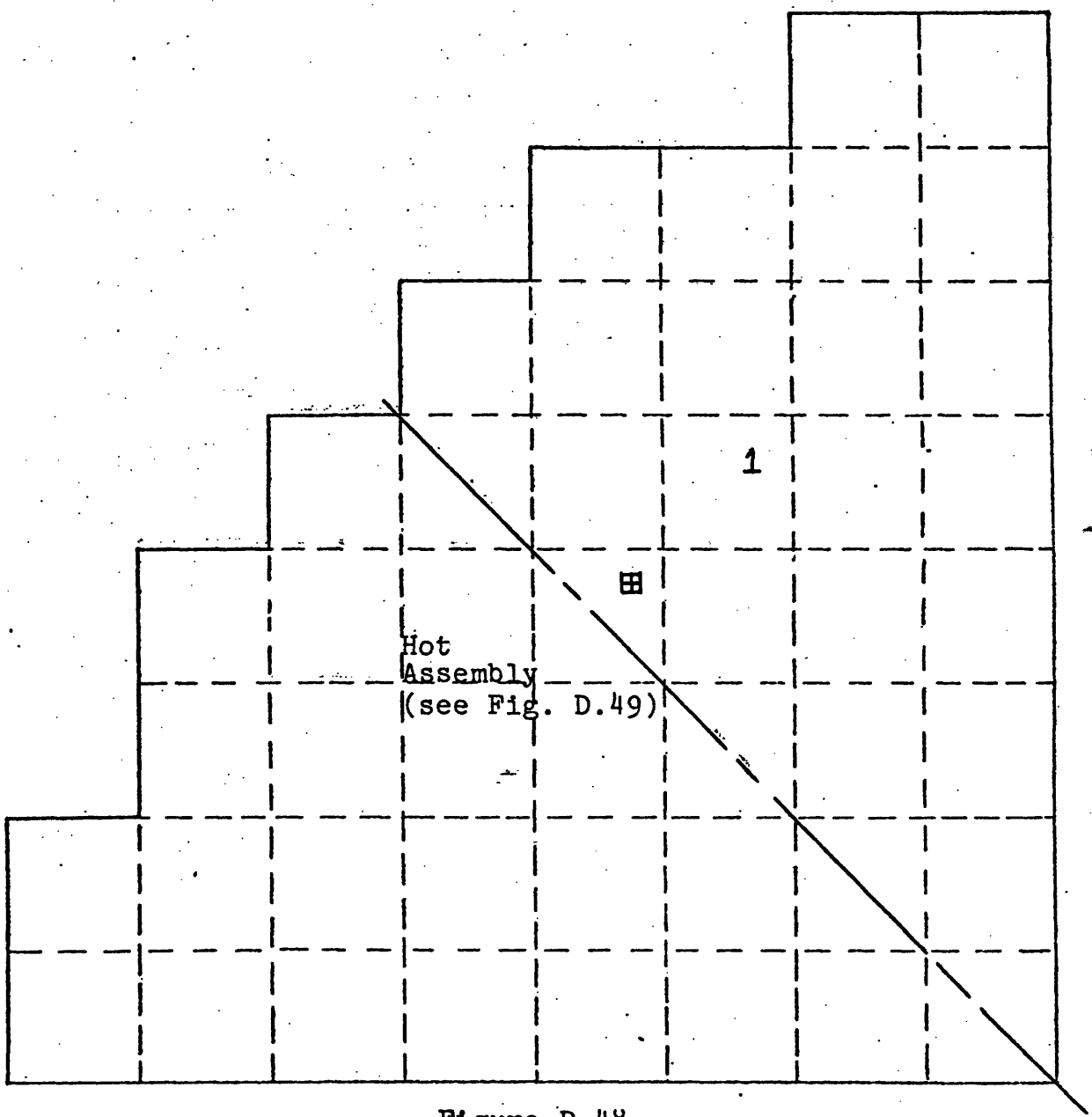

Figure D.48

Pattern of Channels Used to Represent the Core (Case No. 35)

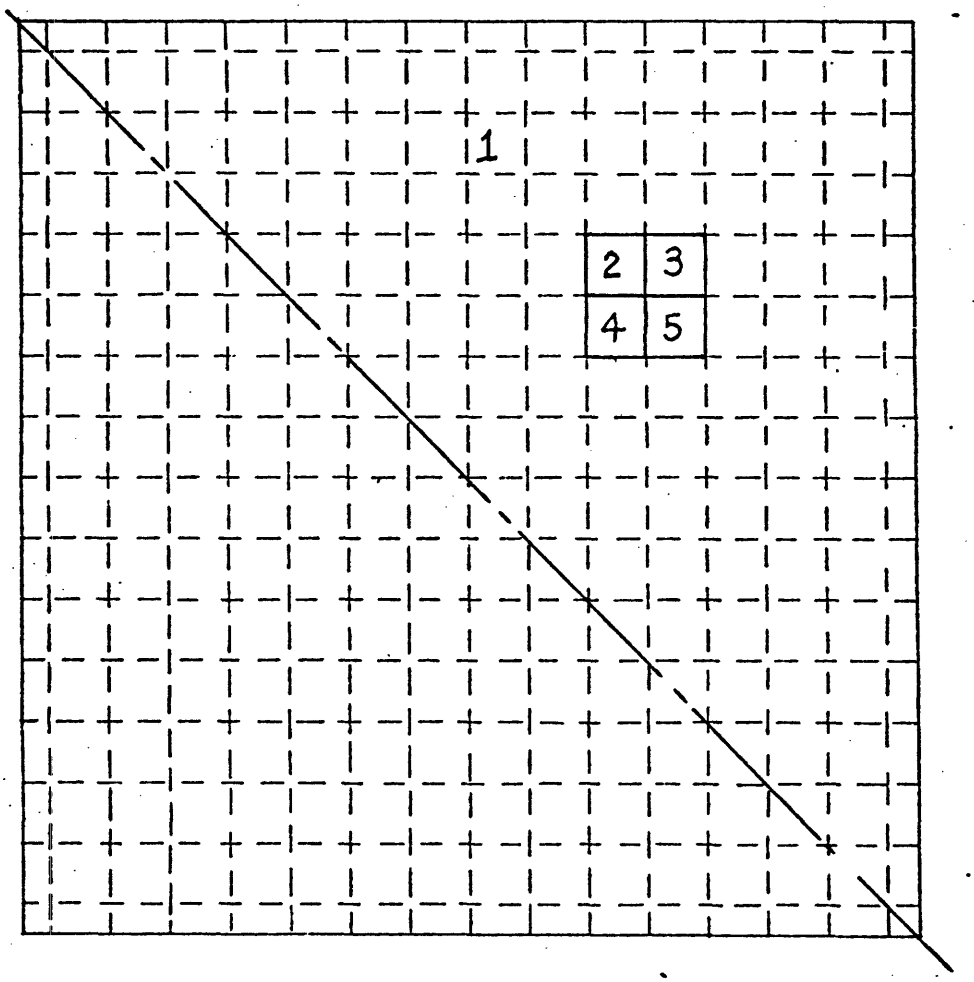

Figure D.49
Detail of the Hot Assembly (Case No. 35)

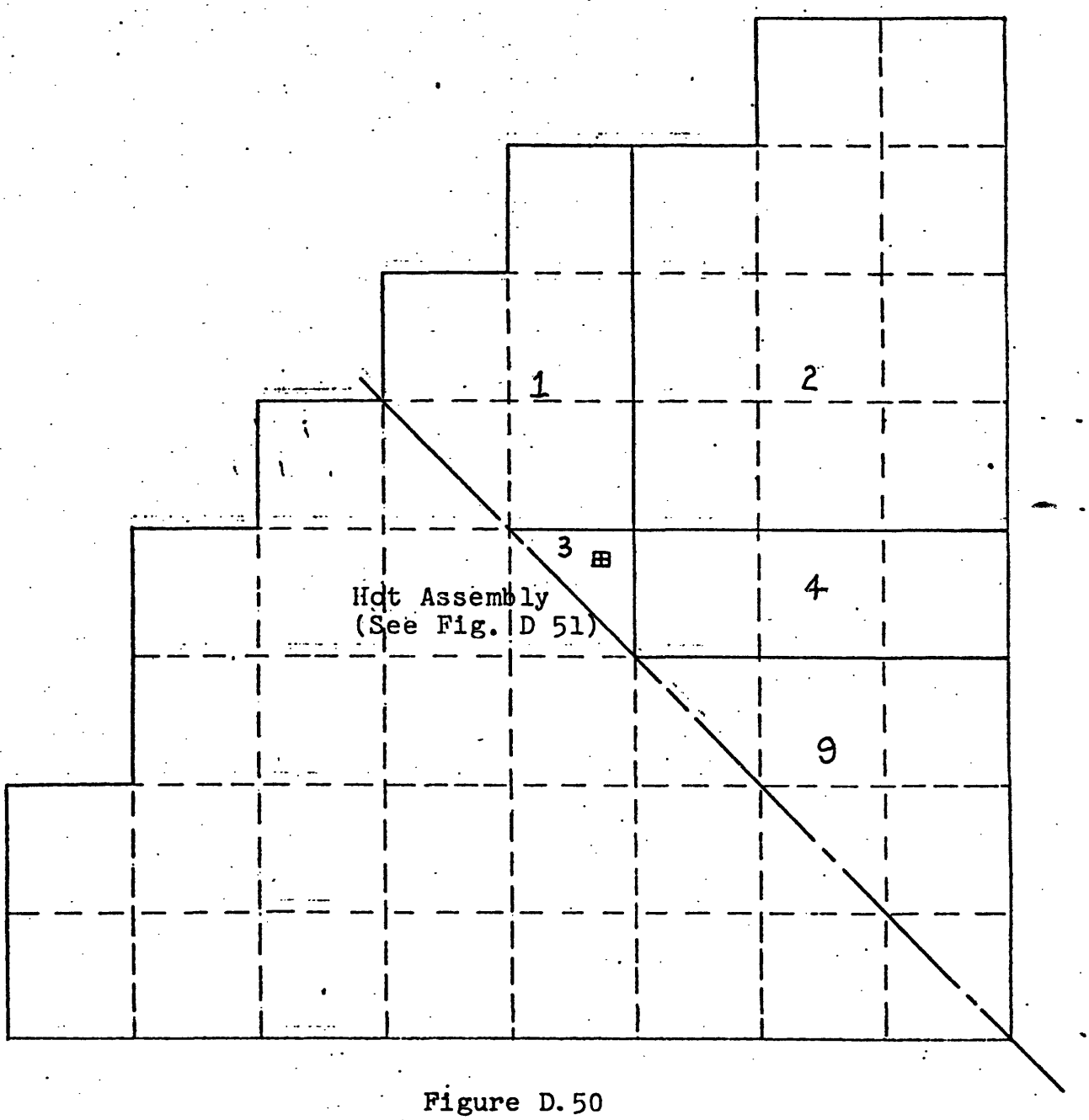

Figure D.50

Pattern of Channels Used to Represent the Core (Case No. 36)

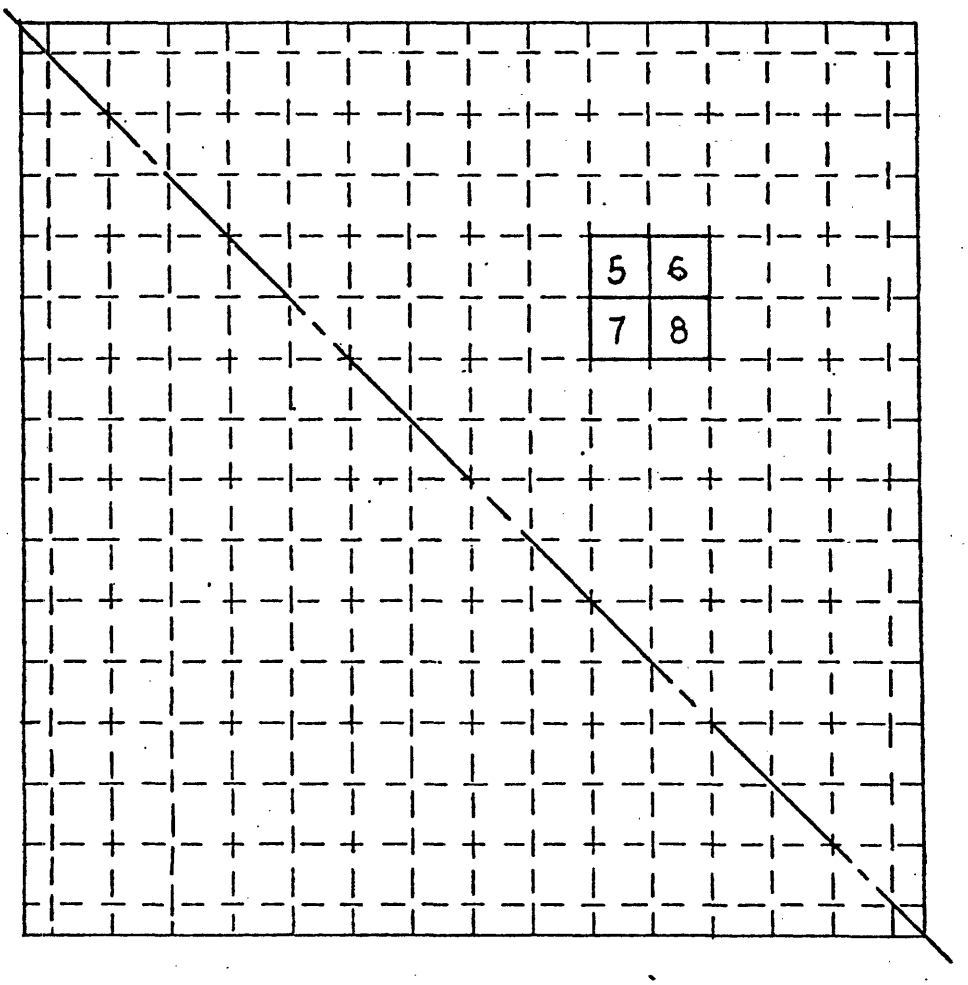

Figure D. 51

Detail of the Hot Assembly (Case No. 36)

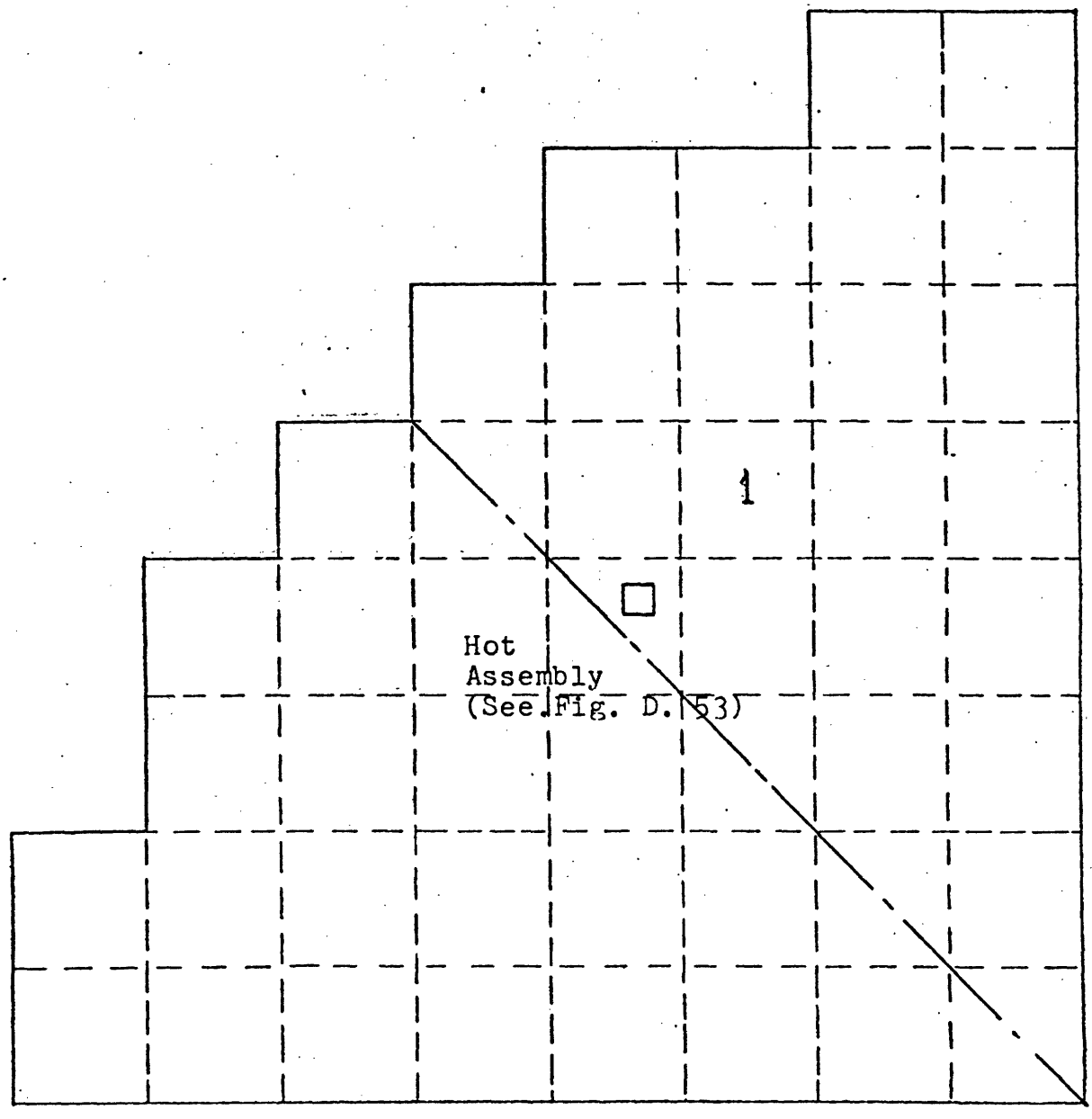

Figure D. 52

Pattern of Channels Used to Represent the Core (Case No. 37)

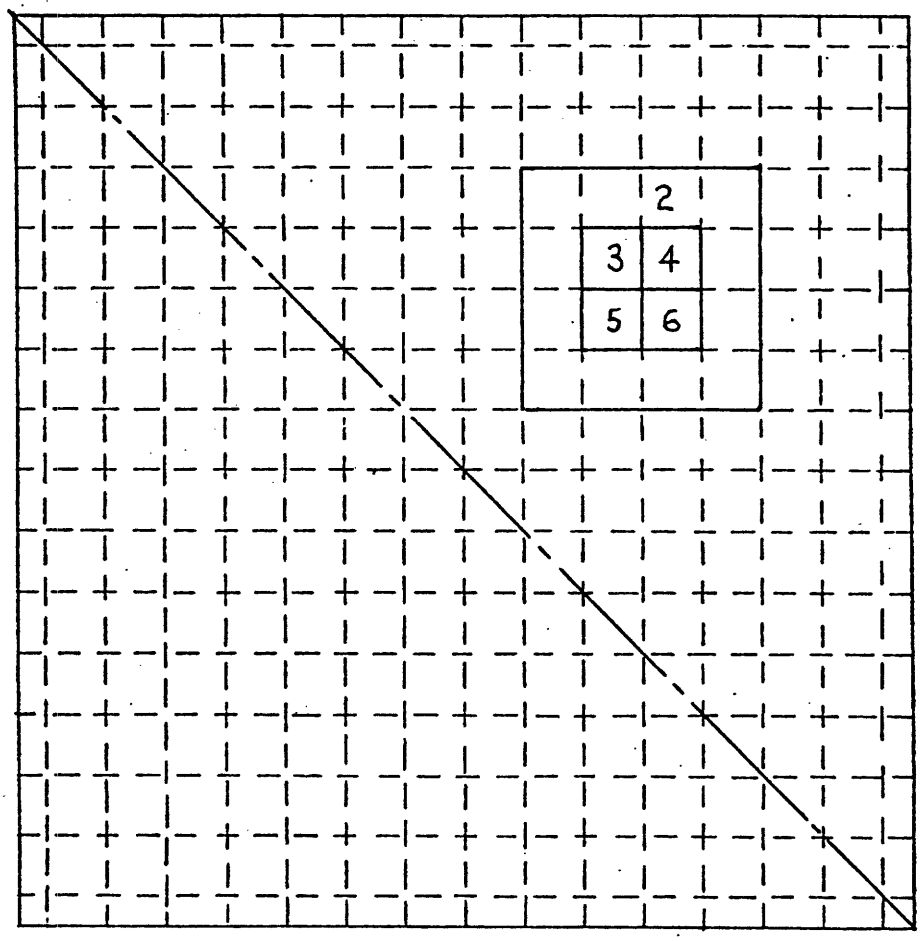

Figure D. 53

Detail of the Hot Assembly (Case No. 37)

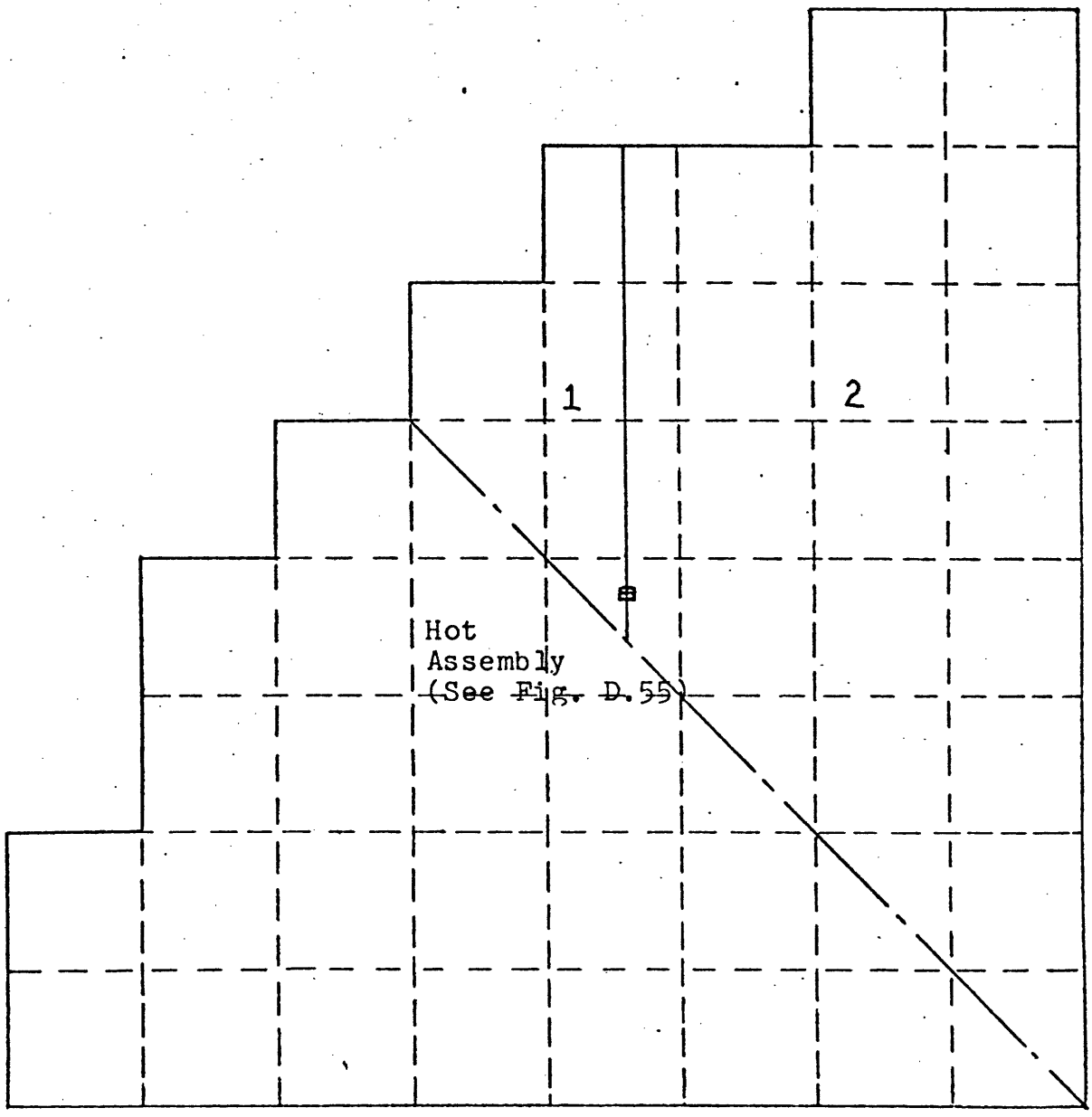

Figure D.54

Pattern of Channels Used to Represent the Core (Case No. 38)

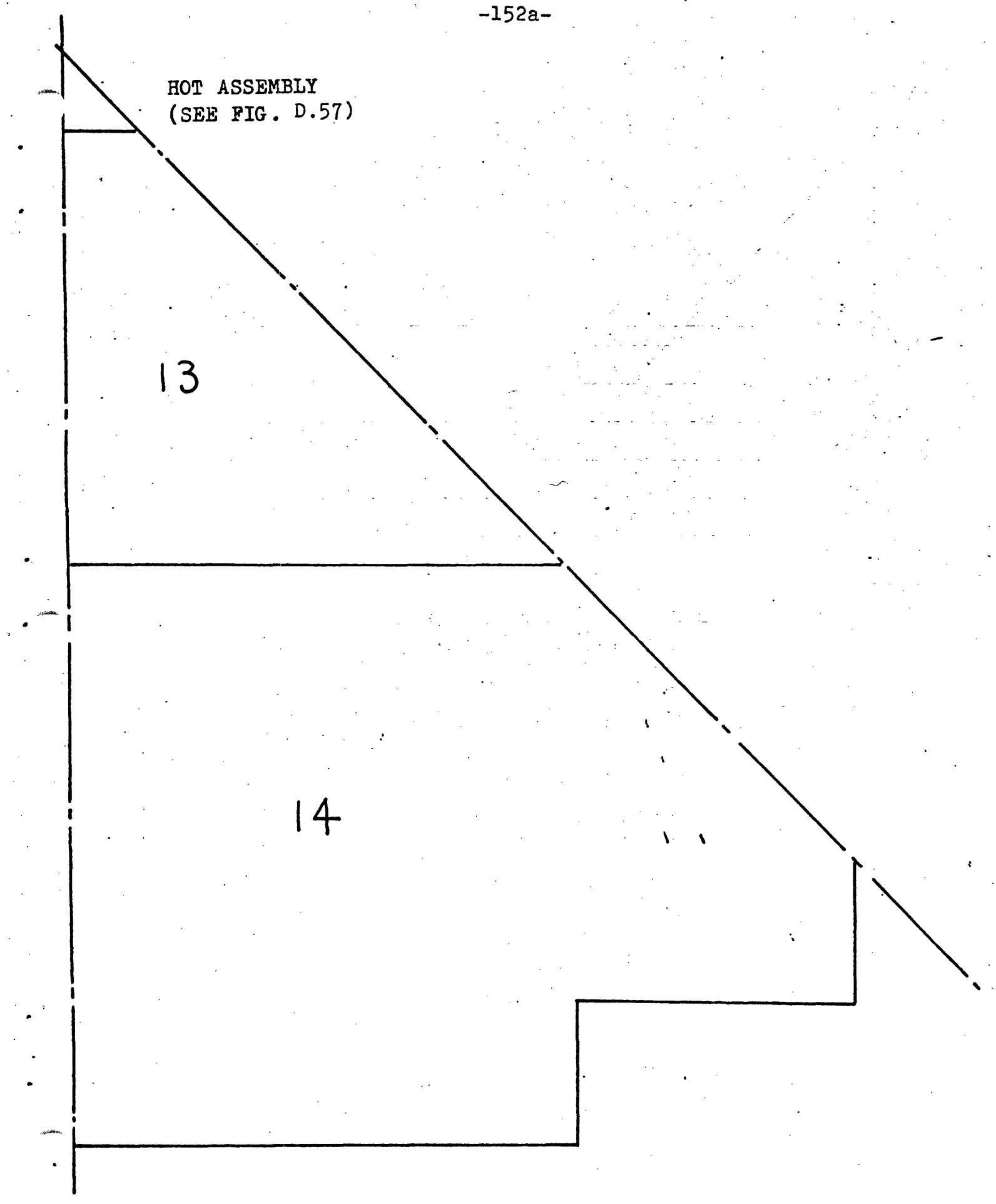

Figure D.56 1/8 Core Channel Mapping Scheme (Case No. 39)

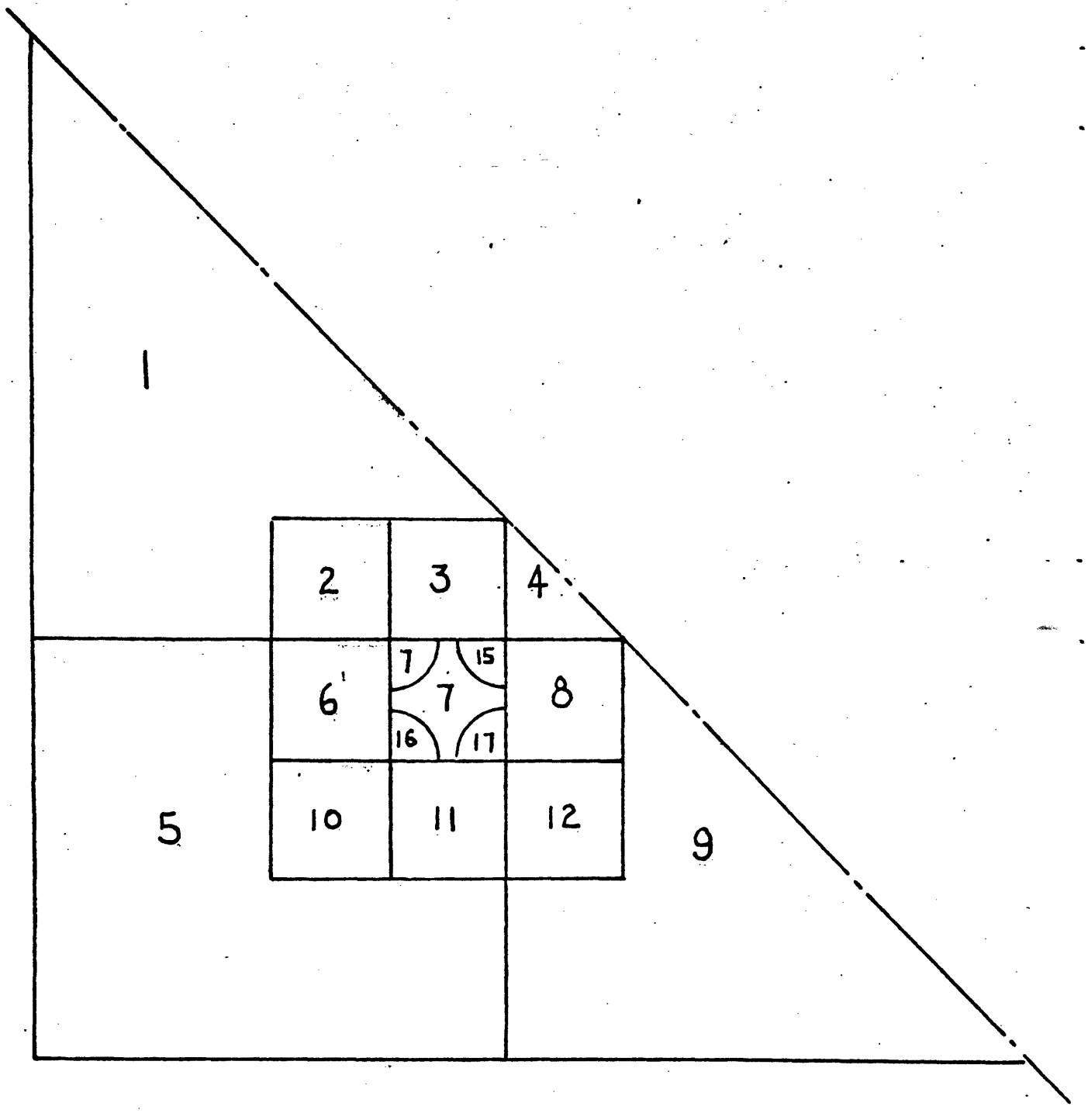

Figure D.57 Hot Assembly Channel Mapping Scheme (Case No. 39)

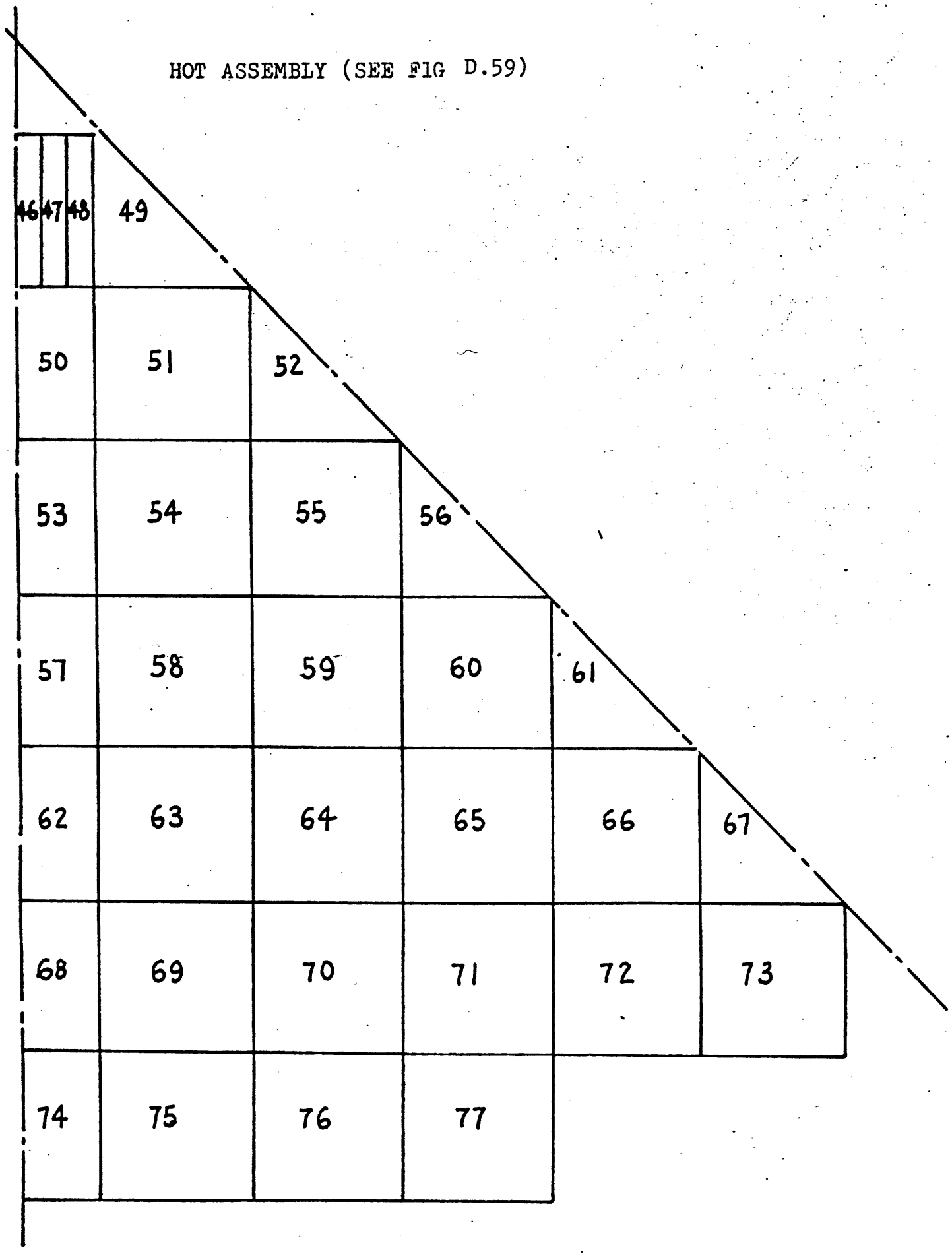

Figure D.58 1/8 Core Channel Mapping Scheme (Case No. 40)

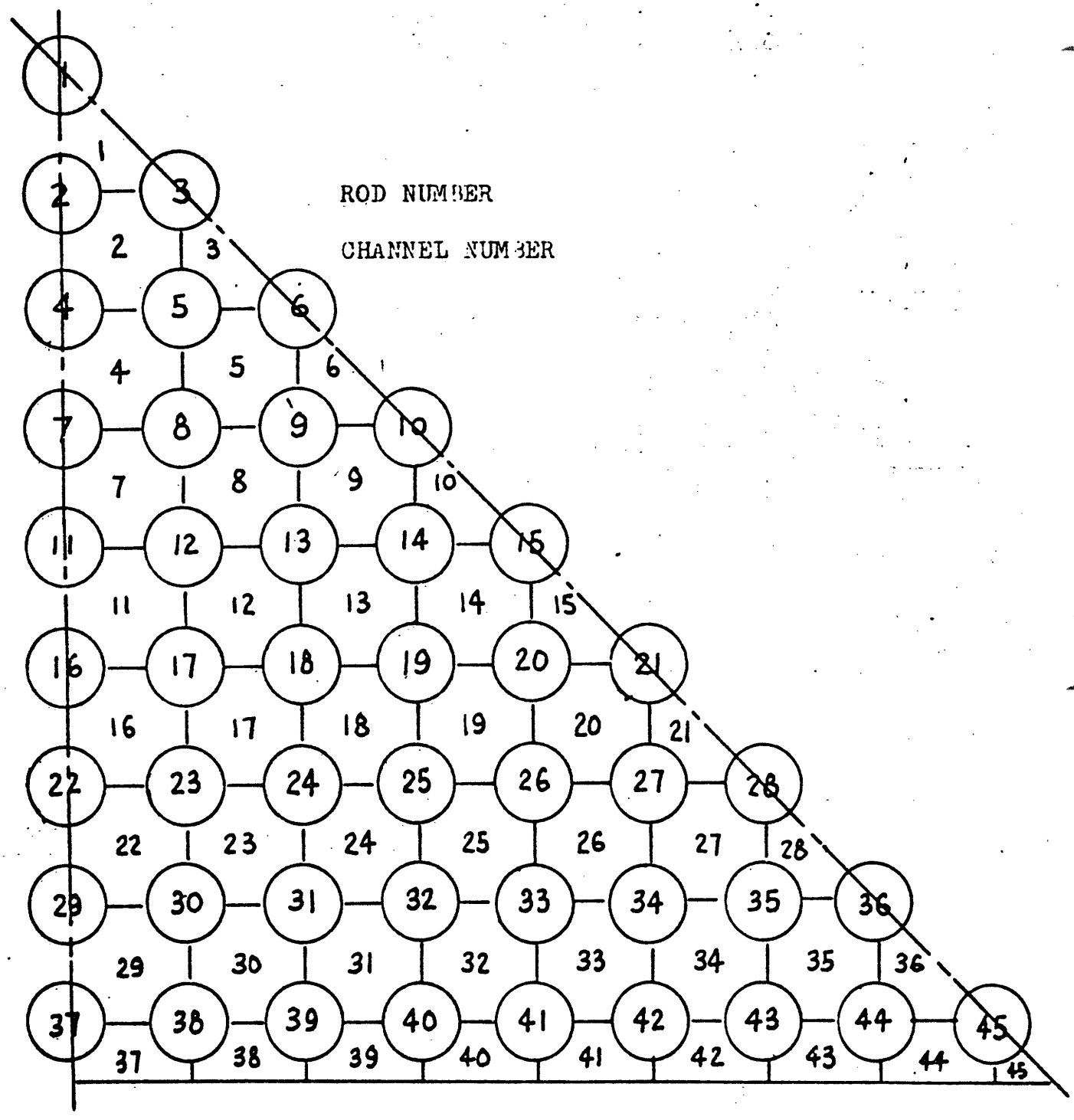

Figure D.59 1/8 Hot Assembly Channel and Rod Mapping Scheme (Case No. 40)

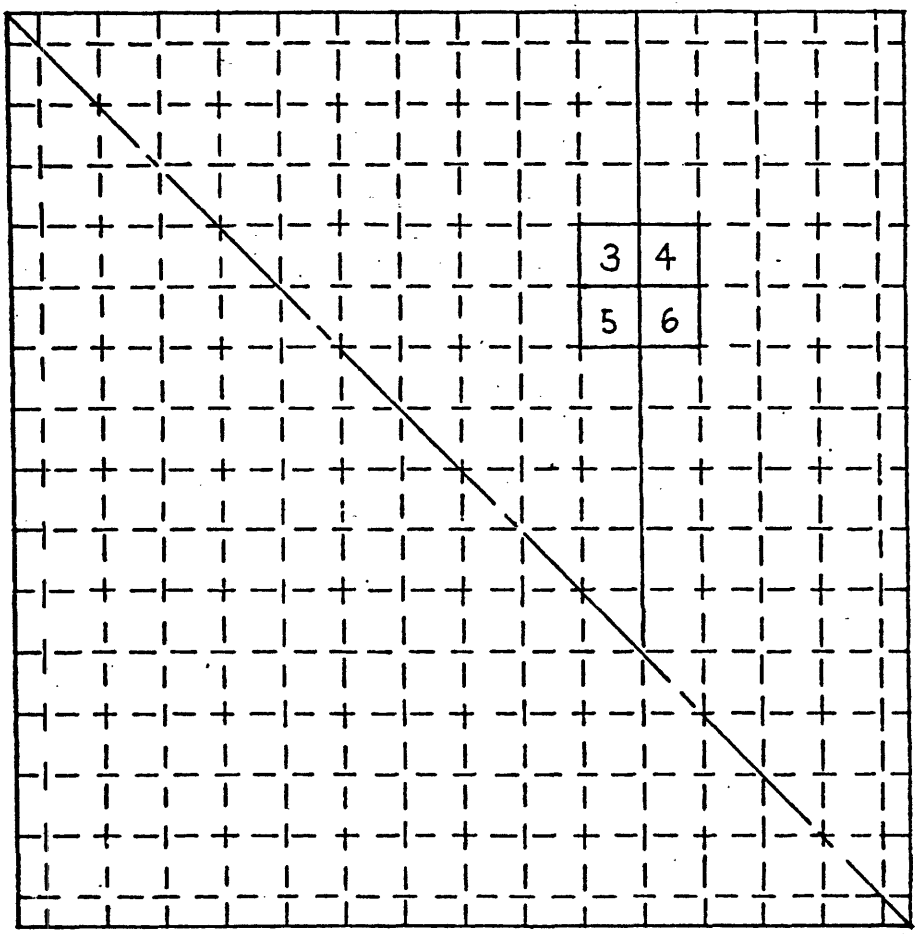

Figure D.55

Detail of the Hot Assembly (Case No. 38)

APPENDIX E

PREDICTION OF ENTHALPY RISE IN THE HOT ZONE FOR MULTIREGION AND HOMOGENIZED REPRESENTATIONS

Define the difference between the enthalpy rises in the hot zone for the multi-subchannel and homogenized representations as the enthalpy rise deviation. The purpose of the factor $N_H(z)$ is to reduce this deviation to zero. In this appendix we derive relations for this deviation in the absence of application of this correction factor, i.e., taking $N_H = 1$, for the ENTHALPY UPSET CASE, ENTHALPY AND FLOW CASE, POWER UPSET CASE and the POWER AND FLOW UPSET CASE.

The defining equation for the enthalpy deviation is

$$\text{Enthalpy deviation for hot zone} \equiv \left.\frac{h_{EXIT}(\text{homogenized}) - h_{EXIT}(\text{multi-subchannel})}{h_{EXIT}(\text{multi-subchannel}) - h_{INLET}}\right|_{\text{hot zone}} \qquad \text{(E.1.a)}$$

Now

$$h_{EXIT}(\text{multi-subchannel}) \equiv \sum^{\text{no. of hot side subchannels}} h_i \Big/ \text{no. of hot side subchannels} \equiv \bar{h}$$

$$h_{EXIT}(\text{homogenized}) \equiv H$$

$$\Delta H \equiv H - h_{IN}$$

$$\Delta \bar{h} \equiv \bar{h} - h_{IN}$$

Hence equation (E.1.a) becomes

$$\text{Enthalpy deviation for hot zone} = \frac{\Delta H - \Delta \dot{h}}{\Delta h} \qquad \text{(E.1.b)}$$

In the evaluation of equation (E.1.b) in terms of bundle parameters that follows, we assume that the amount of enthalpy interchange between channels due to turbulent mixing is much more than that due to diversion crossflow. Therefore

$$\Delta \dot{h} = \Delta \dot{h}_{q'} - \Delta \dot{h}_{T.I} \qquad \text{(E.2.a)}$$

$$\text{and} \quad \Delta H = \Delta H_{Q'} - \Delta H_{T.I} \qquad \text{(E.2.b)}$$

where the minus sign is introduced for the hot zone and

$$\Delta H_{T.I.} = \int_{\text{INLET}}^{\text{EXIT}} Q'_{T.I} dz \qquad \text{(E.3)}$$

Since per Appendix A for either side L or R

$$Q' = \sum_i q'_i \qquad \text{(E.4.a)}$$

and

$$M = \sum_{i} m_i \qquad \text{(E.4.b)}$$

then

$$\Delta H_{Q'} = \Delta h_{q'} \qquad \text{(E.4.c)}$$

From (E.2.a), (E.2.b) and (E.4.c), the following equation can be derived:

$$\Delta H - \Delta h = \Delta h_{T.I.} - \Delta H_{T.I.} \qquad \text{(E.5)}$$

Hence we can rewrite equation (E.1.b) as

$$\text{Enthalpy deviation for hot zone} = \frac{\Delta h_{T.I.} - \Delta H_{T.I.}}{\Delta h_{q'} - \Delta h_{T.I.}} \qquad \text{(E.6)}$$

Now from equations (A.1.6a and A.1.7a) for an axial step

$$\sum_{i=A}^{C} (\delta h_i m_i)_{T.I} = -(h_C - h_D) w'_{CD} \Delta X$$

and

$$(\delta H_L M_L)_{T.I} = -\frac{H_L - H_R}{N_H^{(x)}} W'_{L,R} \Delta X$$

Since N_H is established so that the LHS of both equations are equal,

$$N_H(x) = \frac{(H_L-H_R)\Delta X}{(h_C-h_D)\Delta X} \left[\frac{W'_{L,R}}{W'_{C,D}}\right] \tag{E.7}$$

Now since

$$\delta H_{T.I} \equiv (H_L-H_R) \left[W'_{L,R}/M_L\right] \tag{E.8a}$$

$$\delta h_{T.I} \equiv (h_C-h_D) \left[W'_{C,D}/\Sigma_i m_i\right] \tag{E.8b}$$

$$M_L = \Sigma_i m_i \tag{E.4b}$$

then

$$N_H(x) = \frac{\delta H_{T.I}}{\delta h_{T.I}} \tag{E.9a}$$

or when summed over the axial length of the fuel pin

$$\bar{N}_H = \frac{\Delta H_{T.I}}{\Delta h_{T.I}} \tag{E.9b}$$

Also per equation (E.4b)

$$\Delta\dot{h}_{q'} = \Delta H_{Q'} \qquad \text{(E.4b)}$$

Insertion of equations (E.9b) and (E.4b) into (E.6) yields:

$$\text{Enthalpy deviation for hot zone} = \frac{\frac{1}{\overline{N}_H} - 1}{\frac{\Delta H_{Q'}}{\Delta H_{T.I}} - \frac{1}{\overline{N}_H}} \qquad \text{(E.11)}$$

Now to evaluate equation (E.11) we express the ratio $\frac{\Delta H_{Q'}}{\Delta H_{T.I}}$ in terms as follows.

First we introduce power, flow and enthalpy ratio definitions

$$\text{Power Ratio} \equiv P_R \equiv \frac{Q_{HOT}}{Q_{COLD}} \qquad \text{(E.12a)}$$

$$\text{Flow Ratio} \equiv F_R \equiv \frac{G_{HOT}}{G_{COLD}} \qquad \text{(E.12b)}$$

$$\text{Inlet Enthalpy Ratio} \equiv H_R = \frac{H_{HOT}(z=0)}{H_{COLD}(z=0)} \qquad \text{(E.12c)}$$

and we recall the definition of β

$$w' \equiv \beta s \frac{G_i + G_j}{2} \qquad \text{(E.13)}$$

then

$$\frac{\Delta H_{Q'}}{\Delta H_{T.I}} = \frac{[H' q'_{hot} L] / N' G_{hot} A_s}{\int_{Inlet}^{Exit} \frac{[H_{hot}(z) - H_{cold}(z)]\, \beta S\, \bar{G}\, dz}{N' A_s\, G_{hot}}}$$

$$= \frac{[N' q'_{hot}]/(\bar{G}\, \beta\, S)}{\left[\frac{q'_{hot} N' L}{N' G_{hot} A_s} - \frac{q'_{cold} N' L}{N' G_{cold} A_s} - H_{cold}(0) + H_{hot}(0)\right]}$$

$$= \frac{[N' q'_{hot}]\; N' A_s/(\bar{G}\beta S)}{\left[\frac{q'_{hot} N' L}{G_{hot}} - \frac{q'_{cold} N' L}{G_{cold}}\right] + \left[\frac{H_{hot}(0)}{\frac{1}{N' A_s}} - \frac{H_{cold}(0)}{\frac{1}{N' A_s}}\right]}$$

$$= \frac{[N' P_r]\; N' A_s/(\bar{G}\beta S)}{\left[\frac{P_R N' L}{G_{hot}} - \frac{N' L}{G_{cold}}\right] + \left[\frac{H_{hot}(0)}{\frac{q'_{cold}}{N' A_s}} - \frac{H_{cold}(0)}{\frac{q'_{cold}}{N' A_s}}\right]}$$

$$= \frac{[N' P_R]\, N' A_s/(\beta S)}{\left[\frac{P_R N' L\bar{G}}{G_{hot}} - \frac{N' L\bar{G}}{G_{cold}}\right] + \left[\frac{H_{hot}(0)}{\frac{q'_{cold}}{N' A_s}} - \frac{H_{cold}(0)}{\frac{q'_{cold}}{N' A_s}}\right]}$$

$$= \frac{[N' P_R]\, N' A_s/(\beta S)}{\left[\frac{P_R N' L\bar{G}}{G_{hot}} - \frac{N' L\bar{G}}{G_{cold}}\right] + \left[H_{hot}(0) - H_{cold}(0)\right]\frac{GN' A_s}{q'_{cold}}}$$

$$= \frac{[N' P_R]\, N' A_s/(\beta S)}{\frac{1}{2}\left[P_R\ N'\ (1+\frac{1}{F_R}) - N'\ (1+\frac{1}{F_R})\right] L + \left[\frac{H_{hot}(0)}{\bar{H}_{in}} - \frac{H_{cold}(0)}{\bar{H}_{in}}\right]\frac{\overline{HG} N' A_s}{q'_{cold}}}$$

$$= \frac{[N' P_R]\, \bar{q}'\, N' A_s/(\beta S)}{\bar{q}'\, \frac{1}{2}\left[P_R\ N'\ (1+\frac{1}{F_R}) - N'\ (1+F_R)\right] L + \left[\frac{2}{1+\frac{1}{\bar{H}_R}} - \frac{2}{1+H_R}\right]\frac{\overline{HG} N' A_s \bar{q}'}{q'_{cold}}}$$

$$= \frac{P_R\ \bar{q}'\, N' A_s/(\beta S)}{-\frac{1}{2} L \bar{q}'\left[P_R(1+\frac{1}{F_R}) - (1+F_R)\right] + \left[\frac{H_R - 1}{1-H_R}\right]\overline{HG}\ A_s\ (1+P_R)}$$

(E.14)

For ENTHALPY UPSET CASE, since $F_R = 1$, $P_R = 1$ and $q' = 0$, equation (E.14) can be reduced to:

$$\frac{\Delta H_{Q'}}{\Delta H_{T.I}} = \frac{q'}{\left[\frac{H_R - 1}{H_R + 1}\right] \overline{HG}\ \beta S} = 0 \qquad (E.15)$$

then equation (E.11) for this case becomes:

$$\frac{\frac{1}{\overline{N_H}} - 1}{\frac{1}{\overline{N_H}}} = -\overline{N_H} \qquad (E.16)$$

For ENTHALPY and FLOW UPSET CASE, since $q' = 0$, equation (E.14) can be reduced to:

$$\frac{\Delta H_{Q'}}{\Delta H_{T.I}} = 0 \qquad (E.17)$$

then equation (E.11) for this case becomes:

$$\frac{\frac{1}{\overline{N_H}} - 1}{\frac{1}{\overline{N_H}}} = (1 - \overline{N_H}) \qquad (E.18)$$

For POWER UPSET CASE, since $H_R = 1$, $F_R = 1$, equation (E.14) can be reduced to:

$$\frac{\Delta H_{Q'}}{\Delta H_{T.I}} = \frac{P_R N' A_s}{(P_R-1)L\beta S} \qquad (E.19)$$

then equation (E.11) for this case becomes:

$$\frac{(1 - \frac{1}{N_H})}{\frac{P_R N' A_s}{(P_R-1)L\beta S} - \frac{1}{N_H}} \qquad (E.20)$$

For FLOW and POWER UPSET CASE since $H_R = 1$, equation (E.14) can be reduced to:

$$\frac{\Delta H_{Q'}}{\Delta H_{T.I}} = \frac{N' A_s}{\frac{1}{2}\beta S L \left[P_R(1+\frac{1}{F_R}) - (1+F_R)\right]} \qquad (E.21)$$

then the equation (E.11) for this case becomes:

$$\frac{\frac{1}{\overline{N_H}} - 1}{\frac{P_R N' A_s}{\frac{1}{2} \beta S L \left[P_R(i + \frac{1}{F_R}) - (1+F_R)\right]} - \frac{1}{\overline{N_H}}} \qquad \text{(E.22)}$$

From equations (E.18) and (E.20) we know that the difference of enthalpy for the hot channel at the exit between the homogenized case with $N_H = 1$ and multi-subchannel case for the power upset case and the power and flow upset case is a strong function of β, H_R, F_R, P_R, N' and $\overline{N}_H$.

APPENDIX F

DERIVATION OF N_H, N_U AND N_{TP} FOR LINEAR GRADIENTS OF ENTHALPY, VELOCITY AND PRESSURE

From Equations (A.1.1.6), (A.2.1.6a) and (A.3.1.6) we define N_H, N_U, N_{TP} in the following way:

$$N_H = \frac{H_L - H_R}{h_C - h_D}$$

$$N_U = \frac{U_L - U_R}{U_C - U_D}$$

$$N_{TP} = \frac{P_L - P_R}{P_A - P_E}$$

If we assume the transverse enthalpy profile through channels is linear with slope S_h, N_H becomes:

$$N_H = \frac{\left(\frac{H_L+H_R}{2} + S_h \cdot \frac{N'}{2} \cdot S_{ij}\right) - \left(\frac{H_L+H_R}{2} - S_h \cdot \frac{N'}{2} \cdot S_{ij}\right)}{\left(\frac{H_L+H_R}{2} + S_h \cdot \frac{S_{ij}}{4}\right) - \left(\frac{H_L+H_R}{2} - S_h \cdot \frac{S_{ij}}{4}\right)}$$

$$= \frac{\frac{N'}{2} + \frac{N'}{2}}{\frac{1}{4} + \frac{1}{4}} = 2N' = N \qquad \text{for N odd} \qquad \text{(F.1)}$$

$$N_H = \frac{\left(\frac{H_L+H_R}{2} + S_n \cdot \frac{N'}{2} \cdot S_{ij}\right) - \left(\frac{H_L+H_R}{2} - S_h \cdot \frac{N'}{2} \cdot S_{ij}\right)}{\left(\frac{H_L+H_R}{2} + S_h \cdot \frac{S_{ij}}{2}\right) - \left(\frac{H_L+H_R}{2} - S_h \cdot \frac{S_{ij}}{2}\right)}$$

$$= \frac{\frac{N'}{2} + \frac{N'}{2}}{\frac{1}{2} + \frac{1}{2}} = N' \qquad \text{for N even} \qquad \text{(F.2)}$$

For the same reason for N_U, N_{TP}, we obtain:

$$N_U = \frac{\left(\frac{U_L+U_R}{2} + S_u \cdot \frac{N'}{2} \cdot S_{ij}\right) - \left(\frac{U_L+U_R}{2} - S_u \cdot \frac{N'}{2} \cdot S_{ij}\right)}{\left(\frac{H_L+H_R}{2} + S_u \cdot \frac{S_{ij}}{4}\right) - \left(\frac{H_L+H_R}{2} - S_u \cdot \frac{S_{ij}}{4}\right)}$$

$$= 2N' = N \qquad \text{for N odd} \qquad \text{(F.3)}$$

$$N_U = \frac{\left(\frac{U_L+U_R}{2} + S_u \cdot \frac{N'}{2} \cdot S_{ij}\right) - \left(\frac{U_L+U_R}{2} - S_u \cdot \frac{N'}{2} \cdot S_{ij}\right)}{\left(\frac{H_L+H_R}{2} + S_u \cdot \frac{S_{ij}}{2}\right) - \left(\frac{H_L+H_R}{2} - S_u \cdot \frac{S_{ij}}{2}\right)} = N'$$

$$\text{for N even} \qquad \text{(F.4)}$$

$$N_{TP} = \frac{\left(\frac{P_L+P_R}{2} + S_p \cdot \frac{N'}{2} \cdot S_{ij}\right) - \left(\frac{P_L+P_R}{2} - S_p \cdot \frac{N'}{2} \cdot S_{ij}\right)}{\left(\frac{P_L+P_R}{2} + S_p \cdot S_{ij} \cdot (N'-\frac{1}{2})\right) - \left(\frac{P_L+P_R}{2} - S_p \cdot S_{ij} \cdot (N'-\frac{1}{2})\right)}$$

$$= \frac{\frac{N'}{2} + \frac{N'}{2}}{N'+N'-1} = \frac{N'}{2N'-1} \qquad \text{for N odd or even} \qquad \text{(F.5)}$$

where S_h, S_p and S_u = transverse slopes of enthalpy, pressure and velocity.

from the bottom of the channel to the location of MDNBR needs to be considered.

G.1.1 Changes of Enthalpy

The energy equation neglecting the conduction term for the hot subchannel was written in Equation 1 as:

$$h_{HC}(J) = h_{HC}(J-1) + \frac{q'_{HC}(J-\frac{1}{2})}{m_{HC}(J-1)} \cdot \Delta x - \sum_{i=1}^{4} \frac{(h_{HC}(J-1)-h_i(J-1))w'_{HC,i}(J-1)\cdot\Delta x}{m_{HC}(J-1)}$$

$$- \sum_{i=1}^{4} \frac{(h_{HC}(J-1)-h^*(J-1))w_{HC,i}(J-1)\cdot\Delta x}{m_{HC}(J-1)} \qquad (G-1)$$

Let $$A = \frac{q'_{HC}(J-\frac{1}{2})}{m_{HC}(J-1)}$$

$$B = \sum_{i=1}^{4} \frac{(h_{HC}(J-1)-h_i(J-1))w'_{HC,i}(J-1)\cdot\Delta x}{m_{HC}(J-1)}$$

$$C = \sum_{i=1}^{4} \frac{(h_{HC}(J-1)-h^*(J-1))w_{HC,i}(J-1)\cdot\Delta x}{m_{HC}(J-1)}$$

For the hot channel from Table G.1, the value of each term (A,B,C,), the ratios B/A and C/A in percent at different locations and the overall summation value from bottom to the location of MDNBR are listed in Table G.2. Table G.2 also lists the total values (summation from inlet to exit) for reference. The amount of enthalpy change due to the linear power in the hot subchannel is around 174 BTU/lbm, the turbulent interchange and cross flow terms are 16.2% and 2.8% of the linear power term. Therefore the net enthalpy change due to turbulent interchange and cross flow of the hot subchannel (Channel A) is around 33 BTU/lbm (174 BTU/lbm (16.2% + 2.8%)).

Using the same information (Table G.1 and Fig. G.1), for a colder subchannel (say channel 56 with a radial power factor of 2.060) calculation of the net enthalpy change due to turbulent interchange and cross flow can be performed in the following three steps:(Referring to Fig. G.1): First, from Table G.1, the turbulent interchange term (B) and cross flow term (C) at different locations between the hot subchannel (Channel 57, was designated as Channel A in Fig. G.1) and the surrounding adjacent subchannels (Channels 49, 56, 58, 63 were designated as Channels B in Fig. G.1) have been calculated and listed in Table G.3. Also, from Table G.1 for Channel 56, the total enthalpy change from inlet to the location of MDNBR is 136.72 BTU/lbm (685.52 - 548.8). Second, the enthalpy increase from inlet to location of MDNBR due to heat flux term ($A = \frac{q'_{56}(J-\frac{1}{2})}{m_{56}(J-1)}$) is calculated to be 157.94 BTU/lbm. Third, from Table G.3 (which was obtained in the first step), the enthalpy across from Channel 57 to 56 due to turbulent interchange and cross flow is 1.2 (.7978 + .4028). Based on the values obtained from above calculations, the enthalpy leaving from Channel 56 is 22.42 BTU/lbm (157.94 + 1.2 - 136.72). Therefore the net enthalpy change due to turbulent interchange and crossflow is -21.22 BTU/lbm (-22.42 + 1.2).

G.1.2 Changes of Mass Flow Rate

From Table G.1 the difference of mass flow rate between inlet and the location of MDNBR for each subchannel was calculated. The percentage changes in each of the four subchannels were listed in

Table G.4. The hot subchannel (Channel 57) has a larger mass flow rate decrease than the other subchannels, but the difference is small.

G.2 The Effect of Enthalpy Versus Linear Power on MDNBR

Two radial power factors (2.060, 2.266 having been marked as Curves A and B respectively in Fig. 2.3) and a sequence of difference inlet enthalpies have been used in the adiabatic subchannel analysis. According to Case No. 13, a base case has been consistently set up. Due to the adiabatic boundary, the variation of enthalpy at the location of MDNBR is the same as at inlet. As shown in Fig. 2.3, for a constant radial power factor the MDNBR changes slightly with the enthalpy variation at the location of MDNBR in a linear mode. The value of MDNBR is larger if the radial power factor is smaller. Curve B is always above Curve A and these two curves are parallel to each other. For the base case, the difference of MDNBR between Curve B and Curve A is .252. Referring to Fig. G.1, the hot subchannel with a radial power factor of 2.266 and with a radial power factor of 2.060 were designated as Channel A and B respectively. So Channel A will vary along Curve A, Channel B will vary along Curve B. The enthalpy of hot subchannel and adjacent subchannel will decrease due to the turbulent interchange and cross flow. The amount of changes have been obtained in Section G.1.1 and are repeated here: the net enthalpy change due to turbulent interchange and cross flow of Channel A and B is -33.0 BTU/lbm and -21.22 BTU/lbm respectively.

When enthalpy changes due to turbulent interchange and cross flow are considered between the two channels, the difference of MDNBR between Channel A and Channel B can be obtained along Curve A and Curve B as indicated by the dash line in Figure 1. The difference was marked as the margin with a value of 0.11. From this positive margin value, a conclusion can be drawn: even when enthalpy changes due to trubulent interchange and cross flow are considered between the two channels with maximum power factors, the channel with higher radial power factor still has the lower value of MDNBR. So the channel with the highest radial power factor is the crucial channel which needs more consideration.

G.3 The Effect of Mass Flow Rate Versus Linear Power on MDNBR

The same base case, the same two radial power factors have been used as in Section G.2, but the mass flow rate has been considered as the variable instead of the enthalpy. The results were plotted on Figure 2.4. The value of MDNBR is larger if the radial power factor is smaller. Also the value of MDNBR decreases with the decreasing of mass flow rate. Due to the effect of cross flow, the mass flow rate is different at each location. From the results in Section G.1.2 (Table G.4) the amount of change in mass flow rate of Channel A and B (Figure G.1) are -18.0% and -17.2% respectively. The difference of MDNBR between Channel A and B after the reduced mass flow rate effect can be found along Curves A and B as indicated by dash lines in Figure 2.4. The

difference was marked as the margin with a value of 0.29. Again from the positive margin value a conclusion can be stated that with the reduced mass flow rate considered, the channel with higher radial power factor still possesses the lower value of MDNBR.

G.4 The Effect of Cold Wall on MDNBR

In case both the hottest rod (highest power) and coldest rod (zero power) exist in the same channel, the predicted MDNBR might occur on the hottest rod even though the channel is not the hottest one. This is due to the cold wall effect of the coldest rod (zero power rod). The predicted CHF (by W-3 correlation) should be evaluated using the heated equivalent diameter (1.202 in.) versus the wetted equivalent diameter (1.435 in.) and should be multiplied by a factor F:

$$F = (1.36 + 0.12e^{9x})\ (1.2-1.6e^{-1.9D_h})\ (1.33-0.237e^{5.66x})$$

where D_h = heated equivalent diameter

X = local quality

For example, if the local quality is zero, the predicted CHF due to Cold Wall effect considering both the use of D_H and F will decrease around 5%. Referring to Figure G.2, G.3, and G.4, if the hot rod (with a power factor 2.266) is in cold channel (with a power factor 2.060), along with a zero power rod due to the cold wall effect curve A (Figure G.3, G.4) will shift to Curve C. This net shift to lower MDNBR is because the cold

channel effect on MDNBR dominates the opposing effect of decrease of channel power.

Therefore, if rod power peaking factors are available, the procedure to identify the worst location (place of lowest MDNBR) is: first, to identify the highest rod power factor, as the hottest rod, second, to check the existence of any cold rod (zero power rod) in the neighborhood of the hottest rod. The predicted MDNBR might occur on the hottest rod with cold wall effect even if the channel is not hot. Figures G.3 and G.4 can quantitatively demonstrate this point. Curves A in both figures is the MDNBR of a hot rod in hot channel. Curve C in both figures is the MDNBR of a hot rod with cold wall effect but in cold channel.

A positive initial margin of 0.045 in both figure G.3 and G.4 can be seen for the base case. It means that the MDNBR of curve C is smaller than curve A at the base initial situation. But due to the cross flow and the energy interchange from the channel inlet till the location of MDNBR, both the mass flow rate and enthalpy in each channel will change. From the calculation in Section G.2, and Section G.3 the percentage change of enthalpy and mass flow rate for each channel can be used which were indicated on both figures by the dash lines as the enthalpy and mass flow rate shift. Even after those shift the margin is still positive which can be seen on figure G.3 and G.4 as the margin of 0.019 and 0.035 respectively.

Therefore the MDNBR of the hot rod with cold wall effect is still less than the hot rod without cold wall effect even with the shift of mass flow rate and enthalpy in the channel. This result does depend on the numerical values of rod peaking factors. The values in any particular situation should be compared to those used in this appendix to permit determination of the applicability of the result of this appendix to a new case.

Therefore the predicted MDNBR would rather occur on the hottest rod which is in the cold channel side than in the hot channel side.

G.5 Relative Effect of Rod Power and Channel Power on MDNBR

This section presents the comparison of MDNBR between cases of hot rod in cold channel and cold rod in hot channel, say hot rod with power peaking factor "A" located in cold channel with peaking factor "D" (channel power is obtained from the averaged power of the fuel rods comprising the channel) and cold rod with power peaking factor "B" located in hot channel with peaking facotr "C". So, the following relations are always true: $A-B > 0$; $C-D > 0$. The relative effect of rod power and channel power on MDNBR is the only purpose of this section. Therefore, cross flow and turbulent interchange which are only magnitude effect were not included in the analysis.

The location of MDNBR which is either on the hot rod or on the cold rod depends on the following four numerical values:

(1) A-B: differences between rod powers

(2) C-D: differences between channel powers

(3) A: power of hot rod

(4) C: power of hot channel

These values are different from core to core, therefore, case by case analysis has to be performed to decide the location of MDNBR.

Datum generated from a series of single channel thermal hydraulic computer runs have been used to plot the curves in Fig. G.5. The location of MDNBR for this example case can be determined from this figure. For example, suppose that the power factors were assigned as: A = 1.8, B = 1.4, C = 2.2, D = 1.4 (the same definition of A, B, C, D as mentioned at the beginning of this section). From the plot (as shown by the dashed line), the location of MDNBR is on the cold rod which is located in the hot channel (DNBR = 1.544) not on the hot rod which is located in the cold channel (DNBR = 1.818). The outcome depends solely on the numerical value of these power factors.

Even though the individual value of the power factors plays a decisive role in determining the location of MDNBR, still from Fig. G.5 a qualitative conclusion can be made as follows:

(1) The probability that the hot rod is the location of MDNBR will decrease first in case of C-D increases but "A" and "B" are kept constant; second in case of A increases but A-B, "C" and "D" are kept constant.

(2) The same probability as (1) will increase instead of decrease first in case of A-B increases but "C" and "D" are kept constant; second in case of "C" increase but C-D, "A" and "B" are kept constant.

G.6 Conclusion

The location of predicted MDNBR can be identified by the numerical values of rod power peaking factors and channel power peaking factors. The hot channel is the limiting case for DNBR evaluation when the rod power peaking factors are not available. If the rod power peaking factors are available, and the hot rod is located in the hot channel, the hot rod is the limiting case for DNBR evaluation. Also if a zero power rod is present, region which faces the zero power rod is the location of MDNBR. Since the numerical values of the rod power peaking factors are different from core to core, a simple single channel quantitative analysis like Fig. G.5 might be necessary to confirm the location of MDNBR.

ocations	Enthalpy (BTU/LB)					Mass Flux (MLB/HR-FT^2)				
	Channels					Channels				
istance (in)	49	56	57	58	63	49	56	57	58	63
	h(49)	h(56)	h(57)	h(58)	h(63)	G(49)	G(56)	G(57)	G(58)	G(63)
0.0	548.80	548.80	548.80	548.80	548.80	2.2170	2.2170	2.2170	2.2170	2.2170
6.0	549.87	550.20	550.34	549.88	549.87	2.2163	2.2158	2.2156	2.2163	2.2163
12.1	552.58	553.63	554.03	552.64	552.61	2.2144	2.2125	2.2118	2.2143	2.2143
18.1	556.91	558.94	559.62	557.10	557.04	2.2117	2.2081	2.2069	2.2114	2.2115
24.1	562.82	565.98	566.93	563.20	563.10	2.2084	2.2036	2.2022	2.2078	2.2079
30.2	570.18	574.56	575.74	570.78	570.67	2.2038	2.1971	2.1954	2.2029	2.2030
36.2	578.86	584.47	585.83	579.69	579.58	2.1974	2.1890	2.1872	2.1963	2.1963
42.2	588.74	595.42	596.74	589.85	589.80	2.1913	2.1817	2.1802	2.1900	2.1898
48.3	599.53	607.29	608.54	600.85	600.84	2.1783	2.1650	2.1647	2.1769	2.1744
54.3	611.07	619.79	620.85	612.55	612.65	2.1755	1.9969	1.9828	2.1805	2.1709
60.3	623.21	633.96	634.85	625.53	624.71	2.1635	1.9867	1.9529	2.1698	2.1639
66.4	635.92	647.46	647.64	637.41	637.96	2.0590	1.9763	1.9451	2.0583	2.0565
72.4	649.01	660.06	659.73	649.79	651.55	2.0643	1.9353	1.9146	2.0686	2.0565
78.4	661.23	672.69	672.54	661.52	663.20	2.0351	1.8857	1.8692	2.0407	2.0209
84.5*	673.19	685.52	685.06	673.88	675.37	1.9893	1.8360	1.8193	1.9875	1.9716
90.5	683.74	696.61	696.15	684.59	685.97	1.9565	1.8241	1.8141	1.9511	1.9396
96.5	693.27	705.50	704.34	693.97	695.94	1.9358	1.8289	1.8293	1.9296	1.9161
02.6	701.54	711.94	709.88	701.99	703.82	1.9205	1.8454	1.8610	1.9206	1.8963
08.6	707.81	717.13	714.83	708.15	709.74	1.9160	1.8443	1.8583	1.9173	1.8959
14.6	712.53	721.60	717.96	712.83	713.89	1.9057	1.8591	1.8999	1.9116	1.8851
20.7	715.57	723.26	718.97	714.98	716.17	1.8785	1.8675	1.9297	1.8977	1.8658
26.7	716.66	722.76	718.72	715.51	717.10	1.8732	1.8375	1.8755	1.8862	1.8674

Table G.1. Output Data for Example Case

*Location of MDNBR

Locations	Mass Flow Rate (lb/sec) Channels					Cross Flow Between Adjacent Channels W (i,j) (lb/sec ft) Boundaries			
DISTANCE (IN.)	49 M(49)	56 M(56)	57 M(57)	58 M(58)	63 M(63)	1 W(49,57)	2 W(56,57)	3 W(57,58)	4 W(57,63)
0.0	0,7292	0.7292	0.7292	0.7292	0.7292	0.0	0.0	0.0	0.0
6.0	0.7289	0.7288	0.7287	0.7289	0.7289	-0.00065	0.00295	0.00357	-0.00037
12.1	0.7283	0.7277	0.7274	0.7283	0.7283	-0.00196	0.01039	0.01216	-0.00118
18.1	0.7274	0.7262	0.7258	0.7273	0.7274	-0.00359	0.01159	0.01394	-0.00277
24.1	0.7263	0.7247	0.7243	0.7261	0.7262	-0.00381	0.00856	0.01095	-0.00311
30.2	0.7248	0.7226	0.7221	0.7245	0.7245	-0.00445	0.00878	0.01182	-0.00304
36.2	0.7227	0.7199	0.7194	0.7223	0.7223	0.03675	0.05449	0.05613	0.04066
42.2	0.7207	0.7176	0.7171	0.7203	0.7202	0.02988	0.05887	0.06068	0.03261
48.3	0.7164	0.7121	0.7120	0.7160	0.7152	0.03839	0.06824	0.07458	0.04202
54.3	0.7155	0.6568	0.6521	0.7171	0.7140	-0.03408	0.17355	0.21970	0.03887
60.3	0.7116	0.6534	0.6423	0.7136	0.7117	0.11778	0.09514	0.10428	0.12847
66.4	0.6772	0.6500	0.6398	0.6770	0.6764	0.16928	0.07271	0.09189	0.15543
72.4	0.6789	0.6365	0.6297	0.6804	0.6764	-0.07311	-0.02925	-0.08924	-0.04217
78.4	0.6694	0.6202	0.6148	0.6712	0.6647	0.05788	0.05715	0.08834	0.05673
84.5*	0.6543	0.6039	0.5984	0.6537	0.6485	-0.01898	0.00904	0.03027	-0.00203
90.5	0.6435	0.6000	0.5967	0.6417	0.6379	-0.03834	-0.03802	-0.03660	-0.03627
96.5	0.6367	0.6015	0.6017	0.6346	0.6302	-0.08824	-0.08207	-0.08941	-0.08999
102.6	0.6316	0.6069	0.6121	0.6317	0.6237	-0.04941	0.01635	0.00940	-0.06365
108.6	0.6302	0.6066	0.6112	0.6306	0.6236	-0.01722	0.11929	0.12416	-0.01933
114.6	0.6268	0.6115	0.6249	0.6287	0.6200	0.01552	0.11835	0.11536	-0.00782
120.7	0.6178	0.6142	0.6347	0.6241	0.6136	-0.00242	0.02454	0.02601	-0.02193
126.7	0.6161	0.6043	0.6168	0.6204	0.6142	-0.08876	-0.05896	-0.08805	-0.01787

Table G.1 Output Data for Example Case
(continued)

Locations	Enthalpy Change Btu/lb			Enthalpy Change In Percentage Form	
	Due To Heat Flux A	Due To Turbulent B	Due To Cross Flow C	$B/_A$ (%)	$C/_A$ (%)
0.0	0	0	0	-	-
6.0	2.693	.1453	.0004049	5.40	.0150
12.1	4.969	.3058	.005314	6.15	.0106
18.1	7.119	.2942	.005483	4.13	.0770
24.1	9.101	1.192	.001391	13.10	.0153
30.2	10.92	1.584	.01794	14.51	.1643
36.2	12.45	1.959	.2308	15.73	1.854
42.2	13.69	2.188	.2221	15.98	1.622
48.3	14.70	2.426	.3045	16.50	2.071
54.3	16.64	2.701	.1418	16.23	0.852
60.3	16.89	3.178	1.139	18.82	6.744
66.4	16.96	3.088	1.626	18.21	9.587
72.4	16.62	2.796	.5868	16.82	3.531
78.4	15.97	3.104	.5283	19.44	3.308
84.5*	15.00	3.184	.01303	21.23	0.0869
90.5	13.22	3.299	.6676	24.95	5.05
96.5	10.96	2.819	1.436	25.72	13.102
102.6	8.441	1.939	.2891	22.97	3.425
108.6	5.914	1.581	-.1448	26.73	-
114.6	3.141	1.042	-.2532	33.17	-
120.7	.5378	.5514	-.03477	-	-
126.7	0.	.2731	.1232	-	-
Total	215.9	42.11	6.92	19.4	3.0
MDNBR	173.7	28.15	4.84	16.2	2.8

Table G.2 Percentage Contribution to the enthalpy change by the different energy transport modes. For the hot subchannel (Channel 57)

*Location of MDNBR

Locations	Turbulent interchange term (B) Btu/lbm				Cross flow term (C) Btu/lbm			
	Boundaries*				Boundaries			
	1	2	3	4	1	2	3	4
0.0	0.	0.	0.	0.	0.	0.	0.	0.
6.0	.04435	.01321	.0434	.04435	0.	.0002849	0.	.00012
12.1	.1369	.03775	.1312	.1340	0.	.002872	0.	.001158
18.1	.2560	.06215	.2380	.2437	0.	.005458	0.	.00495
24.1	.3882	.08965	.3523	.3618	0.	.005643	0.	.008268
30.2	.5225	.1113	.4687	.4791	0.	.007213	0.	.01073
36.2	.6590	.1283	.5804	.5907	.1790	.05179	0.	0.
42.2	.7565	.1245	.6513	.6560	.1676	.05448	0.	0.
48.3	.8525	.1179	.7273	.7280	.2442	.06023	0.	0.
54.3	.9674	.1003	.8221	.8113	0.	.1418	0.	0.
60.3	1.157	.08468	.9280	1.008	1.073	.06627	0.	0.
66.4	1.138	.01711	.9931	.9392	1.559	.01028	0.	0.
72.4	1.051	-.0313	.9755	.8002	0.	0.	.3114	.2754
78.4	1.114	-.01421	1.087	.9169	.5353	-.00701	0.	0.
**84.5	1.172	-.04359	1.103	.9524	0.	.003494	0.	.01653
*** MDNBR	10.21	.7978	9.101	8.665	3.758	.4028	.3114	.3172

Table G.3 Amount of Energy Across the Hot Subchannel (Channel 57) Boundaries by Turbulent Interchange and Cross Flow

* For Boundary number scheme see Fig. G.1

** Location of MBNDR

*** Total from inlet to the location of MDNBR (i.e. from 0. inch to 84.5 inches)

Percentage Change of Mass Flow Rate From Inlet To Location of MDNBR				
CHANNELS				
49	56	57	58	63
-10.3	-17.2	-18.0	-10.4	-11.1

Table G.4 Percentage changes of Mass Flow Rate in the example case. (Minus sign means Mass Flow Rate has been reduced.)

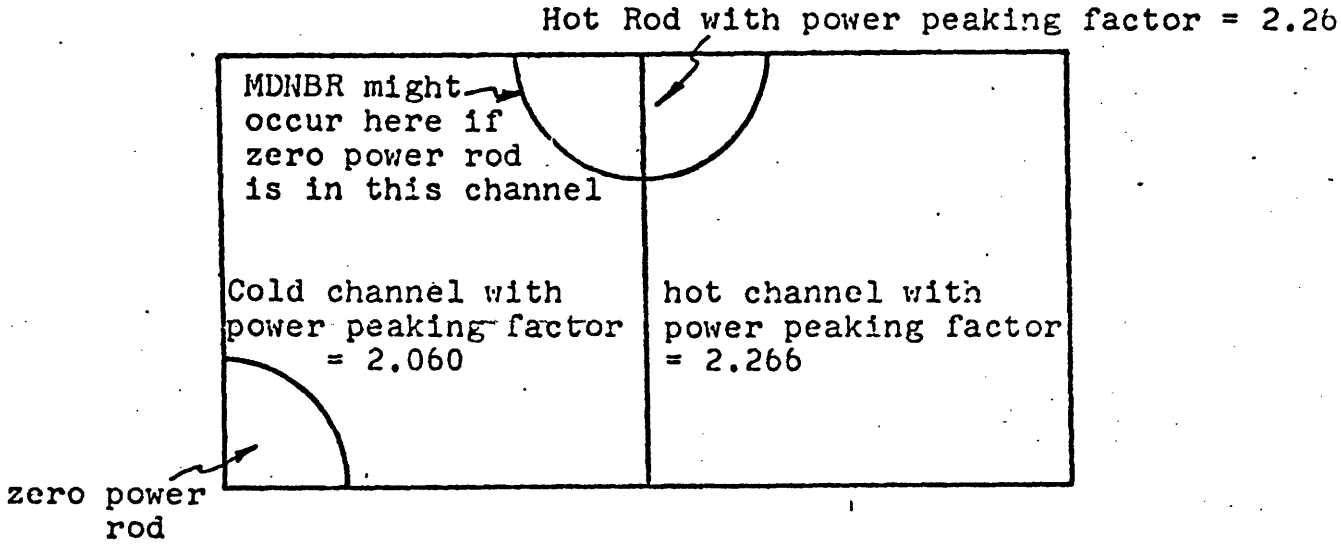

Figure G.2 Example case of the Cold Wall Effect

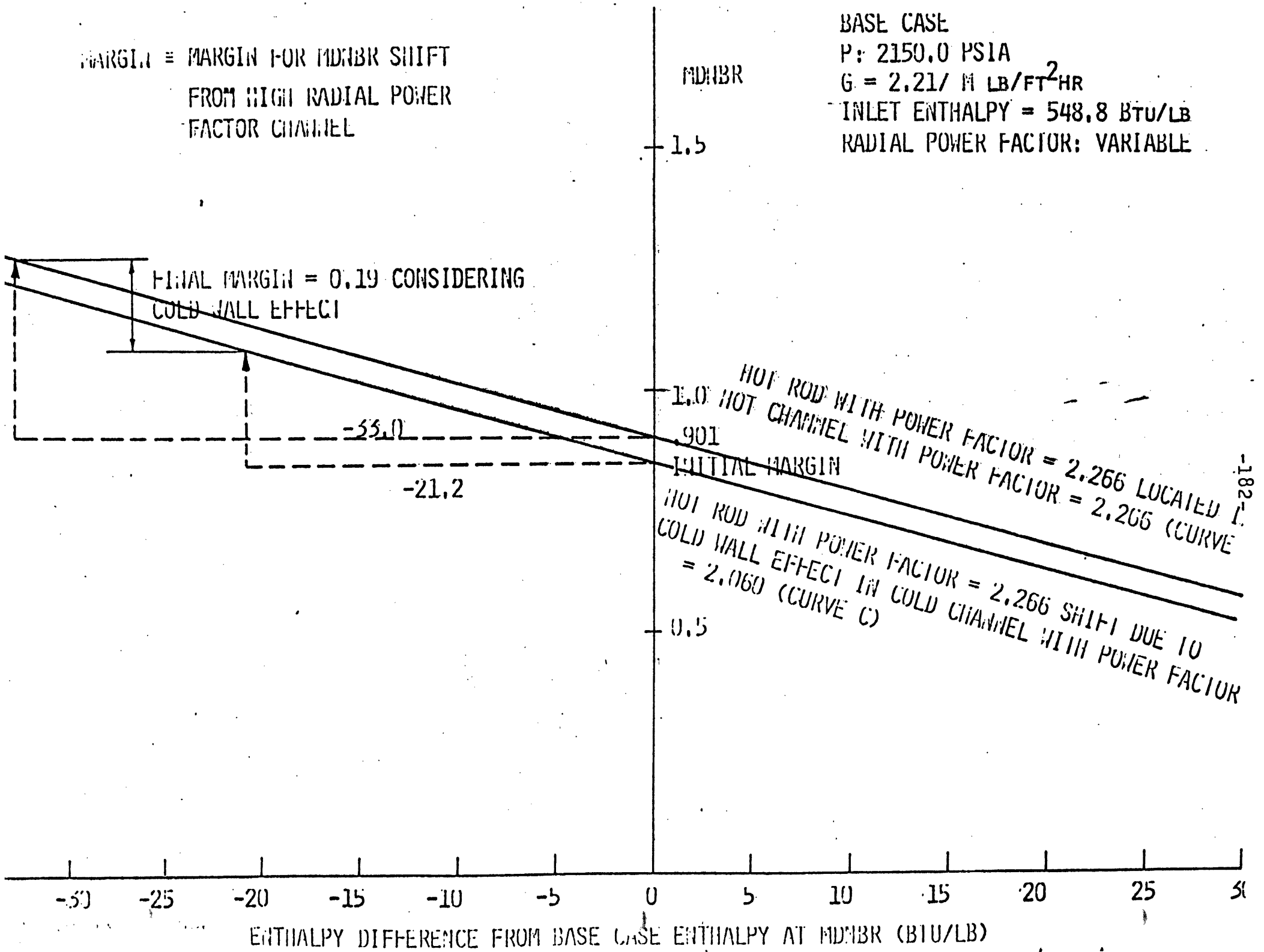
MARGIN = MARGIN FOR MDNBR SHIFT FROM HIGH RADIAL POWER FACTOR CHANNEL
MDNBR
BASE CASE
P: 2150.0 PSIA
G = 2.21/ M LB/FT2HR
INLET ENTHALPY = 548.8 BTU/LB
RADIAL POWER FACTOR: VARIABLE
1.5
FINAL MARGIN = 0.19 CONSIDERING COLD WALL EFFECT
1.0 HOT CHANNEL WITH POWER FACTOR = 2.266 (CURVE
HOT ROD WITH POWER FACTOR = 2.266 LOCATED I
-55.0
.901
INITIAL MARGIN
-21.2
HOT ROD WITH POWER FACTOR = 2.266 SHIFT DUE TO COLD WALL EFFECT IN COLD CHANNEL WITH POWER FACTOR = 2.060 (CURVE C)
0.5
-182-
-30
-25
-20
-15
-10
-5
0
5
10
15
20
25
ENTHALPY DIFFERENCE FROM BASE CASE ENTHALPY AT MDNBR (BTU/LB)

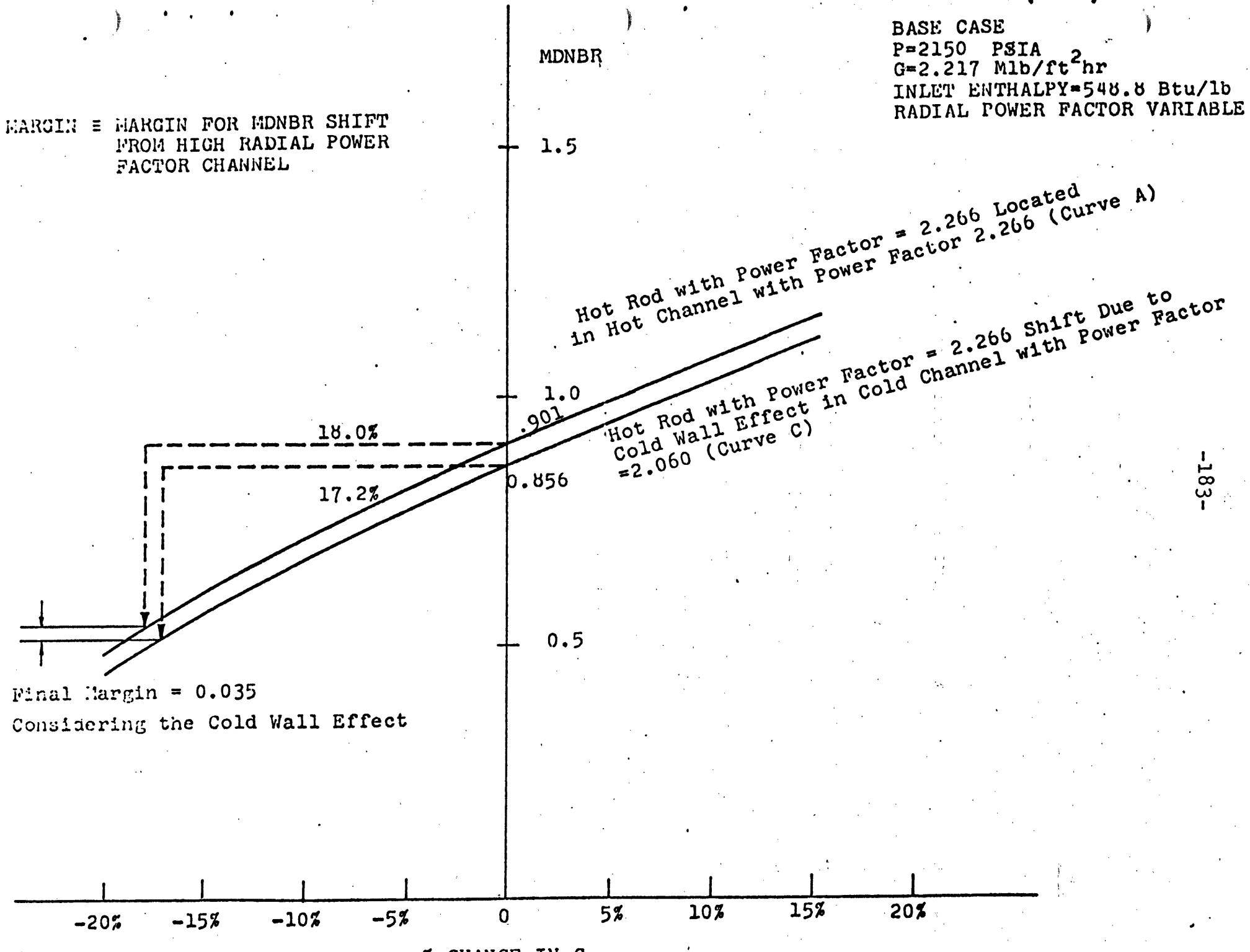

Figure 3.4-1 Margin Versus % Change in Mass Flow Rate for Different Rod

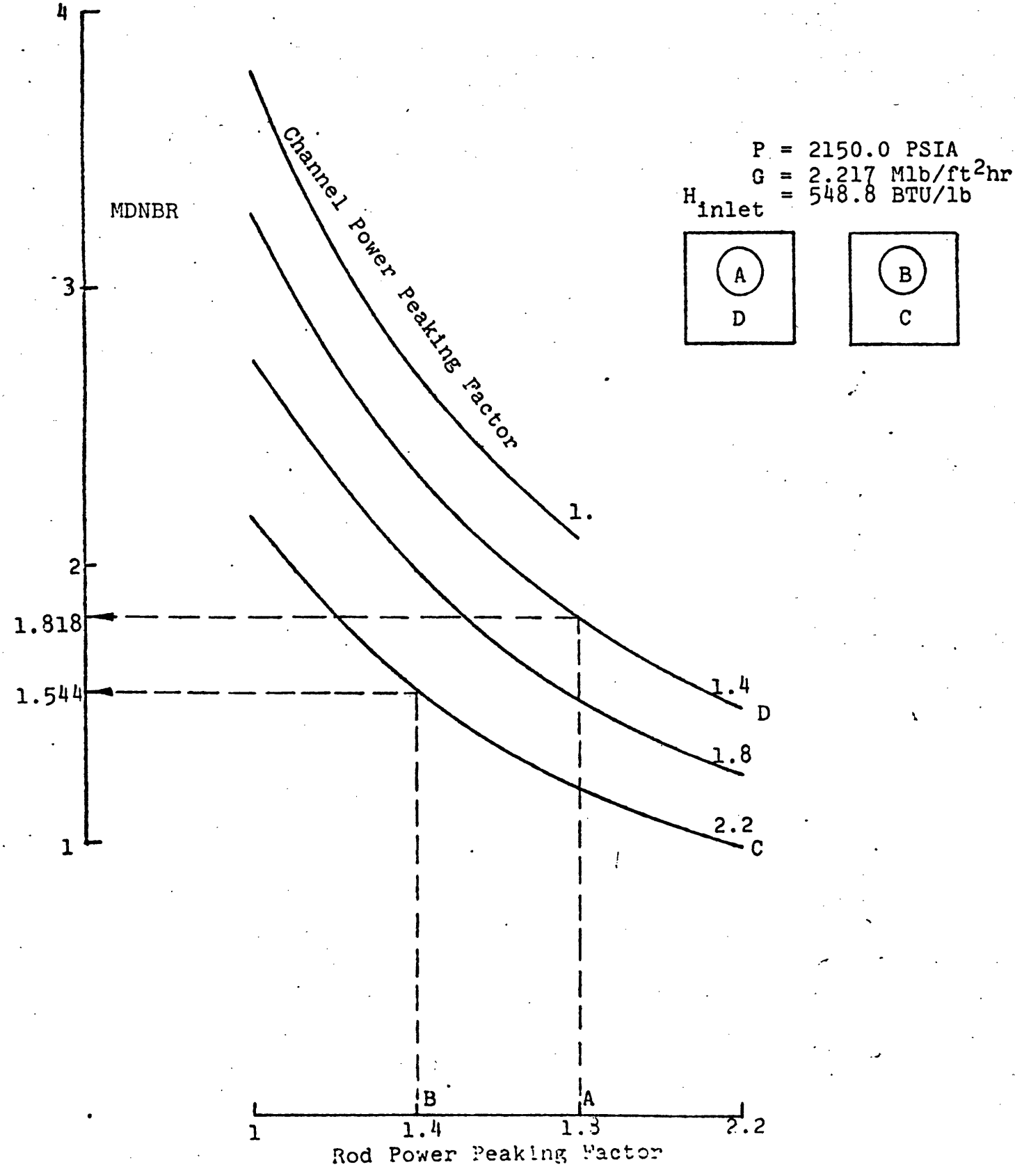

FIGURE G.5 RELATIVE EFFECT OF ROD POWER AND CHANNEL POWER ON MDNBR

Volume II

2-D TRANSPORT COEFFICIENT

AUTHORS: CHONG CHIU
PABLO MORENO
ROBERT BOWRING
NEIL TODREAS

Volume II

TABLE OF CONTENTS

TABLE OF CONTENTS(continued)

TABLE OF CONTENTS(continued)

LIST OF FIGURES

LIST OF FIGURES(continued)

LIST OF TABLES

VOLUME II

LIST OF APPENDICES

NOMENCLATURE

A_i	cross-section area for subchannels i, (L^2)
A_s	cross-section area for any subchannel (L^2)
A_k	cross-section area for homogenized subchannels k (L^2)
$c_{i,j}$	thermal conduction coefficient for subchannels i and j (H/TθL)
$C_{L,R}$	thermal conduction coefficient for homogenized subchannels L and R (H/TθL)
c_i	crossflow friction force for subchannel i (F)
C	crossflow friction force for homogenized subchannels (F)
Δx	axial elevation increment, (L)
$\Delta \bar{h}$	axial change of radially averaged enthalpy in the multi-subchannel representation, (H)
ΔH	axial change of radially averaged enthalpy in the homogenized representation, (H)
F	axial friction force per unit length (F/L)
F_R	Flow ratio
$\bar{F}$	average flow rate
g	gravitational constant, (L/T^2)
g_i	mass flux of channel i
$\bar{G}$	averaged mass flux
h_i	enthalpy for subchannel i, (H)

h^*	effective enthalpy carried by diversion crossflow (H)
$\overline{h}_k$	radially averaged multi-subchannel enthalpy, (H)
H_k	homogenized enthalpy for region k, (H)
H_R	inlet enthalpy ratio
K	crossflow resistance coefficient
L	channel length, (L)
m_i	flow rate for subchannel i (M/T)
M_k	flow rate for homogenized region k, (M/T)
N	Total number of rods
$N_H, N_U, N_{TP}, N_{TF}, N_{TU}$	coupling coefficients
$\overline{N}_H$	averaged coupling coefficient
N'	total number of subchannels equal to N/2 for N even N/2 + 1/2 for N odd
p_i	pressure for subchannel i (F/L^2)
P_k	pressure for homogenized region k (F/L^2)
P_R	power ratio
q'_i	heat addition per unit length, for subchannel i (H/L)
$\overline{q}$	averaged heat addition per unit length (H/L)
Q_k	heat addition per unit length for homogenized region k (H/L)
R_H, R_p	ratio of $\overline{N_H}$ in the FLOW UPSET CASE
S	rod spacing (L)
u^*	effective velocity carried by diversion
$\overline{u}$	effective averaged velocity for adjacent channels

u_i	effective momentum velocity for subchannel i, (L/T)
U_k	effective momentum velocity for homogenized region k, (L/T)
$\bar{U}$	effective averaged velocity for homogenized region L and R
$w_{i,j}$	diversion crossflow between adjacent subchannels (M/TL)
$W_{L,R}$	diversion crossflow between homogenized region L and R (M/TL)
$w'_{i,j}$	turbulent interchange between adjacent subchannels i and j (M/TL)
$W'_{L,R}$	turbulent interchange between adjacent homogenized region L and R (M/TL)
ρ^*	density carried by the diversion crossflow (M/L3)
β	turbulent mixing parameter

Subscripts

i	subchannel identification number
k	homogenized region identification number

Variables

J	axial elevation node along the subchannels

CHAPTER 1

INTRODUCTION

1.1 Background

Thermal hydraulic design studies of Pressurized Water Reactor (PWR) core performance are carried out using lumped parameter computational methods typified by the COBRA[1] and THINC[2] developments. In analyses of these cores the smallest homogenized segment is a subchannel which is characterized by properties of interest such as enthalpy, flow rate and pressure. For typical PWR open lattice core configurations, detailed core analyses are performed in a cascade fashion. In this approach, crossflows between fuel assemblies are first determined by treating each fuel assembly as a homogenized region and these crossflows are subsequently imposed as boundary conditions in the subchannel analysis of the hot assembly. Alternatively, some analyses are performed by representing the core by increasing coarsely homogenized regions around the hot subchannel of interest.

The common requirement of each of these procedures is for transport or coupling coefficients to represent exchange of momentum and energy between the homogenized regions. These coefficients are properly developed

when they produce properties in a homogenized region which are equivalent to those obtained by averaging local distributions of the same properties over the same region. The work of France and Ginsberg[3] and Ramm, Johannsen and Todreas[4] on developing transport coefficients for adjacent subchannels from local property distributions within a subchannel represents the solution to an analogous problem. In our case the smallest region is the subchannel so that our homogenized representation of the individual subchannels comprising an assembly becomes analogous to the earlier France et al. homogenized representation of the subchannel. However, as opposed to this previous work, in the case we now address, crossflows between subchannels exist and must be considered in the analysis.

1.2 General Problem Statement

We desired to represent a PWR assembly comprised of a square array of N by N rods as a single node in a corewide lumped parameter analysis. We seek those transport coefficients which when used in the lumped analysis will yield node enthalpies for all axial stations equivalent to those obtained by averaging the subchannel enthalpies over all subchannels comprising the single node. It is assumed that the axial enthalpy dis-

tribution of every subchannel in the N by N array is known. In our example we obtain this known distribution from analysis of the N by N assembly using arbitrary coefficients for interaction between subchannels. This known axial enthalpy distribution of course is ultimately to be derived from experiment. Interpretation of such experiments to yield coefficients and this known distribution is a topic separate from the task of this work.

1.3 Cases of Interest

Let us identify cases of interest and test the usefulness of our hypothesis in solving these cases.

a) Case 1: The prime case of interest is that of adjacent heated bundles with different linear power ratings and different inlet mass flow rates. Within each bundle the linear power and mass flow rate is taken constant. We identify this case as the POWER/FLOW UPSET CONDITION. This case has been studied for the condition leading to the maximum crossflow which occurs when the higher power and lower inlet flow exist together in the same bundle. Other variables in this case are the power and flow ratios between assemblies. These ratios were both taken as 1.2, the maximum anticipated in practice.

b) Case 2: A degenerate version of Case 1 is that of linear power upset but the same inlet mass flow to each assembly. This case was studied since crossflow is reduced versus Case 1 and is only due to radial enthalpy gradients between assemblies. This case is called the POWER UPSET CONDITION.

The following two non-prototypic reactor cases were also examined. These cases permitted almost complete separation of the enthalpy and crossflow effects. Additionally, they are of interest in themselves since experiments based on these cases may be performed since they are considerably less complex and costly than heated, multipin assembly tests. These cases are:

c) Case 3: Unheated rods with all subchannels in each of the two adjacent assemblies at a uniform inlet enthalpy. Each assembly however, has a different inlet enthalpy. Both assemblies have the same inlet mass flux to each subchannel. This case is called the ENTHALPY UPSET CONDITION.

d) Case 4: Same as Case 3 except the upset condition is in inlet mass flux plus the inlet enthalpy. This case is called the ENTHALPY/FLOW UPSET CONDITION.

For each case of interest, a range of bundle sizes, $N' = f(N)$ and subchannel mixing rates, β, were investi-

gated spanning the range of interest to PWR application. The input parameters K and S/L for the crossflow resistance and the control volume of the crossflow are kept constant as 0.5.

CHAPTER 2

METHODS OF PROBLEM SOLUTION

2.1 Detailed Problem Definition

Figure 1 illustrates a typical N by N assembly of interest (N odd) surrounded by neighboring assemblies. We develop a one dimensional solution by selecting adjacent strips of N' subchannels where for N odd, $N' = \frac{N}{2} + \frac{1}{2}$, the edge subchannel being half the size of the interior subchannels (for N even, $N' = \frac{N}{2}$ and the edge subchannel is equal to the interior subchannel). The selected adjacent strips shown in Figure 2 are assumed to be bounded by adiabatic, impervious boundaries. The homogenized representation of Figure 2 is shown in Figure 3 which has flow area, wetted perimeter, heat flux and mass flow equivalent to that of the strip of N' subchannels. It should be recognized that many equivalent pictorial homogenized representations satisfying these conditions are possible. However, since the following prescribed prediction technique does not utilize the distance between subchannel centroids of Figure 2, any equivalent pictorial representation can be adopted.

We require that at every axial position of the homogenized region, the total flow, the energy content and

the pressure drop from inlet should be the same as those obtainable by averaging the values of the individual subchannels. These conditions are met if the mass, heat and momentum transfer across the boundary between the adjacent strips at every axial position are the same in both cases. In calculating the boundary transport, we use subchannel values of the pressure and enthalpy differences in the multi-subchannel case but the difference in the averaged values in the homogenized representation.

For the homogenized representation calculation, we require a method of calculating the lateral transport in terms of what would have been the local parameter difference while knowing only the average differences.

2.2 Problem Solution by Analysis of the Differential Form of the Conservation Equations

We postulate that this can be accomplished by applying suitable coefficients to the terms in the conservation equations of the homogenized representation. The form of these coefficients which transform average (homogenized representation) parameter differences to local (multi-channel representation) differences are derived in Appendix A (Volume I) from the differential expression of the conservation equations. These forms are

$$N_H \equiv \frac{H_L - H_R}{h_C - h_D}$$

$$N_U \equiv \frac{U_L - U_R}{u_C - u_D}$$

$$N_{TU} \equiv \frac{\dfrac{\partial(\bar{U}W_{L,R})}{\partial x}}{\dfrac{\sum_{i=A}^{E}\left(\partial\ \bar{u}\ w_{i,i+1}\right)}{\partial x}}$$

$$N_{TP} \equiv \frac{P_L - P_R}{P_A - P_F}$$

$$N_{TF} = \frac{C}{\sum_{i=A}^{E} c_i} = \frac{\dfrac{W_{L,R}}{\rho^*_{L,R}}\ W_{L,R}}{\sum_{i=A}^{E} \dfrac{|w_{i,i+1}|\,w_{i,i+1}}{\rho^*_{i,i+1}}}$$

where ρ^* is the density of fluid at the donor channel for the diversion crossflow. (Refer to Figures 2 and 3 for subscripts A, B, C, D, E and F; L and R).

Appendix A (Volume I) further presents detailed formula for these coefficients in terms of parameters available from multi-channel analysis. In the remainder of this volume, we

a) assess the validity of these formula when analyses are made using the difference forms of the conservation equations used in COBRA IIIC,

b) utilize these formula to present recommended values of the coefficients for the 4 cases of Chapter 1 for a selected range of β and N',

c) assess the errors which still remain in homogenized representation results when these coefficients are employed.

2.3 Problem Solution by Analysis of the Difference (i.e. COBRA IIIC) Form of the Conservation Equations

For reactor analysis which is to be done by lumped channel methods, i.e., COBRA IIIC, difference approximations to the differential form of the conservation equations are employed. Appendix B,(Volume I) formulated with the assistance of Pablo Moreno, presents the conservation equations for both the multi-subchannel case and the homogenized representation in difference form. Unfortunately the complexity of these equations precludes the possibility of employing simple but exact coupling coefficients in the transverse momentum equations. However the simple, albeit approximate, forms of coupling coefficients summarized in the previous section, will

yield satisfactory results for most practical reactor conditions. The most limiting assumptions imposed in using these simple forms of coupling coefficients in the difference equations concern the diversion crossflow terms. Therefore, results utilizing these approximate coefficients for analysis of conditions of severe flow and/or power upset conditions can be in significant error.

Specifically from Appendix B these assumptions are:

a) Use of the following expression for h_C^* in the energy equation:

$$h^* = \frac{H_L + H_R}{2} + \frac{H_L - \frac{H_L + H_R}{2}}{N_H} \quad W_{L,R}>0 \qquad (2.3.1)$$

b) Use of the following expression for u_C^* in the axial momentum equation:

$$u^* = \frac{U_L + U_R}{2} + \frac{U_L - \frac{U_L + U_R}{2}}{N_U} \quad W_{L,R}>0 \qquad (2.3.2)$$

This assumption holds for the condition of symmetric enthalpy profile with respect to the boundary. If not, $\frac{H_L + H_R}{2}$ can not be regarded as the enthalpy at the boundary of two strips, L and R. Appendix B is written to show this asymmetric enthalpy feature around the boundary where diversion crossflow is large.

2.4 Proposed Approach of Utilizing Only One Coupling Coefficient

Study of these five coupling coefficients indicates that N_H is the most important in calculating the changes in enthalpy and axial velocity of the homogenized representation over the axial region of interest. Thus the method of solution can be further simplified by employing only one coupling coefficient, i.e., N_H. However, it is suggested that N_U, N_{TF} and N_{TU} be employed if the diversion crossflow plays an important role in the transverse energy transport between channels. For N less than 23 and flow ratio between assemblies at the inlet less than 1.2, the utilization of only one coupling coefficient (N_H) yields satisfactory results for all cases. Therefore an analytical evaluation of the coupling coefficient (N_H) has been carried out in Appendix A.

Current approaches for the lumped-parameter calculations either adopt $N_H = 1$ or $N_H = N$ (refer to Reference 5, pg. 276). Further, in these approaches the coupling coefficient is used only in the turbulent mixing component term of the energy equation. With the approach of using $N_H = 1$, the energy transport by the turbulent mixing and the diversion crossflow in the homogenized region calculation is highly exaggerated. Therefore, optimistic results for the axial enthalpy changes in the hot channel are to be expected. On the other hand,

use of $N_H = N$ can excessively suppress the energy transport by the turbulent mixing. Therefore in the case of $N_H = N$, results for axial enthalpy changes of the hot channels in the homogenized region calculation are expected to be conservative but the deviation of the lumped enthalpy change from the averaged values in the multi-subchannel calculation is still rather large with respect to the approach employing $N_H = 1$. However, with the linear enthalpy profile throughout the subchannels, N_H becomes N. (Refer to Appendix D (Volume I) for the derivation).

2.5 Assessment of Errors with the One Coefficient Approach

Since only one coupling coefficient (N_H) is used in our approach, deviations of the results in the homogenized region calculation from that in the multi-subchannel calculation are expected. The major reasons for these deviations are summarized below.

a) due to improper computation of the momentum and the energy carried by the diversion cross-flow through the boundary between homogenized regions, i.e., assumptions of equations (2.3.1) and (2.3.2),

b) due to the lack of a corrective method for

matching the homogenized region axial and transverse momentum to the standard values of the multichannel calculation, i.e., N_U, N_{TU}, N_{TF} and N_{TP} are not employed.

The general expectation for predictions using only N_H in the homogenized region calculation is discussed below under the specific cases of interest since the importance of N_H varies under different conditions, i.e., enthalpy upset, flow upset, power upset and power and flow upset. For the cases of small diversion crossflow, the importance of N_H can be studied by assuming there is no diversion crossflow through the boundary. In Appendix E (Volume I) a relation between the errors of the homogenized region axial enthalpy changes and the operational conditions, i.e., F_R, H_R, P_R, $\bar{q}'$ and β under the no crossflow condition has been derived. A qualitative study for the role of N_H under different conditions has been made in the following sections. Also a comparison between analytical result and computer result is presented in Appendix A. It is convenient to study these cases in the order of ENTHALPY UPSET Case, ENTHALPY AND FLOW Case, POWER UPSET Case and POWER AND FLOW UPSET Case.

2.5.1 Unheated Cases

2.5.1.1 Enthalpy Upset Cases

Since there is no flow upset in this case, significant diversion crossflow does not occur. It is expected that good homogenized region enthalpy rise results can be obtained in this case by only employing N_H.

From the derivation in Appendix E,(Vclume I) the error for the homogenized region axial enthalpy change using N_H = 1 of the hotter channel can be expressed as:

$$\text{ERROR} = (1 - \bar{N}_H) \qquad (B.9)$$

where $\bar{N}_H$ is the axially averaged N_H computed by our suggested method.

Since $\bar{N}_H$ is slightly proportional to the number of channels, i.e., N, and always larger than 1, the error is always negative and increases slightly as N increases. The negative error means the predicted hot channel exit enthalpies are always less than that in the multi-subchannel calculation.

If N_H = N is employed in the homogenized region calculation, the error for the homogenized region axial enthalpy change can be expressed as:

$$\text{ERROR} = (N - \bar{N}_H) \qquad (2.5.1.1)$$

which is always positive. Since $\bar{N}_H$ is usually less

than one third of N, it is expected that the error in the case of N_H = N is about two times larger than that in the case of N_H = 1.

The effect of β and H_R do not directly come into play. However, the error is expected to increase as β decreases. This is because the axial rise of the homogenized enthalpy decreases as β decreases.

2.5.1.2 Enthalpy and Flow Upset Case

The role of the diversion crossflow in this case is between that in the enthalpy upset case and that in the power and flow upset case. Therefore the error in the axial enthalpy changes is expected to lie between that in the enthalpy upset case and in the power and flow upset case.

Furthermore, the error for the axial enthalpy changes in the hot channel by employing N_H = 1 can be expressed in the same way as that in the enthalpy upset case. Therefore, N_H has the same importance as that in the enthalpy upset case.

2.5.2 Heated Cases

2.5.2.1 Power Upset Case

Axial enthalpy changes are due to three mechanisms: heat added from the rods, energy transport by

the turbulent interchange between channels and energy transport by the diversion crossflow between channels.

From equation E.14 in Appendix E, (Volume I) the error for the enthalpy change in hot channel by using N_H=1 can be expressed as the following:

$$\text{ERROR} = \frac{\frac{1}{N_H} - 1}{\frac{P_R A_S N'}{(P_R-1)\beta SL} - \frac{1}{N_H}} \qquad \text{(E.20)}$$

Since the axial enthalpy change due to the heat added from the fuel rods is generally larger than that due to the diversion crossflow, the errors in the determination of the lumped energy transport by the diversion crossflow have less effect on the total axial enthalpy change than in the unheated cases. Thus, favorable results in the homogenized region predictions are expected to be obtained for even crude estimates of N_H.

It is interesting to note that the error is not a function of the heat generation rate ($\bar{q}'$). In the meanwhile, the error decreases as N increases and as P_R approaches unity. Thus, the larger the P_R and the smaller the N, the more important the N_H.

2.5.2.2 Power and Flow Upset Condition

For the same reason as stated in 2.2.1, good

results are expected to be obtained even though the diversion crossflow in this case is larger than that in the power upset case. The importance of N_H is also the same as that in the power upset case. However, the error increases as F_R increases.

CHAPTER 3

RECOMMENDED COUPLING COEFFICIENTS FOR UNHEATED BUNDLES

Two cases are discussed in this chapter, i.e., the enthalpy upset case and the enthalpy and flow upset case. Numerical values of N_H of these two cases are obtained for three values of N and three values of β, i.e., N = 5, 11 and 23; β = 0.005, 0.02, and 0.04. Other input data in COBRA IIIC, $\frac{S}{L}$ and K, are kept constant and equal to 0.5.

3.1 Enthalpy Upset Case

The numerical values of N_H are evaluated from the results of multi-channel computation utilizing a step shaped inlet enthalpy upset. It is suggested that two half-sized subchannels C and D always be utilized to obtain the subchannel parameters h_C and h_D. The reason is that the required difference, $h_C - h_D$, in the definition of N_H is generally poorly approximated by the enthalpies of the subchannel B and E (refer to Figure 2 for subscripts B, C, D and E). For instance, if we compute N_H by the following relation

$$N_H = \frac{H_L - H_R}{\frac{h_B - h_E}{4}} \tag{3.1}$$

the error of the enthalpy rise involved in the homogenized region case will be 45% higher than that using N_H evaluated by the parameters of the half-sized subchannels C and D.

It is worthwhile noting that the numeric solution of COBRA IIIC imposes a limitation on β due to enthalpy fluctuation when the energy transport is assumed to occur only by the turbulent interchange which is more restrictive in the half-size channel computation than in the full-sized computation. The maximum allowable value for this case is 0.048 (refer to Appendix C for the derivation). Therefore β=0.04 is picked as the upper bound of β in our approach.

3.1.1 Comparison Between Various Forms of N_H

In this section the results of hot zone enthalpy in the homogenized case using the following expressions for N_H are examined

$N_H(z)$

$\overline{N}_H$

$N_H = 1.0$, all z

$N_H = N$, all z

where

$$\overline{N_H} = \frac{\Delta H_{T.I.}}{\sum_i \frac{\Delta H_{i,T.I.}}{N_{H_i}}} \qquad (3.1.1)$$

$i \equiv$ subscript of elevation node

$\Delta H_{T.I.} \equiv$ enthalpy rise of the "homogenized representation" due to turbulent interchange.

The results are illustrated in Figure 4. As we have seen in this figure, the enthalpy changes of the homogenized case by using $N_H(z)$ and $\overline{N_H}$ coincide with that of the multi-subchannel case. On the other hand, $N_H = 1$ and $N_H = N$ have errors of enthalpy rise equal to -203% and 57.4% respectively compared with the results of the multi-subchannel representation. This example demonstrates the need for utilizing a value of N_H other than 1 for application in ENTHALPY and ENTHALPY AND FLOW UPSET CASES.

3.1.2 N_H Values for ENTHALPY UPSET CASE

In this section N_H values for the enthalpy upset condition with different values of β and N are presented. The method used to compute N_H from the multi-subchannel computation is illustrated in Appendix D. The values of $N_H(z)$ versus axial elevation is shown in Figures 5, 6 and 7. Tha analytical result is shown in Appendix A. The dips and humps of N_H at low elevation positions for β=0.04 are due to enthalpy fluctuation by turbulent interchange as mentioned previously. Note that the fluctuation amplitude of N_H is not going to be damped out if values of β larger than 0.048 are used.

The validity of these recommended N_H values is determined by comparing the hot zone enthalpy of the homogenized case with that of the multi-subchannel case at each axial node. The results for β = 0.005, 0.02 and 0.04; N = 5, 11 and 23 of the homogenized cases coincide with that calculated in the multi-subchannel case just as we expect. This equivalence is demonstrated in Figures 8, 9 and 10.

The inlet enthalpy shape for this case is a step function, abruptly changing at the center of the strip of the subchannels. For example, the inlet enthalpies of channel A, B and C are taken as a constant value and the inlet enthalpies of subchannel C, D and E are taken as another constant value. In the case of gradual enthalpy change at the center of the strip of subchannels, e.g., the inlet enthalpy at the center subchannel for N odd is taken as the averaged value of the inlet enthalpy of the hot zone and that of the cold zone, the N_H will have a completely different shape versus channel length from that of step inlet enthalpy case. N_H in this case will be infinite at the inlet of the channel and abruptly dips and then gradually increase. The $N_H(z)$ for N = 23 in this case is shown in Figure 11. It is good to see

that even though N_H is changed abruptly versus channel length, the results for homogenized case still coincide with the multi-subchannel results (Figure 11a).

3.1.3 Recommended Values of N_H for Design Use

In this section, two methods are investigated to illustrate the behavior of N_H versus β, N and the axial position of the subchannel. One is curve fitting of our predicted $N_H(z)$ results, the other is the averaging of the $N_H(z)$ over the axial enthalpy increment of the hot zone to give an $\overline{N_H}$. Each of them provides a convenient way to incorporate the N_H concept in design practice.

3.1.3.1 Curve Fits

The $N_H(z)$ predictions can be represented using a continuous function f(z) versus channel position z.

$$f(z) = 1.0 + \frac{bz}{a + z} \qquad (3.1.3.1)$$

The values of "a" and "b" can be evaluated by fitting two values of N_H with smallest deviation from the true value at every elevation node. The values of "a" and "b" for the nine cases we have analyzed are tabulated in Table 1.

3.1.3.2 Averaged Value of $N_H(z)$, i.e. $\overline{N_H}$

From the definition of $\overline{N_H}$ (refer to equation 3.1.1), it is expected that the enthalpy of the hot zone at any axial position z in the homogenized representation predicted using $\overline{N_H}$ will coincide with that in the multi-subchannel case. The $\overline{N_H}$ for β = 0, 0.005, 0.02 and 0.04,; N = 2, 5, 11 and 23, and L = 144 inches are tabulated in Table 2. For β = 0.02, $\overline{N_H}$ for a range of channel lengths and N = 2, 5, 11, 17 and 23 are plotted in Figure 12. It is interesting to notice that $\overline{N_H}$ increases with channel length due to the development of the enthalpy profile along the channel (refer to Figure 13). Further, the $\overline{N_H}$ curve becomes asymptotic as N increases for certain β and N. The phenomenon is due to the average parameters $\bar{h}_L$ and $\bar{h}_R$ which becomes less dependent on the subchannel parameters of the center half-sized subchannels, i.e., h_C and h_D when N is large.

3.2 Enthalpy and Flow Upset Case

For the step inlet flow upset with the higher flow rate in the hot zone, together with the inlet enthalpy upset, N_H will increase as the flow ratio increases. It is convenient to define the ratio between these cases in terms of a multiplier, R where

$$R_H = \frac{\bar{N}_H \text{ (ENTHALPY AND FLOW UPSET)}}{\bar{N}_H \text{ (ENTHALPY UPSET)}} \qquad (3.2)$$

Figure 14 demonstrates that this multiplication factor for $H_R = 1.22$ is roughly directly proportional to F_R, where F_R is defined as:

$$F_R = \frac{F_{HOT}}{F_{COLD}}$$

F_{HOT} = inlet flow of the hot zone in the homogenized representation

F_{COLD} = inlet flow of the cold zone in the homogenized representation

The comparison between the results of the homogenized cases using $N_H(z)$ and $N_H = 1$ and the results of the multi-subchannel case is illustrated in Figure 15. It should be noticed that the result of the homogenized representation, using only one coupling coefficient N_H, is not as good as that in the enthalpy upset case, Figure 4.

The 13% error for the enthalpy rise of the homogenized region case can be explained as follows:

1) Assumption (A.1.12a) (Volume I) made to derive the N_H' in terms of N_H and known parameters becomes invalid

when flow upset goes up, i.e., diversion cross-flow becomes significant.

2) Under the large diversion crossflow condition in this case the neglect of N_U, N_{TF}, N_{TP} and N_{TU} effects the results.

3) Error exists due to the difference approximation made in COBRA IIIC computation as assessed in Appendix B. (Volume I)

CHAPTER 4

RECOMMENDED COUPLING COEFFICIENTS FOR HEATED BUNDLES

Two cases are discussed in this chapter, i.e., the POWER UPSET CASE and the POWER AND FLOW UPSET CASE. The analytical result is shown in Appendix A.

4.1 POWER UPSET CASE

The numerical values of N_H are evaluated for three values of N and three values of β, i.e., N = 5, 11 and 23; β = 0.005, 0.02 and 0.04. The maximum β in this case is limited to 0.048 when half-sized subchannels are used to obtain the subchannel parameters required in the evaluation of N_H. Because the exit enthalpy difference between the homogenized representation and the multi-subchannel representation in this case is less sensitive to N_H then that for ENTHALPY UPSET CASE (as mentioned in section 2.5.2.1), N_H can be evaluated by equation (3.1) without the half-sized subchannels in the center region and yields good results of the homogenized representation.

4.1.1 Comparison Between Various Forms of N_H

In this section the results of the hot zone enthalpy in the homogenized representation using the following expressions for N_H are examined:

$N_H(z)$

$\overline{N_H}$

$N_H = 1.0$, all z

$N_H = N$, all z

where $\overline{N_H}$ is defined by equation (3.1.1).

The results are illustrated in Figure 16 for a typical N, β combination. The predicted hot zone enthalpies for the homogenized representation using $N_H(z)$ coincide with that of the multi-subchannel representation. However, result for $N_H = 1$ and $N_H = N$ have errors of enthalpy rise equal to -3.2% and 2.1% respectively. Note that for the POWER UPSET CASE the error in hot side enthalpy for the homogenized representation is not as sensitive to the form of N_H as in the unheated bundle cases. This example demonstrates that the need for computing N_H in the heated bundle is not as crucial as that in the unheated bundle case .

4.1.2 N_H Values for POWER UPSET CASE

In this section N_H values for the power upset condition with different values of β and N are presented. The method used to compute the N_H from the multi-subchannel computation is illustrated in Appendix D. The values of $N_H(z)$ versus axial elevation are shown in Figs. 17, 18

and 19. The dips and humps of N_H at low elevation positions which were present in the analogous plots of the ENTHALPY UPSET CASE are not shown in these figures. The reason is that the heat added from the rods overcomes the small axial enthalpy fluctuation due to the turbulent interchange. However, the computational impossibility for the enthalpy fluctuation due to the turbulent interchange still imposes an upper limit on β, i.e. 0.048, in the homogenized calculation with half-sized subchannels in the center region.

The validity of these recommended N_H values is determined by comparing the hot zone enthalpy of the homogenized representation with that of the multi-subchannel representation at each axial elevation. The results are shown in Figs. 20, 21, and 22. As demonstrated in Figure 16, the enthalpies of the homogenized representation employing $N_H(z)$ and $\overline{N_H}$ coincide with that of the multi-subchannel representation.

4.1.3 Recommended Values of N_H for Design Use

In this section, the same methods are employed to illustrate the N_H versus β, N and the axial position of the subchannel as those discussed in 3.1.3. The details for each method are discussed in the following section.

4.1.3.1 Curve Fits

The N_H can be presented by using a continuous function f(z) versus channel position z for β = 0.005, 0.02 and 0.04; N = 5, 11, 23.

$$f(z) = a + \frac{cz}{b+z} \qquad (4.1.4.1)$$

The values of a, b and c can be evaluated by fitting three values of N_H with the smallest error deviating from the true value at every elevation node. The values of a, b and c for the nine cases (three β and three N) are tabulated in Table 3.

4.1.3.2 Average Value of N_H

The $\overline{N_H}$ for β = 0, 0.005, 0.02, and 0.04; N = 2.5, 11 and 23 are tabulated in Table 4. For β = 0.02, $\overline{N_H}$ for a range of channel lengths and N = 2, 5, 11 and 23 are plotted in Figure 23. As we can observe, N_H saturates faster when N increases than it does in the unheated bundle case. This is because the transverse power profile contributes much to the transverse enthalpy profile which determines the $\overline{N_H}$.

4.1.4 Effectiveness of Coupling Coefficients (N_H, N_U, N_{TP}, N_{TF} and N_{TU}) in POWER UPSET CASE

The total enthalpy transport across the boundary between homogenized regions can be broken into three components.

These components listed below are consistent with the COBRA representation of the overall transport process as due to turbulent interchange and diversion crossflow where the enthalpy transport due to crossflow is itself broken into two components:

a) turbulent interchange

b) enthalpy of the diversion crossflow

c) mass flowrate of the diversion crossflow.

In this section three parameters of the homogenized representations are examined to compare with those of the multi-subchannel representation in order to evaluate the effectiveness of using several coupling coefficients simultaneously.

The first component, the enthalpy change in the hot zone due to turbulent interchange only, gives us an idea of the effectiveness of each coupling coefficient for the homogenized representation on the energy transport due to turbulent mixing. The second parameter is the enthalpy increment in the hot zone due to the diversion crossflow transport. This will illustrate the effectiveness of each coupling coefficient on the energy transport by the diversion crossflow. The third parameter is the total diversion crossflow across the boundary in the homogenized representation. In the case we examine here, the diversion crossflows at the boundary always move toward the cold zone for any channel axial position, and therefore it is considered convenient to utilize the total diversion crossflow through the boundary as a para-

meter to illustrate the effectiveness of the coupling coefficients on the transverse momentum transport.

The results are shown in Tables 5, 6 and 7. Table 5 tabulates the parameters which are the enthalpy change with respect to the inlet enthalpy of the hot zone due to the turbulent interchange only. As can be observed in this table, the $N_H(z)$ used in the homogenized computation is most effective in matching the homogenized results to that of the multi-subchannel computation. All the other coupling coefficients show negligible effects on this parameter. Table 6 tabulates the second parameters for the multi-subchannel representation and homogenized representation, i.e., $\Delta h_{D.C.}$ and $\Delta H_{D.C.}$ respectively. It is worth noting that the results of the homogenized representation using all the coupling coefficients have the best agreement with that of the multi-subchannel representation. However, $N_H(z)$ and $N_U(z)$ are most effective compared to the other three coupling coefficients. Table 7 tabulates the integral value of diversion crossflow across the central boundary for both the multi-subchannel representation and the homogenized representation. The conclusion we can draw from this table is similar to that from Table 6. However, if accurate diversion crossflow is desired, it is recommended that N_{TP}, N_{TF}, and N_{TU} be used together with N_H and N_U.

4.2 POWER and FLOW UPSET Case

For the step inlet flow upset, together with the step linear heat generation rate, N_H for the homogenized representation will increase as the flow ratio increases. This phenomenon can be expected from the results of the ENTHALPY and FLOW UPSET Case (Section 3.2). The multiplication factor for this case is defined as

$$R_p = \frac{\overline{N_H}\ \text{(POWER and FLOW UPSET)}}{\overline{N_H}\ \text{(POWER UPSET)}},$$

and is plotted versus F_R in Figure 24.

The validity of $N_H(z)$ and $\overline{N_H}$ is illustrated in Figure 25. In this figure, using $N_H = 1.0$ and $N_H = N$, the hot zone enthalpy results of the homogenized representation are also plotted in comparison to the results using $N_H = N_H(z)$. From our calculation, we are aware that there is a slight difference of 0.1% between the hot zone enthalpy results of the homogenized representation using $N_H = N_H(z)$ and that of the multi-sub-channel representation. This small difference is believed to be due to the error caused by the difference computation scheme as we mentioned in Section 2.3 and Appendix B. (Volume I).

CHAPTER 5

SUMMARY OF RESULTS FOR ALL CASES

5.1 Numerical Values of $N_H(z)$ and $\overline{N_H}$

The numerical values for $N_H(z)$ and $\overline{N_H}$ for the two dimensional subchannel layout under different operational conditions considered in this study, are summarized in the following summary tables.

$N_H(z)$

	ENTHALPY UPSET	POWER UPSET
No Flow Upset	Figure 5 (N=5) Figure 6 (N=11) Figure 7 (N=23) Table 1 (best fit curves)	Figure 17 (N=5) Figure 18 (N=11) Figure 19 (N=23) Table 3 (best fit curves)

$\overline{N_H}$

	ENTHALPY UPSET	POWER UPSET
No Flow Upset	Table 2 (z=114") Figure 12(β=0.02)	Table 4 (z=144") Figure 23(β=0.02
Flow Upset	Figure 14 (multiplication factor	Figure 24(multiplication factor

Figures 5, 6 and 7 plot the $N_H(z)$ versus the channel length for β = 0.005, 0.02 and 0.04, N = 5, 11 and N, under the enthalpy upset condition. Figures 17, 18 and 19 plot the $N_H(z)$ versus the channel length for β = 0.005, 0.02 and

0.04, N = 5, 11 and 23, under the power upset condition. Tables 1 and 3 tabulate the parameter values to obtain $N_H(z)$ from the best fitting correlation for $\beta = 0.005$, 0.02 and 0.04, N = 5, 11 and 23, for the ENTHALPY UPSET CASE and the POWER UPSET CASE, respectively. Tables 2 and 4 tabulate the $\overline{N_H}$ values for $\beta = 0.005$, 0.02 and 0.04, N = 5, 11 and 23 with the channel length equal to 12 ft., for the ENTHALPY UPSET CASE and the POWER UPSET CASE, respectively. Figures 12 and 23 plot the $\overline{N_H}$ values versus N and L for $\beta = 0.02$ for channel length less than 12 ft. Figures 14 and 23 give the multiplication factors which are a function of F_R and are needed to evaluate $\overline{N_H}$ from equations (3.2) and (4.2) for the ENTHALPY UPSET CASE and the POWER UPSET CASE, respectively.

For subchannels with axial length less than 12 ft., $N_H(z)$ gives detailed values at each axial position up to the exit, whereas $\overline{N_H}$ has been calculated for only certain specific axial locations (Figs. 12 and 23). However, it is easy to incorporate $\overline{N_H}$ into the computer code. Two empirical correlations for $\overline{N_H}$ for the cases we discussed in this volume are represented as follows by equations (5.1.1) and (5.1.2) which can be used directly without resorting to the tables and figures listed in the summary tables.

$$\overline{N_H} = \{1+\ln[1+4200(\frac{N-2}{N})^{1+1008\beta^{1.43}(\frac{L}{144})^{1.5}}]\} R_H \} \pm 15\% \quad (5.12$$

Equation (5.1.1) determines the value of $\overline{N_H}$ for the POWER

UPSET CASE and the POWER and FLOW UPSET CASE.

$$\overline{N_H} = \{1+\ln[1+353(\frac{N-2}{N})^{\frac{3.58}{0.015+\beta}} \beta^{1.1}(\frac{L}{144})^{1.5}]\}R_p \quad +15\% \quad (5.1.1)$$

Equation (5.1.2) determines the value of $\overline{N_H}$ for the ENTHALPY UPSET CASE and the ENTHALPY and FLOW UPSET CASE.

These correlations are valid for $N<23$, $\beta<0.04$ and $L<144$ inches, where

$L \equiv$ channel length in inches

R_H and $R_p \equiv$ multiplication factors for Enthalpy Upset and Power Upset respectively, which can be obtained from Figs. 14 and 24 respectively. Under no flow upset condition, $R_H = 1.0$ and $R_p = 1.0$.

5.2 Suggestions on the N_H Values Under Exceptional Conditions

As we mentioned in Section 5.1, the characteristics of $\overline{N_H}$, together with some understanding of the basics of the coupling coefficient N_H, suggest some reasonable values for $\overline{N_H}$ under exceptional conditions. They are as follows:

1) Since $\overline{N_H}$ approaches a saturated value as N increases, $\overline{N_H}$ for $N>23$ has the same value as $N = 23$.

2) For the homogenized representation with two homogenized strips of subchannels with uneven subchannel numbers, $\overline{N_H}$ can be obtained by the following formula:

$$\overline{N_H} = \frac{\overline{N_{H_L}} + \overline{N_{H_R}}}{2}$$

under the criteria

$$\frac{N_L - N_R}{\min(N_L, N_R)} < 0.3$$

where

$\overline{N_{H_L}} \equiv \overline{N_H}$ value for $N = 2N_L$

$\overline{N_{H_R}} \equiv \overline{N_H}$ value for $N = 2N_R$

(refer to Appendix E for the derivation).

3) Since $\overline{N_H}$ is not a function of power level and P_R, $\overline{N_H}$ can be taken as a constant value through the period of power transient (power excursion or shut down transient) when $\overline{N_H}$ is used in the transient computation.

CHAPTER 6

CONCLUSIONS AND RECOMMENDATIONS FOR FUTURE WORK

6.1 Characteristics of Coupling Coefficients

Listed below are several conclusions relating to the characteristics of the coupling coefficients.

6.1.1 Overall Characteristics

6.1.1.1 Use of a single coupling coefficient $N_H(z)$ can lead to favorable results in the homogenized representation as long as the diversion crossflow does not play a major role in the energy transport between channels.

6.1.1.2 $N_H(z)$ and $N_U(z)$ are most effective in getting good results for cases with diversion crossflow in the homogenized representation.

6.1.2 Thermal Entry Development Characteristics

6.1.2.1 $N_H(z)$ is strongly dependent on the transverse enthalpy profile among subchannels at channel elevation z.

6.1.2.2 $\overline{N_H}$ approaches a saturated value as the number of subchannels, N, increases.

6.1.3 Basic Characteristics

6.1.3.1 $\overline{N_H}$ is not a function of $\overline{q}'$, H_R OR P_R. (Refer to Figs. 26, 27, and 28). This was demonstrated analytically in Appendix A and confirmed here for the case of numerical determination of coupling coefficients.

6.1.3.2 The effectiveness of $N_H(z)$ is not a function of heat generation rate ($\bar{q}'$). This characteristic can be illustrated by equation (E.20) (Volume I) and Figure 26 which show that the error of hot channel enthalpy rise between multi-subchannel case and homogenized case is independent of $\bar{q}'$.

6.2 Effectiveness of $N_H(z)$ Under Different N and β Combinations

In this section, the effectiveness of $N_H(z)$ is explored under POWER UPSET CASE which is encountered in the practical application with different N and β combinations. The effectiveness of N_H on the homogenized case can be numerically indicated by the error of exit enthalpy rise between the multi-subchannel case and the homogenized case. A conservative scheme to estimate this error has been derived in Appendix E (Eq. E.20) (Volume I) and quoted in Section 2.5.2.1. With the aid of the correlation 5.1.1, we can evaluate the errors with different N and β combinations. The results are tabulated in Table 8. As can be observed, the maximum error of 14.4% happens at large β and intermediate N, i.e. β = 0.06, N = 4. In other words, $N_H(z)$ is relatively important at this specific combination of N and β.

6.3 Recommendations for Future Work

In response to the problems presented in this Volume, several recommendations for future work are listed below.

1) The characteristics of coupling coefficients N_U, N_{TF}, N_{TP} and N_{TU} need further investigation in order to deal with the homogenized representation with very large diversion crossflows.

2) Two dimensional (planar) linkage of the homogenized representation (with the aid of coupling coefficients) or the 3D problem should be studied in order to analyze the corewide thermal behavior in a more detailed way than that done by the cascade method[5] for the PWR.

3) Corewide study (with the aid of coupling coefficients) on MDNBR under power excursion transient case is recommended. Under this condition, large amount of diversion crossflow is expelled from the hot zone which can cause misleading MDNBR results provided there are no coupling coefficients incorporated.

REFERENCES

1. Rowe, D.S., "COBRA III: A Digital Computer Program for Steady State and Transient Thermal Hydraulic Analysis of Rod Bundle Nuclear Fuel Elements," BNWL-B-82, Pacific Northwest Laboratory (1972).

2. H. Chelemer, J. Weisman and L.S. Tong, Nucl. Eng. and Design 21, 3 (1972).

3. France, D.M. and Ginsberg, T.,"Evaluation of lumped parameter heat transfer techniques for nuclear reactor applications," Nucl. Sci. Eng. 51, 41-51 (1973).

4. Ramm, H., Johannsen, K., and Todreas, N.E., "Single phase transrport within bare rod arrays at laminar, transition and turbulent flow conditions," Nucl. Eng. and Design 30, 186-204 (1974).

5. Joel Weisman and Robert Bowring, "Methods for Detailed Thermal and Hydraulic Analysis of Water Cooled Reactors," Nuclear Science and Engineering 57, 255-276 (1975).

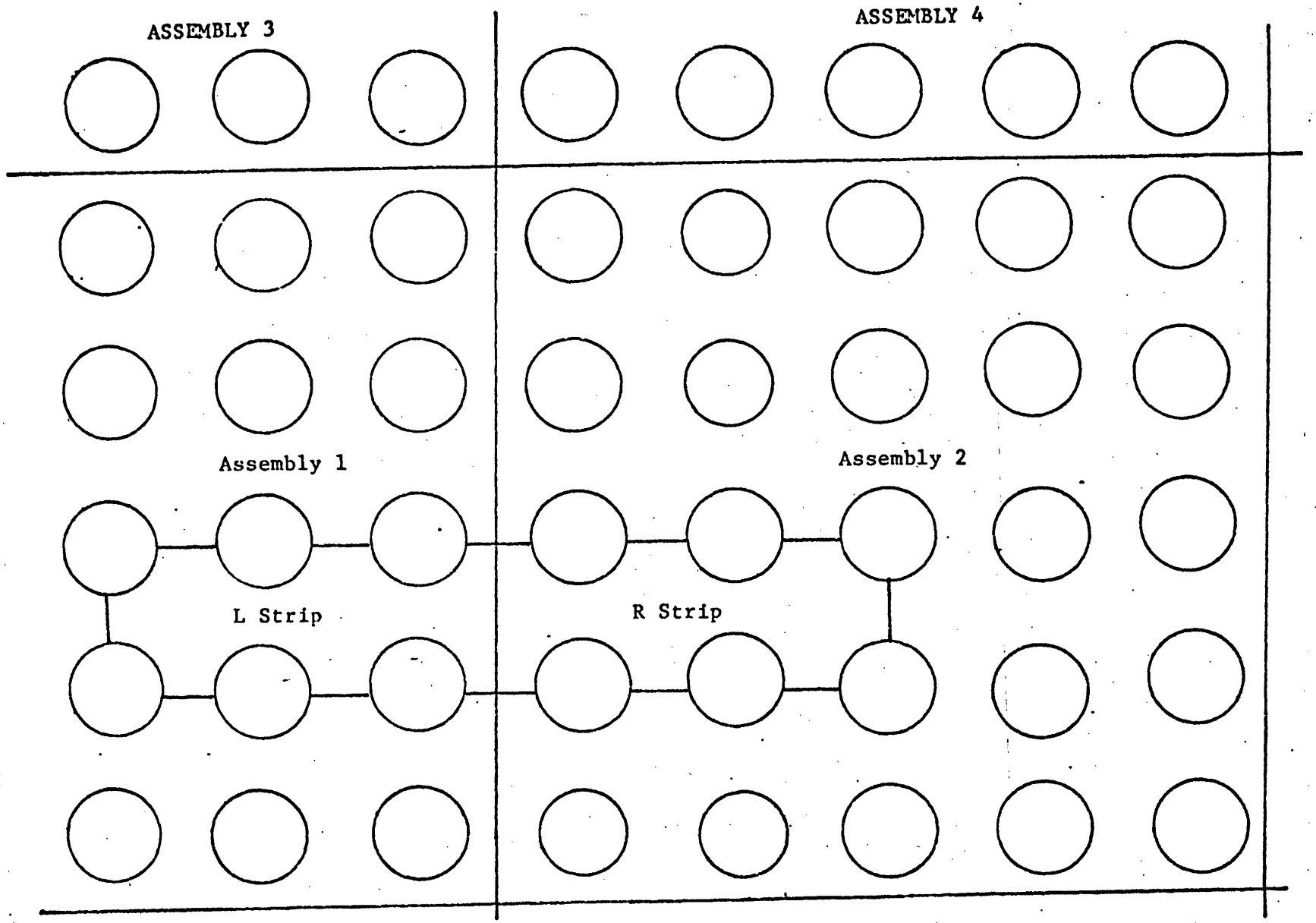

Figure 1. NxN Rod Assemblies in Square Array, N=5

Letters - Channel Subscripts

= Adiabatic Boundary

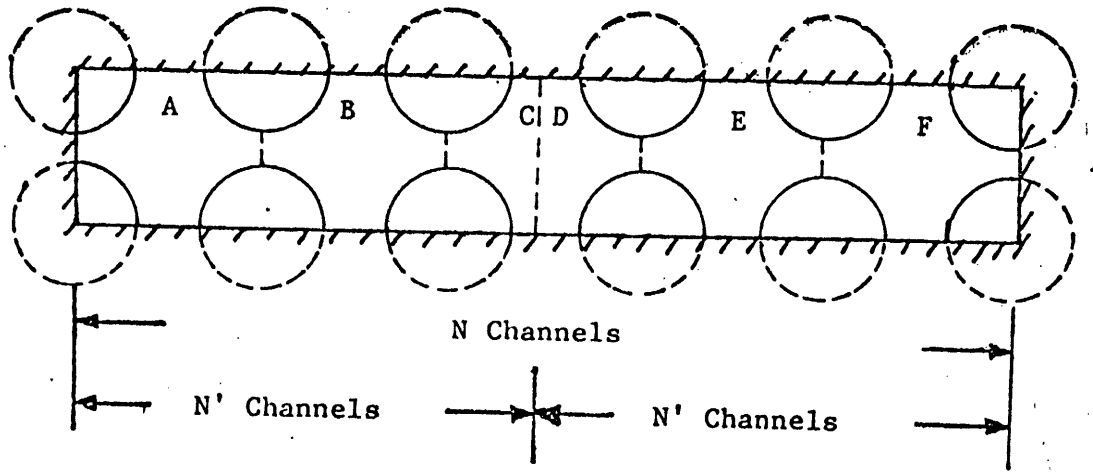

Figure 2. Strips of Adjacent N' Channels

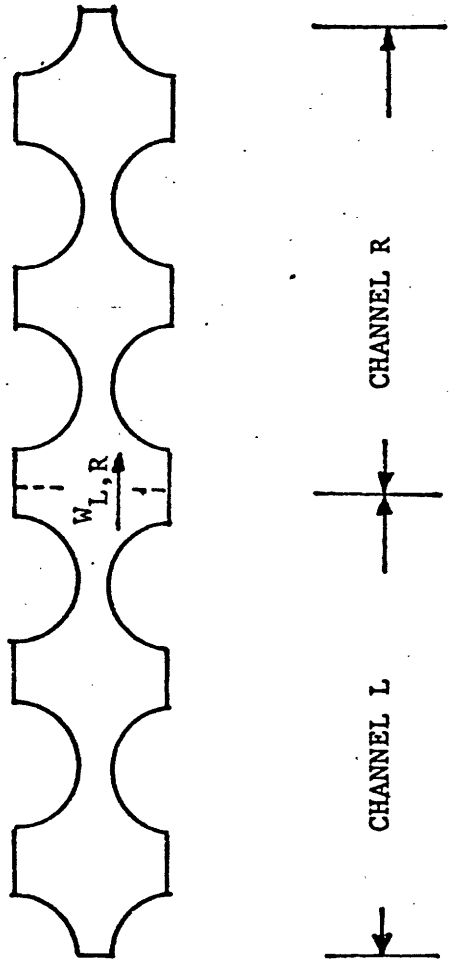

Figure 3. Homogenized Representation of Strips of N' Subchannels

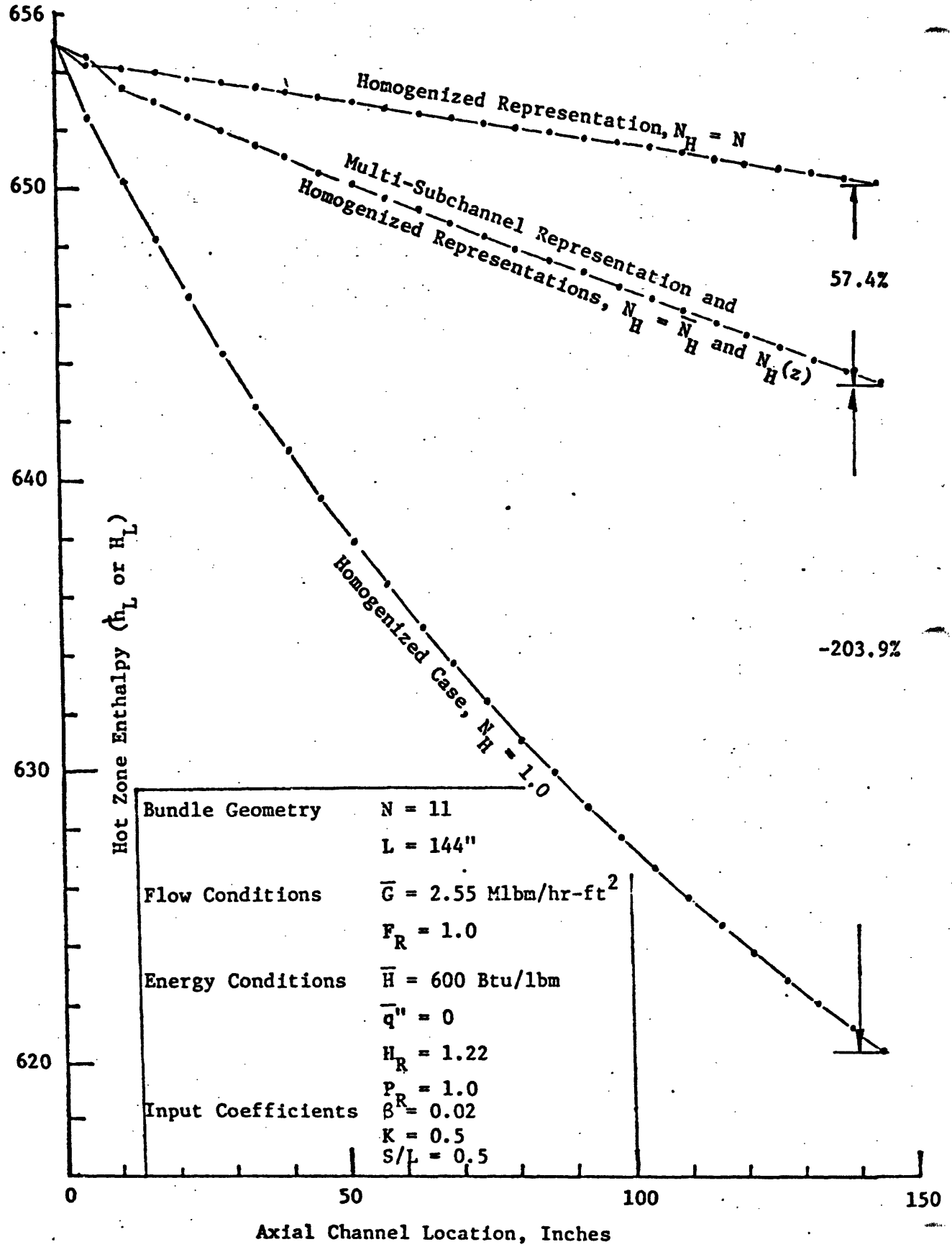

Figure 4. Comparison between results of multi-subchannel representations and homogenized representations

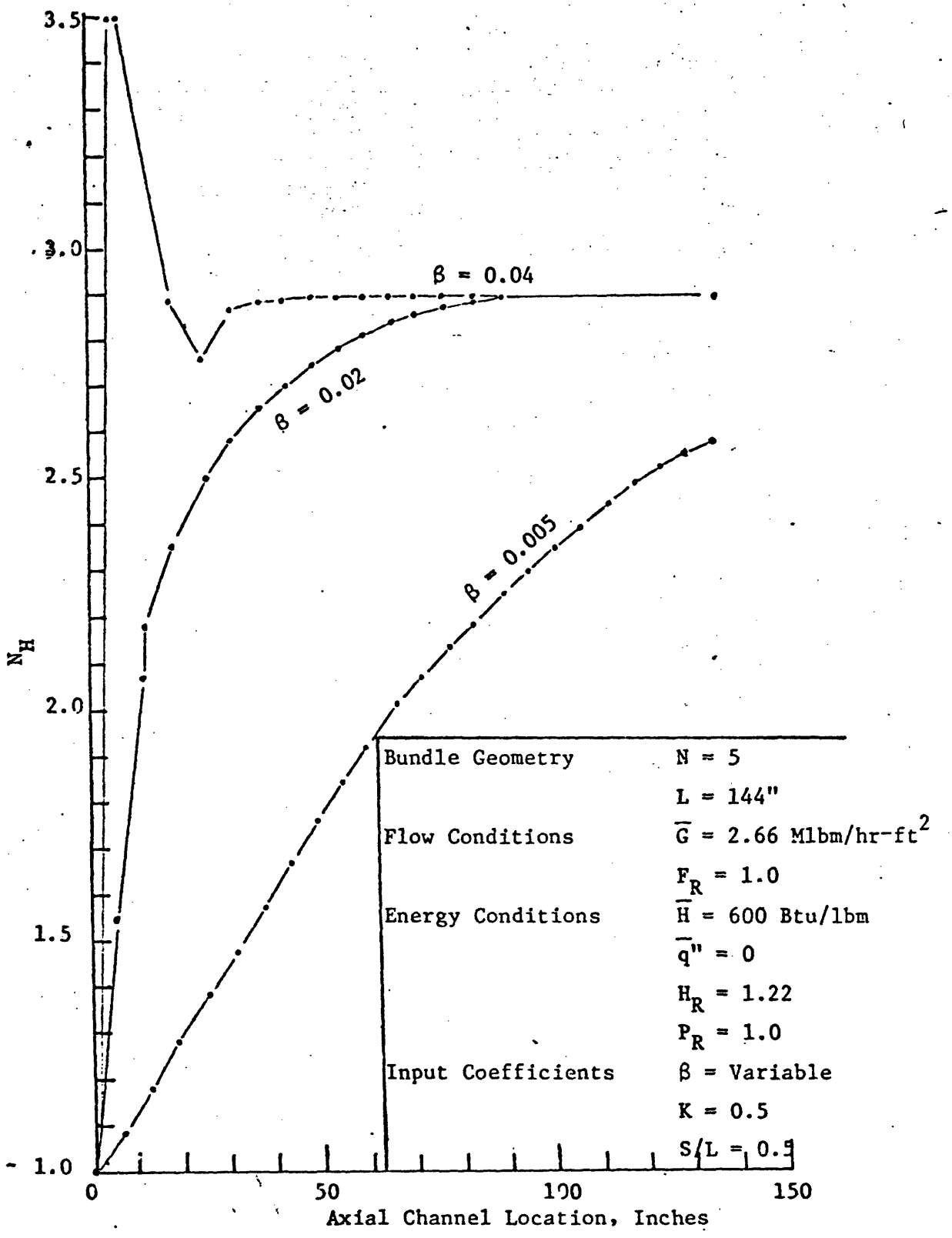

Figure 5. $N_H(z)$ versus channel length for ENTHALPY UPSET CASE N = 5

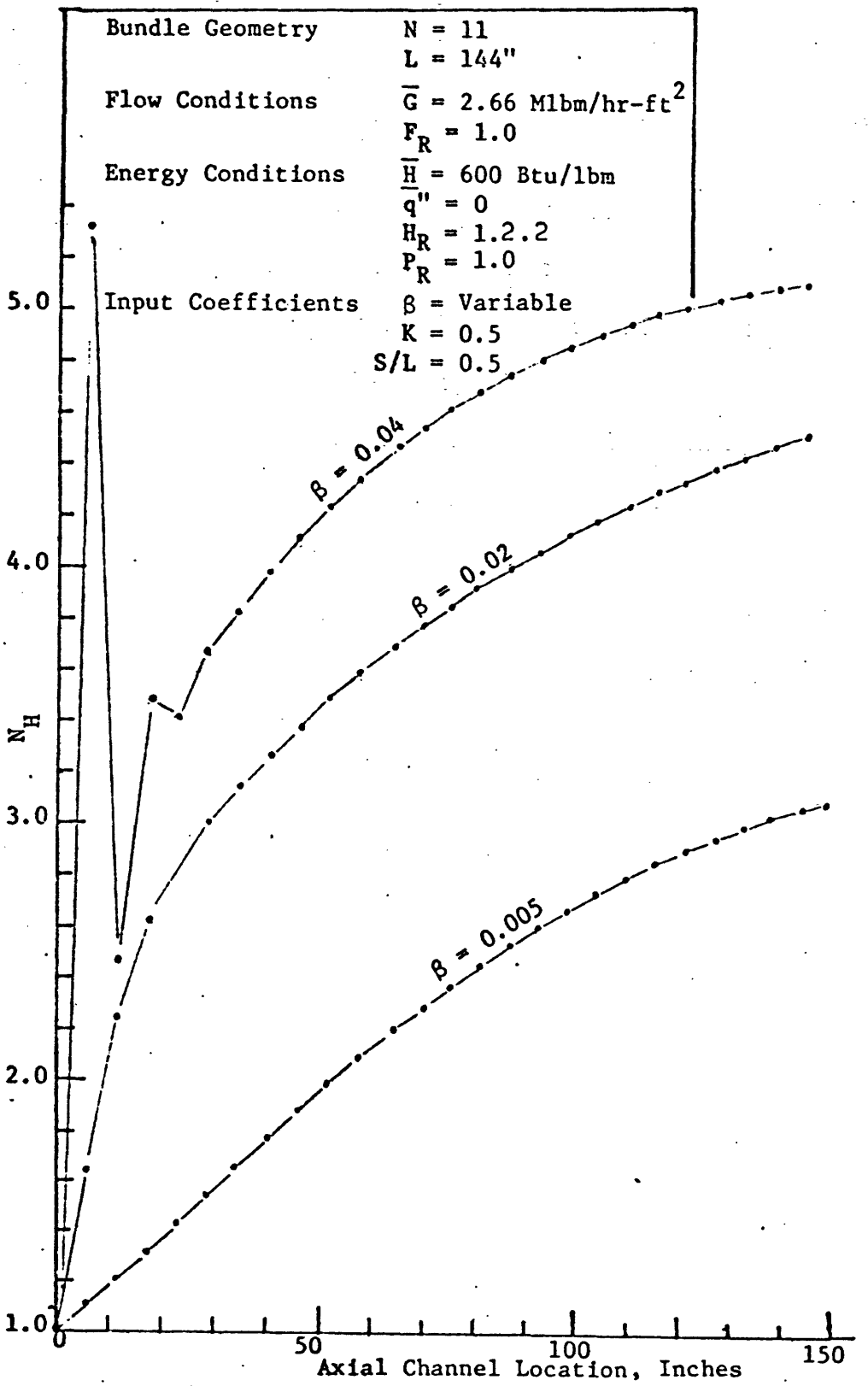

Figure 6. $N_H(z)$ versus channel length for ENTHALPY UPSET CASE N = 11

Bundle Geometry	N = 23
	L = 144"
Flow Conditions	$\overline{G}$ = 2.66 Mlbm/hr-ft^2
	F_R = 1.00
Energy Conditions	$\overline{H}$ = 600 Btu/lbm
	$\overline{q}''$ = 0
	H_R = 1.22
	P_R = 1.0
Input Coefficients	β = Variable
	K = 0.5
	S/L = 0.5

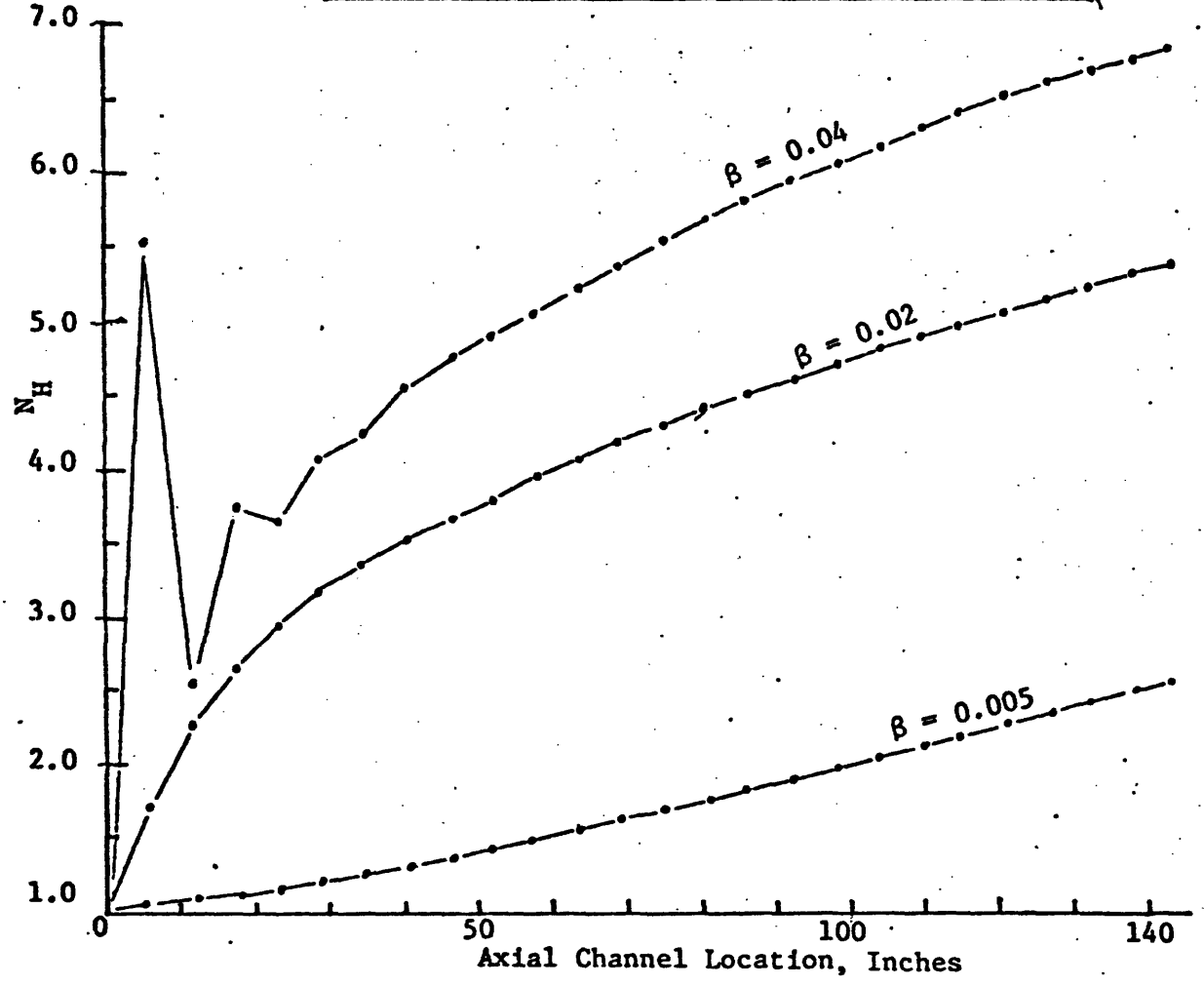

Figure 7. $N_H(z)$ versus channel length for ENTHALPY UPSET CASE N = 23

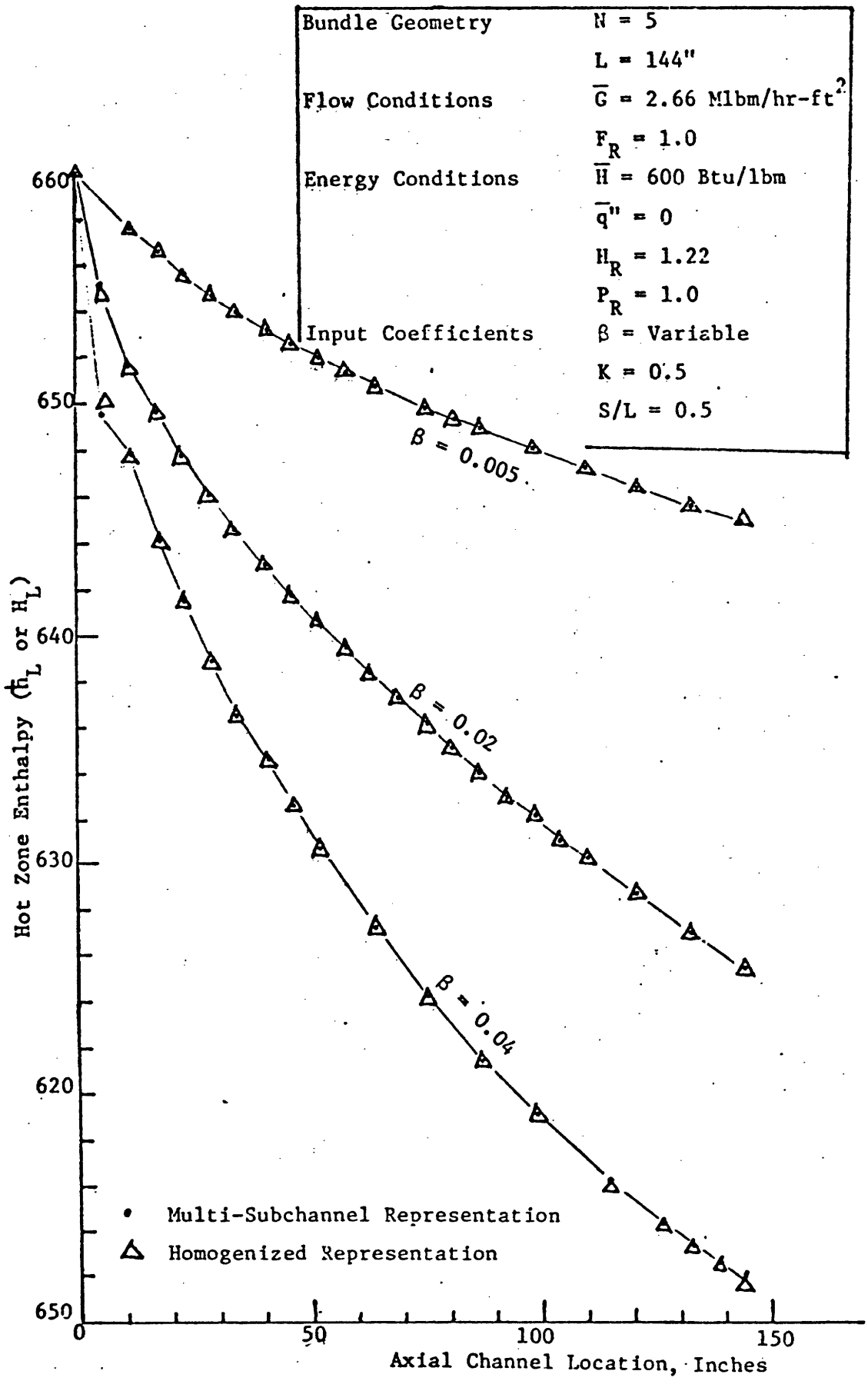

Figure 8. Validity of $N_H(z)$ for ENTHALPY UPSET CASE N = 5

Figure 9. Validity of $N_H(z)$ for ENTHALPY UPSET CASE, N=11

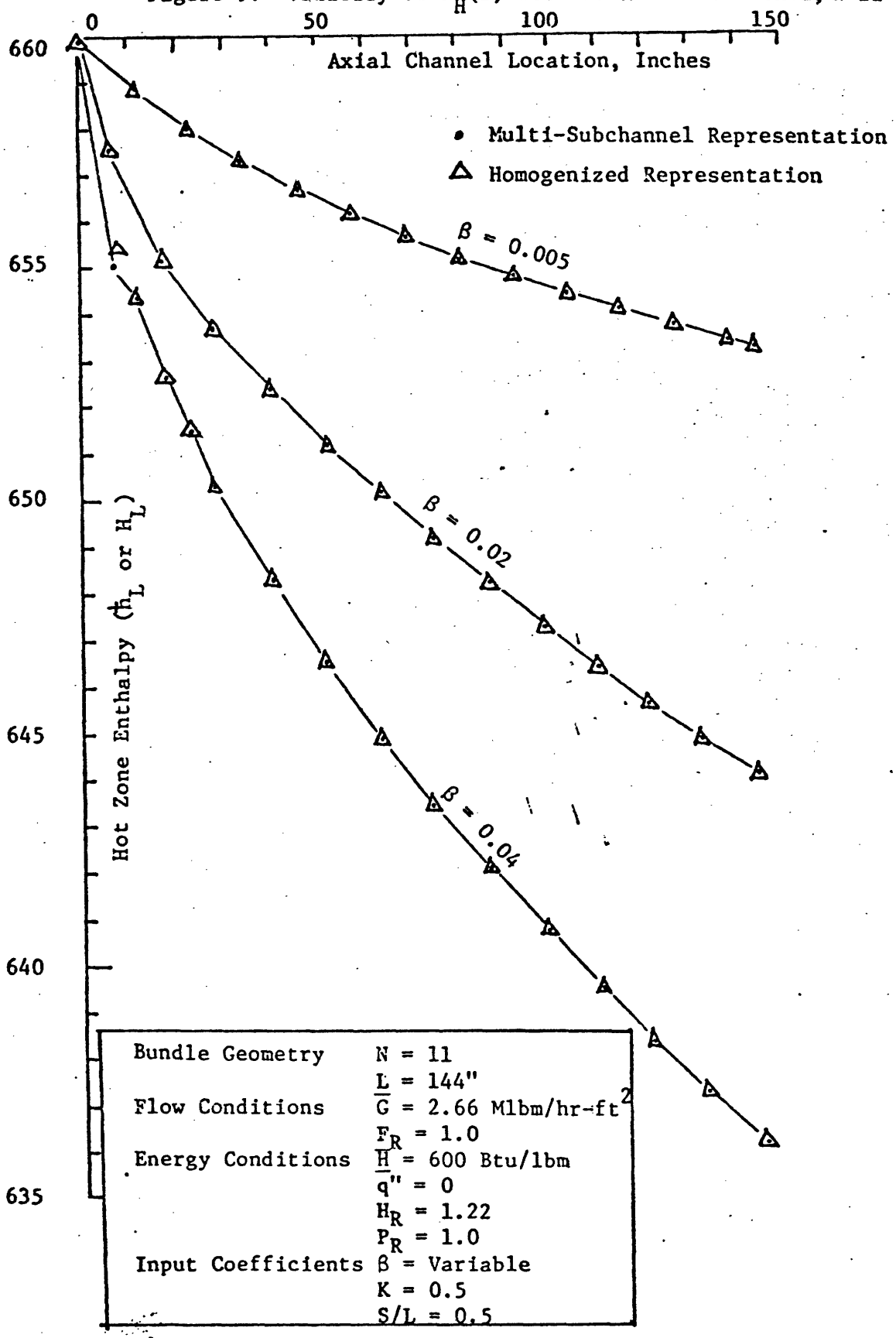

Bundle Geometry	N = 23
	L = 144"
Flow Conditions	$\overline{G}$ = 2.55 Mlbm/hr-ft^2
	F_R = 1.0
Energy Conditions	$\overline{H}$ = 600 Btu/lbm
	$\overline{q''}$ = 0
	H_R = 1.22
	P_R = 1.0
Input Coefficients	β = Variable
	K = 0.5
	S/L = 0.5

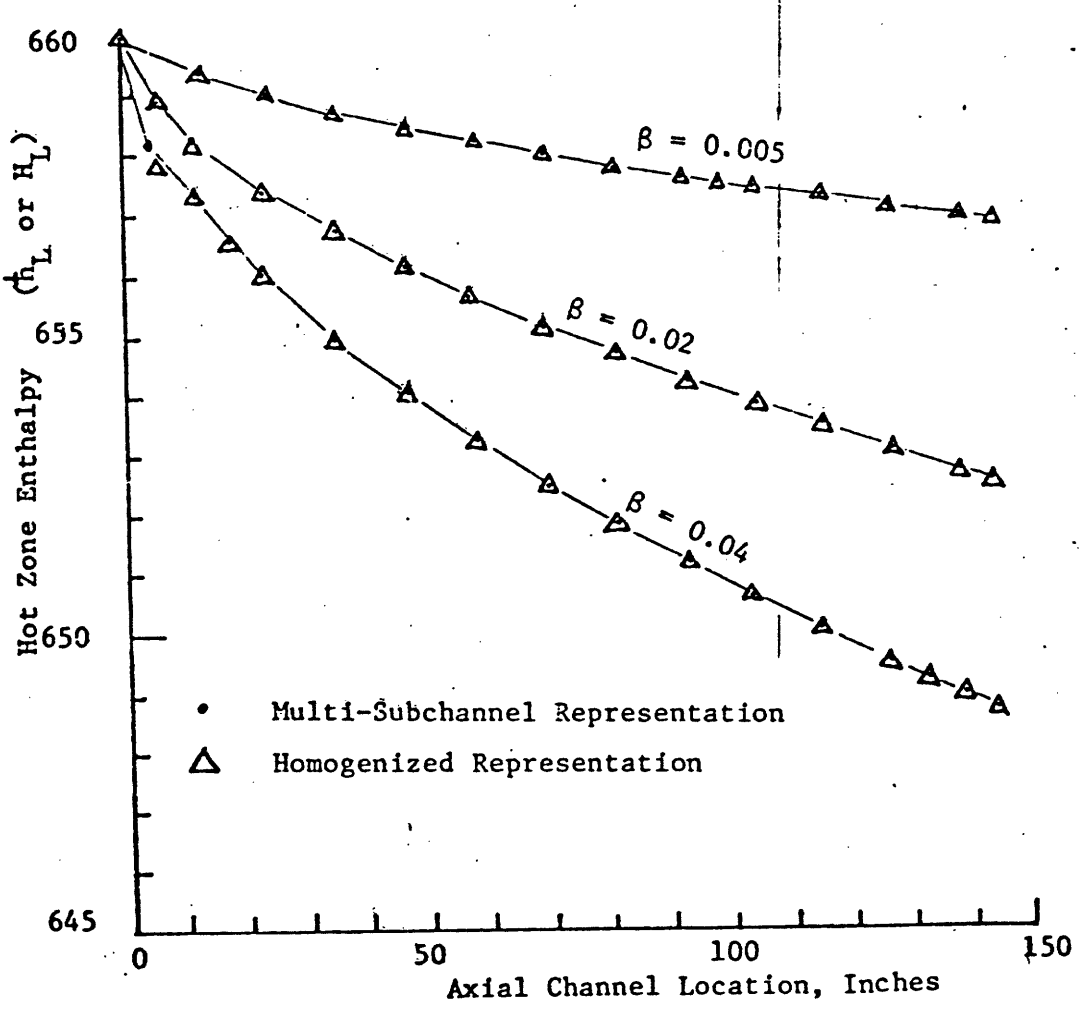

Figure 10. Validity of $N_H(z)$ for ENTHALPY UPSET CASE N = 23

Bundle Geometry	N = 23
	L = 144"
Flow Conditions	$\overline{G}$ = 2.66 Mlbm/hr-ft^2
	F_R = 1.0
Energy Conditions	$\overline{H}$ = 600 Btu/lbm
	$\overline{q}''$ = 0
	H_R = 1.21
	P_R = 1.0
Input Coefficients	β = Variable
	K = 0.5
	S/L = 0.5

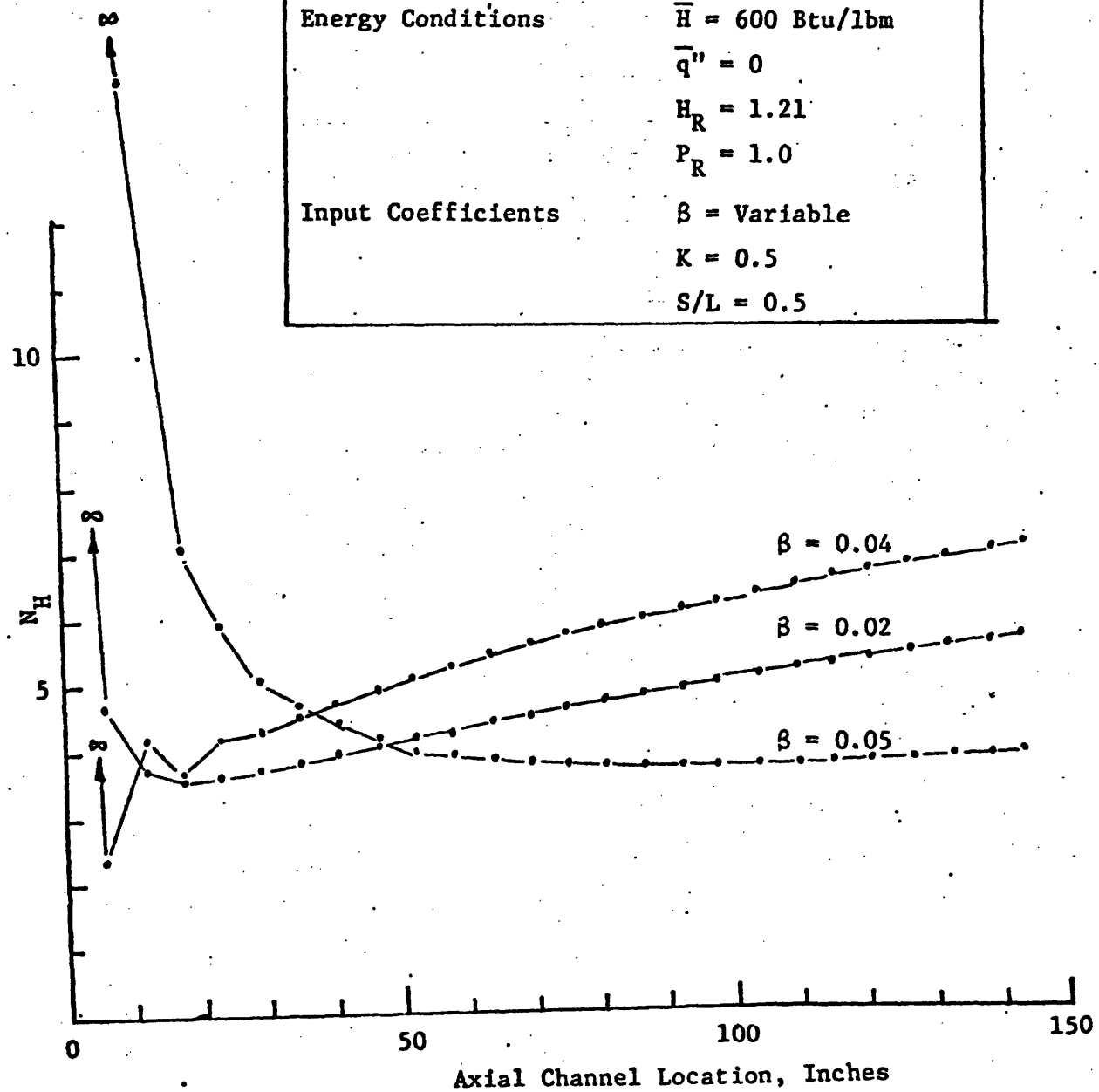

Figure 11. N_H for ENTHALPY UPSET CASE with the gradually changed inlet enthalpy

Bundle Geometry	N = 23
	L = 144"
Flow Conditions	$\bar{G}$ = 2.66 Mlbm/hr-ft^2
	P_R = 1.0
Energy Conditions	$\bar{H}$ = 600 Btu/lbm
	$\bar{q}''$ = 0
	H_R = 1.21
	P_R = 1.0
Input Coefficients	β = Variable
	K = 0.5
	S/L = 0.5

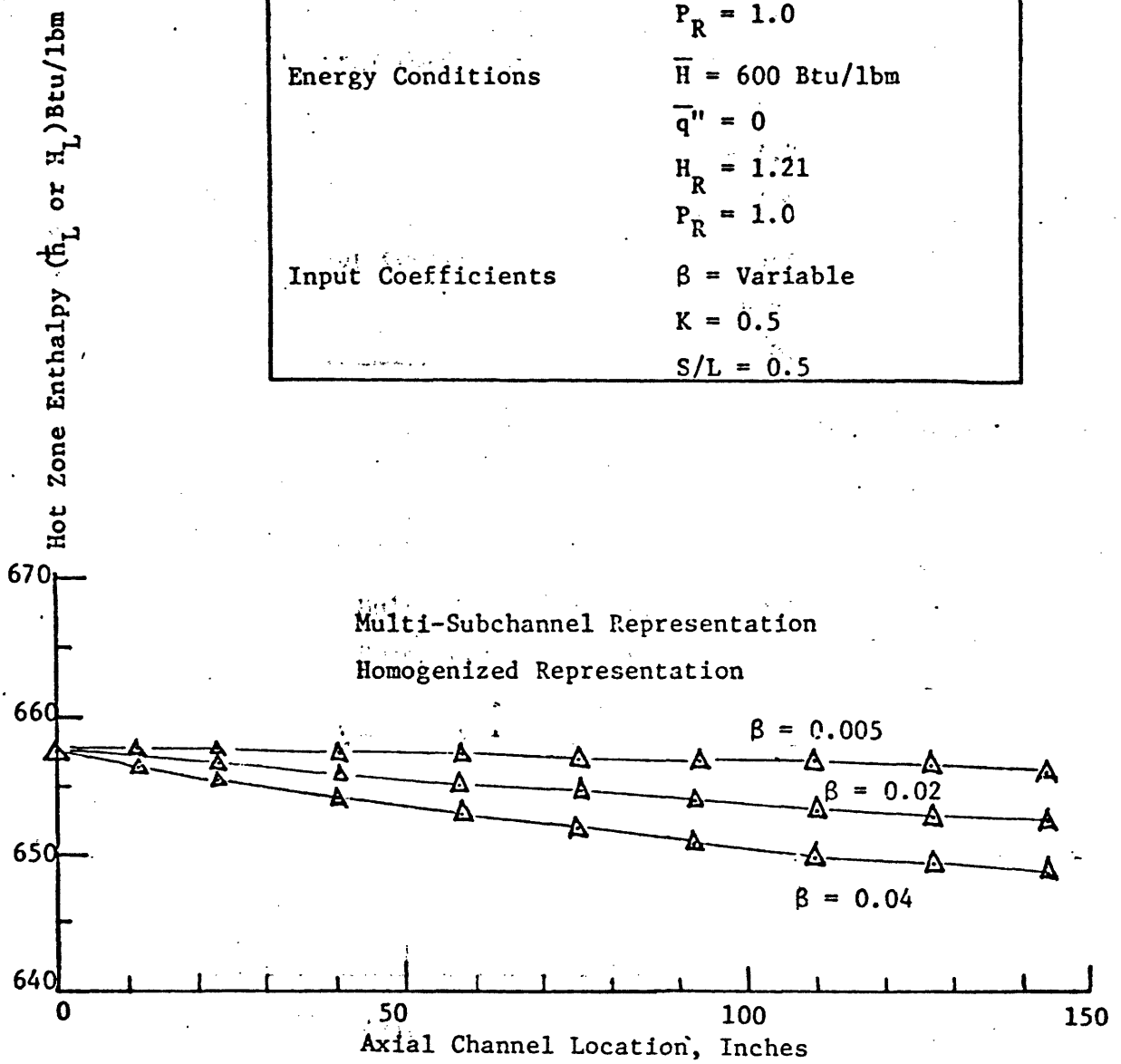

Figure 11a. Validity of N_H for ENTHALPY UPSET CASE

Bundle Geometry	N = Variable
	L = Variable
Flow Conditions	$\overline{G}$ = 2.66 x 10^6 lbm/hr
	F_R = 1.0
Energy Conditions	$\overline{H}$ = 600 Btu/lbm
	$\overline{q}''$ = 0
	H_R = 1.22
	P_R = 1.0
Input Coefficients	β = 0.02
	K = 0.5
	S/L = 0.5

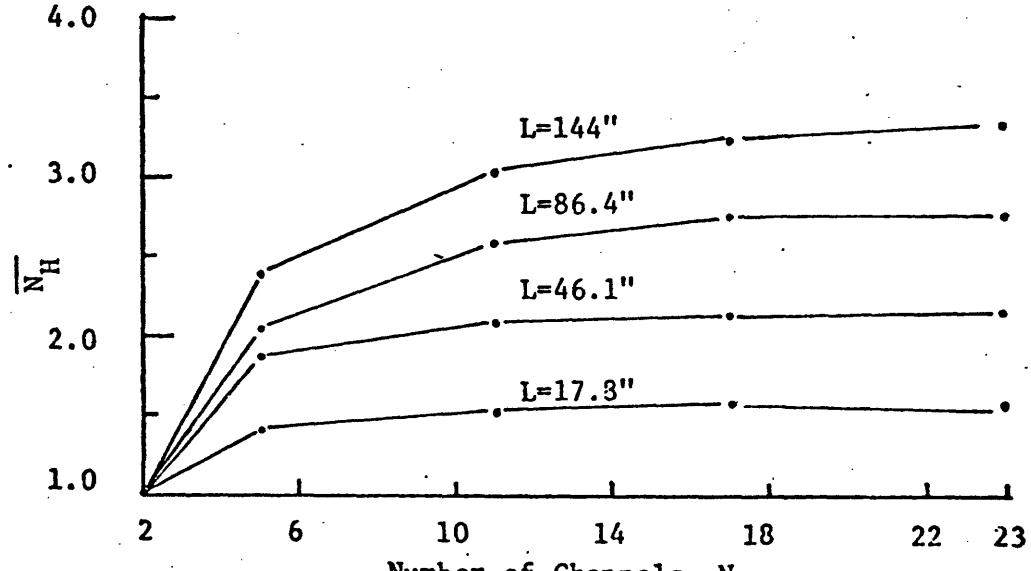

Figure 12. $\overline{N_H}$ versus N

Bundle Geometry	N = 11
	L = Variable
Flow Conditions	$\overline{G}$ = 2.66 Mlbm/ft^2-hr
	F_R = 1.0
Energy Conditions	$\overline{H}$ = 600 Btu/lbm
	$\overline{q}''$ = 0
	H_R = 1.22
	P_R = 1.0
Input Coefficients	β = 0.02
	K = 0.5
	S/L = 0.5

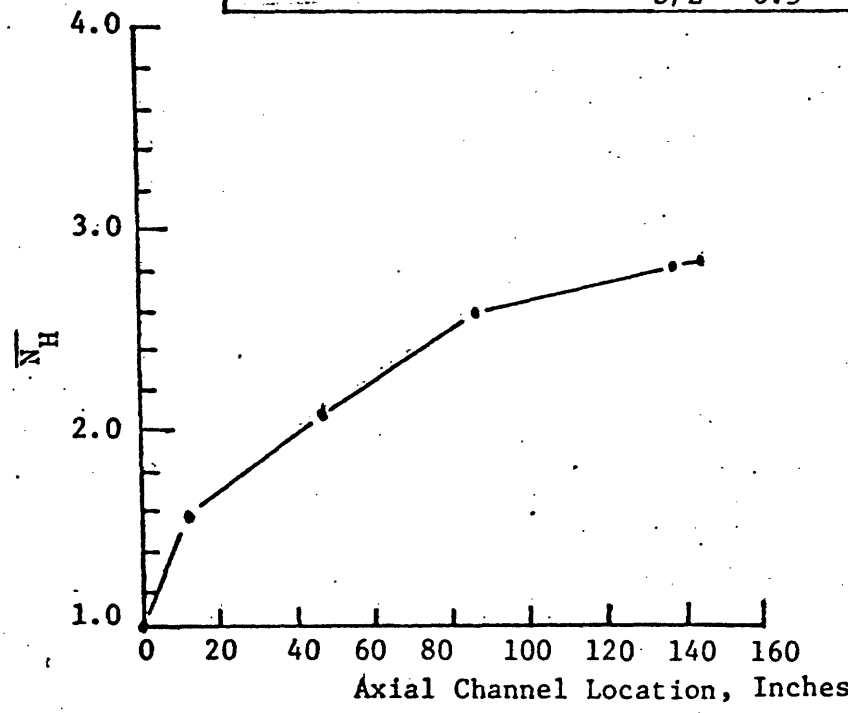

Figure 13. Development of $\overline{N_H}$ through channel length

Bundle Geometry	N = 11
	L = 144"
Flow Conditions	$\bar{G}$ = 2.66 Mlbm/hr-ft^2
	F_R = Variable
Energy Conditions	$\bar{H}$ = 600 Btu/lbm
	$\bar{q}''$ = 0
	H_R = 1.22
	P_R = 1.0
Input Coefficients	β = 0.02
	K = 0.5
	S/L = 0.5

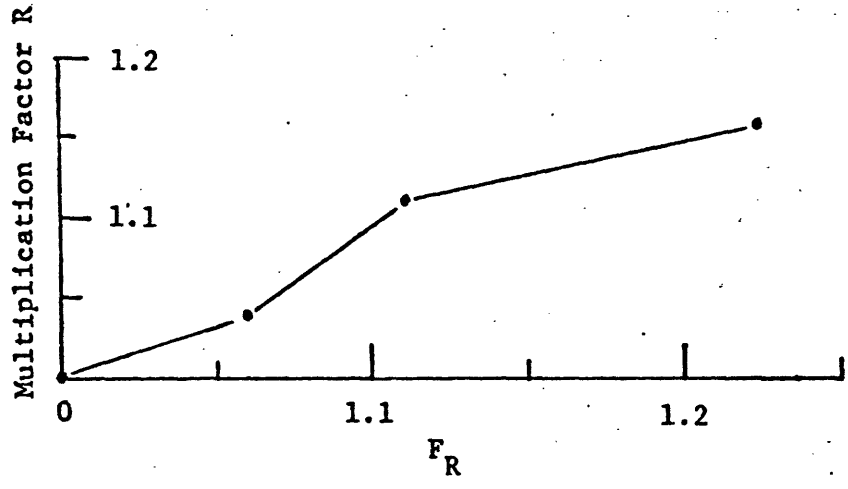

Figure 14. Multiplication factor versus F_R for ENTHALPY and FLOW UPSET CASE

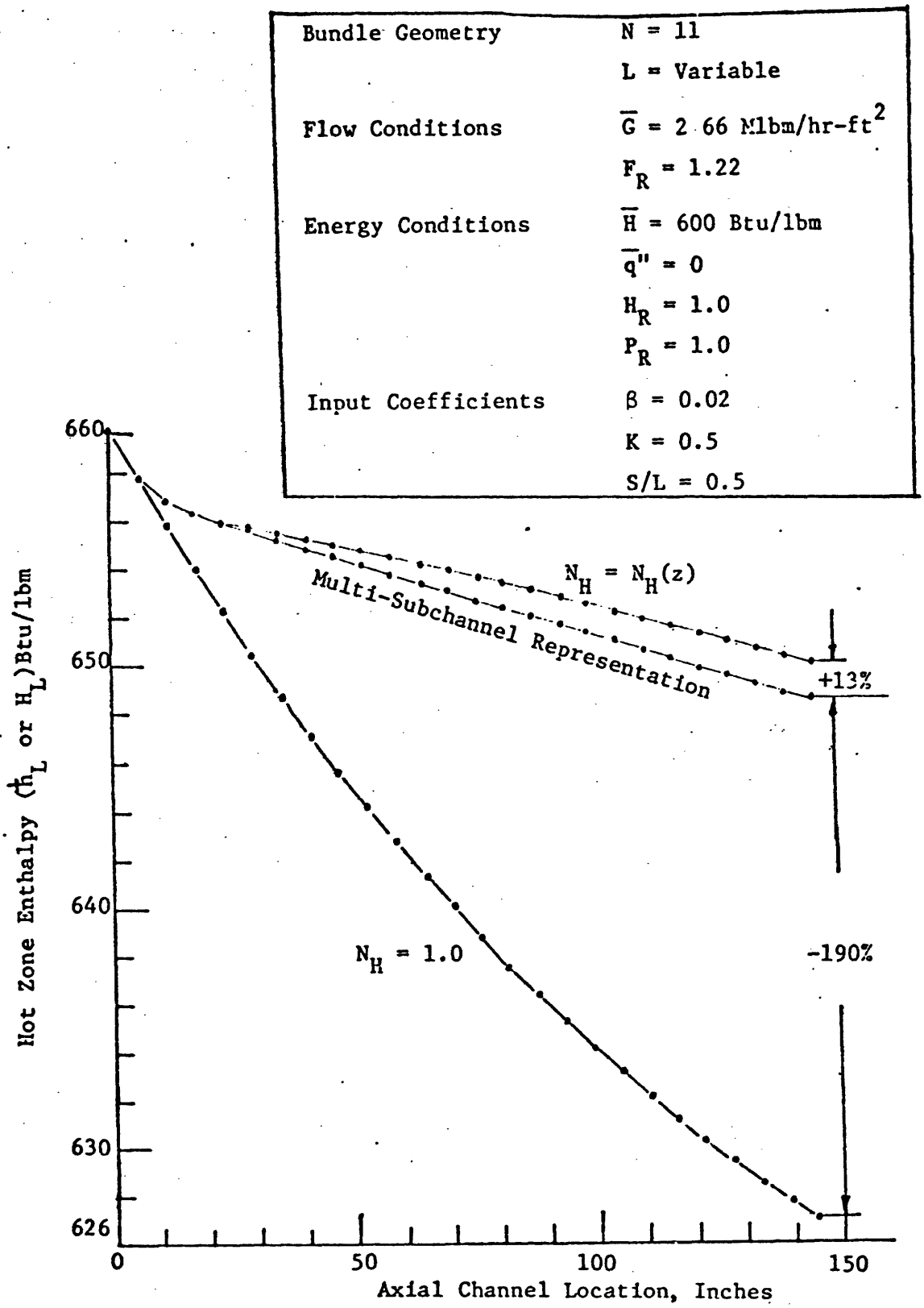

Figure 15. Comparison of multi-subchannel representation and homogenized representations with Enthalpy and Flow Upset

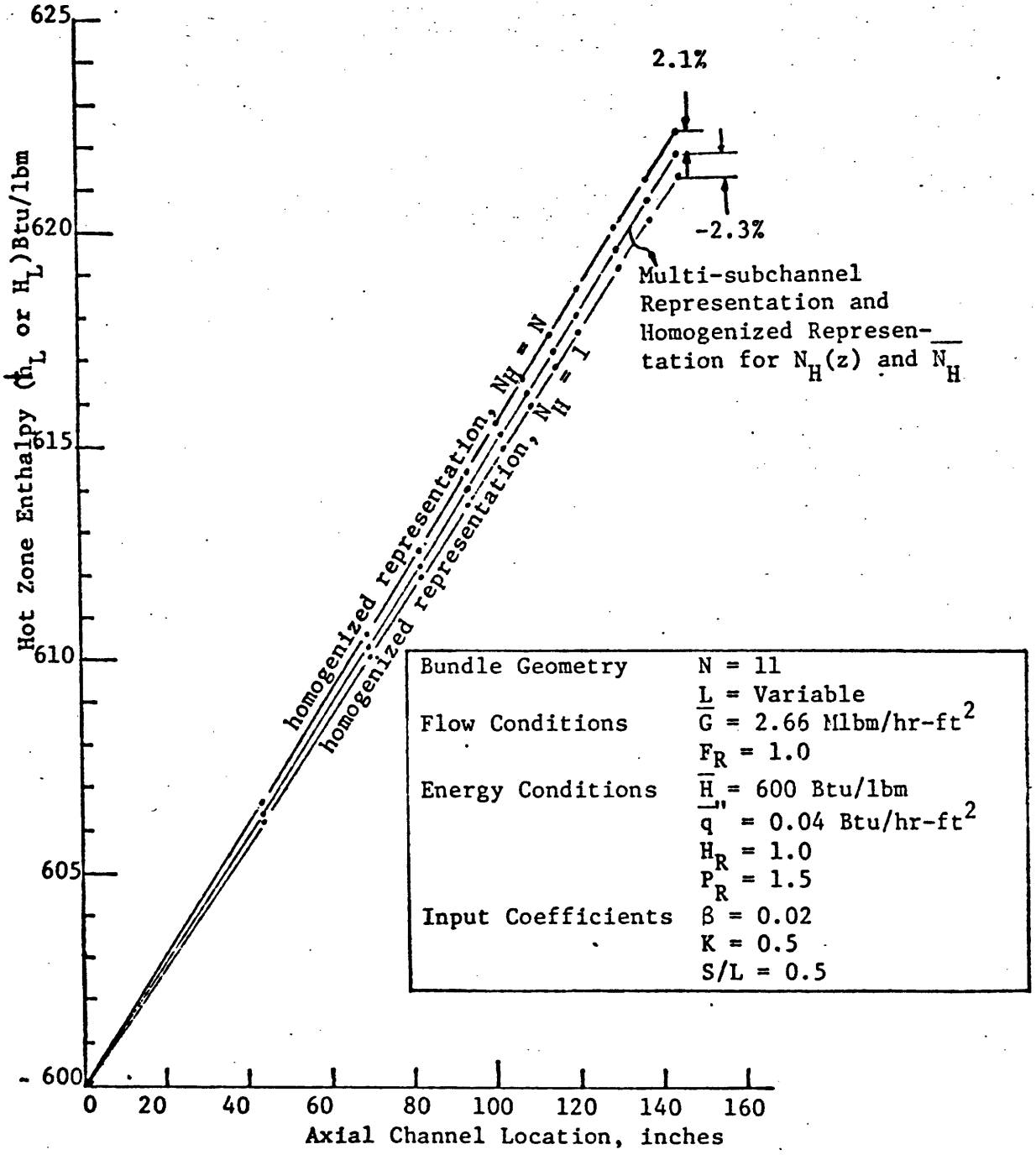

Figure 16. Comparison between results of homogenized representations and multi-subchannel representation for Power Upset Case

Bundle Geometry	N = 5
	L = Variable
Flow Conditions	$\overline{G}$ = 2.66 Mlbm/hr-ft^2
	F_R = 1.0
Energy Conditions	$\overline{H}$ = 600 Btu/lbm
	$\overline{q''}$ = 0.04 MBtu/hr-ft^2
	H_R = 1.0
	P_R = 1.5
Input Coefficients	β = Variable
	K = 0.5
	S/L = 0.5

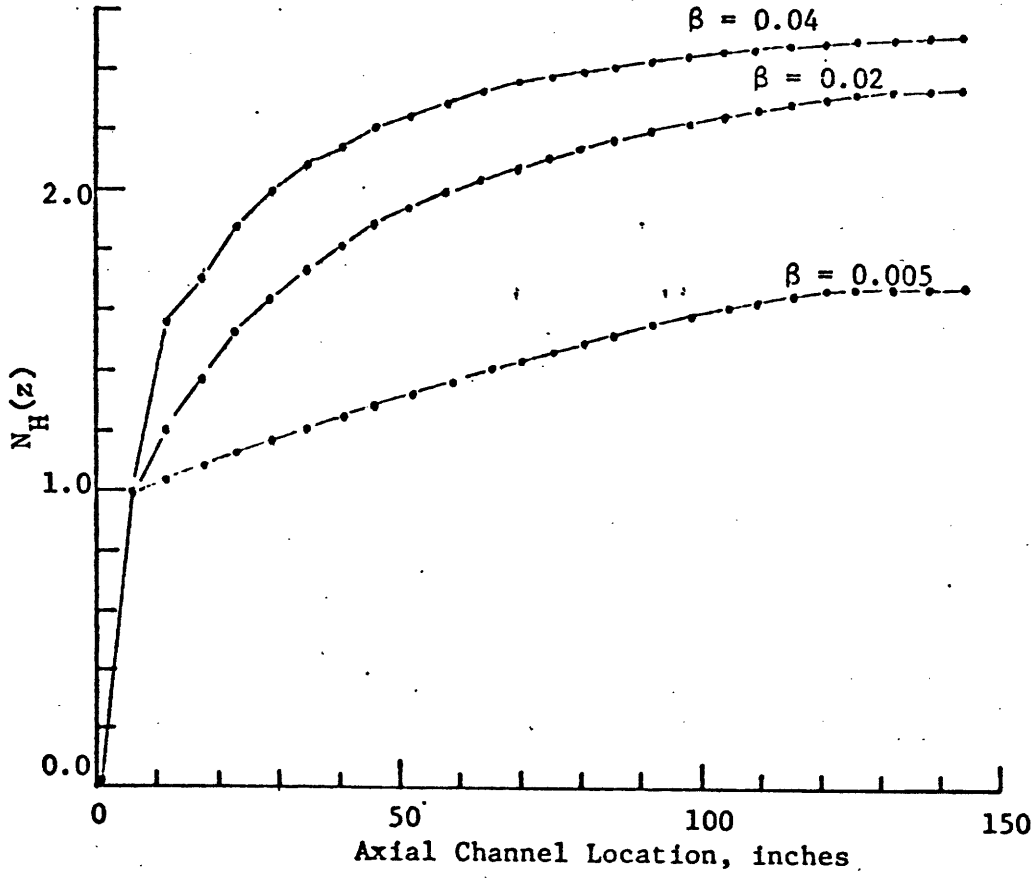

Figure 17. $N_H(z)$ versus channel length for POWER UPSET CASE, N=5

Bundle Geometry	N = 11
	L = Variable
Flow Conditions	$\overline{G}$ = 2.66 Mlbm/hr-ft^2
	F_R = 1.0
Energy Conditions	$\overline{H}$ = 600 Btu/lbm
	$\overline{q''}$ = 0.04 MBtu/hr-ft^2
	H_R = 1.0
	P_R = 1.5
Input Coefficients	β = Variable
	K = 0.5
	S/L = 0.5

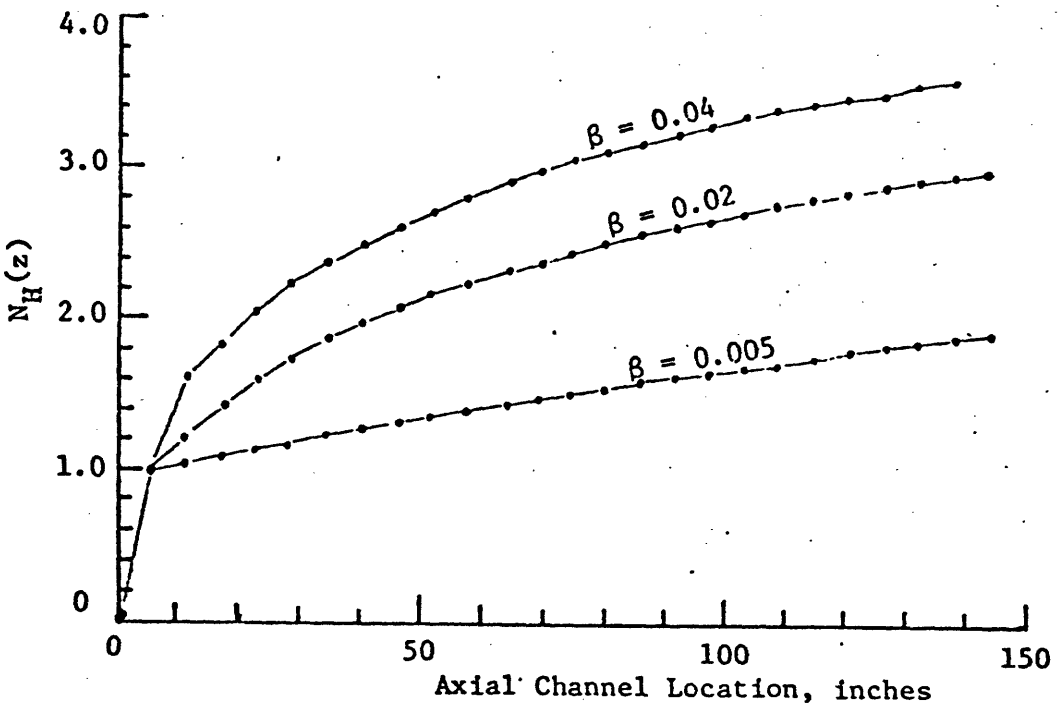

Figure 18. $N_H(z)$ versus channel length for POWER UPSET CASE, N=11

Bundle Geometry	N = 23
	L = Variable
Flow Conditions	$\overline{G}$ = 2.66 Mlbm/hr-ft^2
	F_R = 1.0
Energy Conditions	$\overline{H}$ = 600 Btu/lbm
	$\overline{q''}$ = 0.04 MBtu/hr-ft^2
	H_R = 1.0
	P_R = 1.5
Input Coefficients	β = Variable
	K = 0.5
	S/L = 0.5

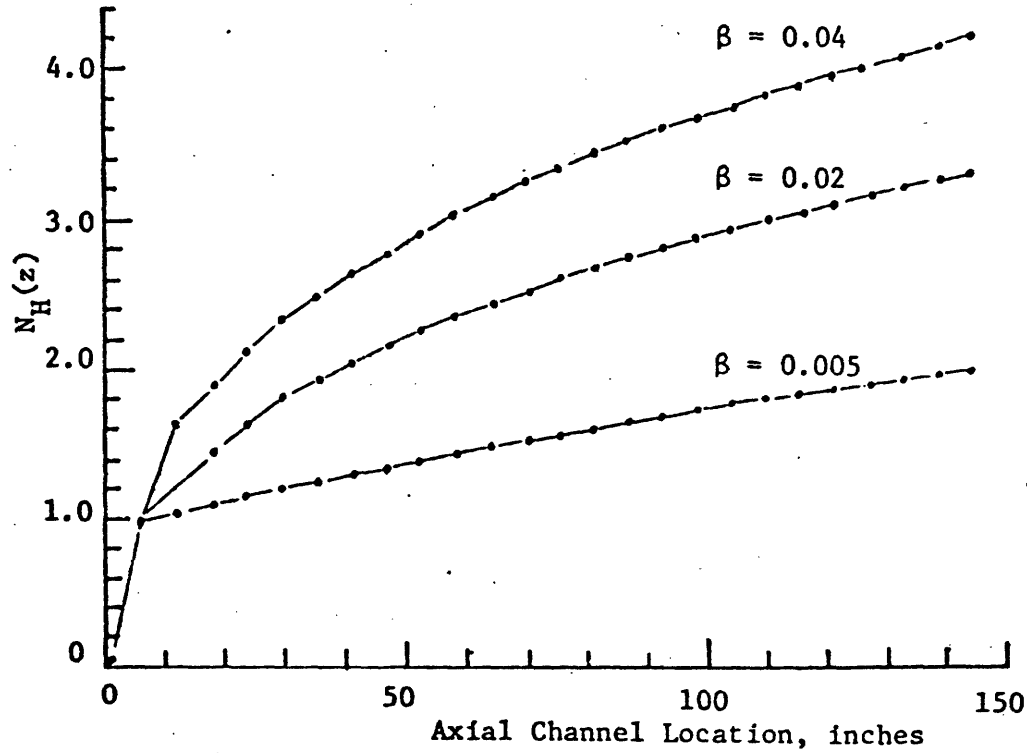

Figure 19. $N_H(z)$ versus channel length for POWER UPSET CASE, N=23

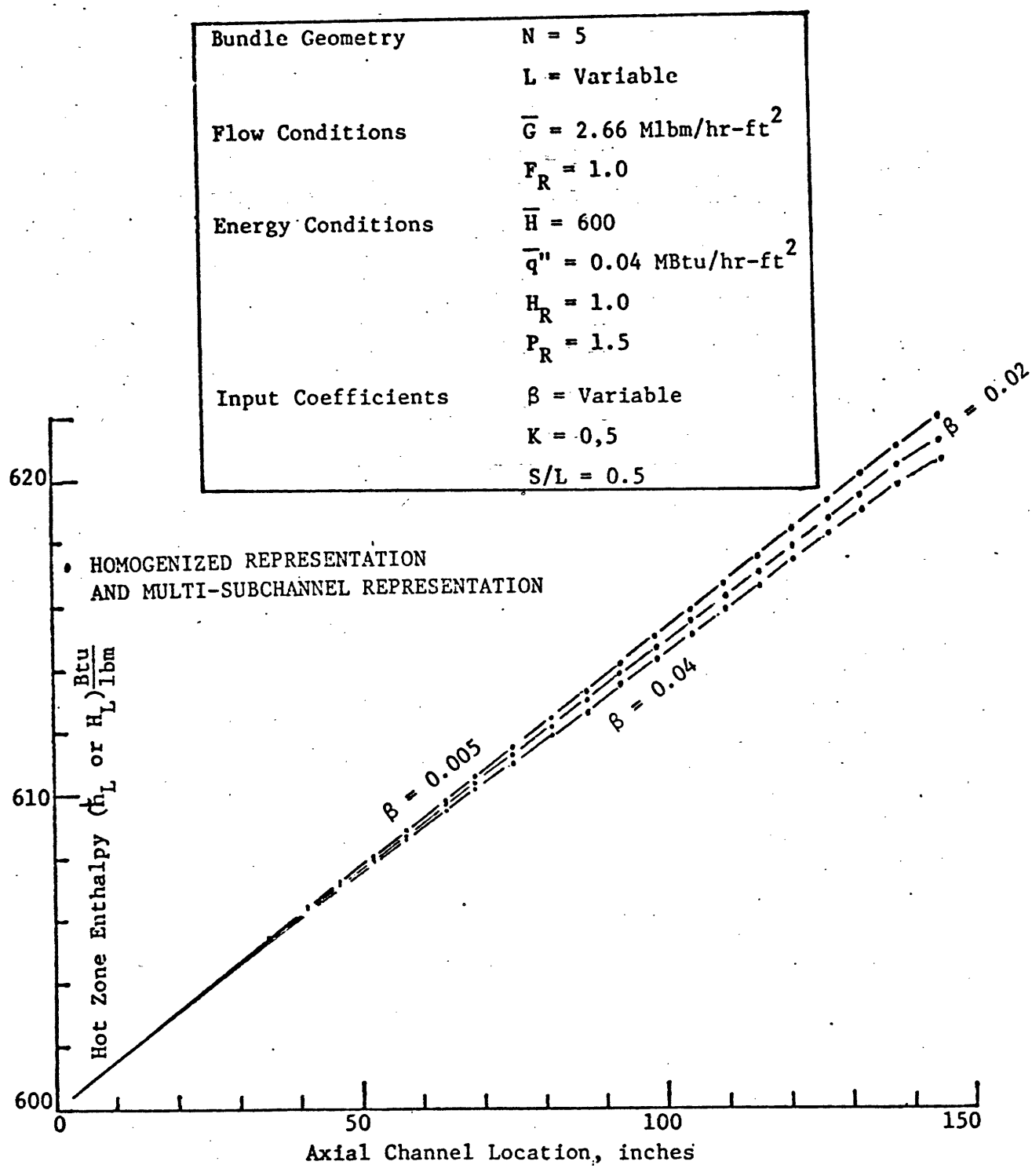

Figure 20. Validity of $N_H(z)$ for POWER UPSET CASE, N=5

Bundle Geometry	N = 11
	L = Variable
Flow Conditions	$\overline{G}$ = 2.66 Mlbm/hr-ft^2
	F_R = 1.0
Energy Conditions	$\overline{H}$ = 600 Btu/lbm
	$\overline{q''}$ = 0.04 x 10^6 Btu/hr-ft^2
	H_R = 1.0
	P_R = 1.5
Input Coefficients	β = Variable
	K = 0.5
	S/L = 0.5

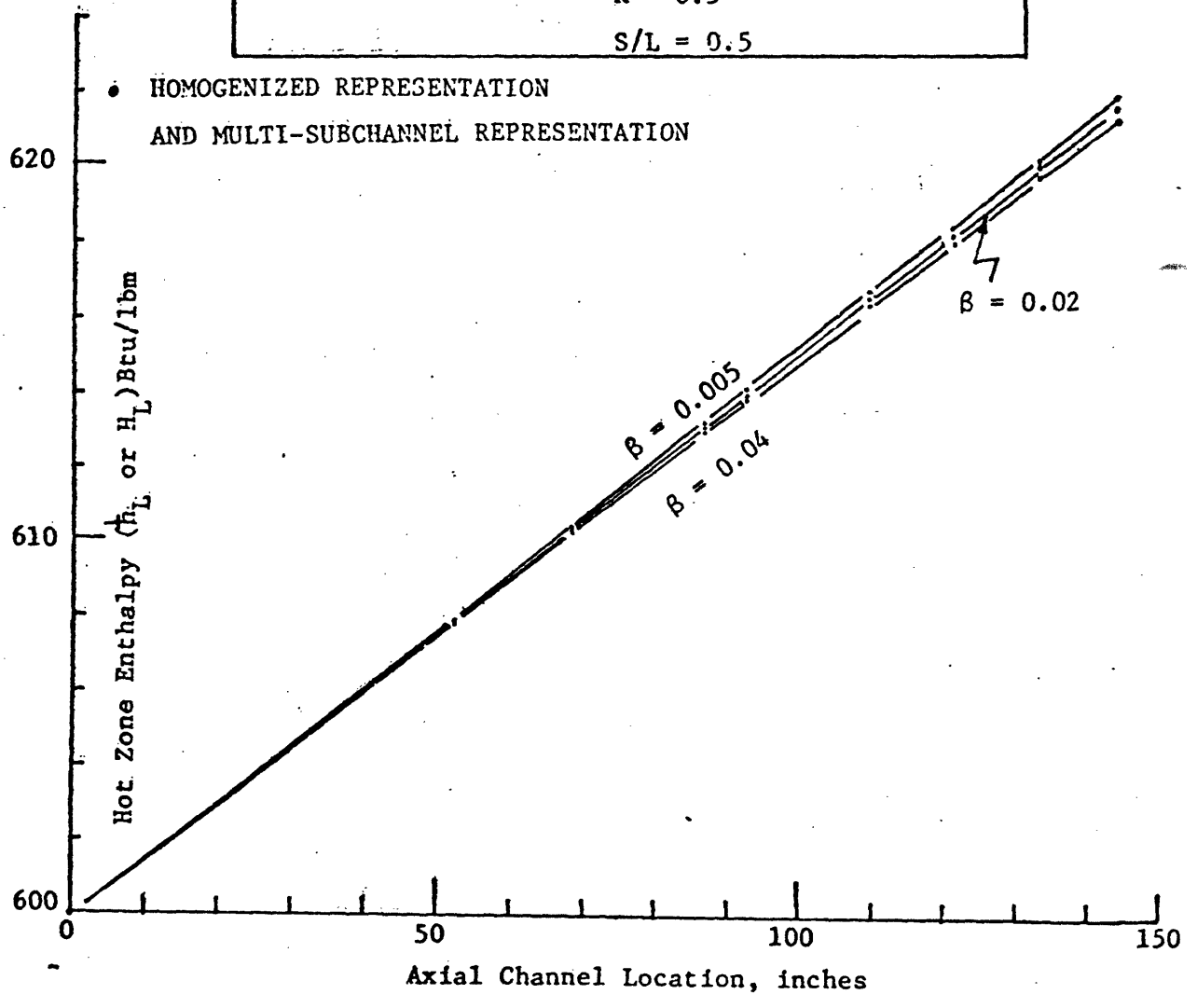

Figure 21. Validity of $N_H(z)$ for POWER UPSET CASE
N = 11

Bundle Geometry	N = 23
	L = Variable
Flow Conditions	$\overline{G}$ = 2.66 Mlbm/hr-ft^2
	F_R = 1.0
Energy Conditions	$\overline{H}$ = 600 Btu/lbm
	$\overline{q}''$ = 0.04 MBtu/hr-ft^2
	H_R = 1.0
	P_R = 1.5
Input Coefficients	β = Variable
	K = 0.5
	S/L = 0.5

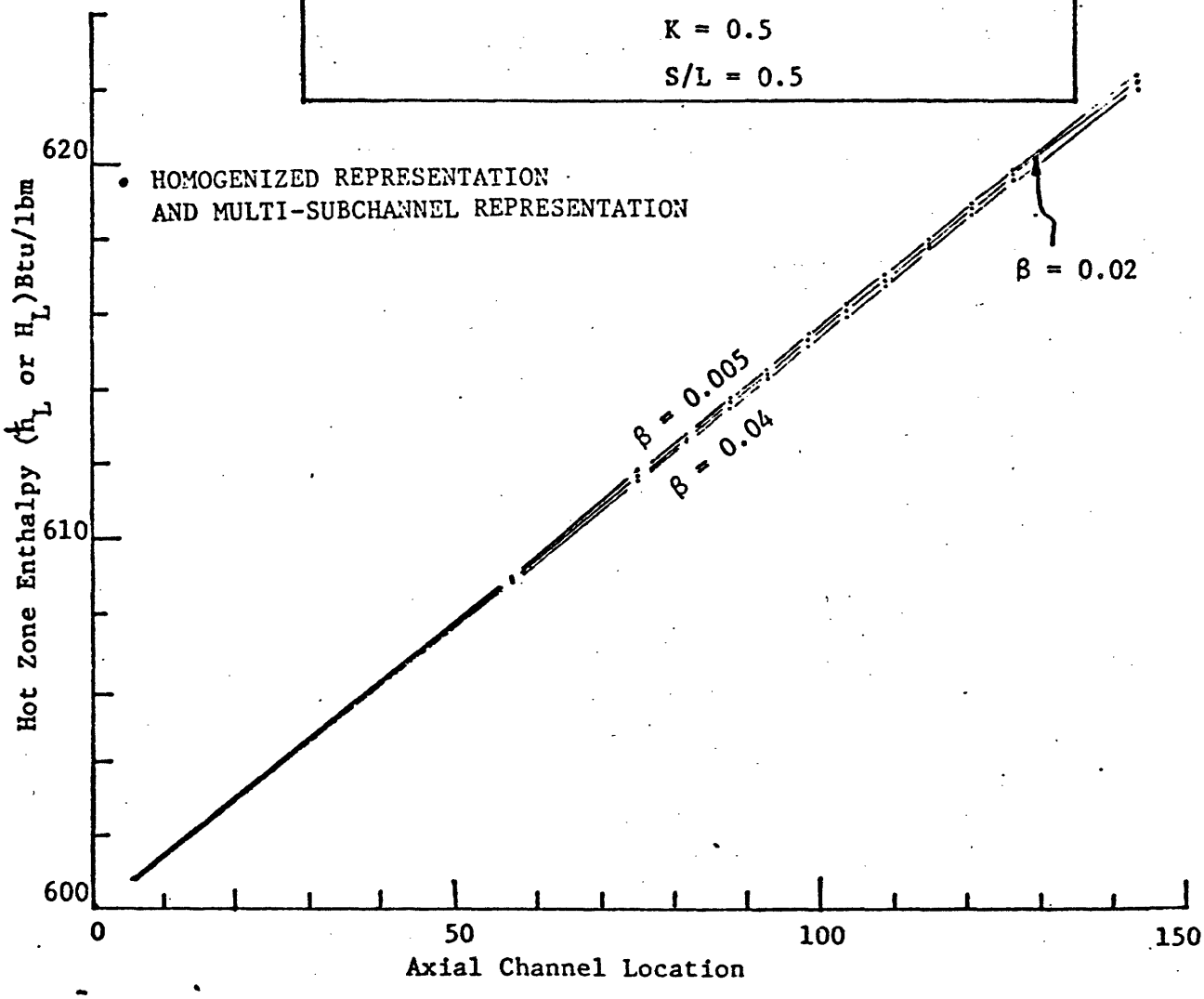

Figure 22. Validity of $N_H(z)$ for POWER UPSET CASE, N=23

Bundle Geometry	N = Variable
	L = Variable
Flow Conditions	$\overline{G}$ = 2.66 Mlbm/ft^2-hr
	F_R = 1.0
Energy Conditions	$\overline{H}$ = 600 Btu/lbm
	$\overline{q}$" = 0.04 MBtu/ft^2-hr
	H_R = 1.0
	P_R = 1.5
Input Coefficients	β = 0.02
	K = 0.5
	S/L = 0.5

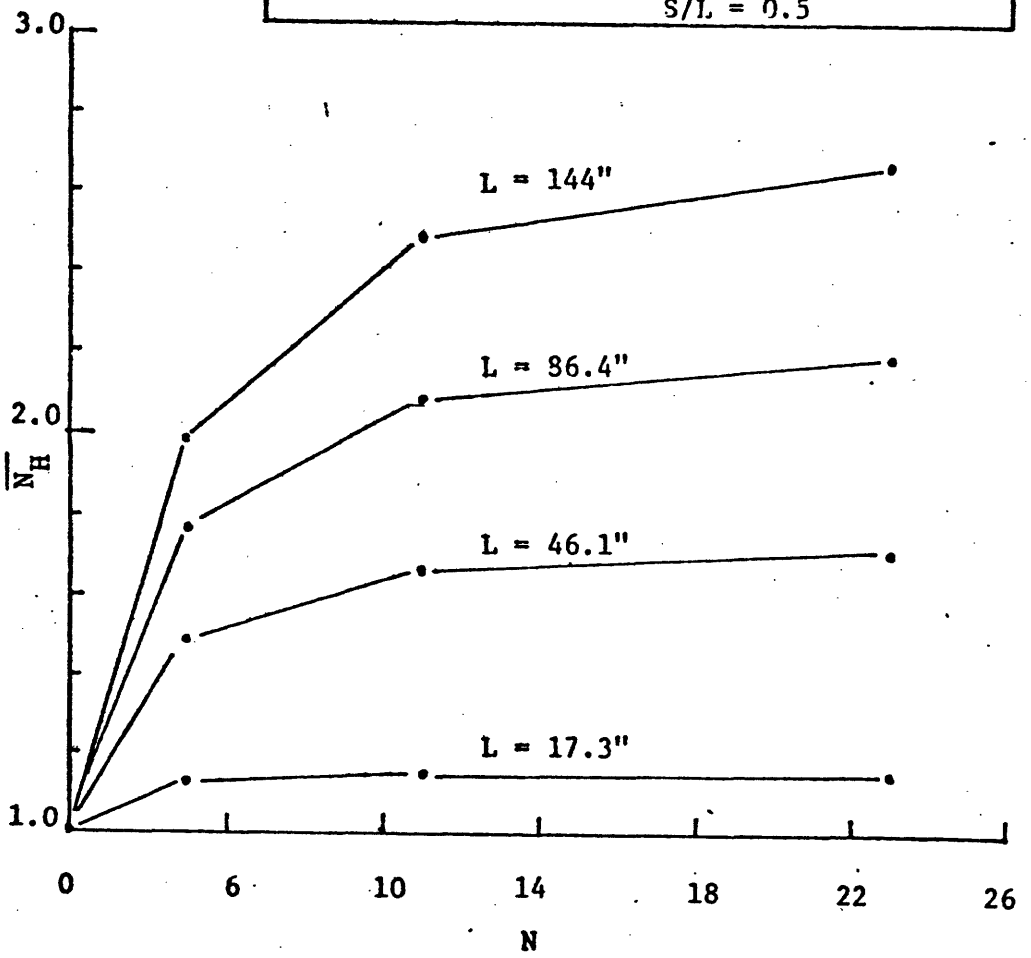

Figure 23. $\overline{N_H}$ versus N and L

Bundle Geometry	N = 11
	L = 144"
Flow Conditions	$\overline{G}$ = 2.66 Mlbm/hr-ft^2
	F_R = Variable
Energy Conditions	$\overline{H}$ = 600 Btu/lbm
	$\overline{q}$"= 0.04 MBtu/hr-ft^2
	H_R = 1.0
	P_R = 1.5
Input Coefficients	β = 0.02
	K = 0.5
	S/L = 0.5

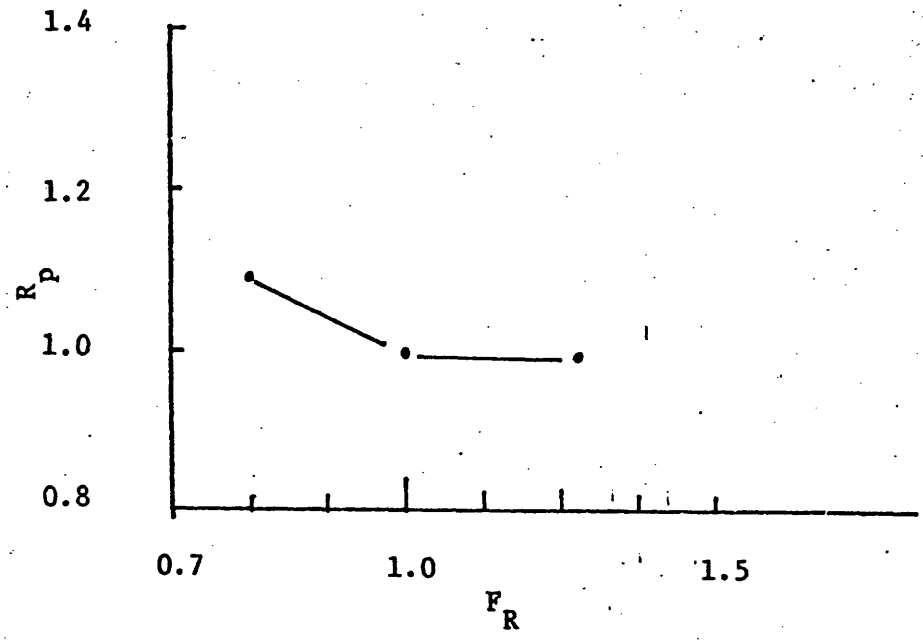

Figure 24. R_p versus F_R

Bundle Geometry	N = 11
	L = 144"
Flow Conditions	G = 2.66 Mlbm/hr-ft^2
	F_R = 1.22
Energy Conditions	$\overline{H}$ = 600 Btu/lbm
	q" = 0.04 MBtu/hr-ft^2
	H_R = 1.0
	P_R = 1.5
Input Coefficients	β = 0.02
	K = 0.5
	S/L = 0.5

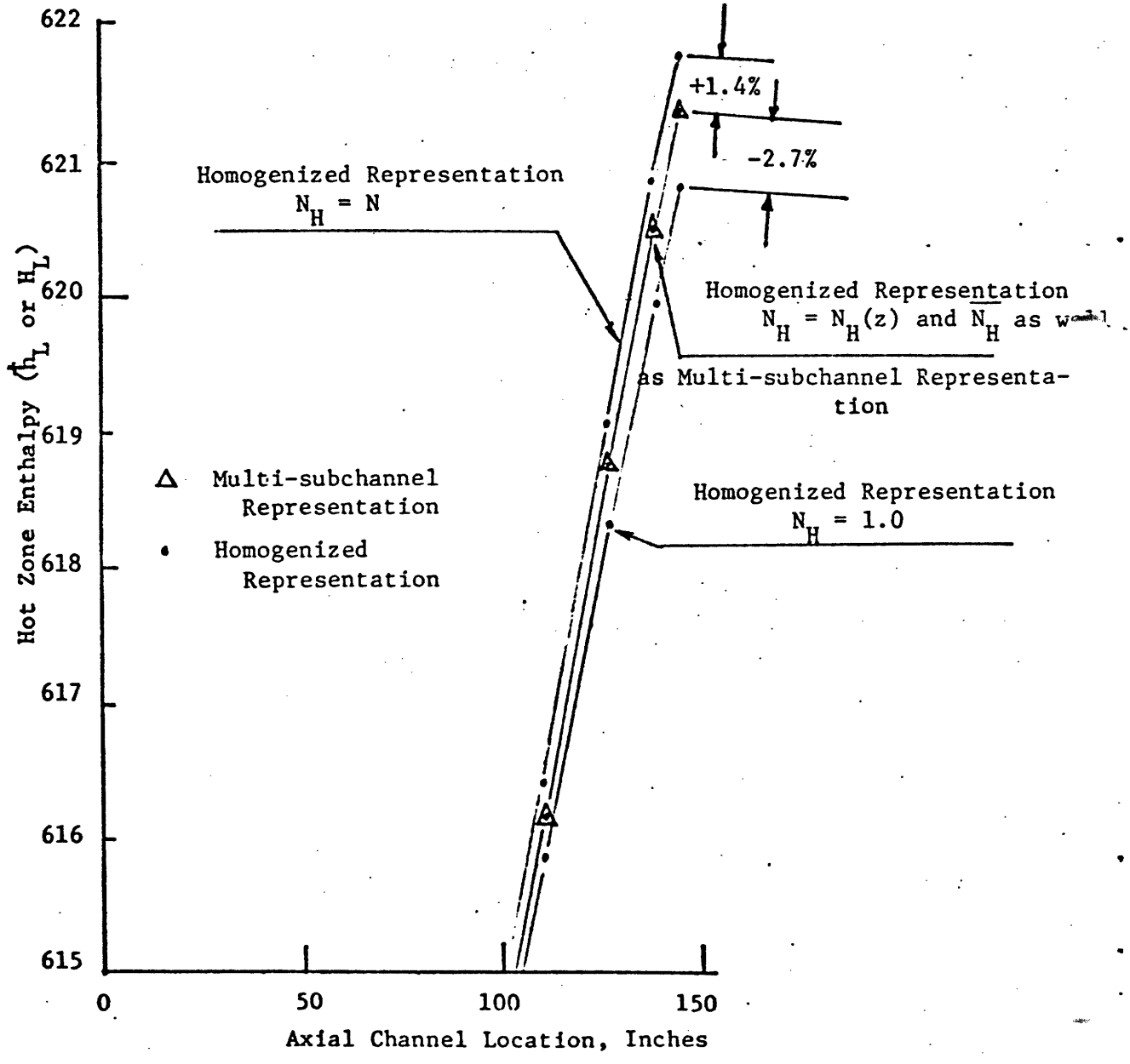

Figure 25. Validity of $N_H(z)$ for POWER and FLOW UPSET CASE in the subchannel exit region

Bundle Geometry	N = 11
	L = 144"
Flow Conditions	$\overline{G}$ = 2.66 Mlbm/ft^2-hr
	F_R = 1.0
Energy Conditions	$\overline{H}$ = 600
	$\overline{q}$" = Variable
	H_R = 1.0
	P_R = 1.5
Input Coefficients	β = 0.02
	K = 0.5
	S/L = 0.5

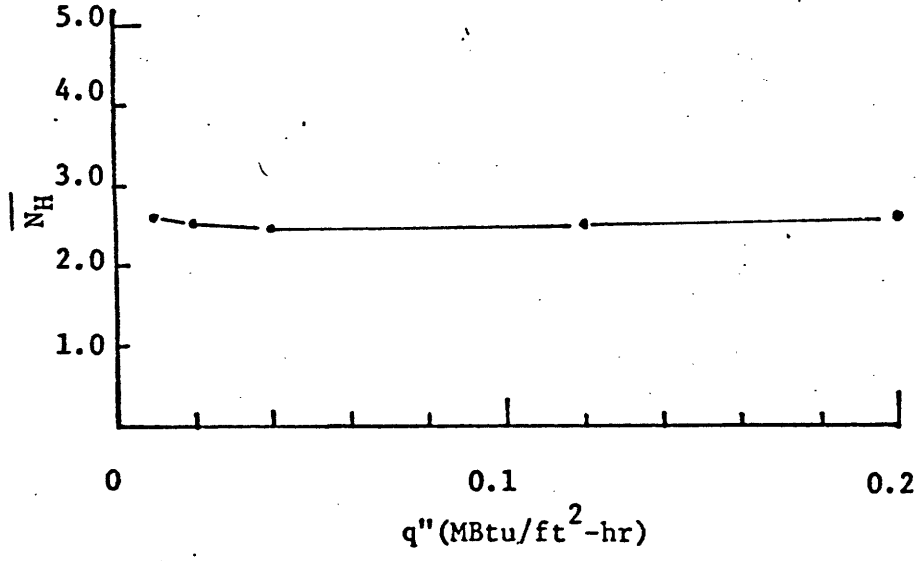

Figure 26. $\overline{N_H}$ versus q"

Bundle Geometry	N = 11
	L = 144"
Flow Conditions	$\overline{G}$ = 2.66 Mlbm/hr-ft^2
	F_R = 1.0
Energy Conditions	$\overline{H}$ = 600 Btu/lbm
	$\overline{q}$" = 0.0
	H_R = Variable
	P_R = 1.0
Input Coefficients	β = 0.02
	K = 0.5
	S/L = 0.5

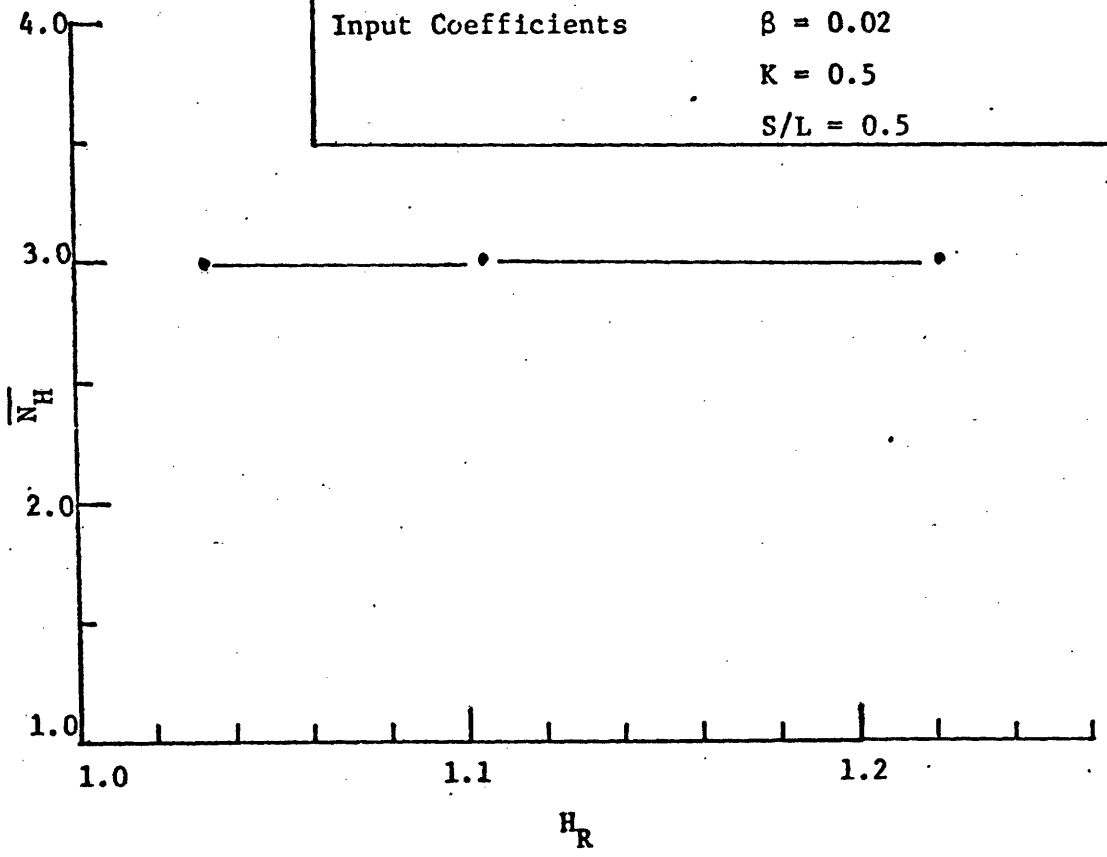

Figure 27. $\overline{N_H}$ versus H_R

Bundle Geometry	N = 11
	L = 144"
Flow Conditions	$\overline{G}$ = 2.66 Mlbm/hr-ft^2
	F_R = 1.0
Energy Conditions	$\overline{H}$ = 600 Btu/lbm
	$\overline{q''}$ = 0.2 MBtu/hr-ft^2
	H_R = 1.0
	P_R = Variable
Input Coefficients	β = 0.02
	K = 0.5
	S/L = 0.5

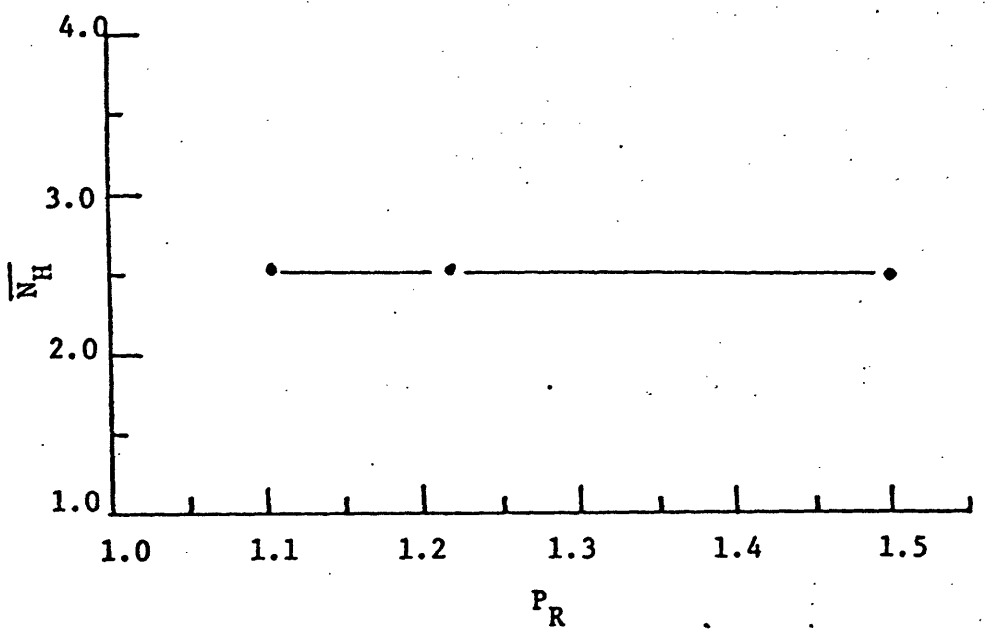

Figure 28. $\overline{N_H}$ versus P_R

Bundle Geometry	N = Variable
	L = 144"
Flow Conditions	$\bar{G}$ = 2.66 Mlbm/hr-ft^2
	F_R = 1.0
Energy Conditions	$\bar{H}$ = 600 Btu/lbm
	$\bar{q}"$ = 0
	H_R = 1.22
	P_R = 1.0
Input Coefficients	β = Variable
	K = 0.5
	S/L = 0.5

β \ N	2	5	11	23
0.005	a = 1.0	a = 3.66 b = 183	a = 6.11 b = 275	a = 6.75 b = 269
0.02	a = 1.0	a = 2.04 b = 9.22	a = 4.36 b = 34.0	a = 5.96 b = 52.4
0.04	a = 1.0	a = 1.93 b = 0.31	a = 4.79 b = 22.7	a = 8.09 b = 54.8

TABLE 1

Coefficients for $N_H(z) = 1.0 + \frac{az}{b+z}$

Under Enthalpy Upset Condition

Bundle Geometry	N = Variable
	L = 144"
Flow Conditions	$\overline{G}$ = 2.66 Mlbm/hr-ft^2
	F_R = 1.0
Energy Conditions	$\overline{H}$ = 600 Btu/lbm
	$\overline{q}''$ = 0
	H_R = 1.22
	P_R = 1.0
Input Coefficients	β = Variable
	K = 0.5
	S/L = 0.5

$\overline{N}_H$

β \ N	2	5	11	23
0	1.00	∿1.00	∿1.00	∿1.00
0.005	1.00	1.77	1.93	2.03
0.02	1.00	2.40	3.03	3.32
0.04	1.00	2.57	3.65	4.23

TABLE 2

$\overline{N}_H$ for Different β and Different N over Z = 0 to 144"
Under Enthalpy Upset Condition

Bundle Geometry	N = Variable
	L = 144"
Flow Conditions	$\overline{G}$ = 2.66 Mlbm/hr-ft^2
	F_R = 1.0
Energy Conditions	$\overline{H}$ = 600 Btu/lbm
	$\overline{q}$" = 0.04 MBtu/hr-ft^2
	H_R = 1.0
	P_R = 1.5
Input Coefficients	β = Variable
	K = 0.5
	S/L = 0.5

β \ N		2	5	11	23
0.005	a	1.0	0.96	0.95	0.94
	b	1.0	314	383	384
	c	0.0	2.60	3.6	3.9
0.02	a	1.0	0.82	0.75	0.73
	b	-	48.5	70.6	81.1
	c	0.0	1.94	3.4	4.0
0.04	a	1.0	0.096	0.47	1.2
	b	1.0	10.8	38.8	124
	c	0.0	2.60	4.00	5.00

TABLE 3

Coefficients for $N_H(z) = a + \frac{cz}{b+z}$ Under Power Upset Condition, Where z is the Channel Location

Bundle Geometry	N = Variable
	L = 144"
Flow Conditions	$\bar{G}$ = 2.66 Mlbm/hr-ft^2
	F_R = 1.0
Energy Conditions	$\bar{H}$ = 600 Btu/lbm
	$\bar{q}$" = 0.04 MBtu/hr-ft^2
	H_R = 1.0
	P_R = 1.5
Input Coefficients	β = Variable
	K = 0.5
	S/L = 0.5

β \ N	2	5	11	23
0	1	∿1	∿1	∿1
0.005	1	1.51	1.61	1.66
0.02	1	2.0	2.49	2.67
0.04	1	2.33	3.05	3.20

TABLE 4

$\bar{N}_H$ For Different N and β Under The Power Upset Condition

z = 144"

Bundle Geometry	N = 11
	L = 144"
Flow Conditions	$\bar{G}$ = 2.66 Mlbm/hr-ft^2
	F_R = 1.0
Energy Conditions	$\bar{H}$ = 600 Btu/lbm
	$\bar{q}''$ = 0.2 MBtu/hr-ft^2
	H_R = 1.0
	P_R = 1.5
Input Coefficients	β = 0.02
	K = 0.5
	S/L = 0.5

	$\Delta\bar{h}_{T.I.}$ (Btu/lbm)
Multi-Subchannel Representation	-3.096

Homogenized Representation	$\Delta H_{T.I.}$ (Btu/lbm)	ERROR %
$N_H(z)$, $N_U(z)$, $N_{TU}(z)$, N_{TF} and N_{TP}	-3.012	-2.7%
$N_H(z)$, $N_U(z)$	-3.012	-2.7%
$N_H(z)$	-3.012	-2.7%
N_H = 1.0	-7.07	+128.4%

$$\text{ERROR} \equiv \frac{\Delta H_{T.I.} - \Delta\bar{h}_{T.I.}}{\Delta\bar{h}_{T.I.}}$$

TABLE 5

Comparison of the hot zone enthalpy increments due to turbulent interchange only between the multi-subchannel representation and the homogenized representations with different combination of coupling coefficients for Power Upset Case

Bundle Geometry	N = 11
	L = 144"
Flow Conditions	$\bar{G}$ = 2.66 Mlbm/hr-ft^2
	F_R = 1.0
Energy Conditions	$\bar{H}$ = 600 Btu/lbm
	$\bar{q}''$ = 0.2 MBtu/hr-ft^2
	H_R = 1.0
	P_R = 1.5
Input Coefficients	β = 0.02
	K = 0.5
	S/L = 0.5

	$\Delta\bar{h}_{D.C.}$ (Btu/lbm)
Multi-Subchannel Representation	0.244

Homogenized Representation	$\Delta H_{D.C.}$ (Btu/lbm)	ERROR %
$N_H(z)$, $N_U(z)$, $N_{TU}(z)$, N_{TF} and N_{TP}	0.251	3.0%
$N_H(z)$, $N_U(z)$	0.253	3.8%
$N_H(z)$	0.261	7.1%
N_H = 1.0	0.001	-99.6%

$$\text{ERROR} \equiv \frac{\Delta\bar{h}_{D.C.} - \Delta H_{D.C.}}{\Delta\bar{h}}$$

TABLE 6

Comparison of the hot zone enthalpy increments due to diversion crossflow only between the multi-subchannel representation and the homogenized representations with different combination of coupling coefficients for Power Upset Case

Bundle Geometry	N = 11
	L = 144"
Flow Conditions	$\bar{G}$ = 2.66 Mlbm/hr-ft^2
	F_R = 1.0
Energy Conditions	$\bar{H}$ = 600 Btu/lbm
	$\bar{q}"$ = 0.2 MBtu/hr-ft^2
	H_R = 1.0
	P_R = 1.5
Input Coefficients	β = 0.02
	K = 0.5
	S/L = 0.5

	$\int w_{C,D}(z)dz$ (Btu/hr)
Multi-Subchannel Representation	0.1758

Homogenized Representation	$\int W_{L,R}(z)dz$(Btu/hr)	ERROR %
$N_H(z)$, $N_U(z)$, $N_{TU}(z)$, N_{TP} and N_{TF}	0.1776	2.2%
$N_H(z)$, $N_U(z)$	0.1798	2.3%
$N_H(z)$	0.1825	3.8%
N_H = 1.0	0.1120	-36.3%

$$\text{ERROR} \equiv \frac{\int W_{L,R}dz - \int w_{C,D}dz}{\int w_{C,D}dz}$$

TABLE 7

Comparison of the total diversion crossflow only across the boundary between the multi-subchannel representation and the homogenized representations with different combination of coupling coefficients for Power Upset Case

TABLE 8

EXPECTED ERRORS IN 2D HOMOGENIZED REGION ENTHALPY FOR POWER UPSET CASE

β \ N	2	3	4	5	7	9	11	15	23
0.0	0	0	0	0	0	0	0	0	0
0.005	0	-0.66	-0.61	-0.53	-0.40	-0.33	-0.27	-0.206	-0.135
0.02	0	-3.4	-3.6	-3.2	-2.3	-2.0	-1.72	-1.3	-0.86
0.04	0	-7.83	-8.5	-7.56	-5.31	-4.63	-3.9	-2.83	-1.83
0.06	0	-13.3	-14.4	-12.3	-9.34	-7.4	-6.12	-4.53	-2.36

NOTE: This table is built by using

$$\text{ERROR\%} = \frac{1 - \frac{1}{\overline{N_H}}}{\frac{P_R N A_s}{(P_R-1)L\beta S} - \frac{1}{\overline{N_H}}} \qquad \text{Equation E.20}$$

where $L = 12'$
$A_s = 0.00519\ ft^2$
$P_r = 1.5$
$S = 0.22"$

$$\overline{N_H} = 1 + \ln\{1 + [353(\frac{N-2}{N})^{\frac{3.5\beta}{0.015+\beta}} \beta^{1.1}]\} \pm 5\% \qquad \text{Equation 5.1.1}$$

APPENDIX A

ANALYTIC DERIVATION OF TWO DIMENSIONAL TRANSPORT COEFFICIENTS FOR THE ENERGY CONSERVATION EQUATION

This Appendix will present, for a two dimensional problem, an analytical deduction of two of such coefficients (N_H, N'_H) that are required in the energy conservation equation. It may be divided into two parts, first an analytical calculation is performed in order to find the enthalpy along the core and across the section chosen.

In the second part those transport coefficients are calculated for two particular cases and they are compared against values obtained by using the computer code COBRA IIIC/MIT and already presented in Chapter 4 of this Volume.

The two most severe simplifications introduced in this analysis are to assume that there is no diversion crossflow, and to solve the problem in only two dimensions.

A.1 Problem Statement

The energy conservation equation used in COBRA IIIC/MIT is

$$h_{J+1}(A) = h_J(A) + \frac{q'_{J+\frac{1}{2}}(A) * \Delta x}{M_J(A)} - \frac{\Delta x}{M_J(A)} \sum_B w'_J(A,B)(h_J(A)-h_J(B)) - \frac{\Delta x}{M_J(A)} \sum_B w_J(A,B)(h^*_J - h_J(A)) \qquad (A.1)$$

where

$h_{J+1}(A)$ is the enthalpy of Channel A at axial station J+1

$h_J(A)$ is the enthalpy of Channel A at axial station J

$q'_{J+\frac{1}{2}}(A)$ is the linear heat generation rate of Channel A at station $J+\frac{1}{2}$

Δx is the length of the axial step

$M_J(A)$ is the massflow rate of Channel A at axial station J

$w'_J(A,B)$ is the interchange of mass between Channel A and one of its adjacent Channels B, due to turbulence at axial station J.

$w_J(A,B)$ is the massflow that leaves Channel A toward Channel B at axial station J

h^*_J is the enthalpy at axial station J of the donor channel (either A or B depending on the sign of $w_J(A,B)$)

Working with lumped channels, the code will take for $h_J(A) - h_J(B)$ and h_J^* the values obtained for the lumped regions (channels A and B) while in fact those enthalpies should be those of the closest subchannel to the lumped region boundaries.

The idea is then to obtain the relationship between these enthalpy values or algebraically to obtain:

$$\frac{1}{N_H(J)} \equiv \frac{(h_J(a) - h_J(b))}{(h_J(A) - h_J(B))} \qquad (A.2)$$

where a and b will be either the two complete subchannels closest to the boundary when that boundary separates two full subchannels or the two half subchannels closest to the boundary when the boundary splits an actual subchannel into two halfs. For the case of Figure(A.1 a and b will be then taken as two half subchannels

$$\frac{1}{N_H'(J)} \equiv \frac{h_J(a)}{h_J(A)} \text{ or } \frac{h_J(b)}{h_J(B)} \qquad (A.3)$$

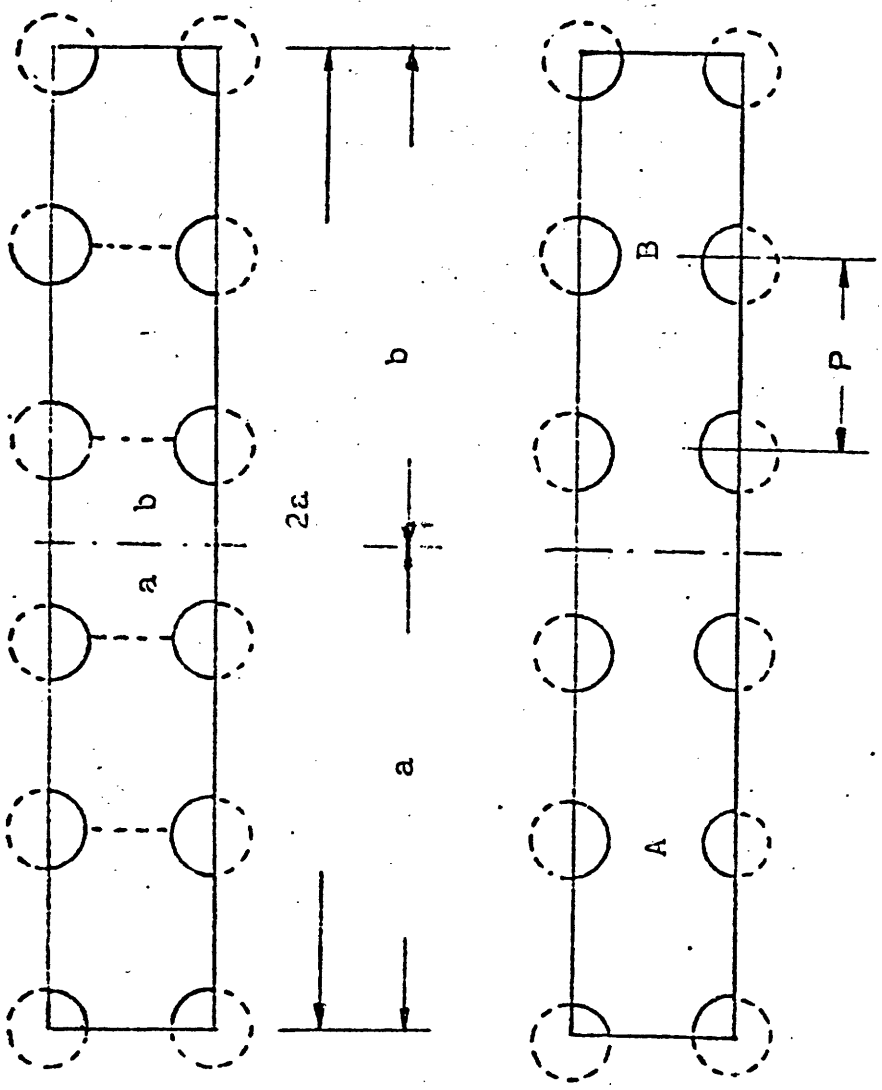

Two Channel Case and Multichannel Case

Figure A.1

depending on which is the donor channel.

In order to find these coefficients the enthalpies should be found first.

A.2 Solution Procedure

The enthalpies will be found for a two dimensional problem utilizing an analytical procedure. Several assumptions will be introduced in the development and they will be pointed out when they appear.

The differential energy conservation equation is:

$$\rho c_p \frac{DT}{Dt} = \text{div}\,(k\nabla T) + w_i + T\beta \frac{DP}{Dt} + \mu\,\Phi \qquad (A.4)$$

Neglecting viscous and compressibility effects (which in fact are not going to affect the present problem) and for two dimensions (x,z):

$$\rho c_p \left[\frac{\partial T}{\partial t} + \frac{\partial}{\partial z}(v_z T) + \frac{\partial}{\partial x}(v_x T)\right] = \left[\frac{\partial}{\partial x}\left(k\frac{\partial T}{\partial x}\right) + \frac{\partial}{\partial z}\left(k\frac{\partial T}{\partial z}\right)\right] + w_i \qquad (A.5)$$

For turbulent flows:

$$v = \bar{v} + v' \quad \text{and} \quad T = \bar{T} + T' \qquad (A.6)$$

where overbars indicate time average.

Inserting equation A.6 into A.5 and time averageing, we obtain the following results:

$$\rho c_p \left[\frac{\partial \bar{T}}{\partial t} + \bar{v}_z \frac{\partial \bar{T}}{\partial z} + \bar{v}_x \frac{\partial \bar{T}}{\partial x} \right] = \left[\frac{\partial}{\partial x} \left(k \frac{\partial \bar{T}}{\partial x} - \rho c_p \overline{v_x' T'} \right) + \right.$$

$$\left. \frac{\partial}{\partial z} \left(k \frac{\partial \bar{T}}{\partial z} \right) - \rho c_p \overline{v_z' T'} \right] + w_i \qquad (A.7)$$

Taking now

$$\overline{v_x' T'} \equiv -\epsilon_H \frac{\partial \bar{T}}{\partial x} \qquad (A.8)$$

$$\overline{v_z' T'} \equiv -\epsilon_H \frac{\partial \bar{T}}{\partial z} \qquad (A.9)$$

Assuming that the flow is fully developed, which in fact it is not, because it is well known that some diversion crossflow exists:

$$\bar{v}_x = 0 \qquad (A.10)$$

Assuming also that k is independent of the temperature we can transform A.7 into the following equation:

$$\rho c_p \left[\frac{\partial \bar{T}}{\partial t} + \bar{v}_z \frac{\partial \bar{T}}{\partial z} \right] = \left[(k + \rho c_p \epsilon_H) \frac{\partial^2 \bar{T}}{\partial x^2} + (k + \rho c_p \epsilon_H) \frac{\partial^2 T}{\partial z^2} \right] + w_1$$

(A.11)

Now we neglect axial conduction relative to radial conduction because in fact the first is much smaller than the second:

$$\frac{\partial^2 \bar{T}}{\partial x^2} >> \frac{\partial^2 \bar{T}}{\partial z^2} \qquad (A.12)$$

If we consider only the steady state problem Equation A.11 reduces further to

$$\rho c_p \bar{v}_z \frac{\partial \bar{T}}{\partial z} = (k + \rho c_p \varepsilon_H) \frac{\partial^2 T}{\partial x^2} + w_i \qquad (A.13)$$

Now we define the variable z^*:

$$z^* = \frac{z}{\bar{v}_z} \qquad (A.14)$$

where $\bar{v}_z$ is not a function of x.

$$\rho c_p \frac{\partial \bar{h}}{\partial z^*} = [k + \rho c_p \varepsilon_H] \frac{\partial^2 \bar{h}}{\partial x^2} + c_p w_i \qquad (A.15)$$

This equation can be transformed to obtain:

$$\frac{1}{\left(\frac{k + \rho c_p \varepsilon_H}{\rho c_p}\right)} \frac{\partial \bar{h}}{\partial z^*} = \frac{\partial^2 \bar{h}}{\partial x^2} + \frac{c_p w_i}{k + \rho c_p \varepsilon_H} \qquad (A.16)$$

It is also known that the interchange of energy due to molecular interactions is much smaller than that due to turbulence, therefore:

$$a_t^* \equiv \frac{k + \rho c_p \varepsilon_H}{\rho c_p} \approx \varepsilon_H \qquad (A.17)$$

and equation (A.16) yields:

$$\frac{1}{a_t^*} \frac{\partial \bar{h}}{\partial z^*} = \frac{\partial^2 \bar{h}}{\partial x^2} + \frac{w_i}{\rho \varepsilon_H} \qquad (A.18)$$

The analogous equation for transient one dimensional heat conduction is:

$$\frac{1}{a_t} \frac{\partial T}{\partial t} = \frac{\partial^2 T}{\partial x^2} + \frac{q'''}{k} \qquad (A.19)$$

Hence analogous parameters are:

$$T \leftrightarrow \bar{h} \qquad (A.20)$$

$$a_t \leftrightarrow a_t^* \qquad (A.21)$$

$$t \leftrightarrow z^* \qquad (A.22)$$

$$k \leftrightarrow \rho \varepsilon_H \qquad (A.23)$$

We need to solve this equation (A.19) for the geometry and boundary conditions given in figure A.2.

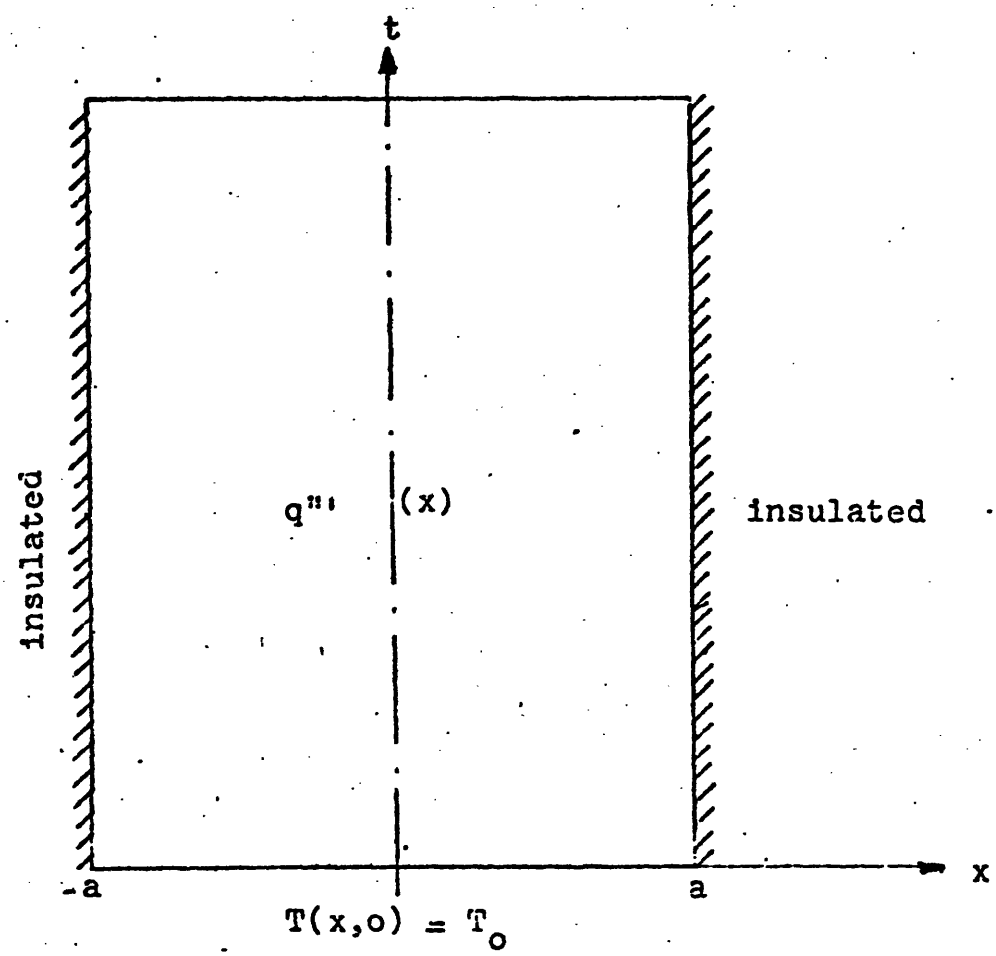

Geometrical Description of the Problem

Figure A.2

A.3 Solution to the Problem

A.3.1 Equation to be solved:

$$\frac{1}{a_t}\frac{\partial T}{\partial t} = \frac{\partial^2 T}{\partial x^2} + \frac{q'''}{k} \qquad \text{(A.24)}$$

A.3.2 Boundary Conditions

For the x-axis:

$$\left.\frac{\partial T(x,t)}{\partial x}\right|_{x = \pm a} = 0 \qquad \text{(A.25)}$$

The initial condition is:

T(x,o) is given by:

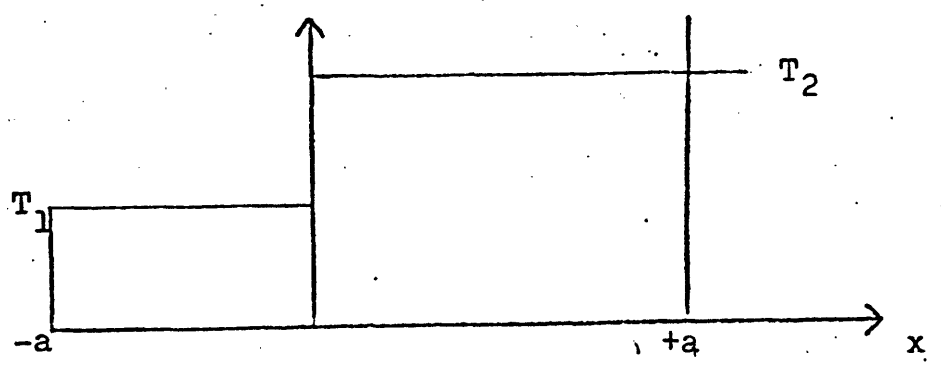

where T_1 and T_2 can be any value.

The heat generation rate will be given by the following equations:

$$q'''(x) = \begin{cases} s_2 - xm_2 & \text{for } -a \leq x < 0 \\ s_1 + (a-x)m_1 & \text{for } 0 < x \leq a \end{cases} \qquad \text{(A.26)}$$

or graphically:

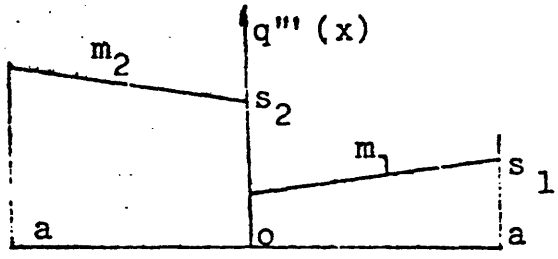

where m_1, m_2, s_1 and s_2 can take any finite value.

A.3.3 Changes of Variables

The following changes of variables will be made:

$$T(x,t) = \psi(x,t) + \phi(x) + \theta(t) \qquad \text{(A.27)}$$

$$q'''(x) = q'''_1 + q'''_2(x) \qquad \text{(A.28)}$$

where q'''_1 will be the average value of $q'''(x)$ along the the x-axis.

$$q_1''' = \frac{\int_{-a}^{a} q'''(x)dx}{\int_{-a}^{a} dx} = \frac{s_1 + s_2}{2} + \frac{a}{4}(m_1 + m_2) = k_1 \qquad (A.29)$$

These changes of variables will produce the following equation:

$$\frac{1}{a_t}\frac{d\theta}{dt} + \frac{1}{a_t}\frac{\partial\psi}{\partial t} = \frac{\partial^2\psi}{\partial x^2} + \frac{d^2\phi}{dx^2} + \frac{k_1}{k} + \frac{q'''_2(x)}{k} \qquad (A.30)$$

From the separation of variables assumed by equation A.27, we can split this equation into three equalities:

$$\frac{1}{a_t}\frac{d\theta}{dt} = \frac{k_1}{k} \qquad (A.31)$$

$$\frac{1}{a_t}\frac{\partial\psi(x,t)}{\partial t} = \frac{\partial^2\psi(x,t)}{\partial x^2} \qquad (A.32)$$

$$\frac{\partial^2\phi(x)}{\partial x^2} = -\frac{q_2'''(x)}{k} \qquad (A.33)$$

The boundary conditions can be also divided as follows:

$$\frac{\partial T(x,t)}{\partial x}\bigg|_{x=\pm a} = 0 \longrightarrow \left(\frac{\partial\psi(x,t)}{\partial x} + \frac{d\phi(x)}{dx}\right)\bigg|_{x=\pm a} = 0 \qquad (A.34)$$

which implies:

$$\left.\frac{\partial \psi(x,t)}{\partial x}\right|_{x=\pm a} = 0 \qquad \text{(A.35)}$$

$$\left.\frac{d\phi}{dx}\right|_{x=\pm a} = 0 \qquad \text{(A.36)}$$

and the initial boundary condition:

$$T(x,o) = \psi(x,o) + \phi(x) + \theta(0) \qquad \text{(A.37)}$$

A.3.3.1 Solution of Equation A.31

This equation is:

$$\frac{d\theta}{dt} = a_t \frac{k_1}{k}$$

which has the solution:

$$\theta(t) = a_t \frac{k_1}{k} t + c_1 \qquad \text{(A.38)}$$

and c_1 will be found from the initial temperature condition, equation A.37.

A.3.3.2 Solution of Equation (A.32)

Assuming it is possible to make the following separation of variables:

$$\psi(x, t) = X(x)\, F(t) \qquad (A.39)$$

Equation A.32 becomes:

$$\frac{1}{a_t F(t)} \frac{dF(t)}{dt} = -\alpha^2 \qquad (A.40)$$

$$\frac{d^2X(x)}{dx^2} + \alpha^2 X(x) = 0 \qquad (A.41)$$

Solving now equation (A.40)

$$F(t) = c_2 e^{-\alpha^2 a_t t} \qquad (A.42)$$

Solving Equation (A.41)

$$X_n(x) = c_3 \sin \alpha_n x + c_4 \cos \alpha_n x \qquad (A.43)$$

Using boundary condition Equation A.35:

$$\left.\frac{\partial \psi(x,t)}{\partial x}\right|_{x=\pm a} = F(t) \left.\frac{iX(x)}{i\,x}\right|_{x=\pm a} = 0 \qquad (A.44)$$

From the previous equation we can conclude:

$$\left.\frac{\partial \bar{X}(x)}{\partial x}\right|_{x=\pm a} = 0 \qquad (A.45)$$

This implies:

$$c_3 \alpha_n \cos \alpha_n a - c_4 \alpha_n \sin \alpha_n a = 0 \qquad (A.46)$$

$$c_3 \alpha_n \cos \alpha_n a + c_4 \alpha_n \sin \alpha_n a = 0 \qquad (A.47)$$

In order to have a solution other than trivial case of $c_3 = c_4 = 0$, we must have

$$0 = \begin{vmatrix} \cos \alpha_n a & -\sin \alpha_n a \\ \cos \alpha_n a & \sin \alpha_n a \end{vmatrix} = \sin 2\alpha_n a \qquad (A.48)$$

From Equation A.48 we can conclude:

$$\alpha_n = \frac{n\pi}{2a} \quad \text{with } n = 0,1,2,3\ldots\ldots \qquad (A.49)$$

From Equation A.46 we can relate c_3 and c_4:

$$c_3 = c_4 \tan \alpha_n a \qquad (A.50)$$

Plugging this equation into Equation A.43 we can obtain:

$$X_n(x) = c_4' \cos \alpha_n (x-a) \qquad (A.51)$$

$$c_3 \sin \alpha_n x + c_4 \cos \alpha_n x =$$

$$= c_4 \left[\frac{\sin \alpha_n a \sin \alpha_n x + \cos \alpha_n a \cos \alpha_n x}{\cos \alpha_n a} \right]$$

$$= \frac{c_4}{\cos \alpha_n a} \left[\cos \alpha_n (x-a) \right]$$

These results lead finally to:

$$\psi(x,t) = \sum_{n=1}^{\infty} c_n \cos \alpha_n (x-a) e^{-\alpha_n^2 a_t t} \qquad (A.52)$$

so far we have obtained $\theta(t)$ and $\psi(x,t)$ and we still have to find $\phi(x)$.

A.3.3.3 Solution of Equation A.3.3

This equation is:

$$\frac{d^2\phi(x)}{dx^2} = - \frac{q_2'''(x)}{k}$$

It is possible to express $q_1'''(x)$ plus $q_2'''(x)$ as a Fourier series:

$$q'''(x) = b_o + \sum_{n=1}^{\infty} b_n \cos \alpha_n(x-a) \qquad (A.53)$$

where

$$b_o = \frac{\int_{-a}^{a} q'''(x)dx}{\int_{-a}^{a} dx} = q_1''' = k_1 \qquad (A.54)$$

and

$$b_n = \frac{\int_{-a}^{a} q'''(x) \cos \alpha_n(x-a)dx}{\int_{-a}^{a} \cos^2 \alpha_n(x-a)dx} \qquad (A.55)$$

It is clear from equations A.53 and A.54 and A.28 that:

$$q_2'''(x) = \sum_{n=1}^{\infty} b_n \cos \alpha_n(x-a) \qquad (A.56)$$

where b_n is calculated from A.55, its value being:

$$b_n = \frac{1}{a\alpha_n}\left[\left[(s_1-s_1) + m_1 a\right] \sin \alpha_n a - \frac{m_1}{\alpha_n}(1-\cos \alpha_n a) - \frac{m_2}{\alpha_n}\right.$$

$$\left.(\cos \alpha_n a - \cos 2\alpha_n a) \right] \qquad (A.57)$$

Now integrating equation A.33:

$$\frac{d\phi(x)}{dx} = \frac{1}{k} \sum_{n=1}^{\infty} \frac{b_n}{\alpha_n} \sin \alpha_n(x-a) + c_5 \qquad (A.58)$$

applying the boundary conditon of equation A.36

$$\left.\frac{d\phi(x)}{dx}\right|_{x=\pm a} = 0 \quad \Longrightarrow \quad c_5 = 0 \qquad (A.59)$$

and integrating again we finally have

$$\phi(x) = \frac{1}{k} \sum_{n=1}^{\infty} \frac{b_n}{\alpha_n^2} \cos \alpha_n(x-a) + c_6 \qquad (A.60)$$

A.3.4 Final Result

Combining equations (A.60), (A.52), and (A.38):

$$T(x,t) = c_1 + \frac{a_t k_1 t}{k} + \sum_{n=0}^{\infty} c_n \cos \alpha_n(x-a) e^{-\alpha_n^2 a_t t} +$$

$$+ \frac{1}{k} \sum_{n=1}^{\infty} \frac{b_n}{\alpha_n^2} \cos \alpha_n(x-a) \qquad (A.61)$$

where we have combined the old c_1 and c_6 in only one constant, c_1.

In this expression, c_1 and c_n are still unknown and they have to be found from the initial boundary condition.

Expressing T(x,o) as the following Fourier series:

$$T(x,o) = b'_o + \sum_{n=1}^{\infty} b'_n \cos \alpha_n(x-a) \qquad (A.62)$$

where:

$$b'_o = \frac{\int_{-a}^{a} T(x,o)dx}{\int_{-a}^{a} dx} = \frac{T_1 + T_2}{2} \qquad (A.63)$$

and b'_n can be found by setting $m_1 = m_2 = 0$,

$s_1 = T_2$ and $s_2 = T_1$ in equation A.57:

$$b'_n = \frac{1}{a\alpha_n} (T_2 - T_1) \sin \alpha_n a \qquad (A.64)$$

Plugging equations (A.63) and (A.64) into (A.62):

$$T(x,o) = \frac{T_1 + T_2}{2} + \sum_{n=1}^{\infty} \frac{T_2 - T_1}{a\alpha_n} \sin \alpha_n a \cos \alpha_n(x-a) \qquad (A.65)$$

Comparing this equation with equation (A.61) when t = 0 we obtain:

$$c_1 + \sum_{n=0}^{\infty} c_n \cos \alpha_n(x-a) + \frac{1}{k}\sum_{n=1}^{\infty} \frac{b_n}{\alpha_n^2} \cos \alpha_n(x-a) =$$

$$= \frac{T_1 + T_2}{2} + \sum_{n=1}^{\infty} \frac{T_2 - T_1}{a\alpha_n} \sin \alpha_n a \cos \alpha_n(x-a) \qquad (A.66)$$

or:

$$c_1 + c_o + \sum_{n=1}^{\infty} \left(c_n + \frac{b_n}{k\alpha_n^2} - \frac{T_2 - T_1}{a\alpha_n} \sin \alpha_n a\right) \cos \alpha_n(x-a)$$

$$= \frac{T_1 + T_2}{2} \qquad (A.67)$$

Equation A.67 leads to the following conclusions:

$$c_1 + c_o = \frac{T_1 + T_2}{2}$$

$$c_n = \frac{T_2 - T_1}{a\alpha_n} \sin \alpha_n a - \frac{b_n}{k\alpha_n^2} \qquad (A.68)$$

By substituting these two values into equation (A.61) we obtain finally:

$$T(x,t) = \frac{T_1 + T_2}{2} + \frac{a_t k_1 t}{k} + \sum_{n=1}^{\infty} \left\{ \left[\frac{T_2 - T_1}{a\alpha_n} \sin \alpha n_a - \frac{b_n}{k\alpha_n^2} \right] \right.$$

$$e^{-\alpha n^2 a_t t} + \frac{b_n}{k\alpha n^2} \Bigg\} \cos \alpha_n (x-a) \qquad (A.69)$$

which expressed in terms of h, ε_H, $\frac{z}{v_z}$ and $\rho\varepsilon_H$ leads to the final expression:

$$h(x,z) = \frac{h_1 + h_2}{2} + \frac{\varepsilon_H k_1 z}{\rho \varepsilon_H v_z} + \sum_{n=1}^{\infty} \Bigg\{ \Big[\frac{h_2 - h_1}{a\alpha_n} \sin \alpha_n a - \frac{b_n}{\rho \varepsilon_H \alpha_n^2} \Big] e^{-\alpha_n^2 \varepsilon_H z / v_z} + \frac{b_n}{\rho \varepsilon_H \alpha_n^2} \Bigg\} \cos \alpha_n (x-a)$$

$$(A.70)$$

All the terms of these equations, i.e. A.69 and A.70 are known except ε_H, the thermal eddy diffusivity. In order to obtain identical results for $N_H(z)$ using the analytical method to those given by the numerical method, we have to match the energy interchange due to turbulence for every boundary of the problem. This implies that ε_H should be dependent of x and z. However in our analytical derivation ε_H had to be assumed constant to permit solution of the differential equation. So an approximation should be made in order to find an average value of ε_H. This value is calculated using the following equation:

$$\underset{\text{Num.}}{\frac{w'(I,J)(h(I)-h(J))}{M(I)}} = \underset{\text{Analytic}}{\frac{\varepsilon_H \rho s_{ij}}{M(I)} \left.\frac{\partial h}{\partial x}\right|_{gap}} \equiv \underset{\text{T.I.}}{\Delta h(I)} \qquad (A.71)$$

where $\Delta h(I)_{T.I.}$ = enthalpy rise of channel I due to turbulent interchange

Taking w'(I,J) as COBRA does:

$$w'(I,J) = \beta s_{ij} \bar{G} \qquad (A.72)$$

we obtain:

$$\varepsilon_H = \beta \bar{v}_z \frac{(h(I)-h(J))}{\left.\frac{\partial h}{\partial x}\right|_{gap}} \left[\frac{M(I)_{analyt.}}{M(I)_{numer.}}\right] \qquad (A.73)$$

The massflow ratio is required due to the different area of the subchannels in the analytic and the numerical method. (Appendix C, Volume I). The analytic method assumes each subchannel of area:

$$A_{analytic} = Ps_{ij} = .666(.1333) = .074 \text{ in}^2 \qquad A.74$$

while the numerical method takes:

$$A_{numerical} = .1705 \text{ in}^2$$

The ratio:

$$\frac{h(I)-h(J)}{\left.\frac{\partial h}{\partial x}\right|_{gap}} = \bar{z}_{ij} \qquad A.75$$

is dependent upon axial position, radial position and power shape across the boundary. With these parameters, equation A.73 reduces to

$$\varepsilon_H = .434\beta \, \bar{v}_z \bar{z}_{ij} \qquad A.76$$

An average value of the product, $l_{ij} = .434\bar{z}_{ij}$, equal to 0.0035 has been selected as the one that yields best results for all cases of Figures A.3, A.4 and A.5. This value was obtained by comparing analytical and numerical values of $N_H(z)$ for a different set of values of l_{ij}.

It is anticipated that because the solutions exhibit a developing length which decreases with small N and large P, the product will be a function of N, β, and z. The significance of these factors on the numerical value of the product and consequently N_H need further exploration.

Therefore equation A.76 becomes to:

$$\bar{\varepsilon}_H = 0.0035\ \beta v_z \qquad (A.77)$$

and the final expression for h(x,z) will be:

$$h(x,z) = \frac{h_1 + h_2}{2} + \frac{k_1 z}{G} + \sum_{n\ =\ \text{odd}}^{\infty} \left\{ \left[\frac{h_2 - h_1}{a\alpha_n} \sin \alpha_n a - \frac{b_n}{0.2\beta\bar{G}\alpha_n^2} \right] e^{-\alpha_n^2 z \beta 0.0035} + \frac{b_n}{0.2\beta\bar{G}\alpha_n^2} \right\}$$

$$\cos \alpha_n (x-a) \qquad (A.78)$$

with:

$$k_1 = \frac{s_1 + s_2}{2} + \frac{a}{4}(m_1 + m_2) \qquad (A.29)$$

$$b_n = \frac{1}{a\alpha_n}\left[\left[(s_1 - s_2) + m_1 a\right]\sin\alpha_n a - \frac{m_1}{\alpha_n}(1 - \cos\alpha_n a) - \frac{m_2}{\alpha_n}(\cos\alpha_n a - \cos 2\alpha_n a)\right] \qquad (A.57)$$

$$\alpha_n = \frac{n\pi}{2a} \qquad (A.49)$$

A.4 Calculation of N_H and N_H'

Once the spatial distribution of h is known the calculation of the N_H and N_H' is very simple:

$$\frac{1}{N_H(z)} \equiv \frac{(h(a,z) - h(b,z))}{(h(A,Z) - H(B,Z))} \qquad (A.2)$$

where if the subchannels are defined as in figure A.1:

$$\frac{1}{N_H(z)} = \frac{\frac{1}{P/2}\left[\int_{-P/2}^{o} h(x,z)dx - \int_{o}^{P/2} h(x,z)dx\right]}{\frac{1}{a}\left[\int_{-a}^{o} h(x,z)dx - \int_{o}^{a} h(x,z)dx\right]} \qquad (A.79)$$

For a different definition of subchannels a and b, the formula will be identical except for the limits of the integrals.

The process for finding $N'_H(z)$ will be analogous.

A.5 Comparison of $N_H(z)$ obtained as previously idicated with the values obtained by using COBRA IIIC/MIT.

A.5.1 Introduction

Parallel to the development of this method to find N_H, the same parameters using the computer code COBRA IIIC/MIT were determined.

In order to establish how the assumptions introduced in the present method effect the results and then how good they are, $N_H(z)$ was compared with that obtained by numerically.

The comparison was made for two of the cases analyzed numerically; enthalpy upset at the inlet without heat generation and heat generation upset with constant inlet enthalpy.

A.5.2 Enthalpy Upset with Heat Generation Rate Equal to Zero.

For this case $b_n = k_1 = 0$ (A.80)

Equation (A.78) becomes:

$$h(x,z) = \frac{h_1 + h_2}{2} + \sum_{n = \text{odd}}^{\infty} \frac{h_2 - h_1}{a\alpha_n} \sin \alpha_n a e^{-\alpha_n^2 z\beta 0.0035} \cos \alpha_n (x-a) \quad (A.81)$$

where:

$$\sin \alpha_n (x-a) \equiv \sin \alpha_n a(\cos \alpha_n x \cos \alpha_n a + \sin \alpha_n a * \sin \alpha_n x) \quad (A.82)$$

but:

$$\sin \alpha_n a \cos \alpha_n a = 0 \quad \text{for } n = 1, 2, 3 \ldots \quad (A.83)$$

$$\sin^2 \alpha_n a = \begin{cases} 0 & \text{for } n = 2, 4, 6 \ldots \\ 1 & \text{for } n = 1, 3, 5 \ldots \end{cases}$$

Applying these conclusions to equation (A.82)

$$\sin \alpha_n a \cos \alpha_n (x-a) = \sin \alpha_n x \quad \text{with } n = 1, 3, 5 \quad (A.85)$$

Bundle Geometry	N = 23
	L = 144"
Flow Conditions	$\bar{G}$ = 2.66 Mlbm/hr-ft^2
	F_R = 1.00
Energy Conditions	$\bar{H}$ = 600 Btu/lbm
	$\bar{q}''$ = 0
	H_R = 1.22
	P_R = 1.0
Input Coefficients	β = Variable
	K = 0.5
	S/L= 0.5

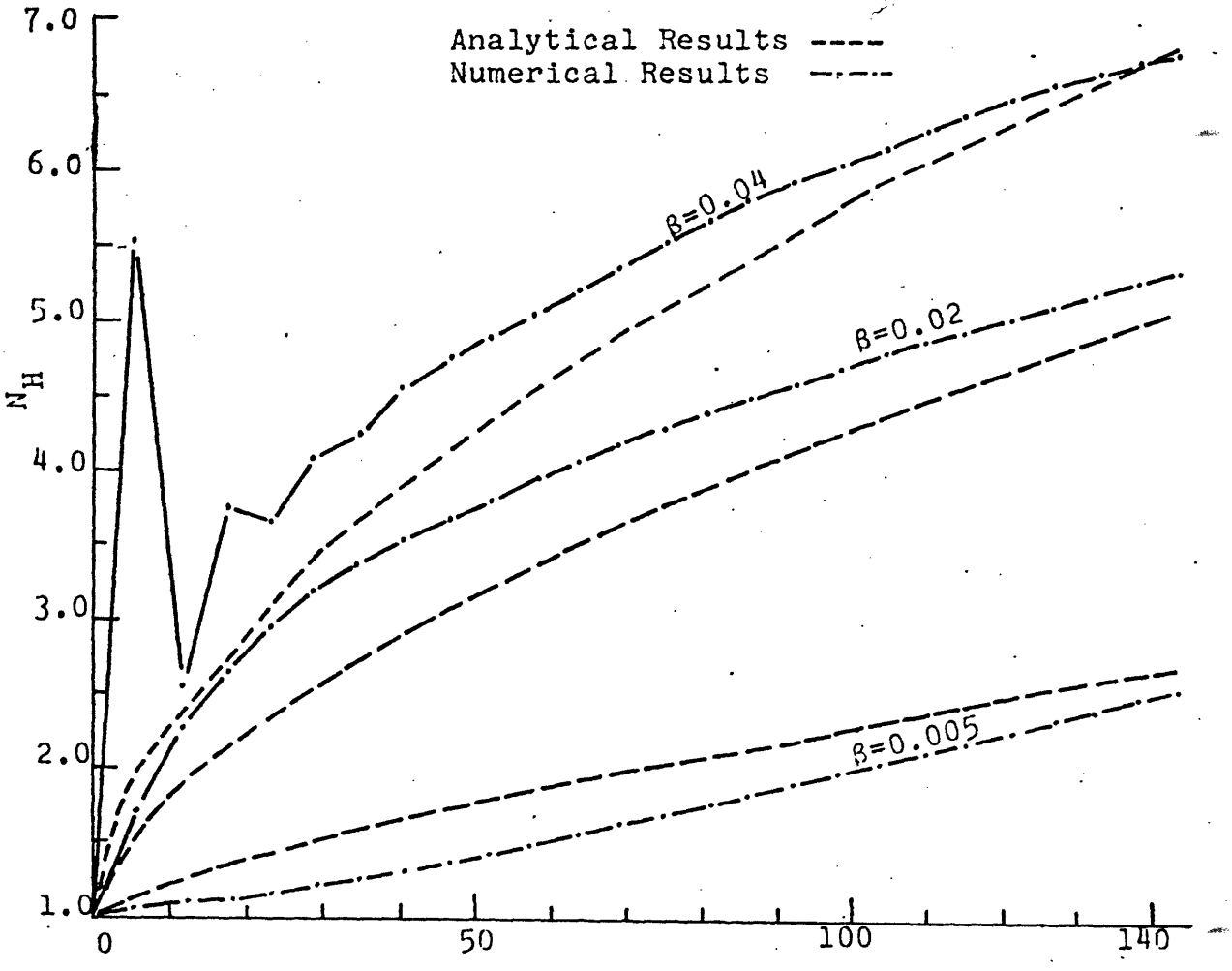

Figure A.3 $N_H(z)$ versus channel length for ENTHALPY UPSET CASE N = 23

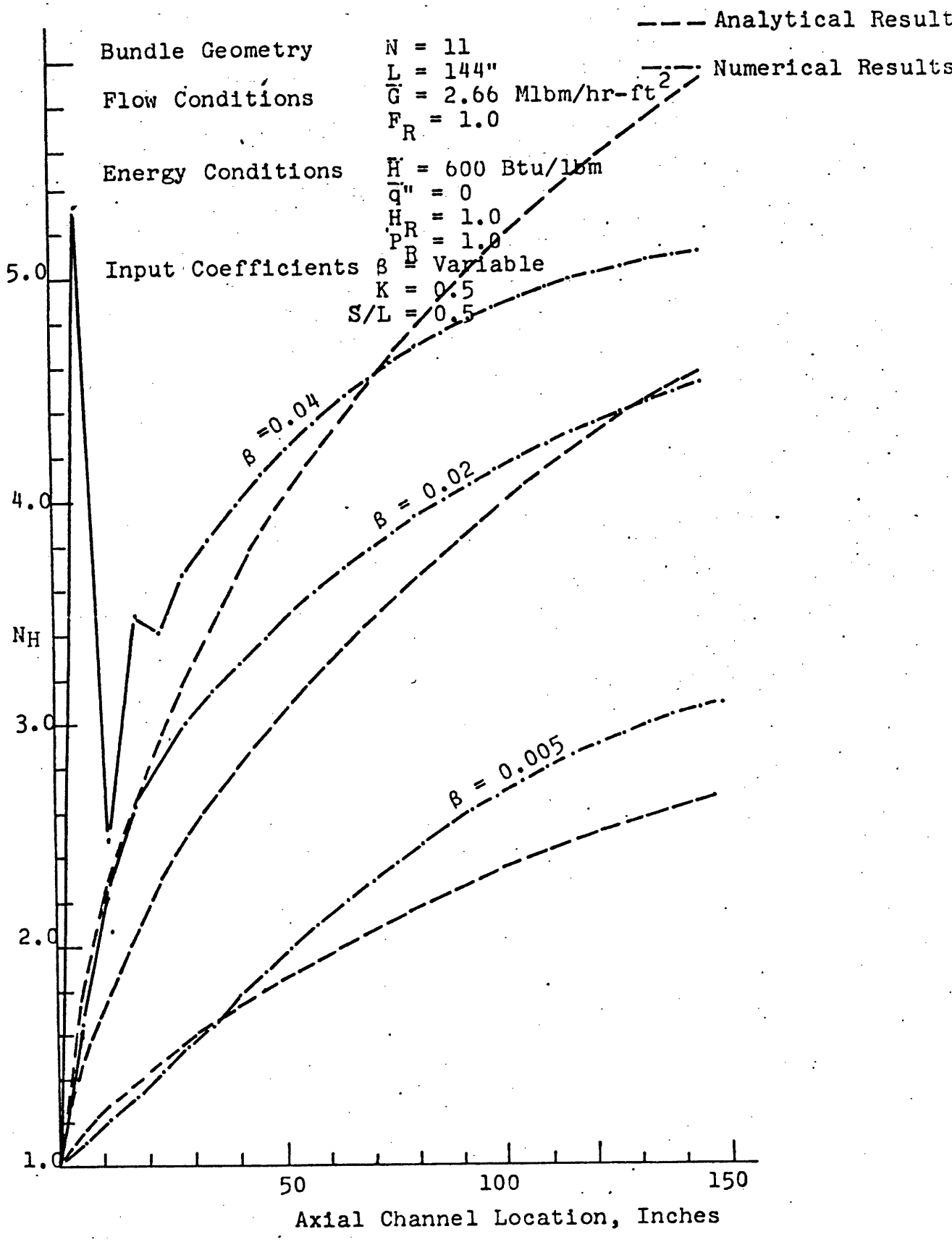

Figure A.4 $N_H(z)$ versus channel length for ENTHALPY UPSET CASE

N = 11

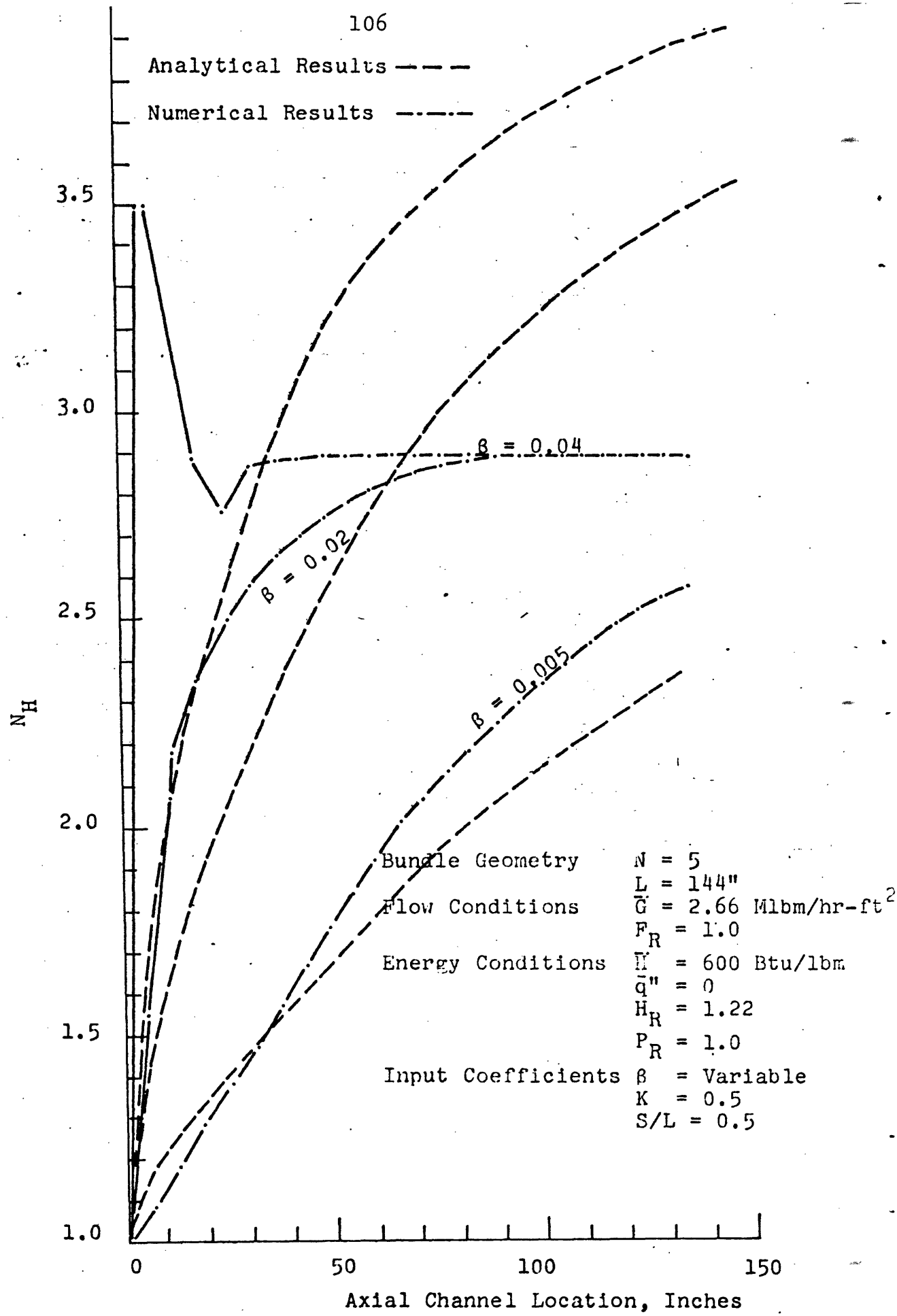

Figure A.5 $N_H(z)$ versus channel length for ENTHALPY UPSET CASE

N = 5

In figures A.3, A.4 and A.5 the values of N_H obtained with both method are compared.

Slight differences can be noticed between results. When the number of subchannels is small, the difference between the analytical results and computer results are largest. When the number of subchannels is large, the curves match well.

The reason for this poor match for small number of subchannels is not completely established. It is known that ε_H is probably a function of rod pitch to diameter ratio, Reynolds number, Prandtl number, axial location, etc. and not a constant. However it was not possible to establish a match for the figure A.5 cases for ang value of ε_H, because all the curves obtained from the numerical method have smaller asymptotic values than those from the analytical method. The other possible reason for some difference is the assumption of zero diversion crossflow in the analytic approach. However very little crossflow was calculated in the numerical cases.

A.5.3 Heat Generation Upset with Constant Inlet Enthalpy.

In this case:

$$h_1 = h_2 \qquad \text{(A.89)}$$

$$m_1 = m_2 = 0 \qquad \text{(A.90)}$$

Then

$$k_1 = \frac{s_1 + s_2}{2} \qquad \text{(A.91)}$$

$$b_n = \frac{1}{a\alpha_n} (s_1 - s_2) \sin \alpha_n a \qquad \text{(A.92)}$$

Introducing these values into equation (A.78) and the value of 0.04 for better match to the computer results we obtain:

$$h(x,z) = \frac{h_1 + h_2}{2} + \frac{s_1 + s_2}{2\rho v_z} z + \sum_{n\ \text{odd}}^{\infty} \frac{(s_1 - s_2)}{a\bar{G}\beta\alpha_n^2\, 0.2} \left(1 - e^{-\alpha_n^2 \beta z 0.04}\right) \sin \alpha_n x \qquad (A.93)$$

which yields the following value of $N_H(z)$:

$$N_H(z) \equiv \frac{P}{2a} \frac{\sum_{n=\text{odd}}^{\infty} \frac{1}{n^3} \left(1 - e^{-\alpha_n^2 \beta z 0.04}\right) \left(\cos \alpha_n a - 1\right)}{\sum_{n=\text{odd}}^{\infty} \frac{1}{n_3} \left(1 - e^{-\alpha_n^2 \beta z 0.04}\right) \left(\cos \frac{\alpha_n P}{z} - 1\right)} \qquad (A.94)$$

In figures A.6, A.7 and A.8, the results obtained are compared against those obtained by Chong Chiu.

An analogous problem to that of the previous case occurs here. The following volumetric energy generation rate profile is taken for the analytical calculation:

For this power upset case, the analytical results and computer results match well in general. But still due to the assumption made in the analytical approaches, slight difference between the two results is expected.

Bundle Geometry	$N = 23$
	L = Variable
Flow Conditions	$\bar{G} = 2.66$ Mlbm/hr-ft^2
	$F_R = 1.0$
Energy Conditions	$\bar{H} = 600$ Btu/lbm
	$\bar{q}'' = 0.04$ MBtu/hr-ft^2
	$H_R = 1.0$
	$P_R = 1.5$
Input Coefficients	β = Variable
	$K = 0.5$
	$S/L = 0.5$

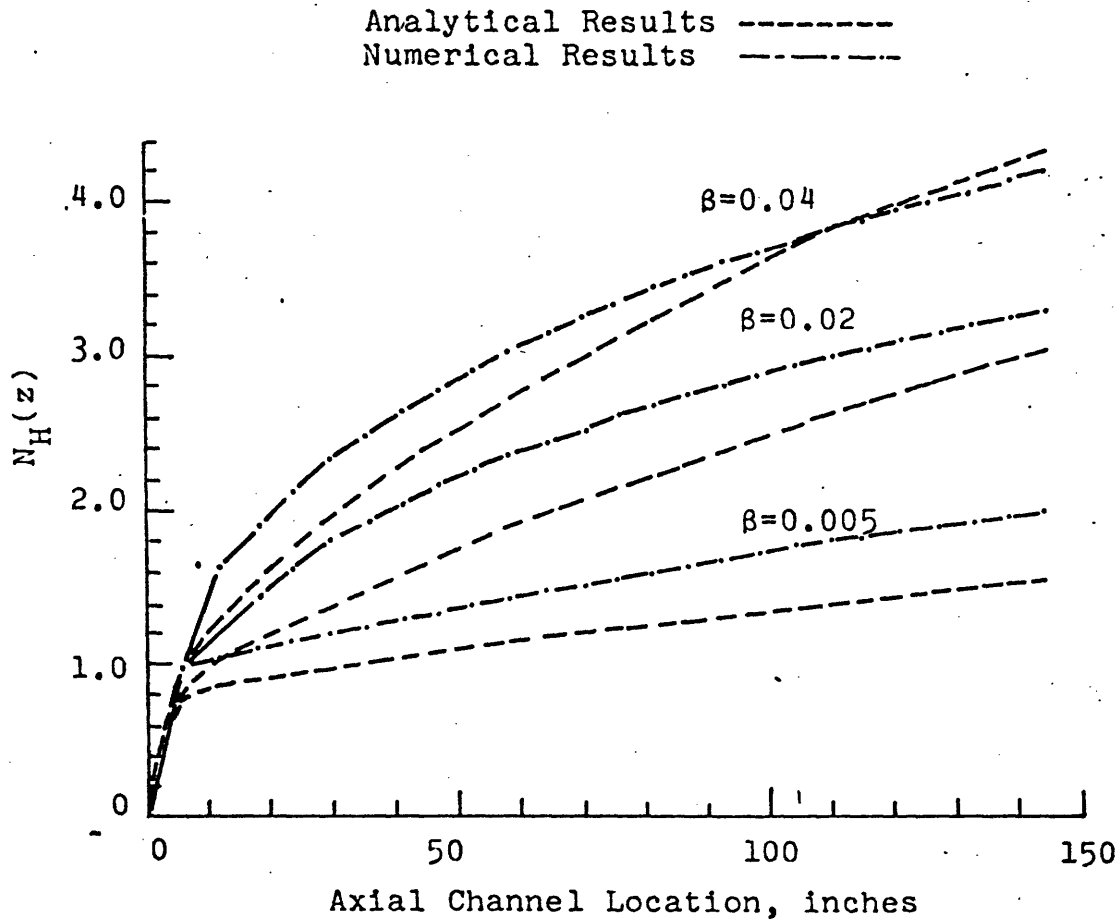

Figure A.6 $N_H(z)$ versus channel length for POWER UPSET CASE, N=23

Bundle Geometry	N = 11
	L = Variable
Flow Conditions	$\bar{G}$ = 2.66 Mlbm/hr-ft^2
	F_R = 1.0
Energy Conditions	$\bar{H}$ = 600 Btu/lbm
	$\bar{q}''$ = 0.04 MBtu/hr-ft^2
	H_R = 1.0
	P_R = 1.5
Input Coefficients	β = Variable
	K = 0.5
	S/L = 0.5

Analytical Results -----
Numerical Results —·—·—

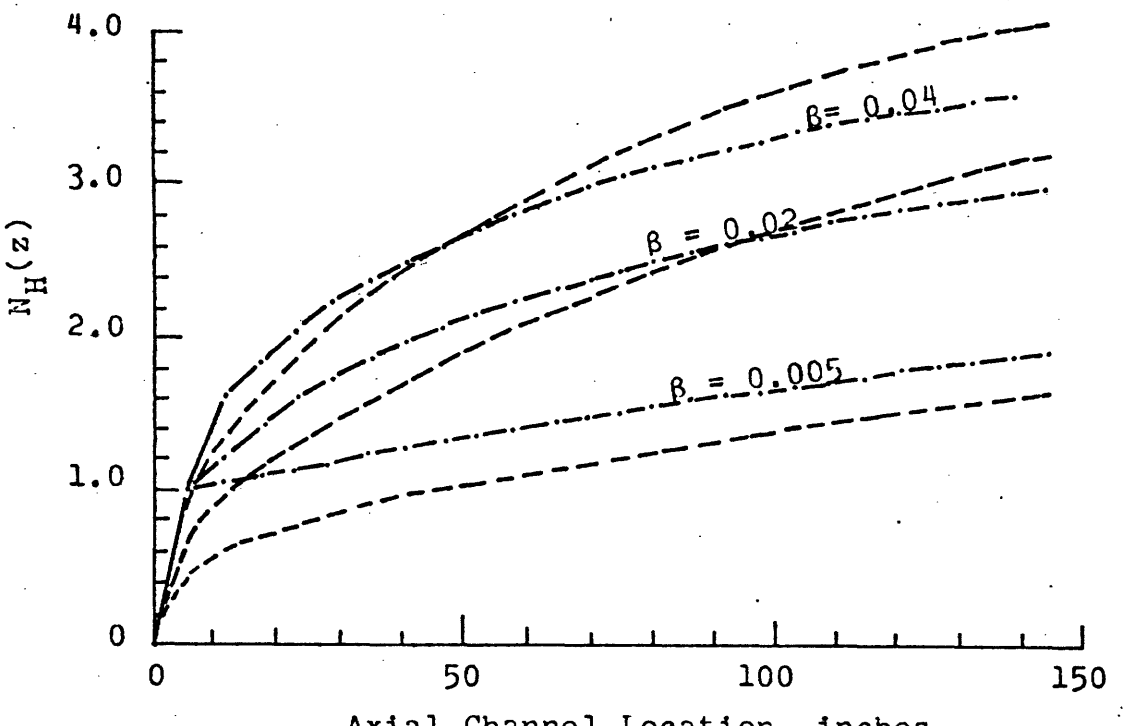

Figure A.7 $N_H(z)$ versus channel length for POWER UPSET CASE, N=11

Bundle Geometry	N = 5
	L = Variable
Flow Conditions	$\bar{G}$ = 2.66 Mlbm/hr-ft^2
	F_R = 1.0
Energy Conditions	$\bar{H}$ = 600 Btu/lbm
	$\bar{q}''$ = 0.04 MBtu/hr-ft^2
	H_R = 1.0
	P_R = 1.5
Input Coefficients	β = Variable
	K = 0.5
	S/L = 0.5

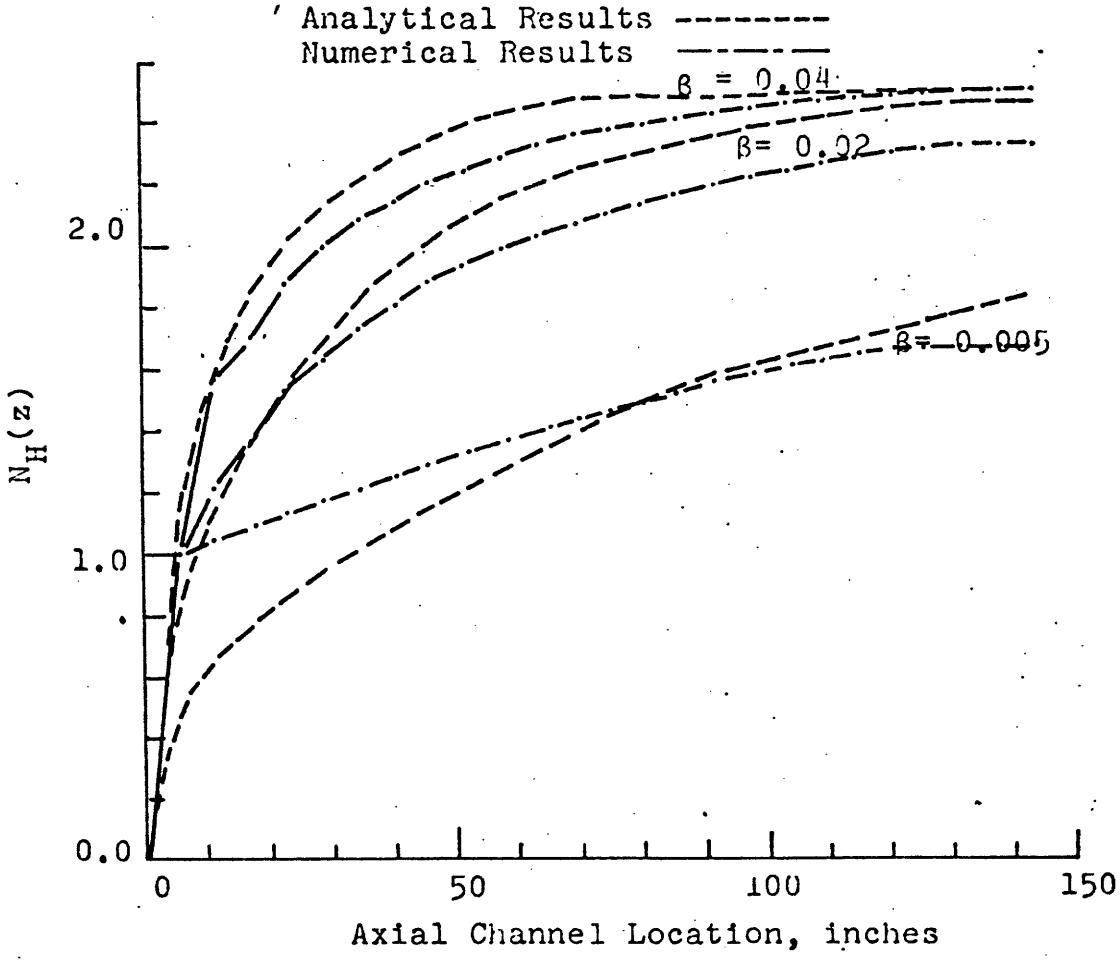

Figure A.8 $N_H(z)$ versus channel length for POWER UPSET CASE, N=5

APPENDIX B

VALIDITY OF EQUATION (2.3.1)

Equation (2.3.1) is written under the assumption that the enthalpy profile is symmetrical with respect to the central boundary. Under this assumption and from the definition of N_H, (Volume I)

$$N_H \equiv \frac{H_L - H_R}{h_C - h_D}$$

we get

$$h_C - h_D = \frac{H_L - H_R}{N_H} \tag{B.1}$$

$$\frac{h_C - h_D}{2} = \frac{H_L - H_R}{2N_H} \tag{B.2}$$

$$\frac{h_C + h_D}{2} = \frac{H_L + H_R}{2} \quad \text{(under the assumption of the symmetrical enthalpy profile)} \tag{B.3}$$

Adding equations (B.3) and (B.2) we obtain

$$h^* = h_C = \frac{h_C - h_D}{2} + \frac{h_C + h_D}{2} = \frac{H_L - H_R}{2N_H} - \frac{H_L + H_R}{2}$$

$$= \frac{H_L - \frac{H_L - H_R}{2}}{N_H} + \frac{H_L + H_R}{2} \quad \text{if } W_{L,R} > 0 \tag{B.4}$$

(B.4) is stated in Appendix A (Volume I) without any comments on it. However, the assumption of symmetrical enthalpy profile used in the derivation of (3.4) is not valid when the diversion crossflow and flow upset exist. This point is verified in detail in the following section (3.1).

B.1 Verification of validity of (B.4) only under the condition of no diversion crossflow and no flow upset

If there are no diversion crossflows and no flow upset between subchannels, equation (B.3) is valid. This can be proven by using equations (A.1.7a) and (A.1.7b) in Appendix A, Volume I with $W_{L,R} = W_{R,L} = 0$,

$$\frac{\partial H_L M_L}{\partial x} = Q_L' - \left(\frac{H_L - H_R}{N_H}\right) W_{L,R}' \qquad (B.7)$$

$$\frac{\partial H_R M_R}{\partial x} = Q_R' - \left(\frac{H_R - H_L}{N_H}\right) W_{R,L}' \qquad (B.8)$$

Since there are no diversion crossflows

$$M_L = \text{constant} \qquad (B.9a)$$

$$M_R = \text{constant} \qquad (B.9b)$$

and from (A.1.8c), (A.1.8d) and (A.1.9b)(Appendix A, Volume I).

$$Q_L' \equiv \sum_{i=A}^{C} q_i' \qquad \text{(A.1.8c)}$$

$$Q_R' \equiv \sum_{i=D}^{F} q_i' \qquad \text{(A.1.8d)}$$

$$N_H \equiv \frac{H_L - H_R}{h_C - h_D} \qquad \text{(A.1.9b)}$$

Equations (B.7) and (B.8) become

$$\Delta H_L = \sum_i \frac{Q_L'}{M_L} \Delta x_i - \sum_i (h_C - h_D) W_{L,R}' \Delta x_i \qquad \text{(B.10a)}$$

$$\Delta H_R = \sum_i \frac{Q_R'}{M_R} \Delta x_i - \sum_i (h_D - h_C) W_{R,L}' \Delta x_i \qquad \text{(B.10b)}$$

Therefore

$$\frac{\Delta H_L + \Delta H_R}{2} \equiv \frac{H_L(z) + H_R(z)}{2} - \frac{H_L(o) + H_R(0)}{2}$$

$$= \frac{\sum_i \frac{Q_L'}{M_L} \Delta x_i + \sum_i \frac{Q_R'}{M_R} \Delta x_i}{2} \qquad \text{(B.11)}$$

and

$$\frac{H_L(z) + H_R(z)}{2} = \frac{H_L(o) + H_R(o)}{2} + \frac{\sum_i \frac{Q_L'}{M_L} \Delta x_i + \sum_i \frac{Q_R'}{M_R} \Delta x_i}{2} \qquad \text{(B.12)}$$

This evaluates the RHS of Eq. (C.3). Next we evaluate $\frac{h_C + h_D}{2}$, the LHS of Eq. (C.3) to show the equality of RHS and LHS.

To obtain the expression for $\frac{h_C(z) + h_D(z)}{2}$, we use a different derivation philosophy which is stated below.

From equations (A.1.3c) and (A.1.3d),(in Volume I), we get

$$\frac{\partial m_C h_C}{\partial x} = q_C' - (h_C - h_D)w_{C,D}' - (h_C - h_B)w_{C,B}' \qquad \text{(A.1.3c)}$$

$$\frac{\partial m_D h_D}{\partial x} = q_C' - (h_D - h_C)w_{D,C}' - (h_D - h_E)w_{D,E}' \qquad \text{(A.1.3d)}$$

In order to proceed with the derivation, we have to recognize the following statement as true:

"If the enthalpy profile at axial node j is transversely symmetrical, we can prove the enthalpy profile at axial node j+1 is also transversely symmetrical as long as the transverse linear heat generation profile is symmetric."

This statement needs an involved proof and we can heuristically prove this by observing equations (A.1.3c) and (A.1.3d) (Volume I) in the difference scheme:

$$m_C \frac{h_C(J+1) - h_C(J)}{\Delta x} = q_C' - (h_C(J) - h_D(J))w_{C,D}' - (h_c(J) - h_B(J))w_{C,B}' \qquad (3.13)$$

$$m_D \frac{h_D(J+1) - h_D(J)}{\Delta x} = q_D' - (h_D(J) - h_C(J))w_{C,D}' - (h_D(J) - h_E(J))w_{D,E}' \qquad (3.14)$$

Because of symmetry at the axial node J, we have

$$(h_C(J) - h_B(J)) = (h_D(J) - h_E(J)) \qquad (3.15)$$

and

$$w'_{D,C} = w'_{C,D} \qquad (3.16)$$

$$w'_{C,B} = w'_{C,E} \qquad (3.17)$$

Thus we know is $q'_C = q'_D = 0$, the enthalpy increment in subchannel C equals the enthalpy decrease in subchannel D. Also because the transverse linear heat generation rate is symmetrical, then $h_C(J+1)$ and $h_D(J+1)$ must be symmetrical with respect to

$$\frac{\frac{q'_C(J)}{m_C} + \frac{q'_D(J)}{m_D}}{2} + \frac{h_C(J) + h_D(J)}{2} .$$

Now we can obtain $\frac{h_C(z) + h_D(z)}{2}$ from equations (A.13c) and (A.13d) (Volume I) by recognizing that $(h_C - h_B) \doteq (h_D - h_E)$.

The result is

$$\frac{h_C(z) + h_D(z)}{2} = \frac{\sum_i \frac{q'_C}{m_C} \Delta x_i + \sum_i \frac{q'_D}{m_D} \Delta x_i}{2} + \frac{h_C(o) + h_D(o)}{2} \qquad (3.18)$$

Since

$$h_C(o) = H_L(o) \tag{B.19a}$$

$$h_D(o) = H_R(o) \tag{B.19b}$$

$$\frac{q'_C}{m_C} = \frac{Q'_L}{M_C} = \frac{\sum_{i=A}^{C} q'_i}{\sum_{i=A}^{C} m_i} \tag{B.19c}$$

$$\frac{q'_D}{m_D} = \frac{Q'_R}{M_R} = \frac{\sum_{i=D}^{F} q'_i}{\sum_{i=D}^{F} m_i} \tag{B.19d}$$

under the condition $q'_A = q'_B = q'_C$, $m_A = m_B = m_C$, $q'_D = q'_E = q'_F$ and $m_D = m_E = m_F$.

Therefore, from equations (B.18) and (B.12) we get

$$\frac{h_C(z) + h_D(z)}{2} = \frac{H_L(z) + H_R(z)}{2} \tag{B.20}$$

However, under large inter-subchannel diversion crossflow or flow upset conditions, equations (B.15), (B.17), (B.19c) and (B.19d) will not hold and hence equations (B.20) and (B.4) become inequalities.

B.2 Suggestions on h* in terms of known parameters

A suggestion is made below regarding h* (stated in

equation (A.1.11a) and (A.1.11b) (Volume I) under the assumptions of no diversion crossflow and no flow upset) in order to cope with the conditions of large diversion crossflow and flow upset.

$$h^* = \frac{H_L(M_{L_{EXIT}} + M_L(o)) + H_R(M_{R_{EXIT}} + M_R(o))}{2(M_L + M_R)} + \frac{H_L - \frac{H_L + H_R}{2}}{N_H} \quad \text{if } W_{L,R} > 0 \quad (B.21)$$

$$h^* = \frac{H_L(M_{L_{EXIT}} + M_L(o)) + H_R(M_{R_{EXIT}} + M_R(o))}{2(M_L + M_R)} + \frac{H_R - \frac{H_L + H_R}{2}}{N_H} \quad \text{if } W_{L,R} < 0 \quad (B.22)$$

These two equations also hold under the conditions of low diversion crossflow and no flow upset, hence it can be used under any conditions we require in this study.

APPENDIX C

LIMITATIONS ON THE NUMERICAL VALUE OF β USED IN CALCULATIONS WITH COBRA IIIC

The mixing coefficient, β, is an input in COBRA IIIC. It is used to calculate the turbulent interchange per unit length between channels in the lumped subchannel approach. Since it is physically impossible to have the axial enthalpy rise in the flow channel fluctuate for each axial step just due to the energy transport by the turbulent interchange between the channels, a limitation is imposed on the input value of β. Derivation of the limiting values for β under different operating conditions are presented in the following sections.

C.1 Derivation of General Expressions

C.1.1 Unheated Bundles

The limiting condition on β is that the enthalpy rise for each axial step k in any channel i by the energy transport with the adjacent channel j should be less than one half of the transverse enthalpy difference between channels i and j. This statement can be formulated by the following expression:

$$\left|\frac{w_{i,j}(h_i-h_j)\Delta x}{m_i}\right|_k < \frac{|h_i-h_j|_k}{2} \qquad (C.1.1)$$

where w_{im}, h_i, h_j are evaluated for any axial node k.

Since

$$w_{i,j} = \beta s \left(\frac{g_i+g_j}{2}\right)_k$$

$$m_i = g_i A_i$$

equation (C.1.1) also can be expressed in a general way:

$$\Delta x \beta s \left(\frac{g_i+g_j}{2(g_i A_i)}\right) \left|(h_i-h_j)\right| < \frac{|h_i-h_j|}{2} \qquad (C.1.2)$$

Therefore

$$\beta < \frac{g_i A_i}{s(g_i+g_j)\Delta x} \qquad (C.1.3)$$

C.1.2 Heated Bundles

Because the limitation set on β has nothing to do with the heat added from heated rods, the expression (C.1.3) is also true for heated bundles.

C.2 Evaluation of Numerical Values for β_{max}

C.2.1 Enthalpy Upset Case

In this case, the diversion crossflow is very small. Therefore, $\frac{g_i}{g_i+g_j}$ is closed to one half throughout the entire length of the channels. For typical PWR geometry, equation (C.1.3) thus can be evaluated by letting:

$$s = 0.122 \text{ inch}$$

$$A_i = 0.0098 \text{ ft}^2$$

$$\Delta x = 5.76 \text{ inch}$$

then

$$\beta_{max} = \frac{0.5 \times 0.00094}{\frac{0.122}{12} \times \frac{5.76}{12}} = 0.096 \qquad (C.2.1.1)$$

In particular, it should be noted that β_{max} in the half-sized channel calculation becomes one half of its nominal value in the full sized channel calculation. Therefore, as long as a half sized channel is used, β_{max} for half-sized channels becomes a limiting value for β provided a constant β is used for every channel in the calculation. The β_{max} in the half-sized channel calculation can be established as follows:

$$\beta_{max}(\text{half-sized channel}) = \frac{g_i A_i}{2s(g_i+g_j)\Delta x}$$

$$= 0.5\beta_{max}$$

$$= 0.048 \qquad (C.2.1.2)$$

C.2.2 Enthalpy and Flow Upset Case

In this case, the limiting value of β occurs in the region where the ratio $\frac{g_i}{g_i+g_j}$ has the smallest value provided a constant β is used throughout the channels.

There are three important features of the maximum β under the flow upset condition; i.e.,

(1) β_{max} under the flow upset condition is always less than that under the enthalpy upset of the power upset condition (since $\frac{g_i}{g_i+g_j} < \frac{1}{2}$).

(2) The limiting β occurs at the inlet under the flow upset condition. This is because the momentum transport between channels tends to increase the value on $\frac{g_i}{g_i+g_j}$ along the channel.

(3) The minimum value of $\frac{g_i}{g_i+g_j}$ depends on the upset flow ratio at the inlet. Generally, the higher the flow upset ratio, the smaller the value of $\frac{g_i}{g_i+g_j}$.

In our application, a step flow upset inlet condition is used where the higher flow rate $\frac{N-1}{2}$ channels at the inlet is 1.1 times larger than that for the center channel and the lower flow rate at the inlet for the rest of the channels is 0.9 times lower than that for the center channel. Therefore, β_{max} in this case can be calculated by the following formula:

$$\beta_{max} = \frac{g_i A_i}{s(g_i+g_j)\Delta x}$$

$$= \frac{0.9A_i}{s(1.1+0.9)\Delta x}$$

$$= \frac{0.9 \times 0.00094}{\frac{0.122}{12} \times (1.8) \frac{5.76}{12}}$$

$$= 0.097 \qquad \text{(C.2.2.1)}$$

If the half-sized channels are used for the center channel to calculate the coupling coefficients, the limiting β occurs in the half sized channel adjacent to the high flowrate channels. Hence the β_{max} can be calculated as follows:

$$\beta_{max} = \frac{g_i A_i}{2s(g_i+g_j)\Delta x}$$

$$= \frac{1.0 \times 0.00094}{2 \times \frac{0.122}{12} (1.0+1.1) \times \frac{5.76}{12}}$$

$$= 0.046 \qquad \text{(C.2.2.2)}$$

C.2.3 Power Upset Case

In this case, the β_{max} is the same as that in the enthalpy upset case.

C.2.4 Power and Flow Upset Case

In this case, the β_{max} is the same as that in the flow upset case.

APPENDIX D

METHODS TO ANALYZE HOMOGENIZED REPRESENTATIONS, MULTI-SUBCHANNEL REPRESENTATIONS AND TO COMPUTE $N_H(z)$

The purpose of this appendix is to illustrate the method to compute the multi-subchannel results, the homogenized results and the coupling coefficients. The procedure to obtain the multi-subchannel and homogenized results is discussed in section D.1. The input data for the homogenized representations which can be determined from the input data for the multi-subchannel representations are discussed in section D.2. Finally, the code changes are briefly discussed in section D.3 on the modifications made to fulfill the computations required in this study.

D.1 Procedures

COBRA IIIC/MIT version is used in this study to analyze the coupling coefficient N_H in the energy conservation equation. The steps to accomplish this purpose are listed below:

1) Run a multi-subchannel case to obtain
   a) Multi-subchannel results - the average parameters for the multi-subchannel steps L and R

(refer to Figure 3 for subscripts L and R).

b) Coupling Coefficients - The following approximations are made so that coupling coefficients can be obtained from the multi-subchannel computation:

$$\tilde{h}_L(z) \equiv H_L(z) \qquad (D.1)$$

$$\tilde{h}_R(z) \equiv H_R(z) \qquad (D.2)$$

For instance, N_H is defined in Appendix A(Volume I)

$$N_H \equiv \frac{\bar{H}_L - \bar{H}_R}{h_C - h_D} \qquad (A.1.9c)$$

insert (D.1) and (D.2) into (A.1.9c)

$$N_H \equiv \frac{\tilde{h}_L - \tilde{h}_R}{h_C - h_D} \qquad (D.3)$$

so N_H is expressible in the multi-subchannel parameters and can be evaluated in the multi-subchannel computation.

2) Run a homogenized case which lumps N subchannels into two homogenized channels L and R. The conservation equations in this case are modified

according to equations (A.1.7), (A.2.5) and (A.3.5) (Volume I) so as to compute the homogenized results with the coupling coefficients evaluated in step 1.

D.2 Input Data for Homogenized Representations

The relationships between the input data for the homogenized representation and for the multi-subchannel representation are summarized as follows:

$$Q_L' = \sum_{i=A}^{C} q_i' \qquad \text{(D.2.1a)}$$

$$Q_R' = \sum_{i=D}^{F} q_i' \qquad \text{(D.2.1b)}$$

$$A_L = \sum_{i=A}^{C} A_i \qquad \text{(D.2.1c)}$$

$$A_R = \sum_{i=D}^{F} A_i \qquad \text{(D.2.1d)}$$

$$H_L = \sum_{i=A}^{C} m_i h_i \Big/ \sum_{i=A}^{C} m_i \quad \text{at inlet} \qquad \text{(D.2.1e)}$$

$$H_R = \sum_{i=D}^{F} m_i h_i \Big/ \sum_{i=D}^{F} m_i \quad \text{at inlet} \qquad \text{(D.2.1f)}$$

$$G_L = \sum_{i=A}^{C} g_i A_i \Big/ A_L \quad \text{at inlet} \qquad (D.2.1g)$$

$$G_R = \sum_{i=D}^{F} g_i A_i \Big/ A_R \quad \text{at inlet} \qquad (D.2.1h)$$

From the above relationships, the input data for the homogenized representation can be determined from the input data for the multi-subchannel representation.

D.3 Code Changes

Part of the code has been modified to fulfill the purpose of this study. The code changes in the required subroutines are listed as follows:

1) Subroutine EXPRIN - Calculate the parameters in the homogenized representation and the coupling coefficients, i.e., N_H, N_U, N_{TP}, N_{TU} and N_TF.

2) Subroutine SCHEME - Read in the coupling coefficient either in a single value form or in a discrete value form. Calculate $\bar{N}_H$.

3) Subroutines DIFFER and DIVERT - Incorporate the coupling coefficients in the conservation equations.

APPENDIX E

N_H FOR THE HOMOGENIZED CASE COUPLING TWO STRIPS OF UNEVEN NUMBERS OF SUBCHANNELS

For the multi-subchannel strip with uneven subchannel numbers, i.e., coupling two multi-subchannel strips L and R with different number of subchannels, N_L and N_R respectively, the N_H can be derived as follows:

Assume the enthalpy at the center is zero as the reference point and

$$N_{H_L} = \frac{\overline{H}_L}{h_{M^-}} \quad \text{for the multi-subchannel strip L} \tag{E.1}$$

$$N_{H_R} = \frac{\overline{H}_R}{h_{M^+}} \quad \text{for the multi-subchannel strip R} \tag{E.2}$$

where

h_{M^-} ≡ enthalpy of the half-sized subchannel in the strip L and adjacent to the strip R

h_{M^+} ≡ enthalpy of the half-sized subchannel in the strip R and adjacent to the strip L.

From the definition of N_H

$$N_H \equiv \frac{\overline{H_L} - \overline{H_R}}{h_{m^-} - h_{m^+}} \tag{E.3}$$

Insert equations E.1 and E.2 into E.3

$$N_H \equiv \frac{N_{H_L} h_{m^-} - H_{H_R} h_{m^+}}{h_{m^-} - h_{m^+}} \tag{E.4}$$

Also assume

$$h_{m+} = - h_{m-} \qquad (E.5)$$

Then equation (E.4) becomes

$$N_H = \frac{N_{H_L} + N_{H_R}}{2} \qquad (E.6)$$

This relationship is expected to be valid as long as N_L and N_R are large enough to make the assumption (E.5) hold and the difference between N_L and N_R is small. An heuristic criteria is suggested to limit the validity of equation (E.6):

$$\frac{|N_L - N_R|}{\min(N_L, N_R)} < 0.3$$

where $\min(N_L, N_R)$ is the smaller number between N_L and N_R.

VOLUME III

3D TRANSPORT COEFFICIENT

AUTHOR: PABLO MORENO

VOLUME III

TABLE OF CONTENTS

VOLUME III

LIST OF FIGURES

3.0 Introduction

In the present volume the methods to calculate transport coefficients for 3D problems (in particular $N_H(z)$) will be given.

An example case will be presented and the results of the numerical method will be compared against the results of the analytical method.

3.1 Numerical Method to Determine $N_H(z)$ for a Multiregion Analysis

3.1.1 Introduction

In order to find $N_H(z)$ for a particular boundary, the following steps should be followed:

1) Define the geometry to be adopted.
2) Using COBRA IIIC/MIT analyze the adopted geometry on an actual subchannel basis, i.e., each radial node being a subchannel.
3) Define $N_H(z)$.
4) Using the results from step 2 and the definition of step 3, find the numerical values of $N_H(z)$.

3.1.2 Solution Strategy

The following strategy is recommended:

3.1.2.1 Define the geometry to be adopted.

If the value of $N_H(z)$ for a boundary has to be calculated it is recommended that the geometry of Figure 13 (Chapter 3 Volume 1) be adopted where the boundary of interest is boundary A, and where now

the homogenized regions will be those of our specific problem. By imbedding the boundary of interest in this mesh of 12 channels we will significantly reduce the effect of $N_H(z)$ of the actual channels which are not considered.

3.1.2.2 Analysis Needs of the Problem

Using COBRA IIIC/MIT the geometry adopted has to be analyzed in order to find the enthalpies of each subchannel that make-up the homogenized regions at each axial elevation. The analysis needs to be done on an actual subchannel basis and then the homogenized regions have to be split into subchannels as indicated in Figure 13, Chapter 3, Volume I.

3.1.2.3 Definition of $N_H(z)$.

In order that the homogenized region analysis yield enthalpy results for these regions identical to those given by an actual subchannel analysis, the following definition of $N_H(z)$ should be used: (See Figure 13, Chapter 3, Volume I).

$$N_H(z) = \frac{\bar{w}'_z(\bar{h}_z(L) - \bar{h}_z(R))}{w'_z(42,43)(h_z(42)-h_z(43))+w'_z(54,55)(h_z(54)-h_z(55))+w'_z(66,67)(h_z(66)-h_z(67))} \qquad \text{(III.1)}$$

where

$$\bar{w}'_z = w'_z(42,43) + w'_z(54,55) + w'_z(66,67) \qquad \text{(III.2)}$$

$\bar{h}_z(L)$ = Average enthalpy of the homogenized region to the left of the boundary (subchannels 40,41,42,52,53 54,64,65 and 66)

$\bar{h}_z(R)$ = Average enthalpy of the homogenized region to the right of the boundary (subchannels 43,44,45,55,56, 67,68 and 69)

However since this definition is very complicated because it also involves the effective massflow for the turbulent interchange, the following approximation is suggested:

$$N_H(z) = \frac{3(\bar{h}_z(L) - \bar{h}_z(R))}{(h_z(42)-h_z(43))+(h_z(54)-h_z(55))+(h_z(66)-h_z(67))} \qquad \text{(III.3)}$$

which can be further transformed to:

$$N_H(z) = \frac{\bar{h}_z(L) - \bar{h}_z(R)}{\left(\frac{h_z(42)+h_z(54)+h_z(66)}{3}\right) - \left(\frac{h_z(43)+h_z(55)+h_z(67)}{3}\right)} \qquad \text{(III.4)}$$

3.1.2.4 Calculation of $N_H(z)$.

Using the previous definition and the enthalpy results found in Step 2, the numerical calculation of $N_H(z)$ is straightforward.

3.2 3D Analytic Transport Coefficients

3.2.1 Solution of the General Equation

The general equation to be solved is:

$$\frac{1}{a_t}\frac{\partial T}{\partial t} = \frac{\partial^2 T}{\partial x^2} + \frac{\partial^2 T}{\partial y^2} + \frac{q'''}{k} \qquad \text{(III.5)}$$

where the following analogy has been built into the equation in order to transform the 3-D thermal/hydraulic problem into a 2D, transient, thermal conduction problem:

$$T \overset{\leftarrow}{\rightarrow} h \qquad \text{(III.6)}$$

$$t \overset{\leftarrow}{\rightarrow} z/\sigma_z \qquad \text{(III.7)}$$

$$a_t \overset{\leftarrow}{\rightarrow} \varepsilon_H \qquad \text{(III.8)}$$

$$k \overset{\leftarrow}{\rightarrow} \rho\varepsilon_H \qquad \text{(III.9)}$$

The boundary conditions are:

$$\left.\frac{\partial T}{\partial x}\right|_{x=0} = 0 \quad ; \quad \left.\frac{\partial T}{\partial x}\right|_{x=x_4} = 0 \qquad \text{(III.10)}$$

$$\left.\frac{\partial T}{\partial y}\right|_{y=0} = 0 \quad ; \quad \left.\frac{\partial T}{\partial y}\right|_{y=y_3} = 0 \qquad \text{(III.11)}$$

$$T(x,y,0) = T_0(x,y) \qquad \text{(III.12)}$$

Equation (III.5) can be divided as follows:

$$\frac{1}{a_t}\frac{\partial T_1}{\partial t} = \frac{\partial^2 T_1}{\partial x^2} + \frac{\partial^2 T_1}{\partial y^2} \qquad \text{(III.13)}$$

$$\frac{1}{a_t}\frac{\partial T_2}{\partial t} = \frac{q'''}{k} \qquad \text{(III.14)}$$

$$\frac{\partial^2 T_3}{\partial x^2} + \frac{\partial^2 T_3}{\partial y^2} + \frac{q'''}{k} = 0 \qquad \text{(III.15)}$$

where:

$$T(x_1 y_1 t) = T_1(x_1 y_1 t) + T_2(t) + T_3(x,y) \qquad \text{(III.16)}$$

and where:

$$q''' = \bar{q}''' + q_1''' \qquad \text{(III.17)}$$

The general solution for $T(x_1 y_1 t)$ will be a Fourier series of sines and cosines, but because our boundary conditions are adiabatic the terms with sines will disappear and the solution will only have cosine terms.

Expression the heat generation as a Fourier series in cosines:

$$q''' = C_{oo} + \sum_{m=0}^{\infty}\sum_{n=0}^{\infty} C_{mn} \cos\frac{m\pi x}{x_4} \cos\frac{n\pi y}{y_3} \qquad \text{(III.18)}$$

except m=n=0

where

$$C_{oo} = \frac{\int_o^{y_4}\int_o^{x_4} q'''\,dxdy}{\int_o^{y_3}\int_o^{x_4} dxdy} = \bar{q}''' \qquad \text{(III.19)}$$

and

$$C_{mn} = \frac{\int_o^{x_4}\int_o^{y_3} q'''\ \cos\frac{m\pi x}{x_4}\cos\frac{n\pi y}{y_3}\,dxdy}{\int_o^{x_4}\int_o^{y_3} \cos\frac{m\pi x}{x_4}\cos\frac{n\pi y}{y_3}\,dxdy} \qquad \text{(III.20)}$$

Solving Equation (III.15)

$$T_3(x,y) = \sum_{m=0}^{\infty}\sum_{n=0}^{\infty} C'_{mn}\cos\frac{m\pi x}{x_4}\cos\frac{n\pi y}{y_3} \qquad \text{(III.21)}$$

except m=n=0

where C'_{mn}:

$$\left(\frac{m\pi}{x_4}\right)^2 C'_{mn} + \left(\frac{n\pi}{y_3}\right)^2 C'_{mn} = \frac{C_{mn}}{k} \qquad \text{(III.22)}$$

To solve equation (III.13):

$$T_1(x,y,t) = 0(x,y)\ F(t) \qquad \text{(III.23)}$$

$$\frac{1}{a_t F(t)} \frac{dF(t)}{dt} = \frac{1}{\theta(x,y)} \frac{\partial^2 \theta}{\partial x} + \frac{\partial^2 \theta}{\partial y} \frac{1}{\theta} = -\alpha_{mn}^2 \qquad \text{(III.24)}$$

Then:

$$F(t) = C\, e^{-a_t \alpha_{mn}^2 t} \qquad \text{(III.25)}$$

$$\theta = B_{mn} \cos\alpha_n x \cos\alpha_n y \qquad \text{(III.26)}$$

$$\text{with} \quad \alpha_m = \frac{m\pi}{x_4} \quad ; \quad \alpha_n = \frac{n\pi}{y_3} \qquad \text{(III.27)}$$

where α_{mn}:

$$\alpha_{mn}^2 = \alpha_m^2 + \alpha_n^2 \qquad \text{(III.28)}$$

Then

$$T_1(x,y,t) = \sum_{m=0}^{\infty} \sum_{n=0}^{\infty} A_{mn}\, e^{-a_t \alpha_{mn}^2 t} \cos\alpha_m x \cos\alpha_n y \qquad \text{(III.29)}$$

except m=n=0

Solving finally Equation (III.14)

$$T_2(t) = \frac{\overline{q'''}}{k} a_t\, t + C \qquad \text{(III.30)}$$

The final solution is then:

$$T(x,y,t) = \frac{\bar{q}'''}{k} a_t t + C + \sum_{m=0} \sum_{n=0} (A_{mn} e^{-a_t \alpha_{mn}^2 t} + C'_{mn}) \cos\alpha_m x \cos\alpha_n y$$

except m=n=0 (III.31)

Using now the initial boundary condition:

$$t = 0; \quad T(x,y,0) = T_o(x,y) = 0 \tag{III.32}$$

$$C = 0 \tag{III.33}$$

$$A_{mn} = -C'_{mn} \tag{III.34}$$

$$T(x,y,t) = \frac{\bar{q}''' a_t t}{k} + \sum_{m=0} \sum_{n=0} C'_{mn} (1 - e^{-a_t \alpha_m^2 t}) \cos\alpha_m x \cos\alpha_n y$$

except m=n=0 (III.35)

where

C'_{mn} is given by Equation (III.22) and

C_{mn} is a function of the heat source distribution and is calculated from Equation (III.20).

3.2.2 Derivation of N_H

For boundary 9 (Figure III.1) between channels F and G, N_H is defined as:

$$N_H(z) = \frac{\dfrac{\int_{x_1}^{x_2}\int_{y_1}^{y_2} h(x,y,z)dxdy}{\int_{x_1}^{x_2}\int_{y_1}^{y_2} dxdy} - \dfrac{\int_{x_2}^{x_3}\int_{y_1}^{y_2} (h(x,y,z)dxdy}{\int_{x_2}^{x_3}\int_{y_1}^{y_2} dxdy}}{\dfrac{\int_{x_2-P}^{x_2}\int_{y_1}^{y_2} h(x,y,z)dxdy}{\int_{x_2-P}^{x_2}\int_{y_1}^{y_2} dxdy} - \dfrac{\int_{x_2}^{x_2+P}\int_{y_1}^{y_2} h(x,y,z)\,dxdy}{\int_{x_2}^{x_2+P}\int_{y_1}^{y_2} dxdy}}$$

Then once h(x,y,z) is known, the derivation of N_H is straight forward.

3.2.3 Calculation of N_H of a Specific Problem:

The case of Figure III.1 was solved using constant power input for each of the channels that make up the core.

The powers are specified as follows:

Channel	Power
I	P11
J	P21
K	P31
L	P41
E	P12
F	P22
G	P32
H	P42
A	P13
B	P23
C	P33
D	P43

The constant C_{mn} takes the following values:

$$C_{mn} = \frac{4}{x_4 y_3 \alpha_m \alpha_n} \Big\{ [P11 \sin\alpha_m x_1 + P21(\sin\alpha_m x_2 - \sin\alpha_m x_1) +$$

$$+ P31(\sin\alpha_m x_3 - \sin\alpha_m x_2) - P41 \sin\alpha_m x_3] \sin\alpha_n y_1 +$$

$$[P12 \sin\alpha_m x_1 + P22(\sin\alpha_m x_2 - \sin\alpha_m x_1) +$$

$$+ P32(\sin\alpha_m x_3 - \sin\alpha_m x_2) - P42 \sin\alpha_m x_3] +$$

$$+ [\sin\alpha_n y_2 - \sin\alpha_n y_1] \quad [P13 \sin\alpha_m x_1 +$$

$$+ P23(\sin\alpha_m x_2 - \sin\alpha_m x_1) + P33(\sin\alpha_m x_3 - \sin\alpha_m x_2)$$

$$P43 \sin\alpha_m x_3] \sin\alpha_n y_2 \Bigg\} \qquad \text{(III.37)}$$

and

$$C'_{mn} = \frac{C_{mn}}{k(\alpha_m^2 + \alpha_n^2)} \qquad \text{(III.38)}$$

when $n = 0$:

$$C_{mo} = \frac{2}{x_4 \alpha_m} \left\{ \left[\frac{P13(y_3-y_2)+P12(y_2-y_1)+P11(y_1)}{y_3} \right] \sin\alpha_m x_1 + \right.$$

$$+ \left[\frac{P23(y_3-y_2)+P22(y_2-y_1)+P21(y_1)}{y_3} \right] \left[\sin\alpha_m x_2 - \sin\alpha_m x_1 \right] +$$

$$+ \left[\frac{P33(y_3-y_2)+P32(y_2-y_1)+P31(y_1)}{y_3} \right] \left[\sin\alpha_m x_3 - \sin\alpha_m x_2 \right] -$$

$$\left. - \left[\frac{P43(y_3-y_2)+P42(h_2-y_1)+P41(y_1)}{y_3} \right] \sin\alpha_m x_3 \right\} \qquad \text{(III.39)}$$

and

$$C'_{mo} = \frac{C_{mo}}{k\alpha_m^2} \qquad \text{(III.40)}$$

when $m = 0$

$$C_{on} = \frac{2}{\alpha_n y_3}\left\{\left[\frac{P11(x_1)+P21(x_2-x_1)+P31(x_3-x_2)+P41(x_4-x_3)}{x_4}\right]\sin n y_1 + \right.$$

$$+\left[\frac{P12(x_1)+P22(x_2-x_1)+P32(x_3-x_2)+P42(x_4-x_3)}{x_4}\right]\left[\sin\alpha_n y_2-\sin\alpha_n y_1\right]$$

$$\left.-\left[\frac{P13(x_1)+P23(x_2-x_1)+P33(x_3-x_2)+P43(x_4-x_3)}{x_4}\right]\sin\alpha_n y_2\right\} \qquad \text{(III.41)}$$

and:

$$C'_{on} = \frac{C_{on}}{k\alpha_n^2} \qquad \text{(III.42)}$$

The final expression necessary is the series representation of the power, which is:

$$q''' = \bar{q}''' + \sum_{m=1}^{\infty}\sum_{n=1}^{\infty} C_{mn}\cos\alpha_m x\cos\alpha_n y +$$

$$+\sum_{m=1}^{\infty} C_{mo}\cos\alpha_m x + \sum_{n=1}^{\infty} C_{on}\cos\alpha_n y \qquad \text{(III.43)}$$

This series was tested to find the number of terms required to converge to the actual value of the power. Results are tabulated below.

Point		Actual	Power With	Power with
x	y	Power	n = m = 30	n = m = 100
.8	1.3	.6	.598	.601
.8	5.0	.9	.891	.907
.8	10.0	.8	.790	.798
3.0	1.3	1.0	.996	1.002
3.0	5.0	1.3	1.277	1.304
3.0	10.0	.7	.706	.705
6.0	1.3	1.2	1.204	1.202
6.0	5.0	.8	.871	.804
6.0	10.0	1.7	1.695	1.696
9.0	1.3	1.4	1.408	1.395
9.0	5.0	1.7	1.707	1.694
9.0	10.0	2.0	2.006	1.998

It can be noticed that a large number of terms have to be considered to find the correct value of the power distribution. This point is very important since it has a large influence on the limitations of the analytical method for calculation of N_H values.

Once the constants C_{mn}, C_{mo}, and C_{on} are known, the calculation of N_H is quite simple.

Using Equation (III.36)

$$N_H(z) = \frac{\text{NUMERATOR}}{\text{DENOMINATOR}} \qquad \text{(III.44)}$$

where:

$$\text{NUMERATOR} = \sum_{m=1}^{\infty}\sum_{n=1}^{\infty}\left\{\frac{C'_{mn}}{\alpha_m\alpha_n}\left(1-e^{-a_t\alpha_{mn}^2 t}\right)\left(\frac{\sin\alpha_m x_2-\sin\alpha_m x_1}{x_2-x_1}-\right.\right.$$

$$\left.\left.-\frac{\sin\alpha_m x_3-\sin\alpha_m x_2}{x_3-x_2}\right)\left(\sin\alpha_n y_2-\sin\alpha_n y_1\right)\right\}+$$

$$+\sum_{m=1}^{\infty}\left\{\frac{C'_{mo}}{\alpha_m}\left(1-e^{-a_t\alpha_m^2 t}\right)\left(\frac{\sin\alpha_m x_2-\sin\alpha_m x_1}{x_2-x_1}-\right.\right.$$

$$\left.\left.-\frac{\sin\alpha_m x_3-\sin\alpha_m x_2}{x_3-x_2}\right)\right\} \qquad \text{(III.45)}$$

and

$$\text{DENOMINATOR} = 2\sum_{m=1}^{\infty}\sum_{n=1}^{\infty}\left\{\frac{C'_{mn}}{\alpha_m\alpha_n}\left(1-e^{-a_t\alpha_{mn}^2 t}\right)\left(\sin\alpha_m x_2\right)\left(1-\cos\alpha_m P\right)\right.$$

$$\left.\left(\sin\alpha_n y_2-\sin\alpha_n y_1\right)\right\}+$$

$$+2\sum_{m=1}^{\infty}\left\{\frac{C'_{mo}}{\alpha_n}\left(1-e^{-a_t\alpha_m^2 t}\right)\left(\sin\alpha_m x_2\right)\left(1-\cos\alpha_m P\right)\right\}$$

(III.46)

and where:

$$a_t = \varepsilon_H \qquad \text{(III.47)}$$

$$t = \frac{z}{v_z} \qquad \text{(III.48)}$$

$$\alpha_{mn}^2 = \alpha_m^2 + \alpha_n^2 \qquad \text{(III.49)}$$

All the terms of these equations, i.e. (III.45) and (III.46) are known except ε_H, the thermal eddy diffusivity. In order to obtain identical results for $N_H(z)$ using the analytical method to those given by the numerical method, we have to match the energy interchange due to turbulence for every boundary of the problem. This implies that ε_H should be dependent on x, y and z. However in our analytical derivation ε_H had to be assumed constant to permit solution of the differential equation. So an approximation should be made in order to find an average value of ε_H. This value is calculated using the following equation:

$$\underset{\text{Num.}}{\frac{w'(I,J)(h(I)-h(J))}{M(I)}} = \underset{\text{Analytic}}{\frac{\varepsilon_H \rho s_{ij}}{M(I)} \left.\frac{\partial h}{\partial x}\right|_{gap}} \equiv \underset{\text{T.I.}}{\Delta h(I)} \qquad \text{(III.49)}$$

where $\underset{\text{T.I.}}{\Delta h(I)}$ = enthalpy rise of channel I due to turbulent interchange

Taking w'(I,J) as COBRA does:

$$w'(I,J) = \beta s_{ij} \bar{G} \qquad \text{(III.50)}$$

we obtain:

$$\varepsilon_H = \beta \bar{v}_z \frac{(h(I)-h(J))}{\left.\frac{\partial h}{\partial x}\right|_{gap}} \left[\frac{M(I)}{M(I)}\begin{matrix}\text{analyt.}\\ \text{numer.}\end{matrix}\right] \qquad \text{(III.51)}$$

The massflow ratio is required due to the different area of the subchannels in the analytic and the numerical method (Appendix C Volume I). The analytic method assumes each subchannel of area:

$$A_{analytic} = Ps_{ij} = .666(.1333) = .074 \text{ in}^2 \qquad \text{(III.52)}$$

while the numerical method takes:

$$A_{numerical} = .1705 \text{ in}^2 \qquad \text{(III.53)}$$

The ratio:

$$\frac{h(I)-h(J)}{\left.\frac{\partial h}{\partial x}\right|_{gap}} = \bar{z}_{ij} \qquad \text{(III.54)}$$

is dependent upon axial position, radial position and power shape across the boundary. With these parameters, equation (III.51) reduces to

$$\varepsilon_H = .434\beta\, \bar{v}_z \bar{z}_{ij} \qquad \text{(III.55)}$$

An average value of the product:

$$l_{ij} = .434 z_{ij} \qquad \text{(III.56)}$$

has been correlated as a function of β (Figure III.2). This value was obtained by comparing analytical and numerical values of $N_H(z)$

for a different set of values of l_{ij}. However, Figure III.2 is not a general one and in order to apply the analytical method to different problems (different channel dimensions or power shapes) a new correlation should be obtained.

Using now Equations (III.56), (III.55), (III.46), (III.45), and (III.44) we obtain the following expression for $N_H(z)$:

$$N_H(z) = \frac{\text{NUMERATOR}}{\text{DENOMINATOR}} \tag{III.57}$$

$$\text{NUMERATOR} = \sum_{m=1}^{\infty}\sum_{n=1}^{\infty}\left\{\frac{C'_{mn}}{\alpha_m\alpha_n}(1-e^{-\beta l_{ij} z\alpha_{mn}^2})\left(\frac{\sin\alpha_m x_2-\sin\alpha_m x_1}{x_2-x_1}-\frac{\sin\alpha_m x_3-\sin\alpha_m x_2}{x_3-x_2}\right)(\sin\alpha_n y_2-\sin\alpha_n y_1)\right\} +$$

$$+\sum_{m=1}^{\infty}\left\{\frac{C'_{mo}}{\alpha_m}(1-e^{-\beta l_{ij} z\alpha_{mn}^2})\left(\frac{\sin\alpha_m x_2-\sin\alpha_m x_1}{x_2-x_1}-\frac{\sin\alpha_m x_3-\sin\alpha_m x_2}{x_3-x_2}\right)\right\} \tag{III.58}$$

$$\text{DENOMINATOR} = 2\sum_{m=1}^{\infty}\sum_{n=1}^{\infty}\left\{\frac{C'_{mn}}{\alpha_m\alpha_n}(1-e^{-\beta l_{ij} z\alpha_{mn}^2})(\sin\alpha_m x_2)(1-\cos\alpha_m P)(\sin\alpha_n y_2-\sin\alpha_n y_1)\right\} +$$

$$+2\sum_{m=1}^{\infty}\left\{\frac{C'_{mo}}{\alpha_m}(1-e^{-\beta l_{ij} z\alpha_{mn}^2})(\sin\alpha_m x_2)(1-\cos\alpha_m P)\right\} \tag{III.59}$$

3.3 Comparison Between the Numerical and the Analytical Methods

The Case of No. 29 (Section 3.3) ($\beta = 0.2$) was run numerically and analytically using two different values for the parameter l_{ij}. The results are presented in Figure III.3. It can be observed that the results do not match exactly even for the recommended value of l_{ij} (i.e., $l_{ij} = .11$). As indicated in the previous section it is due to the fact that in order to match the numerical results exactly l_{ij} should be a variable with x, y and z.

3.4 Conclusion

The development of transport coefficients should be based on three dimensional model considering arbitrary bundle power generation rates. In our investigation we did develop the general methodology and applied it to a specific case. The result indicated that

a) enthalpy errors in the 3D case without application of coupling coefficients were greater than an analogous 2D problem

b) N_H values from 2D problem exhibited the same trends but different numerical values from those from the 3D problem.

c) the N_H values from 3D problems are sensitive to power levels in regions adjacent to the boundary of interest.

From these results we conclude that practical 3D recommendations for N_H will require development of a means to consolidate the large number of boundaries having unique neighboring region power profiles that would be encountered in analysis of any one core.

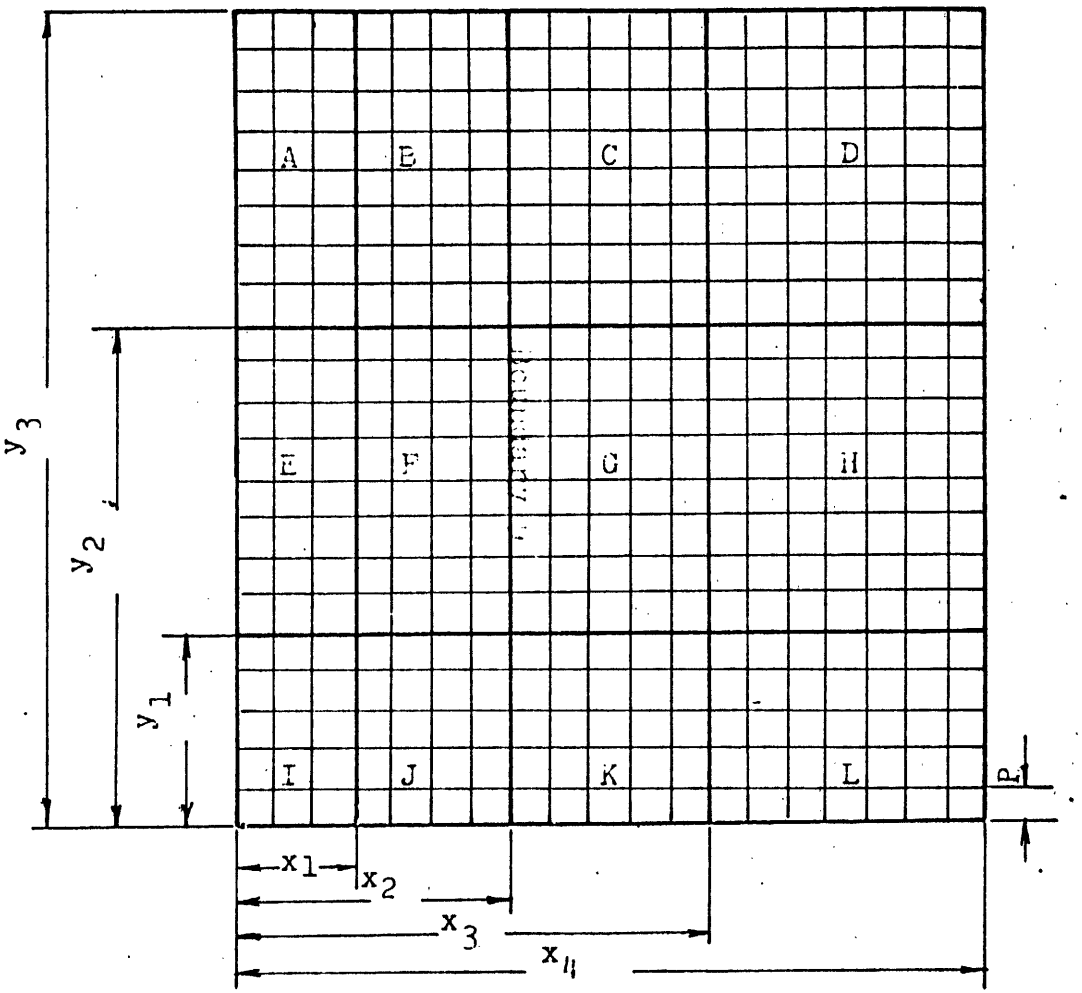

Figure III.1

3D Example Case

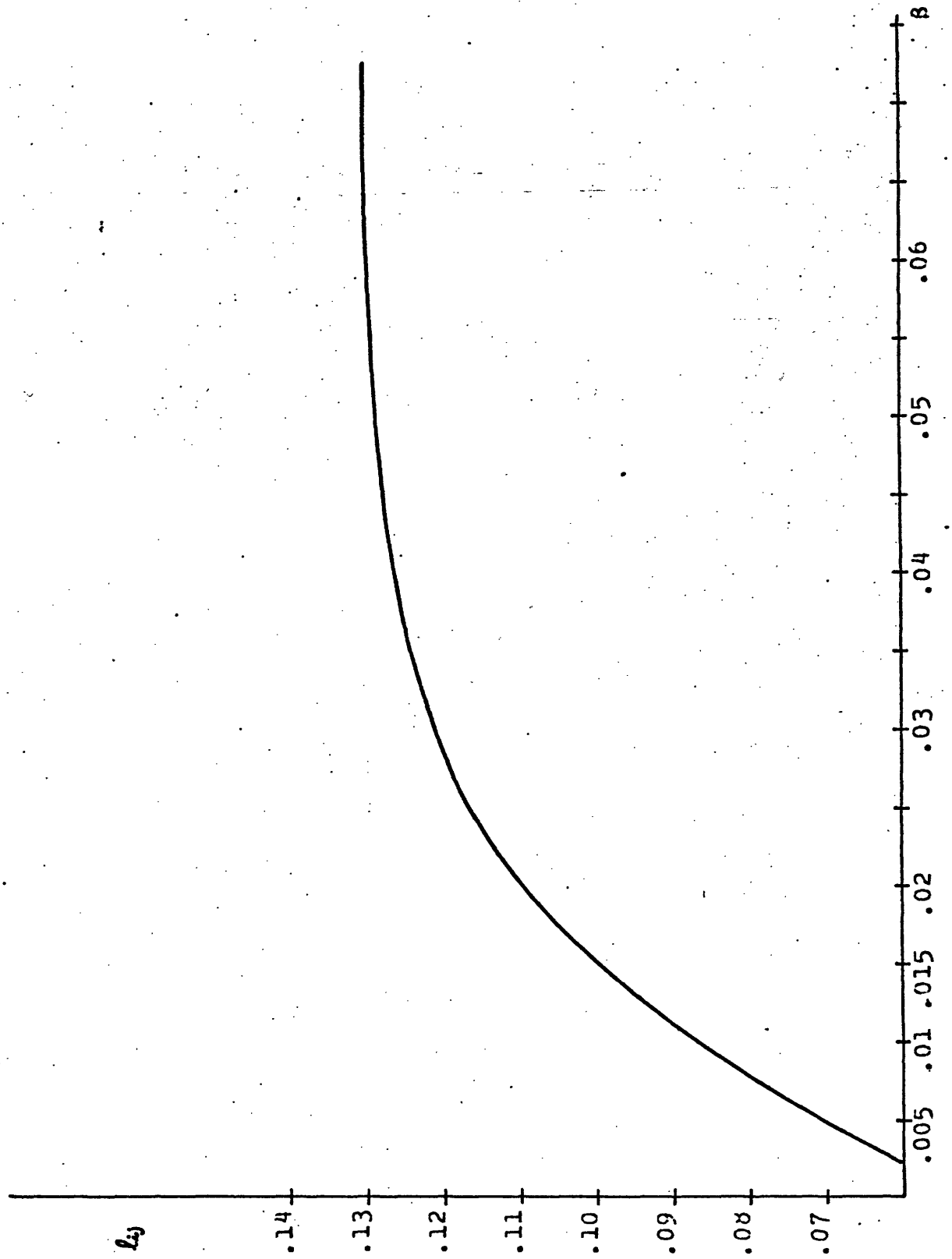

Figure III.2

Recommended Values of l_{ij} as Function of β

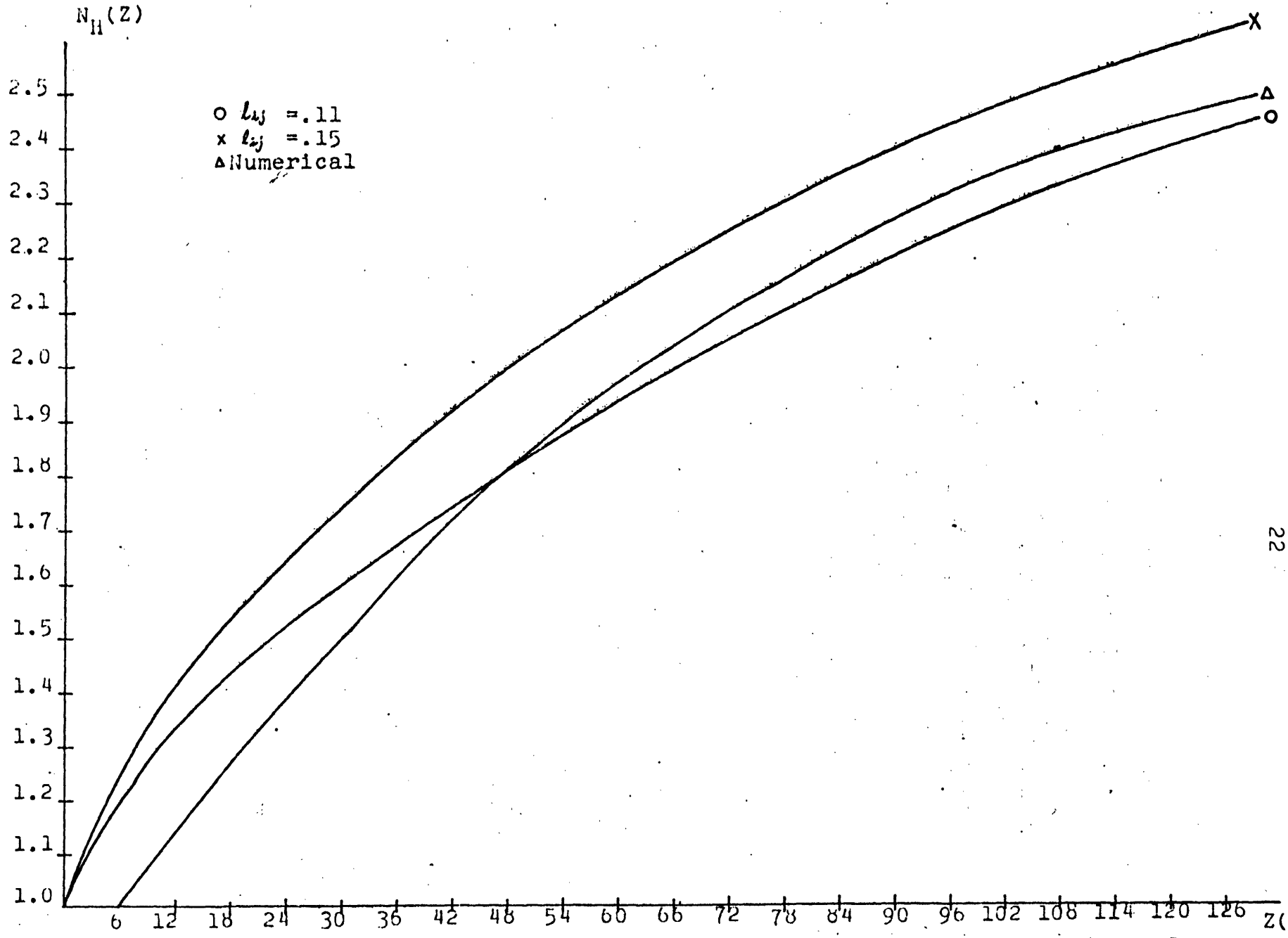

Comparison between $N_H(z)$ determined by analytical and numerical methods for the case of figure 13 (Chapter 3, Volume I)

Figure III.3